

Gdański Uniwersytet Medyczny

Wydział Farmaceutyczny



mgr farm. Adrianna Skwira

**Biokompatybilne nośniki substancji leczniczej do tkanki kostnej
na bazie mezoporowatych materiałów krzemionkowych**

Miejsca realizacji pracy:

Katedra i Zakład Chemii Fizycznej, Wydział Farmaceutyczny
Gdańskiego Uniwersytetu Medycznego

Zakład Enzymologii i Onkologii Molekularnej,
Instytut Biotechnologii Medycznej i Onkologii Doświadczalnej,
Międzyuczelniany Wydział Biotechnologii
Uniwersytetu Gdańskiego i Gdańskiego Uniwersytetu Medycznego

Promotorzy pracy:

Prof. dr hab. n. farm. Magdalena Prokopowicz
Dr hab. n. med. Rafał Sądej, prof. GUMed

Gdańsk, 2023

*Pragnę złożyć serdeczne podziękowania Pani Promotor,
Profesor Magdalenie Prokopowicz,
za opiekę merytoryczną, inspirację naukową,
zaufanie i poświęcony mi czas.*

*Dziękuję Panu Promotorowi,
Profesorowi Rafałowi Sądejowi,
za życzliwość i cenne wskazówki merytoryczne.*

*Dziękuję wszystkim Koleżankom i Kolegom,
z którymi miałam przyjemność współpracować,
za wszelką pomoc i przyjazną atmosferę w pracy.*

*Dziękuję Najbliższym
za wsparcie i wyrozumiałość.*

*Rozprawę doktorską dedykuję moim Rodzicom,
którym ogromnie dziękuję za nieustanne wsparcie
i nieskończoną wiarę w moje możliwości
na każdym etapie mojej drogi życiowej.*

Spis treści

Wykaz prac naukowych, będących podstawą rozprawy doktorskiej	2
Projekty, w ramach których sfinansowano zadania badawcze, będące przedmiotem niniejszej rozprawy doktorskiej.....	3
Streszczenie w języku polskim	4
Streszczenie w języku angielskim	6
1. Wstęp.....	8
1.1. <i>Osteomyelitis</i> – etiologia i epidemiologia	8
1.2. <i>Osteomyelitis</i> – leczenie	9
1.3. Miejscowe nośniki substancji leczniczej do tkanki kostnej	11
1.4. Wybrane biomateriały wykorzystywane w inżynierii tkanki kostnej do otrzymywania miejscowych nośników substancji leczniczych	12
1.4.1. Polimetakrylan metylu (PMMA)	12
1.4.2. Mezoporowate materiały krzemionkowe	13
1.4.3. Bioszkoło	15
1.4.4. Kolagen typu I.....	18
2. Cel rozprawy doktorskiej.....	22
3. Metodyka, wyniki i dyskusja	24
3.1. Otrzymanie i charakterystyka mezoporowatego materiału krzemionkowego MCM-41 jako nośnika o przedłużonym uwalnianiu substancji leczniczej.....	24
3.2. Otrzymanie i charakterystyka bioszkoła jako materiału o potencjalnych właściwościach regenerujących tkankę kostną	69
3.3. Otrzymanie i charakterystyka rusztowań kolagenowo-krzemionkowych jako potencjalnych systemów dostarczających substancję leczniczą i regenerujących tkankę kostną	92
4. Podsumowanie i wnioski.....	134
5. Bibliografia	137

Wykaz prac naukowych, będących podstawą rozprawy doktorskiej

1. A. Skwira, A. Szewczyk, M. Prokopowicz, The Effect of Polydimethylsiloxane-Ethylcellulose Coating Blends on the Surface Characterization and Drug Release of Ciprofloxacin-Loaded Mesoporous Silica, *Polymers (Basel)*. 11 (2019) 1450. <https://doi.org/10.3390/polym11091450> (IF: 3,426; MNiSW: 100,000).
2. A. Skwira, A. Szewczyk, A. Konopacka, M. Górka, D. Majda, R. Sądej, M. Prokopowicz, Silica-polymer composites as the novel antibiotic delivery systems for bone tissue infection, *Pharmaceutics*. 12 (2020) 28. <https://doi.org/10.3390/pharmaceutics12010028> (IF: 6,321; MNiSW: 100,000).
3. A. Skwira, A. Szewczyk, R. Sądej, M. Prokopowicz, Bioglass obtained via one-pot synthesis as osseointegrative drug delivery system, *Int. J. Pharm.* 633 (2023) 122610. [https://doi.org/https://doi.org/10.1016/j.ijpharm.2023.122610](https://doi.org/10.1016/j.ijpharm.2023.122610) (IF: 6,510; MNiSW: 100,000).
4. A. Skwira, A. Szewczyk, J. Barros, M. Laranjeira, F.J. Monteiro, R. Sądej, M. Prokopowicz. Biocompatible antibiotic-loaded mesoporous silica/bioglass/collagen-based scaffolds as bone drug delivery systems – w trakcie recenzji na dzień złożenia pracy doktorskiej w czasopiśmie *Int. J. Pharm.* (IF: 6,510; MNiSW: 100,000).

Projekty, w ramach których sfinansowano zadania badawcze, będące przedmiotem niniejszej rozprawy doktorskiej

1. Grant OPUS 15 (2018/29/B/NZ7/00533), Narodowe Centrum Nauki, pt. „Dwufunkcyjne kompozyty krzemionkowe dla tkanki kostnej – potencjalne znaczenie terapeutyczne i regeneracyjne”,
kierownik projektu: prof. dr hab. n. farm. Magdalena Prokopowicz.
2. Grant Preludium 20 (2021/41/N/NZ7/01877), Narodowe Centrum Nauki, pt. „Rusztowania kolagenowo-krzemionkowe jako potencjalne systemy dostarczające substancję leczniczą i regenerującą tkankę kostną”,
kierownik projektu: mgr farm. Adrianna Skwira.
3. Grant Młody Twórca Nauki I (664/518/63/73-3318), pt. „Ocena potencjału osseointegracyjnego bioszkieletu w warunkach *in vitro* względem ludzkich osteoblastów”,
kierownik projektu: mgr farm. Adrianna Skwira.
4. Dofinansowanie zadania badawczego Młodego Badacza Gdańskiego Uniwersytetu Medycznego (01-0469/08/518), pt. „Synteza, badania fizykochemiczne, mikrobiologiczne i biologiczne dwufunkcyjnych kompozytów jako potencjalnych nośników leków”,
kierownik projektu: mgr farm. Adrianna Skwira.
5. Projekt POWER1 (POWR.03.02.00-00-I035/16-00) – Program Operacyjny Wiedza Edukacja Rozwój 2014-2020, współfinansowany ze środków Europejskiego Funduszu Społecznego, przyznany przez Narodowe Centrum Badań i Rozwoju.

Część zadań badawczych została zrealizowana podczas stażu zagranicznego w Instytucie Badań i Innowacji w Naukach o Zdrowiu Uniwersytetu w Porto (Portugalia) w ramach współpracy z prof. Fernando Jorge Monteiro, dr Martą Laranjeira oraz dr Joana Barros.

Streszczenie w języku polskim

Zapalenie kości i szpiku kostnego (*osteomyelitis*) jest najczęściej konsekwencją zakażenia metacylino-wrażliwym gronkowcem złocistym (*Staphylococcus aureus*). Obecnie stosowana strategia leczenia wymaga długotrwałej (od 4 do 6 tygodni) doustnej lub parenteralnej antybiotykoterapii. Ze względu na niską penetrację większości antybiotyków do tkanki kostnej, leczenie systemowe wiąże się z koniecznością stosowania ich w wysokich dawkach, co zwiększa ryzyko wystąpienia toksyczności ogólnoustrojowej. W związku z tym, nowoczesna strategia podawania antybiotyków bezpośrednio do tkanki kostnej zyskuje coraz większe zainteresowanie jako skuteczna i stosunkowo bezpieczna terapia uzupełniająca lub zastępująca leczenie systemowe. Obecnie stosowane sferyczne granulaty z polimetakrylanu metylu wykazują skuteczność w miejscowym leczeniu *osteomyelitis*, natomiast nie integrują się z tkanką kostną pacjenta. Wiąże się to z koniecznością ich usunięcia po uwolnieniu całkowitej ilości antybiotyku w trakcie kolejnej procedury operacyjnej, co stanowi ryzyko wtórnego zakażenia bakteryjnego.

Celem niniejszej pracy doktorskiej było otrzymanie biozgodnych nośników substancji leczniczej do tkanki kostnej na bazie mezoporowatych materiałów krzemionkowych o potencjalnym zastosowaniu w miejscowym leczeniu *osteomyelitis*. Założono, że nośniki te powinny nie tylko uwalniać antybiotyk w sposób przedłużony, ale także stymulować procesy regeneracji tkanki kostnej.

W pierwszym etapie otrzymano za pomocą metody zol-żel mezoporowaty materiał krzemionkowy MCM-41, na którym zaadsorbowano modelowy antybiotyk – cyprofloksacynę. Następnie materiał poddano modyfikacji za pomocą odpowiednich polimerowych mieszanin powlekających złożonych z etylocelulozy i polidimetylosiloksanu (PDMS-u). Przeprowadzone analizy dowiodły, że obecność PDMS-u w formulacjach skutkowało oczekiwanym przedłużeniem uwalniania cyprofloksacyny, poprawą parametrów tekstury, zwiększeniem stabilności termicznej antybiotyku, długotrwałą aktywnością przeciwdrobnoustrojową oraz biozgodnością z ludzkimi osteoblastami. Potwierdzono, w ten sposób, możliwość pełnienia przez modyfikowany mezoporowaty materiał krzemionkowy funkcji nośnika substancji leczniczej o przedłużonym uwalnianiu.

Następnie na drodze zmodyfikowanej metody zol-żel otrzymano bioszkło – materiał należący do grupy ceramik bioaktywnych. Jego zdolność do osseointegracji

poddano ocenie w modelu *in vitro* w porównaniu z dwoma bioszkłami komercyjnymi. Wykazano biozgodność otrzymanego bioszka na poziomie komórkowym oraz promujący wpływ uwalnianych z jego struktury jonów wapnia i ortokrzemianów na różnicowanie osteoblastów i proces mineralizacji. Dowiedziono, że charakteryzuje się ono lepszymi właściwościami osteoindukcyjnymi oraz osteokondukcyjnymi niż analizowane materiały komercyjne. Na podstawie otrzymanych wyników potwierdzono potencjalną przydatność otrzymanego bioszka jako materiału stymulującego procesy regeneracyjne tkanki kostnej.

W ostatnim etapie badań otrzymano rusztowania kolagenowo-krzemionkowe w wyniku połączenia modyfikowanego mezoporowatego materiału krzemionkowego zawierającego cyprofloksacynę, bioszka oraz kolagenu typu I. Cylindryczne rusztowania sporządzono za pomocą metody wylewania do form oraz liofilizacji. Następnie poddano je badaniu dostępności farmaceutycznej, ocenie właściwości fizykochemicznych, mikrobiologicznych i biologicznych w modelach *in vitro* oraz *in vivo*. Rusztowania kolagenowo-krzemionkowe charakteryzowały się stabilną, wysoce porowatą strukturą. Stopniowe formowanie się na ich powierzchni hydroksyapatytu o morfologii i składzie pierwiastkowym zbliżonymi do apatytu kostnego w płynie symulującym ludzkie osocze potwierdziło właściwości mineralizacyjne rusztowań. Profil uwalniania cyprofloksacyny charakteryzował się początkowym uwolnieniem (w ciągu pierwszych 24 godzin badania) wynoszącym 44% całkowitej ilości antybiotyku oraz całkowitym czasem uwalniania równym 80 dni. Za pomocą analizy mikrobiologicznej dowiedziono, iż uwalniany z rusztowań kolagenowo-krzemionkowych antybiotyk zapobiega rozwojowi biofilmu bakteryjnego. Otrzymane rusztowania wykazały wysoką biozgodność zarówno na poziomie komórkowym *in vitro*, jak również w modelu *in vivo* CAM (ang. *Chick Chorioallantoic Membrane*, błona kosmówkowo-omoczniowa).

Zrealizowane w ramach pracy doktorskiej zadania badawcze pozwoliły na osiągnięcie wyznaczonego celu. Na podstawie uzyskanych wyników stwierdzono, że proponowane rusztowania kolagenowo-krzemionkowe mogą służyć jako wielofunkcyjne nośniki, które nie tylko zapewniają przedłużone uwalnianie antybiotyku, ale również wykazują potencjalne właściwości regeneracyjne poprzez promowanie formowania hydroksyapatytu oraz adhezji i proliferacji osteoblastów. W celu oceny aplikacyjności proponowanych rusztowań kolagenowo-krzemionkowych w kolejnym etapie badań planuje się przeprowadzenie długookresowej oceny odpowiedzi biologicznej *in vivo* w ssaczych modelach zwierzęcych.

Streszczenie w języku angielskim

Osteomyelitis, an inflammatory process involving the bone and its marrow, is most frequently caused by infection with methicillin-sensitive *Staphylococcus aureus*. The current treatment strategy requires long-term (4 to 6 weeks) oral or parenteral antibiotic therapy. Due to the low penetration of most antibiotics into bone tissue, systemic treatment requires the use of high doses of drugs, thus, increasing the risk of systemic toxicity. Therefore, the local administration of antibiotics directly to the bone tissue is gaining increasing interest as an effective and relatively safe complementary or alternative therapy to systemic treatment. Currently applied polymethyl methacrylate (PMMA) beads have shown efficacy in treating *osteomyelitis* but do not integrate with the patient's bone tissue. This necessitates their removal after the complete release of antibiotic during subsequent surgical procedure, posing a risk of secondary bacterial infection.

The aim of this dissertation was to develop a biocompatible drug delivery system based on mesoporous silica materials dedicated to the local treatment of *osteomyelitis*. Such system was designed to release antibiotics in a prolonged manner and stimulate the process of bone tissue regeneration.

In the first stage, mesoporous silica material MCM-41 was obtained using the sol-gel method, and loaded with the model antibiotic – ciprofloxacin. Subsequently, ciprofloxacin-loaded mesoporous silica material MCM-41 was modified with polymer coating blends composed of ethylcellulose and polydimethylsiloxane (PDMS). The analyses demonstrated that the presence of PDMS in the formulations resulted in the desired prolonged release of ciprofloxacin, improved textural parameters, increased thermal stability of the antibiotic, long-lasting antimicrobial activity, and biocompatibility with human osteoblasts. This confirmed the potential of PDMS-modified mesoporous silica materials to serve as antibiotic carriers with prolonged release.

Next, bioglass, a material belonging to the group of the most bioactive ceramics, was obtained using a modified sol-gel method. The osseointegration capacity of the obtained bioglass was evaluated in an *in vitro* model compared to two commercial bioglasses. This demonstrated the biocompatibility of the obtained bioglass with the osteoblasts, as well as the promoting effect of calcium ions and orthosilicates released from its structure on osteoblast differentiation and mineralization processes. Additionally,

obtained bioglass was characterized by more favorable osteoinductive and osteoconductive properties compared to commercial materials. Based on these results, the potential usefulness of the obtained bioglass as a material for stimulating bone tissue regeneration processes was confirmed.

In the final stage, modified ciprofloxacin-loaded mesoporous silica materials, bioglass, and collagen type I were combined into collagen-silica scaffolds. The cylindrical scaffolds were prepared using molding and freeze-drying method. Then, they were subjected to the drug release study, evaluation of physicochemical, and microbiological properties, as well as biological response using *in vitro* and *in vivo* models. The collagen-silica scaffolds exhibited a stable and highly porous structure. The progressive formation of hydroxyapatite, with morphology and elemental composition similar to bone apatite, onto the scaffolds in a simulated body fluid was confirmed, indicating their mineralization properties. The release profile of ciprofloxacin was characterized by reduced initial burst within the first 24 hours of the study and a total release time of 80 days. The microbiological analysis demonstrated that the released antibiotic prevented the development of bacterial biofilm. The obtained scaffolds showed high biocompatibility both at the cellular level, with human osteoblasts, as well as in an *in vivo* CAM (*Chick Chorioallantoic Membrane*) model.

The stated aim of the dissertation has been achieved. Based on the results, it was concluded that the proposed collagen-silica scaffolds may serve as multifunctional carriers which not only provide prolonged antibiotic release but also exhibit potential regenerative properties by promoting hydroxyapatite formation and osteoblast adhesion and proliferation. To evaluate the applicability of the proposed collagen-silica scaffolds, the next stage of the research is to evaluate the long-term biological response *in vivo* using mammalian model organisms.

1. Wstęp

1.1. *Osteomyelitis* – etiologia i epidemiologia

Osteomyelitis jest definiowane jako zapalenie kości i szpiku kostnego. Według zaproponowanej przez Ciernego i Madera klasyfikacji, u dorosłego człowieka wyróżnia się cztery anatomiczne typy *osteomyelitis*:

- typ I – wewnątrzszpikowy (ang. *medullary*) – zmiana chorobowa znajduje się w jamie szpikowej kości,
- typ II – powierzchowny (ang. *superficial*) – zmiana chorobowa znajduje się na powierzchni kości,
- typ III – ograniczony (ang. *localized*) – wyraźne ognisko chorobowe znajduje się w obrębie stabilnego segmentu kostnego,
- typ IV – rozlany (ang. *diffuse*) – zmiany chorobowe obejmują cały segment kości, a leczenie wymaga jej stabilizacji [1].

Lew i Waldvogel dokonali podziału *osteomyelitis* według:

- mechanizmu zakażenia (krwiopochodny i przyległy),
- czasu trwania choroby (ostrej i przewlekłej) [2].

Osteomyelitis może być konsekwencją zakażenia bakteryjnego, wirusowego lub grzybiczego. Do zakażenia kości i szpiku kostnego może dojść drogą krwiopochodną poprzez przeniesienie drobnoustroju z odległego miejsca zakażenia, wskutek rozprzestrzenienia się zakażenia z otaczających tkanek miękkich oraz stawów lub na drodze bezpośredniego wniknięcia drobnoustroju w wyniku urazu lub w trakcie operacji chirurgicznej. Krwiopochodne zakażenie kości częściej występuje u dzieci i najczęściej dotyka kości długich. U dorosłych zmiany chorobowe obejmują głównie kręgi. Przylegające zakażenie kości i szpiku kostnego zazwyczaj rozwija się u osób predysponowanych do powstawania owrzodzeń skóry. Przykładem są pacjenci cierpiący na cukrzycę typu I lub II z towarzyszącymi owrzodzeniami podszwowej lub grzbietowej części stopy (tzw. stopa cukrzycowa). Do wystąpienia tego wariantu *osteomyelitis* może dojść również w następstwie urazu prowadzącego do zakażenia odsłoniętej skóry i tkanek miękkich. Pourazowe i pooperacyjne zakażenie tkanki kostnej stanowi 80% wszystkich diagnozowanych przypadków [3]. Tylko w samych Stanach Zjednoczonych przeprowadza się rocznie około 600 000 zabiegów implantacji endoprotez i 2 miliony zabiegów implantacji urządzeń do stabilizacji złamań, co prowadzi do ponad 110 000

zakażeń [4]. Ostra postać *osteomyelitis* rozwija się w ciągu kilku dni i trwa do kilku tygodni. Postać przewlekła rozpoznawana jest, gdy objawy utrzymują się powyżej kilku miesięcy lub gdy infekcja nawraca. Niektóre źródła literaturowe wyróżniają także postać podostrą, trwającą od dwóch do czterech tygodni [5].

Przyczyną 75% wszystkich przypadków *osteomyelitis* jest zakażenie tkanki kostnej metycyliny-wrażliwym gronkowcem złocistym (*Staphylococcus aureus*) [6]. Do pozostałych patogenów izolowanych z zakażonej tkanki należą: pałeczka ropy błękitnej (*Pseudomonas aeruginosa*) oraz metycyliny-oporny *Staphylococcus aureus*. W przypadku krwiopochodnego zakażenia tkanki kostnej najczęściej stwierdza się zakażenie pojedynczym patogenem z grupy tlenowych pałeczek Gram-ujemnych, paciorkowcem ropnym (*Streptococcus pyogenes*) lub pałeczką krwawą (*Serratia marcescens*). Niekrwiopochodne *osteomyelitis* zazwyczaj wywołane jest przez wielobakteryjne zakażenie *Staphylococcus aureus* oraz koagulazo-ujemne gronkowce, a także Gram-ujemne tlenowce i beztlenowce [7].

Częstotliwość występowania *osteomyelitis* nie jest w pełni określona, a zgromadzone dane epidemiologiczne różnią się w zależności od kraju, w którym przeprowadzono analizę. Średnia zapadalność roczna w Stanach Zjednoczonych jest szacowana na 21,8 przypadków na 100 000 osób. Obserwuje się przewagę liczby zachorowań w populacji mężczyzn oraz wzrost ryzyka zachorowania wraz z wiekiem (50-procentowy wzrost przypadający na każdą dekadę życia u pacjentów powyżej 60 lat) [8]. W populacji dzieci w krajach wysoko rozwiniętych współczynnik zachorowalności wynosi od 10 do 80 przypadków na 100 000 dzieci [9–11], a w krajach nisko rozwiniętych liczba ta sięga nawet 200 przypadków na 100 000 dzieci [12]. Ponadto zachorowalność na *osteomyelitis* w Stanach Zjednoczonych wzrosła prawie 3-krotnie w ciągu ostatnich dwudziestu lat [13]. Szacuje się, że rocznie na *osteomyelitis* chorują 4 miliony pacjentów na świecie, z czego 0,5 miliona przypada na Stany Zjednoczone i Unię Europejską [14].

1.2. Osteomyelitis – leczenie

Leczenie zapalenia kości i szpiku stanowi kliniczne wyzwanie dla chirurgii ortopedycznej. Obecnie powszechnym postępowaniem w ostrej postaci *osteomyelitis* jest stosowanie antybiotykoterapii doustnej lub dożylniej. Natomiast osiągnięcie pełnego wyleczenia przewlekłej postaci jest skomplikowane i długotrwałe.

Kluczowe etapy leczenia przewlekłej postaci *osteomyelitis* to:

- zabieg operacyjny (usunięcie zakażonych tkanek, wypełnienie przestrzeni martwej, przywrócenie dopływu krwi, stabilizacja i rekonstrukcja uszkodzonej kości),
- usunięcie wszystkich ciał obcych (np. materiału protetycznego),
- systemowa terapia przeciwdrobnoustrojowa trwająca od 4 do 6 tygodni [15].

W przypadku niepowodzenia leczenia istnieje ryzyko nawrotu infekcji miejscowej lub uogólnionej, co może prowadzić do niepełnosprawności, sepsy, niewydolności wielonarządowej, a nawet śmierci [6]. Skuteczność farmakoterapii zależy od wrażliwości bakterii kolonizujących tkankę kostną na podawany antybiotyk oraz stężenia antybiotyku w obszarze objętym infekcją.

W okresie przed rozpoczęciem stosowania antybiotyków śmiertelność wywołana *osteomyelitis* wynosiła ok. 50%. Po odkryciu penicyliny przez A. Fleminga, cztery niezależne grupy badawcze podjęły próbę domięśniowego podania tego antybiotyku łącznie 135 pacjentom z zakażeniem kości wywołanym przez *Staphylococcus aureus*. Po przeprowadzonej interwencji medycznej nie odnotowano żadnych zgonów, a odsetek klinicznych wyleczeń wynosił powyżej 80% [16]. W następnych latach, w wyniku występowania oporności bakteryjnej na stosowane substancje przeciwdrobnoustrojowe, znaczenie w leczeniu zyskiwały kolejne ich grupy, takie jak cefalosporyny, tetracykliny, czy fluorochinolony. W 2019 roku opublikowano wyniki randomizowanego, kontrolowanego badania klinicznego *Oral Versus Intravenous Antibiotics for Bone and Joint Infections (OVIVA)*, w którym porównano skuteczność leczenia antybiotykami podawanymi drogą doustną oraz dożylną. Nie stwierdzono różnic pomiędzy badanymi grupami pacjentów [17]. Niemniej jednak, antybiotyki charakteryzują się niską penetracją do tkanki kostnej (stosunek stężenia kość/surowica dla większości grup antybiotyków stosowanych w *osteomyelitis* wynosi średnio około 0,3 [18]). Mając na uwadze niską penetrację antybiotyków do tkanki kostnej oraz słabe unaczynienie obszaru objętego martwicą, leczenie dożylnie lub doustnie wymaga podawania wysokich dawek antybiotyków w celu osiągnięcia skutecznych stężeń w miejscu zakażenia. Takie postępowanie wiąże się z wysokim ryzykiem wystąpienia toksyczności ogólnoustrojowej, która może znacząco pogorszyć ogólny stan zdrowia pacjentów [19].

Obecnie, w obliczu narastającej oporności, wybór odpowiedniego antybiotyku powinien być poprzedzony wykonaniem antybiogramem. Jeżeli czynnik etiologiczny wywołujący zakażenie i wrażliwość bakterii na antybiotyki są nieznane, dopuszcza się

prowadzenie terapii empirycznej na podstawie objawów klinicznych, potwierdzonych markerów zakażenia czy wyników badań obrazowych. Powszechnie stosowanym schematem leczenia przeciwko zarówno bakteriom Gram-dodatnim, jak i Gram-ujemnym jest podawana dożylnie wankomycyna w połączeniu z cefalosporyną III generacji (np. ceftriaksonem) lub kombinacją antybiotyku β -laktamowego z inhibitorem β -laktamaz (np. piperacylina+tazobaktam).

W przypadku stwierdzonego zakażenia metycylino-wrażliwym *S. aureus* rekomenduje się stosowanie nafcyliny, oksacyliny lub cefazoliny, natomiast w przypadku zakażenia metycylino-opornym *S. aureus* rekomendowanym antybiotykiem jest wankomycyna [20]. W zakażeniu penicylino-wrażliwymi paciorkowcami (*Streptococcus spp.*) stosuje się penicylinę G. Antybiotykiem pierwszego wyboru w zakażeniu wrażliwymi na chinolony bakteriami z rodziny *Enterobacteriaceae* jest cyprofloksacyna, natomiast w zakażeniu wywołanym przez *Pseudomonas aeruginosa* zaleca się stosowanie cefepimu lub ceftazydymu, a alternatywnie cyprofloksacyny. W leczeniu zakażeń wywołanych bakteriami beztlennymi antybiotykiem pierwszego wyboru jest klindamycyna oraz tykarcylina z kwasem klawulanowym [21].

1.3. Miejscowe nośniki substancji leczniczej do tkanki kostnej

Miejscowe podawanie antybiotyków bezpośrednio do tkanki kostnej zyskuje coraz większe zainteresowanie jako skuteczna i stosunkowo bezpieczna terapia uzupełniająca lub zastępująca leczenie ogólnoustrojowe [16]. Biomateriały wykorzystywane do otrzymywania miejscowych nośników substancji leczniczych powinny zapewniać im dwie funkcje: uwalnianie substancji leczniczych zgodnie z pożądaną kinetyką oraz regenerację tkanki kostnej.

Podstawową cechą wszystkich implantowanych systemów dostarczających substancje lecznicze do tkanki kostnej jest biogodność (biokompatybilność) definiowana w sposób ogólny przez normę ISO 10993 (*Biological evaluation of medical devices*) jako „zdolność urządzenia medycznego lub materiału do odpowiedniego działania w określonym zastosowaniu”. Nośniki takie nie powinny powodować cytotoksyczności, genotoksyczności, immunogenności, mutagenności, trombogenności oraz stanu zapalnego [22]. Ważną cechą biomateriałów jest także biodegradowalność, czyli zdolność do rozkładu w środowisku biologicznym do nieszkodliwych produktów. Cecha ta eliminuje konieczność usunięcia implantowanego biomateriału po spełnieniu przez niego funkcji leczniczej. Produkty rozkładu powinny być nietoksyczne oraz ulegać

eliminacji z organizmu biorcy lub wbudowaniu w nowo utworzoną tkankę. Jeśli materiał ulega rozkładowi do produktów naturalnie występujących w organizmie człowieka, to wówczas jest on definiowany jako bioresorbowalny [23]. Przykładami takich materiałów są biopolimery oraz ceramiki. Dla prawidłowego przebiegu procesu regeneracji szybkość degradacji powinna korelować z szybkością wzrostu nowej tkanki kostnej. Implantowane biomateriały powinny również wykazywać zdolność do osseointegracji. Osseointegracja została po raz pierwszy zdefiniowana przez Albrektsson i wsp. jako możliwość tworzenia bezpośredniego funkcjonalnego i strukturalnego połączenia pomiędzy implantem a tkanką kostną biorcy [24]. Powodzenie tego procesu zależy od zdolności biomateriału do stymulacji wnikania, migracji, adhezji i proliferacji osteoblastów (osteokondukcja) oraz różnicowania komórek pluripotencjalnych do osteoblastów poprzez bodźce molekularne lub mechaniczne (osteoidukcja). Dodatkowo jeżeli implant ma uzupełniać duży ubytek tkanki kostnej, powinien posiadać zbliżone do niej właściwości mechaniczne, takie jak moduł sprężystości, wytrzymałość na rozciąganie, odporność na pęknięcie i złamanie [25]. Z drugiej strony, w celu zapewnienia dystrybucji składników odżywczych oraz tlenu dla proliferujących i różnicujących komórek, rusztowania do tkanki kostnej powinny charakteryzować się strukturą wysoce porowatą o wzajemnie połączonych makroporach [26]. Zwiększenie porowatości wiąże się jednak ze zmniejszeniem wytrzymałości mechanicznej. Dlatego też biomateriały wykorzystywane do otrzymywania implantów do tkanki kostnej powinny być starannie dobierane w zależności od tego, jaką funkcję mają pełnić.

1.4. Wybrane biomateriały wykorzystywane w inżynierii tkanki kostnej do otrzymywania miejscowych nośników substancji leczniczych

1.4.1. Polimetakrylan metylu (PMMA)

Wśród biomateriałów niebiodegradowalnych na uwagę zasługują cementy kostne na bazie polimerów metakrylanu metylu (PMMA). PMMA w połączeniu z antybiotykami występuje w dwóch postaciach: cementu stosowanego w artroplastyce oraz sferycznych granulatach wykorzystywanych w infekcjach układu kostnego [19]. Cementy PMMA są uznane za biozgodne i charakteryzują się dobrymi właściwościami mechanicznymi. Jednakże niezachowanie ściśle określonych warunków podczas ich wszczepiania, tj. odpowiednia wilgotność powietrza czy temperatura wiązania polimeru, wiąże się

z wysokim ryzykiem wystąpienia komplikacji. Pęknięcie cementu lub zbyt duży skurcz materiału spowodowany niewłaściwą temperaturą polimeryzacji, mogą prowadzić do obłuzowania i konieczności wymiany endoprotezy [23].

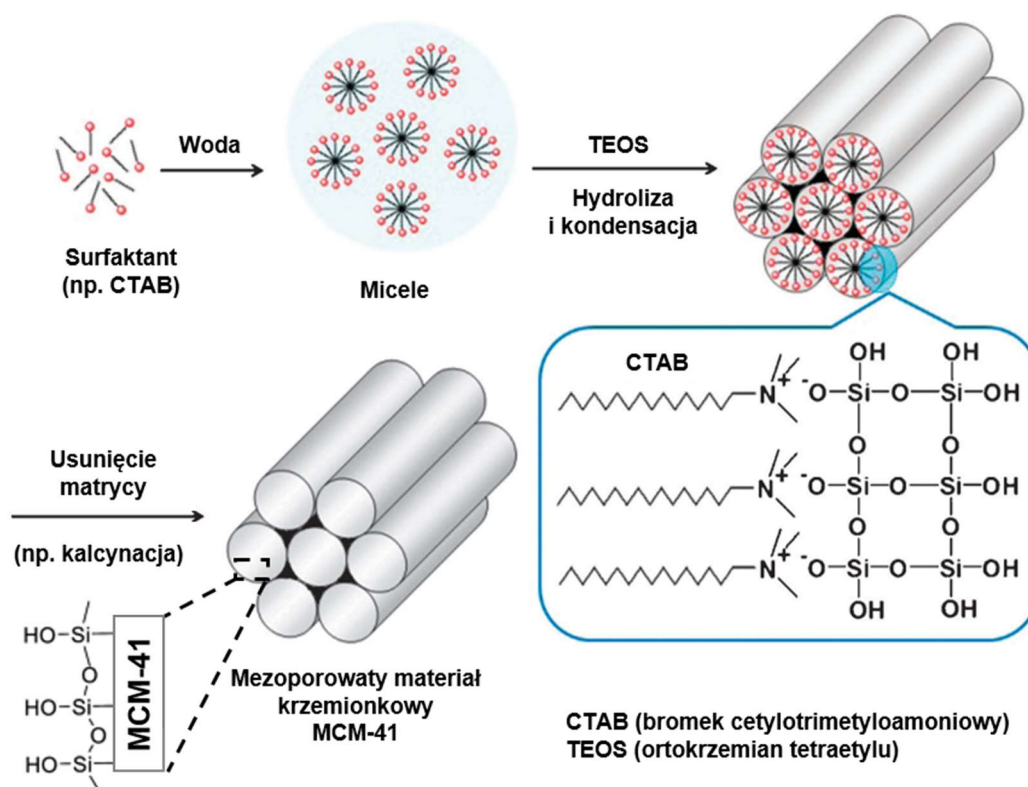
Sferyczne granulaty z PMMA zawierające gentamycynę (np. Septopal™) są obecnie stosowane w celu miejscowego leczenia *osteomyelitis* [27]. Septopal™ okazał się skuteczny w dostarczaniu antybiotyków bezpośrednio do miejsca zakażenia przez co najmniej 14 dni na poziomie znacznie wyższym niż minimalne stężenia hamujące dla większości patogenów wywołujących *osteomyelitis* [28–30]. Jednakże wprowadzanie antybiotyków do PMMA wiąże się z pewnymi ograniczeniami. Przede wszystkim, ze względu na wysoką temperaturę polimeryzacji PMMA (ok. 90°C), stosowane antybiotyki powinny wykazywać względnie wysoką odporność termiczną, aby w trakcie sporządzania cementu nie uległy dezaktywacji. Dlatego też większość cementów komercyjnie dostępnych zawiera w swoim składzie gentamycynę – antybiotyk o odpowiednio wysokiej stabilności termicznej. Produkty te wykazują skuteczność w eradykacji bakterii kolonizujących tkankę, natomiast ze względu na brak zdolności do osseointegracji, muszą zostać usunięte po uwolnieniu całkowitej ilości antybiotyku. Wiąże się to z koniecznością przeprowadzenia kolejnej procedury operacyjnej, co stwarza ryzyko wtórnego zakażenia bakteryjnego [31].

1.4.2. Mezoporowate materiały krzemionkowe

Mezoporowate materiały krzemionkowe zostały po raz pierwszy zsyntezowane w 1990 roku przez naukowców z *Mobil Oil Corporation* oraz Uniwersytetu Waseda. Najlepiej poznanym i scharakteryzowanym w obszarze wykorzystania biomedycznego jest mezoporowaty materiał krzemionkowy MCM-41 (*Mobil Composition of Matter*) o heksagonalnym uporządkowaniu mezoporów o wielkości ok. 2 nm. Przykładem materiału o podobnej strukturze oraz nieco większych porach (do ok. 10 nm) jest SBA-15 (*Santa Barbara Amorphous*). Do pozostałych należą MCM-48, SBA-1 o kubicznym uporządkowaniu porów oraz MCM-50 o uporządkowaniu warstwowym i średnicy do 30 nm [32].

Otrzymywanie materiałów krzemionkowych jest oparte na procesie zol-żel, który składa się z następujących po sobie etapów chemicznych: hydrolizy i kondensacji oraz fizycznych: żelowania, dojrzewania oraz suszenia żelu (Rycina 1). W procesie tym jako prekursor krzemionki wykorzystuje się najczęściej ortokrzemian tetraetylu (TEOS), który w środowisku wodnym ulega hydrolizie z wytworzeniem monomerów krzemionki

(silanoli). W stężeniach powyżej krytycznego stężenia micelnego surfaktanty (np. bromek cetylotrimetyloamoniowy, CTAB) lub polimery blokowe (np. poloksamery) tworzą micelle, stanowiące matrycę, na których zachodzi polikondensacja monomerów krzemionki. Matrycę usuwa się po zakończeniu procesu zol-żel najczęściej na drodze wyprażania wysokotemperaturowego (kalcynacji), co prowadzi do otrzymania materiału krzemionkowego o uporządkowanych, regularnych porach [33].



Rycina 1. Proces otrzymywania mezoporowatego materiału krzemionkowego MCM-41. Opracowano na podstawie [34].

Oprócz uporządkowanej struktury mezoporów materiały krzemionkowe charakteryzują się wieloma ważnymi dla miejscowych nośników substancji leczniczych cechami, tj. biogodnością, względnie dużą powierzchnią właściwą (do 1500 cm²/g), objętością porów ok. 1 cm³/g, występowaniem powierzchniowych grup silanolowych ($\equiv\text{Si-OH}$) oraz możliwością ich chemicznej modyfikacji [35]. Obecne na powierzchni niemodyfikowanych materiałów krzemionkowych grupy silanolowe stanowią miejsca adsorpcji, w których dochodzi do przyłączania odpowiednich cząsteczek substancji leczniczych [36]. Po raz pierwszy użyteczność mezoporowatych materiałów krzemionkowych jako nośników substancji leczniczych została wykazana w roku 2001 dla ibuprofenu [37]. W kolejnych latach, w dziedzinie inżynierii tkanki kostnej, posłużyły

one otrzymani nośników antybiotyków, np. gentamycyny [38], wankomycyny [39], cefazoliny [40], doksycykliny [41]; bisfosfonianów, np. alendronianu sodu [42]; czynników wzrostu, np. białka morfogenetycznego kości BMP-2 [43]; substancji przeciwnowotworowych, np. doksorubicyny [44,45].

Profile uwalniania substancji leczniczych z niemodyfikowanych materiałów krzemionkowych charakteryzują się wysokim wyrzutem początkowym (ang. *burst release*) oraz stosunkowo krótkim (maksymalnie kilkudniowym) czasem uwalniania [46]. Z taką kinetyką uwalniania wiąże się ryzyko wystąpienia efektu cytotoksycznego wywołanego miejscowym wysokim stężeniem substancji leczniczej. Ponadto choroby tkanki kostnej, np. *osteomyelitis*, wymagają długotrwałego podawania substancji leczniczych do miejsca objętego zakażeniem. W związku z tym, podejmuje się różne próby modyfikacji profilu uwalniania polegające na chemicznej funkcjonalizacji powierzchni mezoporowatej krzemionki, np. poprzez reakcję grup silanolowych z grupami aminopropylowymi [47], karboksylowymi [48] lub łańcuchami alkilowymi [49]. Często wykorzystywaną metodą modyfikacji jest również powlekanie materiałów krzemionkowych z zaadsorbowaną substancją leczniczą za pomocą polimerów o potwierdzonej biogodności [50,51].

W doniesieniach literaturowych opisujących zastosowania materiałów krzemionkowych w inżynierii tkanki kostnej, oprócz miejscowego podawania leków, wymienia się także ich zdolności regeneracyjne [52]. Bioaktywność biomateriałów zależy od ich właściwości mineralizacyjnych i jest definiowana jako zdolność do tworzenia hydroksyapatytu o morfologii, składzie jakościowym i ilościowym podobnym do występującego w tkance kostnej człowieka [53]. Należy podkreślić, że najczęściej wykorzystywany mezoporowaty materiał krzemionkowy MCM-41 promuje formowanie hydroksyapatytu węglanowego tylko wtedy, gdy jego struktura zostanie wzbogacona jonami wapnia oraz fosforanami, zwanymi jonami osteogenicznymi [54]. Udowodniono jednak, że bezpośrednie wprowadzenie tych jonów do mezoporowatej krzemionki prowadzi do zmian uporządkowanej struktury porowatej [55], co może znacznie zmniejszyć pojemność adsorpcyjną materiału.

1.4.3. Bioszkło

Wśród implantowanych materiałów na bazie krzemionki należy wyróżnić bioszkła o wzorze ogólnym $\text{SiO}_2\text{-CaO-P}_2\text{O}_5$. Należą one do grupy ceramik bioaktywnych i charakteryzują się znacznym podobieństwem składu chemicznego do nieorganicznej

części tkanki kostnej, co warunkuje ich wysoką biogodność, brak działania cytotoksycznego, drażniącego czy alergizującego. Wykazują one pożądane właściwości osteokondukcyjne oraz osteoindukcyjne zapewniające prawidłową integrację z tkanką kostną. Najważniejszą ich zaletą w stosunku do pozostałych materiałów krzemionkowych jest wysoka bioaktywność.

W literaturze naukowej wyróżnia się dwie metody otrzymywania bioszkieł. Pierwsza z nich, metoda opracowana przez L.L. Hencha, polega na stapianiu odpowiednich tlenków w temperaturze powyżej 1300°C [56]. Otrzymane w ten sposób bioszko charakteryzuje się niską porowatością oraz niewielką powierzchnią właściwą, co skutkuje zmniejszoną biodegradowalnością i bioaktywnością [57]. Bioszkała otrzymane za pomocą drugiej metody, zol-żel, charakteryzują się znacznie większą porowatością i powierzchnią właściwą ze względu na ich otrzymywanie w temperaturze nieprzekraczającej 800°C. Mimo zdecydowanej przewagi korzyści metody zol-żel w stosunku do metody stapiania, jest to wieloetapowy i czasochłonny proces technologiczny, trwający od kilku do kilkunastu dni [58].

Zgodnie z normą ISO 23317 (*Implants for surgery — In vitro evaluation for apatite-forming ability of implant materials*), właściwości mineralizacyjne w warunkach *in vitro* weryfikuje się, poprzez zanurzenie materiału w płynie symulującym ludzkie osocze (ang. *simulated body fluid*, SBF). Jest to roztwór o takim samym pH, sile jonowej i stężeniach jonów nieorganicznych, tj. Na^+ , K^+ , Ca^{2+} , Mg^{2+} , Cl^- , HCO_3^- , HPO_4^{2-} , SO_4^{2-} , jak osocze krwi człowieka. Potwierdzono, iż badanie to jest użyteczne w przewidywaniu bioaktywności materiału *in vivo* [56]. Pierwsze bioszko o nazwie Bioglass® 45S5, otrzymane przez L.L. Hencha, już w ciągu sześciu godzin po zanurzeniu w SBF-ie stymulowało formowanie węglanowej warstwy hydroksyapatytowej na jego powierzchni [59]. W warunkach *in vivo* rozpoczęcie tego procesu można było również zaobserwować w ciągu pierwszej doby od wszczęcia materiału, natomiast utworzenie apatyty o stosunku Ca/P równym stosunkowi apatyty ludzkiego wymagało upływu dwóch tygodni [60]. Znaczenie tworzącej się na powierzchni bioszkała warstwy węglanowego hydroksyapatytu dla procesu osseointegracji zostało potwierdzone zarówno w badaniach *in vitro*, jak i *in vivo* [61].

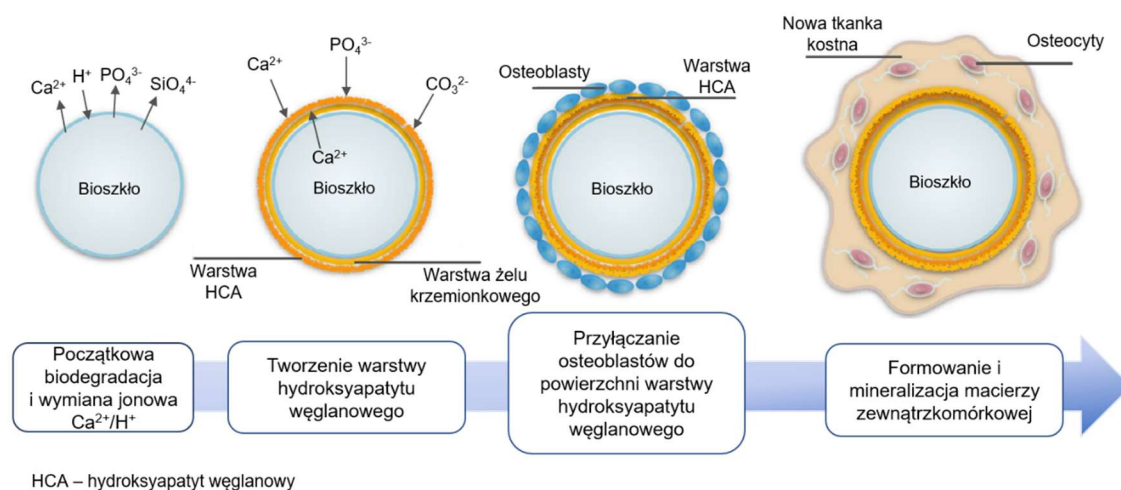
Rycina 2 przedstawia uproszczony schemat procesu tworzenia się nowej tkanki kostnej na bioszkle. W ujęciu bardziej szczegółowym proces ten składa się z następujących etapów:

1. Reakcja wymiany uwalnianych z bioszkle jonów Ca^{2+} na jony H^+ w wyniku kontaktu z płynami fizjologicznymi, prowadząca do powstania grup silanolowych (Si-OH) na powierzchni bioszkle.
2. Kondensacja grup Si-OH, skutkująca zmianą morfologii bioszkle i utworzeniem warstwy powierzchniowej o strukturze żelu.
3. Migracja jonów Ca^{2+} przez warstwę żelu krzemionkowego oraz wiązanie jonów Ca^{2+} z roztworu prowadzące do utworzenia amorficznej warstwy bogatej w $\text{CaO-P}_2\text{O}_5$.
4. Wbudowanie grup OH^- i CO_3^{2-} do warstwy fosforanu wapnia i krystalizacja prowadząca do powstania półkrystalicznego węglanowego hydroksyapatytu.
5. Adhezja białek, a następnie komórek osteoprogenitorowych do warstwy hydroksyapatytu.
6. Stymulacja proliferacji i różnicowania komórek w kierunku osteoblastów.
7. Synteza komórkowa kolagenu typu I – białka tworzącego macierz zewnątrzkomórkową.
8. Mineralizacja macierzy zewnątrzkomórkowej w wyniku krystalizacji hydroksyapatytu na włóknach kolagenowych.
9. Przekształcenie osteoblastów w osteocyty – dojrzałe komórki kostne, niezdolne do podziału, których główną rolą jest wymiana substancji odżywczych i metabolitów [62,63].

W wyniku kontaktu z płynami fizjologicznymi bioszkle ulegają stopniowej biodegradacji [64]. Wykazano, że oprócz jonów wapnia i ortofosforanów, bioszkle uwalniają również jony krzemianowe, które są zaangażowane we wczesne etapy formowania tkanki kostnej i mineralizacji, nawet w stosunkowo niskich stężeniach [65].

Lazzeri i wsp. potwierdzili w swojej pracy skuteczność bioszkle BonAlive[®] jako środka stymulującego regenerację tkanki kostnej u dzieci z przewlekłą postacią *osteomyelitis* [66]. Ponadto w praktyce klinicznej z powodzeniem stosowane są różne preparaty zawierające Bioglass[®] 45S5 do wypełnienia i odbudowy ubytków kostnych, np. PerioGlas[®], Biogran[®], Novabone[®]; uzupełnienia ubytków po ekstrakcji zębów np. Remi[®], czy jako dodatek do past do zębów np. Novamin[®] [67]. Możliwość

wykorzystania bioszkieł jako lokalnych nośników substancji leczniczych była również weryfikowana. Najczęściej jednak uwolnienie całkowitej ilości substancji leczniczej w warunkach *in vitro* następowało w ciągu kilku dni [68–70]. Taki czas uwalniania wydaje się niewystarczający w kontekście zastosowania bioszkieł w miejscowym leczeniu chronicznej postaci *osteomyelitis*.



Rycina 2. Uproszczony schemat tworzenia nowej tkanki kostnej na bioszkle. Opracowano na podstawie [62].

1.4.4. Kolagen typu I

Na początku XXI wieku dziedzinę inżynierii tkanki kostnej zrewolucjonizował rozwój trójwymiarowych rusztowań opartych na kolagenie typu I [71]. Najważniejszą funkcją rusztowań komórkowych stosowanych w celach regeneracyjnych w inżynierii tkankowej jest zapewnienie fizycznego podłoża dla komórek oraz stymulacja ich adhezji, proliferacji i różnicowania. W związku z tym, jednym z najbardziej kluczowych dla procesów regeneracji parametrów rusztowań kolagenowych jest przestrzenna struktura oraz rozmiar porów odpowiedni dla wnikania komórek kostnych. Uznaje się, że jeśli komórkom nie dostarczy się naturalnego rusztowania o odpowiednich parametrach, to szansa na regenerację tkanki jest niewielka [72].

Kolagen typu I jest białkiem włóknistym szeroko rozpowszechnionym we wszystkich tkankach łącznych z wyjątkiem chrząstki szklistej. Jest on głównym białkiem występującym w kościach, skórze, ścięgnach, więzadłach, twardówce, rogówce i naczyniach krwionośnych. Stanowi około 90% całkowitej masy organicznej kości [73]. W tkance kostnej za produkcję kolagenu odpowiadają osteoblasty, a jego włókna stanowią szkielet strukturalny, na którym osadza się hydroksyapatyt [74,75].

Trójwymiarowe rusztowania kolagenowe są otrzymywane na drodze liofilizacji, elektroprzędzenia (ang. *electrospinning*) [76] i drukowania przestrzennego (ang. *three-dimensional (3D) printing*) [77]. Charakteryzują się one biozgodnością, niską immunogennością, biodegradowalnością, plastycznością, wysoką porowatością i względnie dużą powierzchnią właściwą [78,79].

Mimo doskonałych właściwości biologicznych, rusztowania kolagenowe charakteryzują się słabymi właściwościami mechanicznymi oraz stabilnością strukturalną. Aby zwiększyć stabilność struktury porowatej, są one często poddawane sieciowaniu chemicznemu za pomocą aldehydu glutarowego [80] lub N-hydroksysukcynimidu (NHS) i 1-etylo-3-(3-dimetyloaminopropylo)karbodiimidu (EDC) [81]. Jednakże, ze względu na cytotoksyczność tych związków, metoda sieciowania na drodze chemicznej wymaga przeprowadzenia końcowego przemywania wodą destylowaną w celu usunięcia ich pozostałości. Przeprowadzenie tego etapu jest niemożliwe w przypadku rusztowań zawierających substancje lecznicze ze względu na wysokie ryzyko ich niekontrolowanego wymycia. Wśród fizycznych metod sieciowania wyróżnia się naświetlanie promieniami UV oraz proces odwodnienia termicznego (ang. *dehydrothermal treatment*, DHT). Wykorzystanie promieni UV do sieciowania kolagenu typu I eliminuje dodatkową konieczność sterylizacji rusztowań. Druga z metod polega na wykorzystaniu wysokiej temperatury w warunkach próżni, co prowadzi do sieciowania poprzez reakcje kondensacji. Niestety, ze względu na niestabilność termiczną wielu antybiotyków, metoda ta znacznie ograniczyłaby uniwersalność rusztowań kolagenowych [82]. Skuteczną metodą poprawy właściwości mechanicznych rusztowań jest łączenie kolagenu typu I z materiałami nieorganicznymi. Z tego powodu oraz w celu poprawy bioaktywności, do rusztowań kolagenowych wprowadza się bioszkła, hydroksyapatyty, materiały krzemionkowe, czy fosforany wapnia [83]. W Tabeli 1 przedstawiono przykłady połączeń kolagenu typu I z materiałami nieorganicznymi.

Tabela 1. Przykłady kompozytów stanowiących połączenie kolagenu typu I i komponentów nieorganicznych o potencjalnym zastosowaniu w inżynierii tkanki kostnej.

Komponent organiczny	Komponent nieorganiczny	Metoda otrzymywania	Postać	Rodzaj analiz	Lit.
Kolagen typu I	Bioszkło	Liofilizacja	Rusztowania	<i>In vivo</i>	[84]
Kolagen typu I, poliglikolid	Bioszkło	Liofilizacja	Rusztowania	<i>In vitro</i>	[85]
Kolagen typu I, chitozan, glikozaaminoglikany	Bioszkło	Liofilizacja	Rusztowania	<i>In vitro</i>	[86]
Kolagen typu I	Bioszkło	Liofilizacja	Rusztowania	<i>In vitro</i>	[87]
Kolagen typu I	Hydroksyapatyt, krzemian cynku	Drukowanie przestrzenne	Rusztowania	<i>In vivo</i>	[88]
Kolagen typu I	Fosforan α -trójwapniowy, fosforan β -trójwapniowy	Liofilizacja	Rusztowania	-	[89]
Kolagen typu I, chitozan	Hydroksyapatyt	Metoda wylewania do form	Membrany	<i>In vitro</i>	[90]
Kolagen typu I	Hydroksyapatyt	Elektroprzędzenie, elektrorozpylanie	Nanowłókna	<i>In vitro</i>	[91]
Kolagen typu I, chityna	Hydroksyapatyt	Liofilizacja	Rusztowania	<i>In vivo</i>	[92]
Kolagen typu I	Mezoporowaty materiał krzemionkowy	Liofilizacja	Rusztowania	<i>In vivo</i>	[93]
Kolagen typu I	Mezoporowaty materiał krzemionkowy	Drukowanie przestrzenne	Rusztowania	-	[94]
Kolagen typu I	Bioszkło, ziemia okrzemkowa, krzemiany z gąbek morskich	Liofilizacja	Rusztowania	<i>In vitro</i>	[95]

Lit. – odnośnik literaturowy

Do tej pory Agencja Żywności i Leków (ang. *Food and Drug Administration*, FDA) zatwierdziła kilka kolagenowo-ceramicznych materiałów kompozytowych stosowanych jako wypełniacze lub rusztowania do regeneracji tkanki kostnej. Pierwszy zatwierdzony materiał do przeszczepiania kości o nazwie handlowej Collagraft™, to kompozyt porowatej ceramiki fosforanowej (hydroksyapatytu i fosforanu wapnia) zawieszony w kolagenowej matrycy, którą przed wszczepieniem nasącza się świeżo pobranym szpikiem kostnym pacjenta. Rusztowanie to stopniowo zostaje zastępowane przez nową tkankę kostną, która w pełni integruje się z resztą kości pacjenta [96]. Inne,

podobne kompozyty to Healos[®] i OssiMend[®]. Wymienione kolagenowo-ceramiczne rusztowania wykazują wysoką skuteczność w regeneracji tkanki kostnej, natomiast ze względu na brak działania przeciwbakteryjnego nie mogą być stosowane u pacjentów z aktywną infekcją bakteryjną w miejscu operowanym.

Obecnie na rynku dostępne są dwa systemy dostarczające gentamycynę zbudowane z kolagenu typu I, których skuteczność została potwierdzona w leczeniu pacjentów cierpiących na przewlekłe zapalenie kości i szpiku kostnego [97]. Van Vugt i wsp. podsumowali opisywaną w literaturze skuteczność kliniczną gąbek kolagenowych Sulmycin[®] i Septocoll[®] jako porównywalną do sferycznych granulatów z PMMA. Jednakże, w porównaniu z granulatami z PMMA rusztowania kolagenowe (w postaci gąbek) charakteryzowały się niekorzystną kinetyką uwalniania antybiotyku. Już w ciągu pierwszych kilku godzin po implantacji uwolniły one 95% całkowitej ilości gentamycyny, a stężenie przekraczające minimalne stężenia hamujące (MIC) wyznaczone dla analizowanych szczepów bakterii utrzymywało się maksymalnie przez 5-7 dni. Ponadto w przypadku gąbek kolagenowych odnotowano występowanie powikłań takich jak przetoki i wydłużenie czasu gojenia rany. Obserwowane powikłania przypisano miejscowej cytotoksyczności spowodowanej wysokimi początkowymi stężeniami uwolnionej gentamycyny [97]. Niewątpliwie, mimo niekorzystnej kinetyki uwalniania substancji leczniczych, przewagą gąbek kolagenowych nad granulatami z PMMA jest ich biodegradowalność, a w związku z tym, brak konieczności wtórnej operacji chirurgicznej w celu ich usunięcia po uwolnieniu całkowitej ilości antybiotyku.

2. Cel rozprawy doktorskiej

Nadrzędnym celem niniejszej rozprawy doktorskiej było otrzymanie biozgodnych nośników substancji leczniczej do tkanki kostnej na bazie mezoporowatych materiałów krzemionkowych o potencjalnym zastosowaniu w miejscowym leczeniu *osteomyelitis*.

Założono, że nośniki te powinny:

- uwalniać substancję leczniczą w sposób przedłużony,
- wykazywać potencjalne właściwości regeneracyjne.

Realizacja celu nadrzędnego obejmowała następujące cele cząstkowe:

1. Otrzymanie i charakterystyka mezoporowatego materiału krzemionkowego jako potencjalnego nośnika o przedłużonym uwalnianiu substancji leczniczej, które obejmowały:
 - a) otrzymanie mezoporowatego materiału krzemionkowego MCM-41 za pomocą metody zol-żel,
 - b) adsorpcję modelowego antybiotyku (cyprofloksacyny) na powierzchni mezoporowatego materiału krzemionkowego MCM-41,
 - c) uzyskanie modyfikacji uwalniania substancji leczniczej poprzez powleczenie mezoporowatego materiału odpowiednimi mieszaninami polimerowymi złożonymi z etylocelulozy (EC) i polidimetylosiloksanu (PDMS-u); analiza wpływu obecności PDMS-u na profil uwalniania antybiotyku, właściwości fizykochemiczne, aktywność przeciwdrobnoustrojową i biozgodność formulacji.
2. Otrzymanie i charakterystyka bioszklą jako materiału o potencjalnych właściwościach regenerujących tkankę kostną, które obejmowały:
 - a) otrzymanie bioszklą za pomocą zmodyfikowanej metody zol-żel,
 - b) ocenę zdolności bioszklą do osseointegracji (osteokondukcji i osteoindukcji) w modelu *in vitro* w porównaniu z bioszklami komercyjnymi,
 - c) ocenę właściwości adsorpcyjnych bioszklą.
3. Otrzymanie i charakterystyka rusztowań kolagenowo-krzemionkowych jako potencjalnych systemów dostarczających substancję leczniczą i regenerujących tkankę kostną, które obejmowały:
 - a) otrzymanie za pomocą metody wylewania do form oraz liofilizacji rusztowań kolagenowo-krzemionkowych, złożonych z kolagenu typu I,

- modyfikowanego za pomocą PDMS-u mezoporowatego materiału krzemionkowego z zaadsorbowanym antybiotykiem oraz bioszkła,
- b) ocenę struktury i właściwości mechanicznych rusztowań kolagenowo-krzemionkowych,
 - c) analizę właściwości mineralizacyjnych rusztowań kolagenowo-krzemionkowych w płynie symulującym ludzkie osocze (ang. *simulated body fluid*, SBF),
 - d) badanie dostępności farmaceutycznej – wyznaczenie profilu uwalniania antybiotyku z rusztowań kolagenowo-krzemionkowych,
 - e) ocenę właściwości przeciwbakteryjnych – sprawdzenie, czy uwalniany z rusztowań kolagenowo-krzemionkowych antybiotyk zapobiega formowaniu się biofilmu bakteryjnego na ich powierzchni oraz hamuje wzrost bakterii w otaczającym środowisku w modelu *in vitro*,
 - f) ocenę biogodności rusztowań kolagenowo-krzemionkowych w modelu *in vitro*,
 - g) ocenę biogodności i początkowej odpowiedzi tkankowej w modelu *in vivo*.

3. Metodyka, wyniki i dyskusja

Prace naukowe stanowiące przedmiot rozprawy doktorskiej opisują zrealizowane etapy badawcze prowadzące do otrzymania biozgodnych nośników substancji leczniczej na bazie mezoporowatych materiałów krzemionkowych. Poniżej przedstawiono opisy trzech publikacji i jednego manuskryptu w trakcie recenzji (na dzień złożenia rozprawy doktorskiej), które zawierają informacje dotyczące założeń, zastosowanych metod i wyników wraz z syntetyczną dyskusją, najważniejsze dla wyznaczonego celu rozprawy doktorskiej.

3.1. Otrzymanie i charakterystyka mezoporowatego materiału krzemionkowego MCM-41 jako nośnika o przedłużonym uwalnianiu substancji leczniczej

Publikacja 1. A. Skwira, A. Szewczyk, M. Prokopowicz, *The Effect of Polydimethylsiloxane-Ethylcellulose Coating Blends on the Surface Characterization and Drug Release of Ciprofloxacin-Loaded Mesoporous Silica, Polymers (Basel)*. 11 (2019) 1450.

Pierwszy z artykułów przedstawia etapy badawcze zrealizowane w celu otrzymania i modyfikacji profilu uwalniania substancji leczniczej z mezoporowatego materiału krzemionkowego poprzez zastosowanie polimerowych mieszanin powlekających. W tym celu w pierwszej kolejności otrzymano mezoporowaty materiał krzemionkowy MCM-41 za pomocą metody zol-żel z wykorzystaniem ortokrzemianu tetraetylu (TEOS) jako prekursora krzemionki oraz bromku cetylotrimetyloamoniowego (CTAB) jako surfaktantu stanowiącego matrycę do polikondensacji silanoli. Następnie na powierzchni mezoporowatego materiału krzemionkowego zaadsorbowano modelową substancję leczniczą – cyprofloksacynę. Materiały te powleczono na drodze ich bezpośredniej dyspersji w każdej z mieszanin polimerowych, a następnie odparowania rozpuszczalnika, otrzymując końcową postać w formie filmów. Do powlekania użyto 5% etanolowy roztwór etylocelulozy (EC) oraz mieszaniny roztworu etylocelulozy z 1% (obj./obj.) lub 2% (obj./obj.) dodatkiem polidimetylosiloksanu zakończonego grupami hydroksylowymi (PDMS-u) o lepkości 65 cSt. Stosunek masy MCM-41 z zaadsorbowaną cyprofloksacyną do objętości mieszaniny polimerowej został odpowiednio dobrany, tak, aby zapewnić jednolite powleczenie materiału.

Otrzymano następujące formułacje: - niepowleczony mezoporowaty materiał krzemionkowy z zaadsorbowaną cyprofloksacyną (*CIP-loaded MCM-41*); - mezoporowaty materiał krzemionkowy z zaadsorbowaną cyprofloksacyną powleczony etylocelulozą (*MCM-F1*); - mezoporowaty materiał krzemionkowy z zaadsorbowaną cyprofloksacyną powleczony mieszaniną etylocelulozy z 1% (obj./obj.) dodatkiem PDMS-u (*MCM-F2*); - mezoporowaty materiał krzemionkowy z zaadsorbowaną cyprofloksacyną powleczony mieszaniną etylocelulozy z 2% (obj./obj.) dodatkiem PDMS-u (*MCM-F3*) oraz - liofilizowana cyprofloksacyna fizycznie zawieszona w matrycy etylocelulozowej z 2% (obj./obj.) dodatkiem PDMS-u (*CIP-F3*). Po odparowaniu rozpuszczalnika stosunek masowy PDMS:EC w poszczególnych formułacjach wynosił 1:4 (*MCM-F2*) i 1:2 (*MCM-F3*), co odpowiadało masie PDMS-u równej 2,4 mg i 4,8 mg przypadającej na każdy film.

Formułacje w postaci filmów (*MCM-F1*, *MCM-F2*, *MCM-F3*, *CIP-F3*) oraz proszków (*CIP-loaded MCM-41*) poddano badaniu dostępności farmaceutycznej (trwającym 7 dni) oraz ocenie właściwości fizykochemicznych. Analiza struktury molekularnej została przeprowadzona za pomocą spektroskopii w podczerwieni z transformatą Fouriera (FTIR). Ocenę morfologii i chropowatości powierzchni przeprowadzono za pomocą skaningowej mikroskopii elektronowej sprzężonej ze spektroskopią dyspersji energii promieniowania rentgenowskiego (SEM-EDX) oraz profilometrii optycznej, natomiast zwilżalność powierzchni wyznaczono za pomocą pomiaru statycznego kąta zwilżania metodą siedzącej kropli. Analiza dyfrakcji rentgenowskiej (XRD) oraz skaningowa kalorymetria różnicowa (DSC) posłużyły potwierdzeniu obecności cyprofloksacyny w otrzymanych formułacjach.

Badanie dostępności farmaceutycznej przeprowadzone dla *CIP-loaded MCM-41* potwierdziło spodziewany wysoki wyrzut początkowy cyprofloksacyny wynoszący 80% całkowitej ilości antybiotyku po pierwszych 24 godzinach badania (Tabela 2). Powleczenie materiałów krzemionkowych za pomocą mieszanin polimerowych okazało się mieć znaczący wpływ na kinetykę uwalniania cyprofloksacyny. Dla formułacji *MCM-F1* odnotowano zmniejszenie początkowego wyrzutu cyprofloksacyny do 39% w ciągu pierwszych 24 godzin badania. Dla formułacji *MCM-F2* i *MCM-F3* początkowy wyrzut wynosił odpowiednio 16% i 5% całkowitej ilości cyprofloksacyny. Otrzymane wyniki potwierdziły występowanie następującej zależności: im większa była zawartość PDMS-u w formułacji, tym mniejszy był wyrzut początkowy cyprofloksacyny w ciągu pierwszych 24 godzin badania. Przeprowadzone w celach porównawczych

badanie dostępności farmaceutycznej dla *CIP-F3* potwierdziło spodziewany wysoki początkowy wyrzut substancji leczniczej (88% całkowitej ilości po pierwszych 24 godzinach badania). Po tym czasie, uwalnianie cyprofloksacyny z formułacji *MCM-F1*, *MCM-F2* i *MCM-F3* zachodziło zgodnie z kinetyką zerowego rzędu ze stałą szybkością. Czas trwania badania wynoszący 7 dni pozwolił na uwolnienie z formułacji *CIP-loaded MCM-41* oraz *CIP-F3* odpowiednio 98% i 95% całkowitej ilości wprowadzonej cyprofloksacyny, natomiast formułacje *MCM-F1*, *MCM-F2* i *MCM-F3* uwolniły odpowiednio 54%, 20%, 9% całkowitej jej ilości. Analiza kinetyczna potwierdziła dopasowanie profili uwalniania wyznaczonych dla otrzymanych formułacji *MCM-F1*, *MCM-F2*, *MCM-F3* i *CIP-F3* do modelu Higuchiego ($R^2 \geq 0,93$) i Korsmeyera-Peppasa ($n \leq 0,55$; $R^2 \geq 0,87$). Interpretując otrzymane wyniki dowiedziono, że uwalnianie cyprofloksacyny z formułacji zachodziło zgodnie z mechanizmem dyfuzji Ficka. Na podstawie tych danych wnioskowano o prawdopodobnym, zależnym od PDMS-u, przedłużeniu całkowitego czasu uwalniania z otrzymanych formułacji. Zostało to ocenione w drugiej publikacji należącej do cyklu rozprawy doktorskiej, w której czas trwania badania dostępności farmaceutycznej dla wytypowanych formułacji został przedłużony do 30 dni.

Tabela 2. Procentowa ilość uwolnionej cyprofloksacyny z poszczególnych formułacji.

Nazwa formułacji	Procentowa ilość cyprofloksacyny uwolnionej po pierwszych 24 godzinach badania	Procentowa ilość cyprofloksacyny uwolnionej po całkowitym czasie badania – 7 dniach
<i>CIP-loaded MCM-41</i>	80%	98%
<i>MCM-F1</i>	39%	54%
<i>MCM-F2</i>	16%	20%
<i>MCM-F3</i>	5%	9%
<i>CIP-F3</i>	88%	95%

Uzyskane zmniejszenie początkowego wyrzutu cyprofloksacyny *MCM-F1*, *MCM-F2* i *MCM-F3*, uzasadniono w następujący sposób. Powleczenie materiałów krzemionkowych nierozpuszczalnym w wodzie polimerem – etylocelulozą stanowiło fizyczną barierę pomiędzy antybiotykiem zaadsorbowanym w porach materiału krzemionkowego MCM-41 a płynem akceptorowym. Uwalnianie antybiotyku było jednak możliwe dzięki obecności nanoporów w strukturze powstałego filmu etylocelulozowego. Natomiast modyfikacja uwalniania w wyniku dodatku polimeru

hydrofobowego – PDMS-u do formulacji mogła wynikać zarówno z blokowania nanoporów etylocelulozy, jak i okluzji antybiotyku przez PDMS, co dodatkowo utrudniało penetrację płynu akceptorowego w głąb porów z antybiotykiem. W konsekwencji spowalniało to rozpuszczanie i uwalnianie zaadsorbowanej substancji leczniczej. Prawdopodobieństwo występowania takiego mechanizmu modyfikacji uwalniania dodatkowo potwierdzono za pomocą analizy morfologii powierzchni odpowiednich formulacji przy pomocy techniki SEM. W przypadku formulacji niezawierających mezoporowatego materiału krzemionkowego obserwowano wydzieloną fazę PDMS-u w postaci licznych kropli rozproszonych w stałym filmie etylocelulozowym. Natomiast brak wydzielonej fazy PDMS-u w filmach formulacji *MCM-F2* i *MCM-F3* sugerował prawdopodobne jego umiejscowienie w porach materiału krzemionkowego zawierającego cyprofloksacyne. Dodatkowo wykazano, iż zwilżalność powierzchni w formulacjach zawierających MCM-41 zwiększała się wraz ze wzrostem zawartości PDMS-u, co prawdopodobnie było wynikiem specyficznego ułożenia cząsteczek PDMS-u, gdzie hydrofobowe łańcuchy zorientowane są w kierunku MCM-41, a grupy hydroksylowe w kierunku powierzchni zewnętrznej filmu.

Zaobserwowano również zależność wzrostu chropowatości powierzchni filmów wraz ze wzrostem zawartości PDMS-u w formulacji, co ma istotne znaczenie dla integracji biomateriału z tkanką kostną biorcy [98,99]. Wyniki badań przedstawione w niniejszym artykule stanowiły punkt wyjścia do analiz właściwości mikrobiologicznych i biologicznych proponowanych formulacji dostarczających antybiotyków do chorobowo zmienionej tkanki kostnej, opisanych w publikacji drugiej.

Article

The Effect of Polydimethylsiloxane-Ethylcellulose Coating Blends on the Surface Characterization and Drug Release of Ciprofloxacin-Loaded Mesoporous Silica

Adrianna Skwira , Adrian Szewczyk and Magdalena Prokopowicz * 

Department of Physical Chemistry, Faculty of Pharmacy, Medical University of Gdańsk, Hallera 107, Gdańsk 80-416, Poland

* Correspondence: magdalena.prokopowicz@gumed.edu.pl

Received: 12 August 2019; Accepted: 2 September 2019; Published: 4 September 2019



Abstract: In this study, we obtained novel solid films composed of ciprofloxacin-loaded mesoporous silica materials (CIP-loaded MCM-41) and polymer coating blends. Polymer coating blends were composed of ethylcellulose (EC) with various levels of polydimethylsiloxane (PDMS, 0, 1, 2% (*v/v*)). The solid films were prepared via the solvent-evaporation molding method and characterized by using scanning electron microscopy (SEM), optical profilometry, and wettability analyses. The solid-state of CIP present in the solid films was studied using X-ray diffraction (XRD) and differential scanning calorimetry (DSC). The release profiles of CIP were examined as a function of PDMS content in solid films. The surface morphology analysis of solid films indicated the progressive increase in surface heterogeneity and roughness with increasing PDMS content. The contact angle study confirmed the hydrophobicity of all solid films and significant impact of both PDMS and CIP-loaded MCM-41 on surface wettability. DSC and XRD analysis confirmed the presence of amorphous/semi-crystalline CIP in solid films. The Fickian diffusion-controlled drug release was observed for the CIP-loaded MCM-41 coated with PDMS-free polymer blend, whereas zero-order drug release was noticed for the CIP-loaded MCM-41 coated with polymer blends enriched with PDMS. Both the release rate and initial burst of CIP decreased with increasing PDMS content.

Keywords: coating; drug delivery; surface roughness; polymers; mesoporous silica

1. Introduction

Local drug delivery systems have been widely applied in bone tissue diseases [1,2]. They require two most pressing goals to be achieved: a controlled initial release and long-term delivery of drug [3]. At present, mesoporous silica materials, e.g., MCM-41, have been studied as local antibiotic/anticancer drug delivery systems for the bone treatment of osteomyelitis or osteosarcoma due to their desirable features such as large surface area ($\sim 800 \text{ m}^2/\text{g}$), uniform pore size ($\sim 2\text{--}6 \text{ nm}$), modifiable surface properties [4,5]. Moreover, mesoporous silica materials have been found as a nontoxic to the surrounding bone tissue and biocompatible with the osteoblast cells [6]. Furthermore, Braun et al. reported that mesoporous silica materials may release small amounts of Si ($\sim 60 \text{ ppm}$) through dissolution in simulated body fluid [7]. It has been confirmed that even relatively low concentration of Si has a positive impact on bone homeostasis and density [8]. However, another characteristic feature of many drug-loaded mesoporous silica materials is the high amount of drug released in a burst stage [9]. This can lead to a high local concentration of drug which may be cytotoxic to surrounding tissue. The reduction of burst release can be achieved by using polymeric coatings.

Controlled local drug release provides a suitable dosing of drug in a specific area in a prolonged manner. The use of bone drug delivery systems which provide controlled release is considered as an optimal and benign treatment characterized by increased effectiveness, extended duration of therapeutic effect, and reduced adverse effects, e.g., toxicity [10,11]. Nowadays, polymeric coatings have been emphasized as an interesting way to modify drug release from mesoporous silica matrices providing a physical barrier between the drug entrapped in the pores and the fluids [12]. Different polymers, such as poly(ethylene glycol) (PEG) [13], Eudragit RL and Eudragit S [14] were used for this purpose. Furthermore, blends of two types of polymers, which are known to be non-toxic and exhibit different physicochemical characteristics can be also used [15]. In the polymer coatings the release profiles of drug primarily depend on the polymer/polymer blend ratio. By simply modifying the polymer/polymer blend ratio, the properties of the obtained film can be effectively altered and thus broad ranges of drug release profiles can be provided [15,16].

Apart from the appropriate drug release, another requirement for mesoporous silica materials as local drug delivery systems to bone is their integration with the host tissue. Surface roughness has been considered as a crucial limiting factor for applied materials in the context of physical and biological compatibility with surrounding tissue [17]. In recent years, many materials intended for implantation with various surface structure were designed and examined for cellular response, activity, and bone formation [18,19]. It was proved for endosseous dental implants that a relatively rough surface improves implant stability, promotes tissue ingrowth, and enhances bone apposition [19–21]. Multiple methods of textural property modification are available [22,23]. However, two primary trends can be distinguished: control of the porosity of a material during its synthesis (1), and surface post-treatment of a synthesized material (2) among which a coating has been considered as one of the most effective methods [24].

The main features of appropriate implantable coating mixtures are biocompatibility, biostability and desired mechanical properties [25]. These characteristics are well documented for polydimethylsiloxane (PDMS) [26] and ethylcellulose (EC) [27]. EC is the most stable cellulose derivative and a water-insoluble polymer that has been used in many pharmaceutical applications as a coating or time-release agent. In addition, EC, due to its function as binder, flexible film former, water barrier and rheology modifier, has been increasingly applied in bone tissue engineering [27–29]. PDMS is characterized by a water-insoluble hydrophobic nature, good adhesive and plasticizing capacity, which characterize its influence on drug release and the physical properties of coated materials [30].

Therefore, the use of PDMS:EC combinations as new coating blends for ciprofloxacin-loaded MCM-41 (CIP-loaded MCM-41) was investigated in this paper. As the MCM-41 has been previously well described as a drug delivery system, we decided to modify the drug release rate by using a polymeric coating. Ciprofloxacin was chosen as the model drug due to its broad spectrum activity and common application in osteomyelitis [31]. The main idea of our studies was to prepare novel solid films of polymer-coated CIP-loaded MCM-41 which would provide the desired prolonged drug release with low burst release *in vitro*. Furthermore, the physicochemical properties of the obtained solid films were thoroughly investigated.

2. Materials and Methods

2.1. Materials

Tetraethyl orthosilicate (TEOS), cetyltrimethylammonium bromide (CTAB), ethanol, aqueous ammonia (25%), hydroxyl-terminated polydimethylsiloxane fluid (PDMS, 65 cSt, $d = 0.97$ mg/mL) were all obtained from Sigma-Aldrich. Ethylcellulose (EC, Ethocel[®] 20 cP) was obtained from Dow Chemical. Acidic solution of ciprofloxacin lactate (pH = 3.5, 10 mg/mL, Proxacin) was obtained from Polfa S.A. (Warsaw, Poland).

2.2. Synthesis of Mesoporous Silica Materials (MCM-41)

The synthesis of mesoporous silica materials, MCM-41, was carried out by a templating method using tetraethyl orthosilicate (TEOS) as a silica source and the cationic surfactant cetyltrimethylammonium bromide (CTAB) as a template [32]. Briefly, 125 g of water, 12.5 g of ethanol, 9.18 g of ammonia aq. (25 %), and 2.39 g of CTAB were stirred together in polypropylene beaker on a magnetic mixer (300 rpm) at 25 °C for approx. 15 min until a homogenous solution was formed. The pH of the solution was 10. Then, 10.03 g of TEOS was added and the resulting mixture was continuously stirred for 2 h. Next, hydrothermal treatment of the mixture was carried out at 90 °C for 5 days without stirring. The resulting solid product was recovered by vacuum filtration, washed with 100 mL of absolute ethanol and dried at 40 °C for 1 h. The CTAB template was removed from the product by calcination in air at 550 °C (with heating rate of 1 °C/min) for a period of 6 h in a muffle furnace (FCF 7SM, CZYLOK, Jastrzebie-Zdroj, Poland). The final MCM-41 samples in powders form with the fraction size range of 200–500 µm were obtained by micronisation (Mortar Grinder Pulverisette 2, Fritsch, Weimar, Germany). The micronisation lasted 10 min at 50 rpm.

2.3. Ciprofloxacin Adsorption onto MCM-41

Ciprofloxacin (CIP) adsorption onto MCM-41 was performed according to the following procedure (the optimal conditions of adsorption process were determined in preliminary studies). Briefly, the synthesized MCM-41 (particles fraction in the range of 200 µm–500 µm) was immersed in acidic solution (pH = 3.5) of ciprofloxacin lactate (10 mg/mL) at ratio 100 mg of silica per 2 mL of solution and incubated with stirring (300 rpm) at 25 ± 0.5 °C for 3 h to ensure the equilibrium state. Then, CIP-loaded MCM-41 was centrifuged, separated from supernatant, and freeze-dried (−52 °C, 0.1 mBar, 24 h). The absorbance of the CIP remaining in the supernatant was measured spectrophotometrically at 278 nm (model UV-1800 UV-Vis spectrophotometer, Shimadzu, Kyoto, Japan). The amount of CIP adsorbed onto MCM-41 and adsorption efficiency were calculated using Equations (1) and (2), respectively:

$$Q_e = \frac{(C_0 - C_e) \cdot V}{m} \quad (1)$$

$$\%Ads = \left(\frac{C_0 - C_e}{C_0} \right) \cdot 100\% \quad (2)$$

where Q_e (mg/g) is an amount of CIP adsorbed at the equilibrium state, %Ads (%) is an adsorption efficiency coefficient, C_0 (mg/L) is an initial CIP concentration, C_e (mg/L) is a CIP concentration at equilibrium state, V (L) is a volume of CIP solution, and m (g) is the mass of MCM-41 used.

2.4. Fabrication of Solid Films Composed of CIP-Loaded MCM-41 and Polymer Blends

The polymer coating blends were prepared by mixing 5% (w/w) ethylcellulose (EC) ethanolic solutions with 0, 1, 2% (v/v) of hydroxyl-terminated polydimethylsiloxane (PDMS, 65 cSt, $d = 0.97$ mg/mL), giving the various PDMS:EC ratios (Table 1). 95% (v/v) ethanol was used as a solvent in each formulation. The prepared coating blends were homogenized by sonication for 20 min using a cooling bath. The pure solid films of each formulation were prepared via solvent-evaporation molding method as follows. Equal volumes (250 µL) of F1, F2, and F3 coating blends (Table 1) were poured into polypropylene molds, and incubated till complete ethanol evaporation (30 ± 0.5 °C, 60 ± 10% relative humidity, 24 h). The end of the solidification of the polymer coating blends is regarded as the moment when no changes in weight (within the limits of instrumental error (± 0.01 g)) were detected. After complete evaporation of the ethanol, the PDMS:EC ratios in the pure solid films changed from 1:99 and 2:98 (v/v , before solvent evaporation) into 1:4 and 1:2 (w/w , after solvent evaporation) for F2 and F3, respectively (Table 1).

Table 1. Composition of each formulation (F1–F3) with PDMS:EC ratio before (*v/v*) and after solvent evaporation (*w/w*).

Before solvent evaporation			
Formulation	PDMS:EC ratio	PDMS content [μL]	EC ethanolic solution content [μL]
F1	0:100	-	250.0
F2	1:99	2.5	247.5
F3	2:98	5.0	245.0
After solvent evaporation			
Formulation	PDMS:EC ratio	PDMS content [mg]	EC content [mg]
F1	0:1	-	10.0
F2	1:4	2.4	9.9
F3	1:2	4.8	9.8

A constant amount of CIP-loaded MCM-41 (200 μm –500 μm) was immersed in each polymer blend at a ratio 6 mg per 250 μL . Solid films of CIP-loaded MCM-41 coated with F1, F2, and F3 (MCM-F1, MCM-F2, MCM-F3) were fabricated in the same manner as pure solid films. The obtained solid films of F1, F2, and F3 and MCM-F1, MCM-F2, MCM-F3 were then removed from the molds and stored in desiccators at room temperature for further analyses.

2.5. Physicochemical Characterization

Pure solid films of F1, F2, and F3 were characterized using the Fourier transform infrared spectroscopy (FTIR, Jasco FT/IR-4200, Jasco, Pfungstadt, Germany). Samples for analysis were prepared using the KBr tablet technique. For a better comparison, the spectra of F2 and F3 were normalized to a maximum absorption of the dominant peak at 804 cm^{-1} , attributed to the Si–C stretching in the Si–CH₃ group [33].

The morphological characterization of MCM-F1, MCM-F2, and MCM-F3 solid films was carried out by using scanning electron microscopy (SEM). For comparative purposes, SEM analysis of CIP-loaded MCM-41 (before polymer coating) and pure solid films of F1, F2, F3 was performed. In order to identify the components of pure solid films, the samples were analyzed using the energy-dispersive X-ray spectroscopy (EDX). The samples for SEM were fixed on carbon tape and sputter coated with gold, prior to the analysis. SEM images was obtained on electron microscope (Hitachi SU-70, Japan) at an acceleration voltage of 3 kV.

The images of surface roughness with quantitative data of MCM-F1, MCM-F2, MCM-F3 solid films were obtained using an optical profilometer (Contour GTK, Bruker, Billerica, MA, USA). To obtain quantitative characterization, mapping of 46.9 μm \times 62.5 μm size surface was done for 10 samples of each formulation and the average values together with standard deviations of roughness parameters were calculated.

Wettability studies of solid films of F1, F2, F3, and MCM-F1, MCM-F2, MCM-F3 were performed by contact angle measurement at room temperature (DSA G10 goniometer, Kruss GmbH, Hamburg, Germany). The images of sessile drop of water and diiodomethane at the point of intersection (three-phase contact points) between the drop contour and the surface (baseline) were recorded for drop shape analysis (DSA) and determination of contact angle. The contact angle value was determined as an average of 10 measurements of each sample.

The X-ray diffraction (XRD) analysis of F3, MCM-F3, CIP-loaded MCM-41, and CIP (as reference) and differential scanning calorimetry (DSC) of F3, MCM-F3, CIP-loaded MCM-41, CIP, and MCM-41 (as references) were performed to characterize solid-state of CIP present in the obtained solid films. XRD data were collected using diffractometer (Empyrean PANalytical, Malvern, UK) with a CuK α radiation beam operating at 40 kV and 40 mA, in the 2θ range between 5° and 70° with a step width of

0.02° and at a scanning rate of 0.5°/min. DSC measurements were carried out using a DSC instrument (822e Mettler Toledo, Columbus, Ohio, USA). Samples of about 5 mg were placed in an aluminum pan with a hole in the lid. The experiments were performed under an N₂ atmosphere (20 mL/min gas flow rate). The thermal behavior of the samples was investigated by heating the samples from 25 to 230 °C with 10 °C/min step. Calibration of the instrument was performed using an indium standard.

2.6. Drug Release Analysis

The release study was performed under “sink” conditions (considering approx. 100 mg/mL solubility of CIP in water [34]) according to the following procedure. Each solid film of MCM-F1, MCM-F2, MCM-F3 was immersed in 2 mL of purified water and shaken at 37 ± 0. 5°C (80 rpm) for 7 days. The release medium was exchanged every 24 h, and the amount of CIP released was measured spectrophotometrically at wavelength of 278 nm (Shimadzu model UV-1800 UV-Vis spectrophotometer). Quantitative determinations of the amount of released CIP were based on pre-calibration of the spectrometer using standard water solutions of the CIP.

The results were obtained from data groups of n = 7 and expressed as mean values ± standard deviation. The release kinetic parameters were calculated using linearized forms of Korsmeyer-Peppas, Higuchi models and zero order kinetics presented in Equations (3)–(5), respectively:

$$\log Q = \log k + n \log t \quad (3)$$

$$Q = k_H t \quad (4)$$

$$Q = Q_0 + k_0 t \quad (5)$$

where Q (%) denotes the fraction released over time t (h; days), Q_0 (%) is the initial fraction of released drug, n is a release exponent related to the drug release mechanism, k (h^{-n} ; days^{-n}) is a rate constant, the k_H is a Higuchi dissolution constant ($\text{h}^{-1/2}$; $\text{days}^{-1/2}$), and k_0 is the zero order release constant (% of dose released per day). In Equation (3), $n < 0.5$ indicates quasi-Fickian diffusion, $n = 0.5$ indicates a Fickian diffusion, for n between 0.5 and 1, the drug release is considered as non-Fickian diffusion, and $n = 1$ corresponds to zero-order release of case II diffusion. To find out the mechanism of drug release, the data for first 60% of drug release fraction (Q) were fitted with Korsmeyer-Peppas and Higuchi models.

3. Results and Discussion

3.1. Ciprofloxacin Adsorption onto MCM-41

The CIP adsorption onto successfully synthesized MCM-41 was verified by the Fourier transform infrared spectroscopy technique (Jasco model 4700 FTIR). The characteristic bands of the CIP molecule were observed what confirmed the presence of drug onto MCM-41 after the loading procedure (Supplementary Materials). The adsorption efficiency was 56 ± 2% what corresponded to the mean amount of CIP-loaded of 112 ± 4 mg per each 1 g of MCM-41.

3.2. Solid Films Formation

The pure solid films of three formulations of polymer blends were obtained via solvent-evaporation molding method (F1, F2, F3). The solid films of CIP-loaded MCM-41 coated with polymer blends (MCM-F1, MCM-F2, MCM-F3) were obtained in the same manner. The final thickness and mass of the pure solid films of F1, F2, F3 were ranged from 30 to 40 μm, and 10.0 to 14.6 mg, respectively, whereas solid films of MCM-F1, MCM-F2, MCM-F3 were characterized by thicknesses ranging from 50 to 60 μm and masses ranging from 16.0 to 20.6 mg.

3.3. Physicochemical Characterization

3.3.1. FTIR Characterization

The bulk molecular structure of F1, F2, and F3 pure polymer solid films was characterized using FTIR technique (Figure 1). FTIR spectra of the precursors (EC powder and PDMS liquid) are presented for comparative purposes. The spectrum of F1 (the formulation containing 100% of EC) showed the characteristic broad peaks at $\sim 1055\text{ cm}^{-1}$ and $\sim 1095\text{ cm}^{-1}$ attributed to C–O–C stretching vibrations, and $\sim 1377\text{ cm}^{-1}$ attributed to C–H bending vibrations in the EC molecule [35]. For the pure solid films of F2, F3, the characteristic peak at $\sim 1024\text{ cm}^{-1}$ corresponding to Si–O–Si asymmetrical stretching [36] confirmed the presence of PDMS. In addition, sharp peaks at $\sim 1261\text{ cm}^{-1}$ attributed to Si–C stretching and $\sim 804\text{ cm}^{-1}$ attributed to CH₃ deformation in Si–CH₃ group of PDMS were noticed [33]. The intensity of the peak at $\sim 1024\text{ cm}^{-1}$ slightly increased for F3 compared to F2, thus confirming a higher content of PDMS in the F3 sample. Additionally, a small peak at $\sim 1377\text{ cm}^{-1}$ of EC is observed for F2, what confirmed the higher content of EC in F2 compared to F3. For both F2 and F3, a peak at $\sim 1094\text{ cm}^{-1}$ was also observed due to the overlapping of Si–O–Si asymmetrical stretching at $\sim 1089\text{ cm}^{-1}$ from the PDMS together with the C–O–C stretching mode at $\sim 1095\text{ cm}^{-1}$ from the EC.

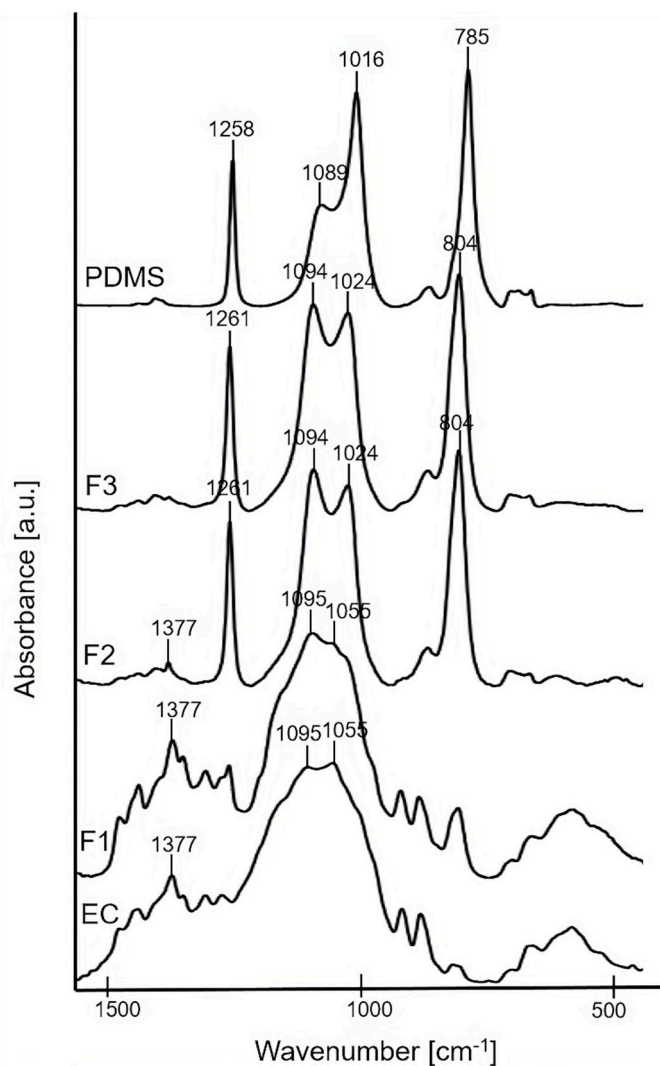


Figure 1. FTIR spectra of F1, F2, F3 solid films, and precursors: EC and PDMS.

3.3.2. Surface Morphology

The morphology of MCM-F1, MCM-F2, MCM-F3 solid films was characterized using SEM analysis (Figure 2). The SEM image of CIP-loaded MCM-41 powder before coating is also presented for comparative purposes (Figure 2A). The CIP-loaded MCM-41 powder was characterized by spherical particles loosely connected to each other. After coating with polymer blends the structure of the obtained solid films was more compact and heterogeneous. Moreover, the results suggested that the surface roughness increases with the increase of PDMS content in the solid films (Figure 2A). In order to confirm the observed differences in surface roughness the SEM-EDX analysis of pure solid films of F1, F2, F3 was also performed (Figure 2B). As it can be seen, the film of EC without PDMS (F1) was characterized by a smooth, gapless surface, whereas F2 and F3 present plain surface structure with an increasing number of cavities distributed in the solid films. The higher the PDMS content in polymer blend, the greater the number of cavities that was observed, indicating that they could be attributed to PDMS droplets (also confirmed by EDX profile in which the presence of silicon in F2 and F3 was noticed). It should be noted that no cavities attributed to PDMS were observed for MCM-F2, MCM-F3 solid films (Figure 2A) contrary to pure solid films of F2, F3 (Figure 2B). This may be related to occlusion of PDMS in the MCM-41 particles.

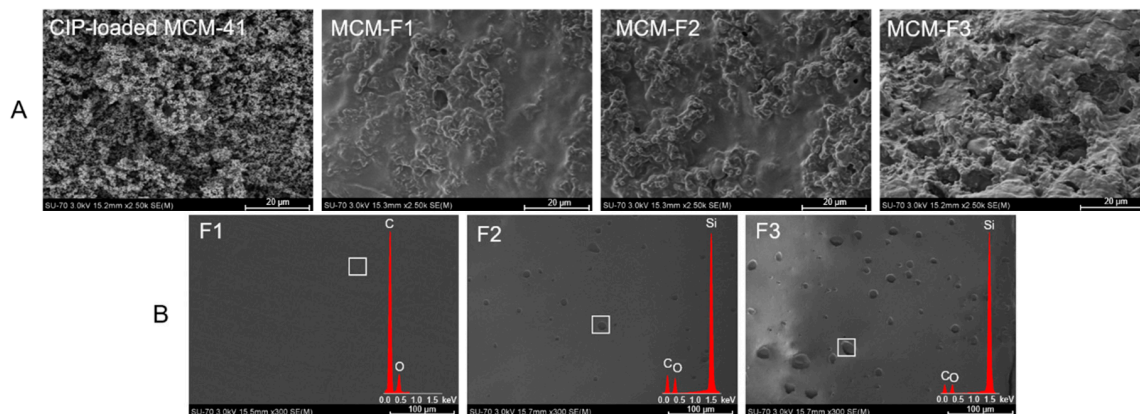


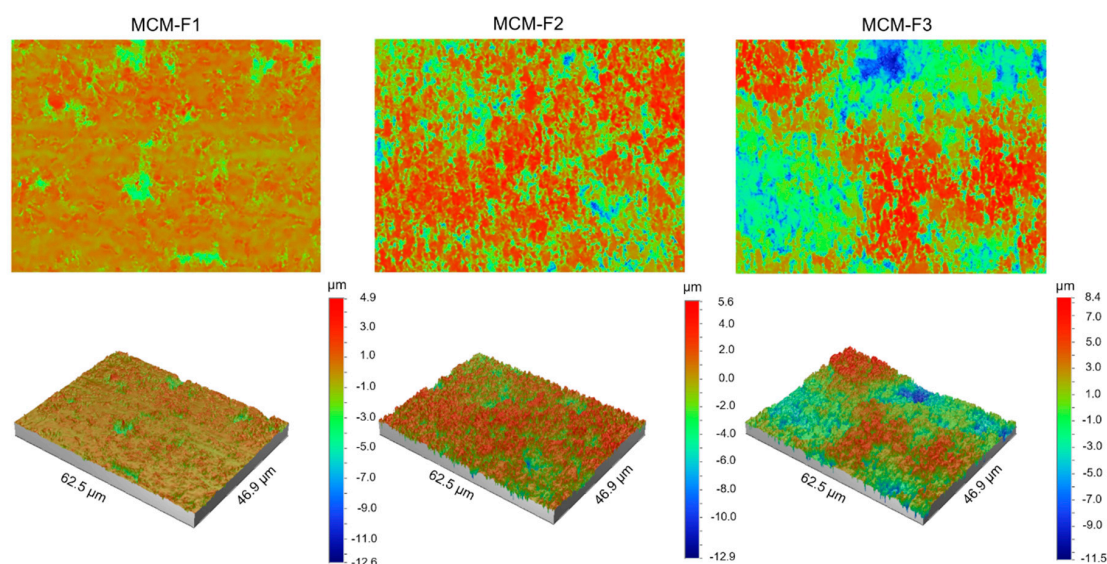
Figure 2. SEM images of CIP-loaded MCM-41, and solid films of: MCM-F1, MCM-F2, MCM-F3 (A); F1, F2, F3 (B).

The quantitative characterization of the surface of MCM-F1, MCM-F2, MCM-F3 solid films was performed by using optical profilometry. Table 2 shows the roughness parameters (R_a —average roughness, R_q —root-mean-square roughness, and R_t —peak-valley difference) calculated over the whole tested area ($46.9 \mu\text{m} \times 62.5 \mu\text{m}$) as the means of 10 samples of each formulation together with standard deviations. As presented in Table 2, the quantitative results confirmed the increase of surface roughness in the following order: MCM-F1 < MCM-F2 < MCM-F3. The R_a value increased with the increase of PDMS content in solid film from $0.57 \pm 0.10 \mu\text{m}$ for MCM-F1 to $2.49 \pm 0.54 \mu\text{m}$ for MCM-F3. The highest values of roughness parameters were observed for MCM-F3 and correlated with the biggest cavities (Figure 3). These data indicate that the surface roughness of solid films is significantly dependent on the PDMS content in polymer blend what might be a promising feature in the context of tissue ingrowth. According to numerous *in vitro* experiments, implant roughness may affect osteoblast morphology, growth, proliferation and differentiation. It has been highlighted that the cells cultured on the rough surfaces show better morphology and proliferation in comparison to the controls cultured on flat surfaces [37].

Table 2. Mean roughness parameters with standard deviations of surface of MCM-F1, MCM-F2, MCM-F3 solid films.

Formulation	$R_a \pm SD$ [μm]	$R_q \pm SD$ [μm]	$R_t \pm SD$ [μm]
MCM-F1	0.57 ± 0.10	0.86 ± 0.17	11.22 ± 2.49
MCM-F2	1.86 ± 0.40	2.30 ± 0.45	19.12 ± 2.85
MCM-F3	2.49 ± 0.54	3.14 ± 0.70	23.67 ± 6.06

SD—standard deviation; R_a —average roughness; R_q —root-mean-square roughness; and R_t —peak-valley difference.

**Figure 3.** The optical profilometer images of $62.5 \mu\text{m} \times 46.9 \mu\text{m}$ surfaces of MCM-F1, MCM-F2, MCM-F3 solid films.

3.3.3. Contact Angle and Wetting Properties

In order to verify the wettability of the solid films of F1, F2, F3, and MCM-F1, MCM-F2, MCM-F3 a contact angle analysis was performed. The average contact angles and surface free energies determined for all samples are shown in Table 3. All of the examined samples were characterized as hydrophobic. For the pure solid films of F1, F2, F3 (Section A in Table 3) the most hydrophilic surface was observed for F1. As expected, for F2 the addition of hydrophobic hydroxyl-terminated PDMS resulted in a higher water contact angle value, suggesting an increase in hydrophobicity, compared to F1. Conversely, for F3 a slight decrease of water contact angle and increase of the polar component of the surface free energy were noticed, compared to F2. This can be explained by gaining insight into the molecular structure of hydroxyl-terminated PDMS which contains hydrophobic PDMS-rich domains (polydimethylsiloxane chains) terminated with hydrophilic hydroxyl groups. For MCM-F1, MCM-F2, MCM-F3 solid films (Section B in Table 3) the water contact angle increased, compared to pure solid films, due to the presence of CIP-loaded MCM-41. Relatively the most hydrophobic surface was found for the solid film of MCM-F1 (without PDMS). The increase of polar component of surface energy as a function of PDMS content was observed. This can be explained by the high adhesion of polydimethylsiloxane chains to hydrophobic CIP-loaded MCM-41. This behaviour results in an increase of the number of hydrophilic hydroxyl groups of PDMS oriented to the sample surfaces and thus an increase of surface polar components.

Table 3. Average contact angle and surface free energy (γ_s) with its dispersive (γ_s^d) and polar (γ_s^p) components of solid films of F1, F2, F3 (A), and MCM-F1, MCM-F2, MCM-F3 (B).

Sample	Average Contact Angle [θ , °]		Surface Free Energy [mJ/m ²]			
	Measuring Liquid		Total (γ_s)	Dispersive (γ_s^d)	Polar (γ_s^p)	
	Water	Diiodomethane				
A	F1	82.2	63.0	29.27	21.35	7.92
	F2	86.3	54.2	32.03	27.81	4.22
	F3	83.5	54.4	32.50	26.99	5.51
B	MCM-F1	112.9	81.9	16.40	16.07	0.33
	MCM-F2	125.1	67.5	29.28	27.97	1.31
	MCM-F3	124.5	62.9	32.86	31.21	1.65

3.3.4. Solid-State Characterization of Ciprofloxacin

The XRD patterns of solid films of MCM-F3 and F3 (as representative examples), CIP-loaded MCM-41 and freeze-dried CIP reference are presented in Figure 4. The freeze-dried CIP reference was characterized by numerous well-defined sharp diffraction peaks demonstrating the crystalline nature of the drug. For the CIP-loaded MCM-41 sample the broad halo in the range of 15–35° derived from the amorphous silica with significant reduction of peaks characteristic for the CIP. Two diffraction peaks at 8 and 27° 2θ observed in CIP-loaded MCM-41 sample suggested the semi-crystalline nature of CIP molecules adsorbed onto the silica surface [38]. In the case of both the F3 and MCM-F3 the XRD patterns showed two broad amorphous halos at 10–15° and 15–30° 2θ which clearly revealed the amorphous nature of the obtained films.

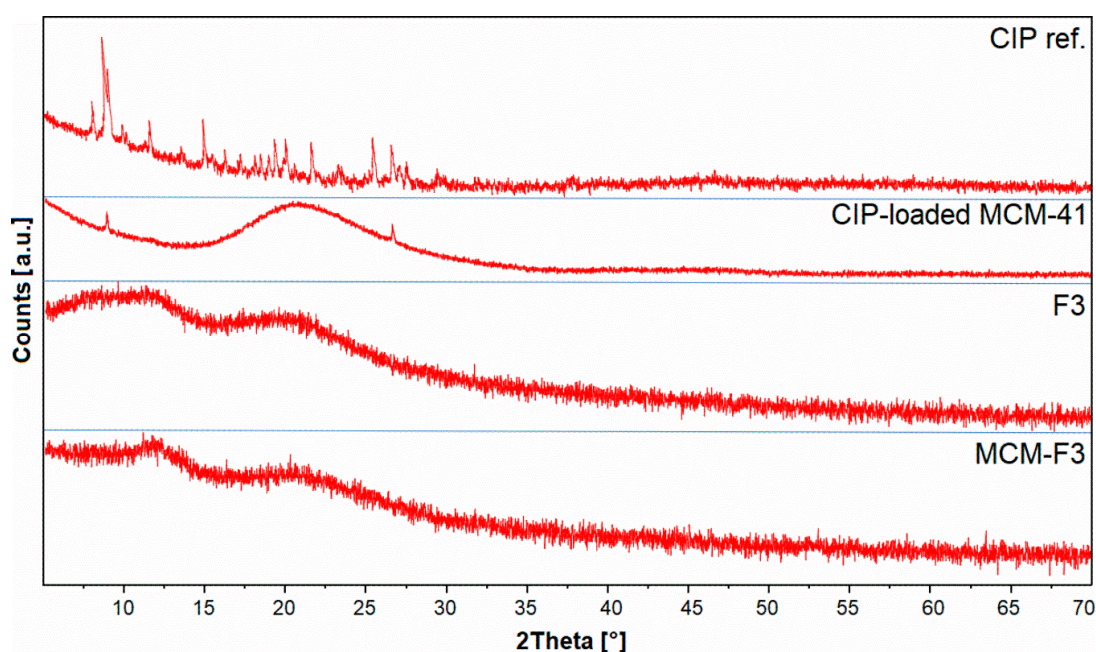


Figure 4. The XRD patterns of solid films of MCM-F3 and F3, CIP-loaded MCM-41, and CIP reference.

The DSC thermograms of solid films of MCM-F3, F3, unloaded MCM-41, freeze-dried CIP (as references) are presented in Figure 5. As selected in the frame the freeze-dried CIP was characterized by the endothermic peak of melting point at approx. 207 °C. MCM-F3 exhibited a small endothermic peak shifted to lower temperatures (approx. 199 °C) corresponding to the melting of drug, which suggested the presence of the CIP in the amorphous or semi-crystalline state what was also confirmed by the XRD results (Figure 4). The amorphous nature of drug loaded into the mesoporous silica is already

known phenomenon [39]. Moreover, the obtained DSC results are in accordance with the observations of Mesallati et al. [34] who have claimed that solid dispersions of CIP with various polymers displayed a clear melting endotherm of the drug, which could be taken as confirmation of the amorphous nature of the CIP inside the polymer matrices.

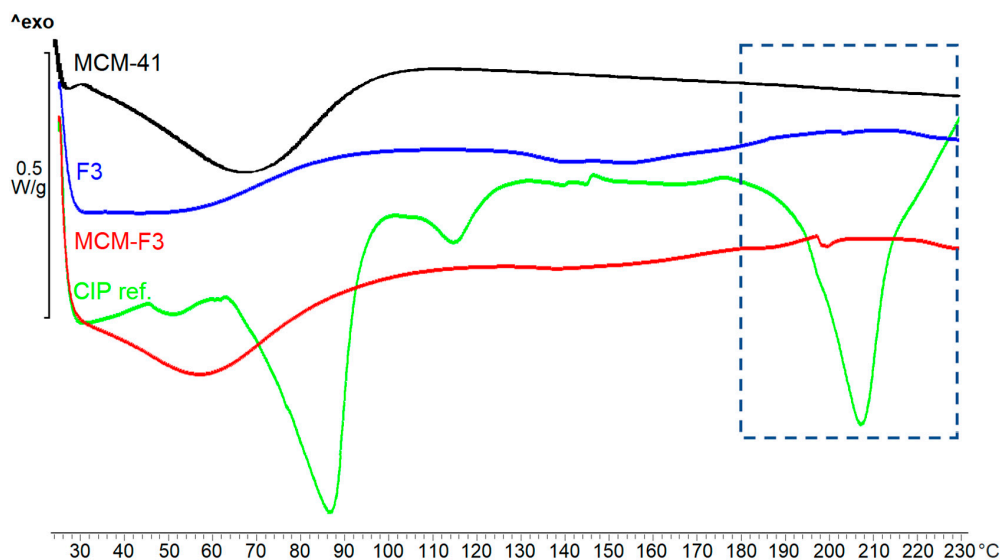


Figure 5. The DSC thermograms of solid films of MCM-F3, F3, unloaded MCM-41 and CIP reference.

3.4. Ciprofloxacin Release

The drug release was studied for MCM-F1, MCM-F2, MCM-F3 solid films to verify the impact of PDMS content on release profiles. Each solid film contained 6 mg of CIP-loaded MCM-41, corresponding to 0.67 ± 0.1 mg of CIP. CIP-elution profiles describing the cumulative percent amount of CIP released as a function of time (1–7 days), are presented in Figure 6A. Inset B shows the non-cumulative percent amount of released CIP at the sampling point as a function of the initial time period (0–2 days, Figure 6B). The CIP release from the CIP-loaded MCM-41 (6 mg, 200 μm –500 μm ; in the powder form) and from solid film F3 with addition of pure CIP (CIP-F3, 0.67 ± 0.2 mg of CIP) are shown in Figure 6 for comparative purposes. As presented in Figure 6C, both CIP-loaded MCM-41 and CIP-F3 solid film were characterised by a relatively rapid release of CIP with a huge burst during the first 24 h (80 and 88%, respectively) with almost complete CIP release after 7 days (98 and 95%, respectively). In contrast, the initial amount of the drug eluted during the first day (initial burst) was reduced to 39% of the total amount of loaded CIP for the MCM-F1 solid film (PDMS-free, Figure 6B). Next, the release kinetics slowed-down and after four exchanges of the medium, the mean value of the recovered CIP from MCM-F1 corresponded to 50% of the total amount of loaded CIP (Figure 6A), whereas it was 75% after 39 daily exchanges (estimated from the release profile). In the case of the PDMS-containing solid films F2 and F3, the initial burst was reduced to 16% and 5% of the total amount of loaded CIP (corresponding to 107.5 and 33.6 μg of CIP released during the first day), respectively (Figure 6B). Then the release kinetics gently slowed down (Figure 6A). The $t_{25\%}$, $t_{50\%}$, and $t_{75\%}$ values (corresponding to 25%, 50% and 75% of the total amount of loaded CIP, respectively), calculated from the release profiles, were 15, 66, and 107 days or 46, 117, and 168 days for MCM-F2 and MCM-F3 solid films, respectively. Thus, the release of CIP from MCM-F1, MCM-F2, MCM-F3 solid films presented a significant modification compared to CIP-loaded MCM-41 and CIP-F3 solid film. The initial burst of CIP was reduced with the increase in content of PDMS in solid films. That is why the greatest reduction in initial burst was reported for MCM-F3 solid film characterized by a prolonged release rate similar to already exist antibiotic drug delivery systems [40].

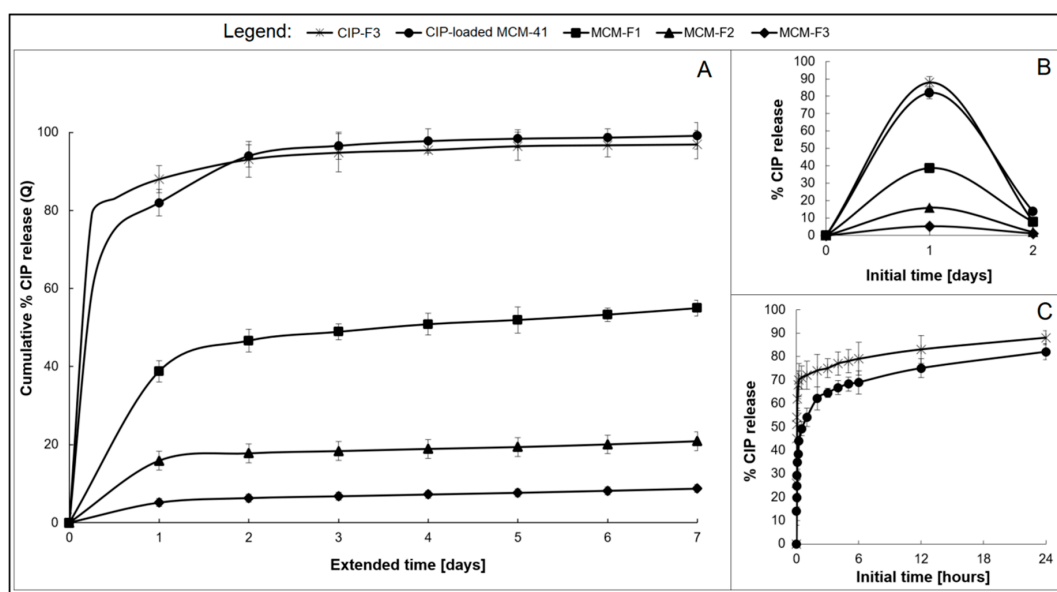


Figure 6. The overall CIP release profiles from MCM-F1, MCM-F2, MCM-F3, CIP-F3 solid films, and CIP-loaded MCM-41 (A); Insets: not-cumulative CIP release during the initial time: 0–2 days; (B) and initial 24 h CIP release from CIP-loaded MCM-41 and CIP-F3 (C).

The calculated kinetic parameters for the obtained release profiles are summarized in Table 4. It can be observed that all release profiles of solid films (excluding the first 24 h initial drug release) were characterized by zero order kinetics ($R^2 \geq 0.89$) with constant drug release rates per day. It should be noted that zero-order release CIP kinetics were observed for all PDMS-containing solid films, even after 7 days of release studies. Moreover, the release profiles of solid films were well described by both the Higuchi model ($R^2 \geq 0.93$) and the release exponent n values ≤ 0.55 suggesting the release of drug is controlled by diffusion of CIP from a non-disintegrating matrix [41]. However the use of CIP-loaded MCM-41 in solid films instead of pure CIP seemed to be essential in order to reduce the burst release, what was manifested in reduction of k_H values from 27.01 to 8.92 for CIP-F3 and MCM-F1 solid films, respectively.

Table 4. The kinetic parameters of fitted experimental data for MCM-F1, MCM-F2, MCM-F3, CIP-F3 solid films and CIP-loaded MCM-41.

Formulation	Korsmeyer-Peppas Model		Higuchi Model		Zero Order Kinetics *	
	n	R^2	k_H	R^2	k_0	R^2
CIP-F3	0.51	0.95	27.01	0.94	0.03	0.89
CIP-loaded MCM-41	0.34	0.92	4.93	0.85	0.02	0.82
MCM-F1	0.17	0.97	8.92	0.93	1.60	0.99
MCM-F2	0.33	0.87	6.80	0.98	0.61	0.99
MCM-F3	0.55	0.93	6.49	0.98	0.48	0.99

R^2 —coefficient of determination; n —release exponent in Korsmeyer-Peppas model; k_H —Higuchi dissolution constant ($h^{-1/2}$; $days^{-1/2}$); k_0 —zero order release constant (% of dose released per day); * Calculated excluding the first 24 h initial release of CIP.

Taking into account both the CIP release profile and the kinetic models the possible mechanism of drug release from CIP-loaded MCM-41 coated with polymer blends can be described as diffusion controlled [42]. In our case the water-soluble CIP molecules loaded into the mesoporous silica channels are entrapped in the EC-PDMS polymeric film which acts as a water-insoluble matrix. The structure of the formed EC film is dependent on the polymer-solvent interaction parameters. Jones et al. found

that after ethanol evaporation, the structure of EC is heterogeneous, with numerous nanopores [43]. This confirms the release of CIP via simple diffusion from CIP-loaded MCM-41 coated with EC (MCM-F1 solid film) through the formed pores (release exponent $n = 0.51$, calculated from the Korsmeyer-Peppas model). However, the observed reduction of both the initial burst and the rate of CIP release from CIP-loaded MCM-41 coated with PDMS:EC blends may be attributed to the adhesion of PDMS chains onto the CIP-loaded MCM-41 surface, which is also in agreement with the obtained SEM results (Figure 2A) and wettability data (Table 3). Another reason can be related to a “locking” of the pore surface of EC due to the greater surface contact and thus easier penetration of the PDMS into the pores. The effect of PDMS on the release rate of water-soluble drugs from silica/PDMS composites has previously been reported [39]. It was found that an increase in PDMS content resulted in a decreasing rate of drug release, and as reported here, with a simultaneous increase in the values of the release exponent n . This phenomenon was correlated with a decrease in the porosity of the studied silica/PDMS composites, explained by the effect of the occlusion of hydrophobic PDMS-rich domains on the silica particles that may delay the penetration of water molecules into the composites, and hence dissolution of a loaded drug [44,45]. To sum up, the increase of PDMS content in solid films of MCM-F2, MCM-F3 may result in an increasing number of PDMS-filled nanopores, and also lock the CIP in the pores of MCM-41, thus slowing down the drug release [46]. Consequently, the zero-order CIP release could be explained by the very small magnitude of the interfacial partition coefficient of the drug and the small thickness of the drug depletion layer.

4. Conclusions

Novel solid films were obtained by coating CIP-loaded MCM-41 with PDMS:EC blends. Solid films with various levels of PDMS addition (0, 1, 2% (v/v)) were characterized in terms of their physicochemical properties. SEM and optical profilometry results indicated a progressive increase in the surface heterogeneity and roughness for the solid films of CIP-loaded MCM-41 coated with polymer blends as a function of PDMS content. The presence of amorphous/semi-crystalline CIP in the obtained films was confirmed by DSC and XRD analyses. Release studies showed a prolonged CIP release from all solid films for over 7 days with Fickian diffusion-controlled drug release for the EC formulation without PDMS and the zero-order drug release for formulations containing PDMS. This is probably related to the adhesion of hydrophobic chains of PDMS onto CIP-loaded MCM-41. The physicochemical characterization of the obtained solid films showed that by simple modification of the PDMS:EC ratio, the roughness and release profile of drug adsorbed into the MCM-41 pores can be easily altered. As the surface roughness has a fundamental significance for the integration with host bone tissue, the provided mesoporous silica coated with polymer blends could be a promising drug delivery system. The most beneficial physicochemical properties in the context of further biological evaluation, such as the greatest reduction of initial burst of CIP and the highest values of roughness parameters were observed for MCM-F3 solid film. The findings presented in this paper may be an excellent starting point for further investigations on the biocompatibility and material/cell interactions of the systems.

Supplementary Materials: The following are available online at <http://www.mdpi.com/2073-4360/11/9/1450/s1>.

Author Contributions: Conceptualization, M.P.; Formal analysis, M.P.; Funding acquisition, A.S. (Adrianna Skwira) and M.P.; Investigation, A.S. (Adrianna Skwira), A.S. (Adrian Szewczyk) and M.P.; Methodology, A.S. (Adrianna Skwira), A.S. (Adrian Szewczyk) and M.P.; Supervision, M.P.; Writing—original draft, A.S. (Adrianna Skwira), A.S. (Adrian Szewczyk) and M.P.

Funding: This research was supported by the project OPUS 15 (2018/29/B/NZ7/00533) co-financed by National Science Centre, and partially supported by the project POWR.03.02.00-00-I035/16-00 co-financed by the European Union through the European Social Fund under the Operational Programme Knowledge Education Development 2014–2020.

Acknowledgments: The authors wish to thank Marta Ziegler-Borowska from Nicolaus Copernicus University in Torun for experimental assistance.

Conflicts of Interest: The authors declare no conflict of interest. The funders had no role in the design of the study; in the collection, analyses, or interpretation of data; in the writing of the manuscript, or in the decision to publish the results.

References

1. Nandi, S.K.; Bandyopadhyay, S.; Das, P.; Samanta, I.; Mukherjee, P.; Roy, S.; Kundu, B. Understanding Osteomyelitis and Its Treatment through Local Drug Delivery System. *Biotechnol. Adv.* **2016**, *34*, 1305–1317. [[CrossRef](#)] [[PubMed](#)]
2. Mouriño, V.; Boccaccini, A.R. Bone Tissue Engineering Therapeutics: Controlled Drug Delivery in Three-Dimensional Scaffolds. *J. R. Soc. Interface* **2010**, *7*, 209–227. [[CrossRef](#)] [[PubMed](#)]
3. Park, K. Controlled Drug Delivery Systems: Past Forward and Future Back. *J. Control. Release* **2014**, *190*, 3–8. [[CrossRef](#)] [[PubMed](#)]
4. Wang, S. Ordered Mesoporous Materials for Drug Delivery. *Microporous Mesoporous Mater.* **2009**, *117*, 1–9. [[CrossRef](#)]
5. Prokopowicz, M.; Czarnobaj, K.; Szewczyk, A.; Sawicki, W. Preparation and in Vitro Characterisation of Bioactive Mesoporous Silica Microparticles for Drug Delivery Applications. *Mater. Sci. Eng. C* **2016**, *60*, 7–18. [[CrossRef](#)] [[PubMed](#)]
6. Beck, G.R.; Ha, S.W.; Camalier, C.E.; Yamaguchi, M.; Li, Y.; Lee, J.K.; Weitzmann, M.N. Bioactive Silica-Based Nanoparticles Stimulate Bone-forming Osteoblasts, Suppress Bone-Resorbing Osteoclasts, and Enhance Bone Mineral Density in Vivo. *Nanomed. Nanotechnol. Biol. Med.* **2012**, *8*, 793–803. [[CrossRef](#)]
7. Braun, K.; Pochert, A.; Beck, M.; Fiedler, R.; Gruber, J.; Lindén, M. Dissolution Kinetics of Mesoporous Silica Nanoparticles in Different Simulated Body Fluids. *J. Sol-Gel Sci. Technol.* **2016**, *79*, 319–327. [[CrossRef](#)]
8. Götz, W.; Tobiasch, E.; Witzleben, S.; Schulze, M. Effects of Silicon Compounds on Biomineralization, Osteogenesis, and Hard Tissue Formation. *Pharmaceutics* **2019**, *11*, 117. [[CrossRef](#)]
9. Pérez-Esteve, É.; Ruiz-Rico, M.; De La Torre, C.; Villaescusa, L.A.; Sancenón, F.; Marcos, M.D.; Amorós, P.; Martínez-Mañez, R.; Barat, J.M. Encapsulation of Folic Acid in Different Silica Porous Supports: A Comparative Study. *Food Chem.* **2016**, *196*, 66–75. [[CrossRef](#)]
10. Lee, J.H.; Yeo, Y. Controlled Drug Release from Pharmaceutical Nanocarriers. *Chem. Eng. Sci.* **2015**, *125*, 75–84. [[CrossRef](#)]
11. Siepmann, F.; Siepmann, J.; Walther, M.; MacRae, R.J.; Bodmeier, R. Polymer Blends for Controlled Release Coatings. *J. Control. Release* **2008**, *125*, 1–15. [[CrossRef](#)] [[PubMed](#)]
12. Duo, Y.; Li, Y.; Chen, C.; Liu, B.; Wang, X.; Zeng, X.; Chen, H. DOX-Loaded pH-Sensitive Mesoporous Silica Nanoparticles Coated with PDA and PEG Induce Pro-Death Autophagy in Breast Cancer. *RSC Adv.* **2017**, *7*, 39641–39650. [[CrossRef](#)]
13. Bhattacharyya, S.; Wang, H.; Ducheyne, P. Polymer-Coated Mesoporous Silica Nanoparticles for the Controlled Release of Macromolecules. *Acta Biomater.* **2012**, *8*, 3429–3435. [[CrossRef](#)] [[PubMed](#)]
14. Trendafilova, I.; Szegedi, Á.; Yoncheva, K.; Shestakova, P.; Mihály, J.; Ristić, A.; Konstantinov, S.; Popova, M. A pH Dependent Delivery of Mesalazine from Polymer Coated and Drug-Loaded SBA-16 Systems. *Eur. J. Pharm. Sci.* **2016**, *81*, 75–81. [[CrossRef](#)] [[PubMed](#)]
15. Smith, J.R.; Lamprou, D.A. Polymer Coatings for Biomedical Applications: A Review. *Trans. IMF* **2014**, *92*, 9–19. [[CrossRef](#)]
16. Lecomte, F.; Siepmann, J.; Walther, M.; MacRae, R.J.; Bodmeier, R. Polymer Blends used for the Coating of Multiparticulates: Comparison of Aqueous and Organic Coating Techniques. *Pharm. Res.* **2004**, *21*, 882–890. [[CrossRef](#)] [[PubMed](#)]
17. Ponche, A.; Bigerelle, M.; Anselme, K. Relative Influence of Surface Topography and Surface Chemistry on Cell Response to Bone Implant Materials. Part 1: Physico-Chemical Effects. *Proc. Inst. Mech. Eng. Part H J. Eng. Med.* **2010**, *224*, 1471–1486. [[CrossRef](#)] [[PubMed](#)]
18. Hokmabad, V.R.; Davaran, S.; Aghazadeh, M.; Rahbarghazi, R.; Salehi, R.; Ramazani, A. Fabrication and characterization of Novel ethyl Cellulose-Grafted-Poly (ϵ -caprolactone)/alginate Nanofibrous/Macroporous Scaffolds Incorporated with Nano-Hydroxyapatite for Bone Tissue Engineering. *J. Biomater. Appl.* **2019**, *33*, 1128–1144. [[CrossRef](#)]

19. Le Guéhennec, L.; Soueidan, A.; Layrolle, P.; Amouriq, Y. Surface Treatments of Titanium Dental Implants for Rapid Osseointegration. *Dent. Mater.* **2007**, *23*, 844–854. [[CrossRef](#)]
20. Krishna Alla, R.; Ginjupalli, K.; Upadhya, N.; Shammas, M.; Krishna Ravi, R.; Sekhar, R. Surface Roughness of Implants: A review. *Trends Biomater. Artif. Organs* **2011**, *25*, 112–118.
21. Linez-Bataillon, P.; Monchau, F.; Bigerelle, M.; Hildebrand, H.F. In Vitro MC3T3 Osteoblast Adhesion with Respect to Surface Roughness of Ti6Al4V Substrates. *Biomol. Eng.* **2002**, *19*, 133–141. [[CrossRef](#)]
22. Wirth, J.; Tahriri, M.; Khoshroo, K.; Rasoulianboroujeni, M.; Dentino, A.R.; Tayebi, L. Surface Modification of Dental Implants. In *Biomaterials for Oral and Dental Tissue Engineering*; Woodhead Publishing: Cambridge, MA, USA, 2017; pp. 85–96.
23. Garg, H.; Bedi, G.; Garg, A. Implant Surface Modifications: A review. *J. Clin. Diagn. Res.* **2012**, *6*, 319–324.
24. Bose, S.; Bogner, R.H. Solventless Pharmaceutical Coating Processes: A review. *Pharm. Dev. Technol.* **2007**, *12*, 115–131. [[CrossRef](#)] [[PubMed](#)]
25. Teo, A.J.T.; Mishra, A.; Park, I.; Kim, Y.J.; Park, W.T.; Yoon, Y.J. Polymeric Biomaterials for Medical Implants and Devices. *ACS Biomater. Sci. Eng.* **2016**, *2*, 454–472. [[CrossRef](#)]
26. Blanco, I. Polysiloxanes in Theranostics and Drug Delivery: A Review. *Polymers (Basel)* **2018**, *10*, 755. [[CrossRef](#)] [[PubMed](#)]
27. Murtaza, G. Ethylcellulose Microparticles: A review. *Acta Pol. Pharm.-Drug Res.* **2012**, *69*, 11–22.
28. Tian, B.; Tang, S.; Li, Y.; Long, T.; Qu, X.H.; Yu, D.G.; Guo, Y.J.; Guo, Y.P.; Zhu, Z.A. Fabrication, Characterization, and Biocompatibility of Ethyl Cellulose/Carbonated Hydroxyapatite Composite coatings on Ti6Al4V. *J. Mater. Sci. Mater. Med.* **2014**. [[CrossRef](#)] [[PubMed](#)]
29. Mehta, R.Y.; Missaghi, S.; Tiwari, S.B.; Rajabi-Siahboomi, A.R. Application of Ethylcellulose Coating to Hydrophilic Matrices: A Strategy to Modulate Drug Release Profile and Reduce Drug Release Variability. *AAPS Pharm. Sci. Tech.* **2014**, *15*, 1049–1059. [[CrossRef](#)]
30. Mata, A.; Fleischman, A.J.; Roy, S. Characterization of Polydimethylsiloxane (PDMS) Properties for Biomedical Micro/Nanosystems. *Biomed. Microdevices* **2005**, *7*, 281–293. [[CrossRef](#)] [[PubMed](#)]
31. Tsourvakas, S. Local Antibiotic Therapy in the Treatment of Bone and Soft Tissue Infections. *Sel. Top. Plast. Reconstr. Surg.* **2012**, 17–46.
32. Vallet-Regi, M.; Rámila, A.; Del Real, R.P.; Pérez-Pariente, J. A new property of MCM-41: Drug delivery system. *Chem. Mater.* **2001**, *13*, 308–311. [[CrossRef](#)]
33. Hanoosh, W.S.; Abdelrazaq, E.M. Polydimethyl Siloxane Toughened Epoxy Resins: Tensile Strength and Dynamic Mechanical Analysis. *Malaysian Polym. J.* **2009**, *4*, 52–61.
34. Mesallati, H.; Umerska, A.; Paluch, K.J.; Tajber, L. Amorphous Polymeric Drug Salts as Ionic Solid Dispersion Forms of Ciprofloxacin. *Mol. Pharm.* **2017**, *14*, 2209–2223. [[CrossRef](#)] [[PubMed](#)]
35. Trivedi, M.K.; Branton, A.; Trivedi, D.; Nayak, G.; Mishra, R.K.; Jana, S. Characterization of Physicochemical and Thermal Properties of Biofield Treated Ethyl Cellulose and Methyl Cellulose. *Int. J. Biomed. Mater. Res.* **2015**, *3*, 83–91.
36. Johnson, L.M.; Gao, L.; Shields, C.W.; Smith, M.; Efimenko, K.; Cushing, K.; Genzer, J.; López, G.P. Elastomeric microparticles for acoustic mediated bioseparations. *J. Nanobiotechnology* **2013**, *11*, 22. [[CrossRef](#)] [[PubMed](#)]
37. Yamashita, D.; Machigashira, M.; Miyamoto, M.; Takeuchi, H.; Noguchi, K.; Izumi, Y.; Ban, S. Effect of surface roughness on initial responses of osteoblast-like cells on two types of zirconia. *Dent. Mater. J.* **2009**, *28*, 461–470. [[CrossRef](#)] [[PubMed](#)]
38. Wang, Z.; Chen, B.; Quan, G.; Li, F.; Wu, Q.; Dian, L.; Dong, Y.; Li, G.; Wu, C. Increasing the oral bioavailability of poorly water-soluble carbamazepine using immediate-release pellets supported on SBA-15 mesoporous silica. *Int. J. Nanomedicine* **2012**, *7*, 5807–5818. [[PubMed](#)]
39. Prokopowicz, M. Correlation between physicochemical properties of doxorubicin-loaded silica/polydimethylsiloxane xerogel and in vitro release of drug. *Acta Biomater.* **2009**, *5*, 193–207. [[CrossRef](#)]
40. Nandi, S.K.; Mukherjee, P.; Roy, S.; Kundu, B.; De, D.K.; Basu, D. Local antibiotic delivery systems for the treatment of osteomyelitis - A review. *Mater. Sci. Eng. C* **2009**, *29*, 2478–2485. [[CrossRef](#)]
41. Costa, P.; Sousa Lobo, J.M. Modeling and comparison of dissolution profiles. *Eur. J. Pharm. Sci.* **2001**, *13*, 123–133. [[CrossRef](#)]
42. Huynh, C.T.; Lee, D.S. Controlled Release. *Encycl. Polym. Nanomater.* **2015**, 439–449. [[CrossRef](#)]

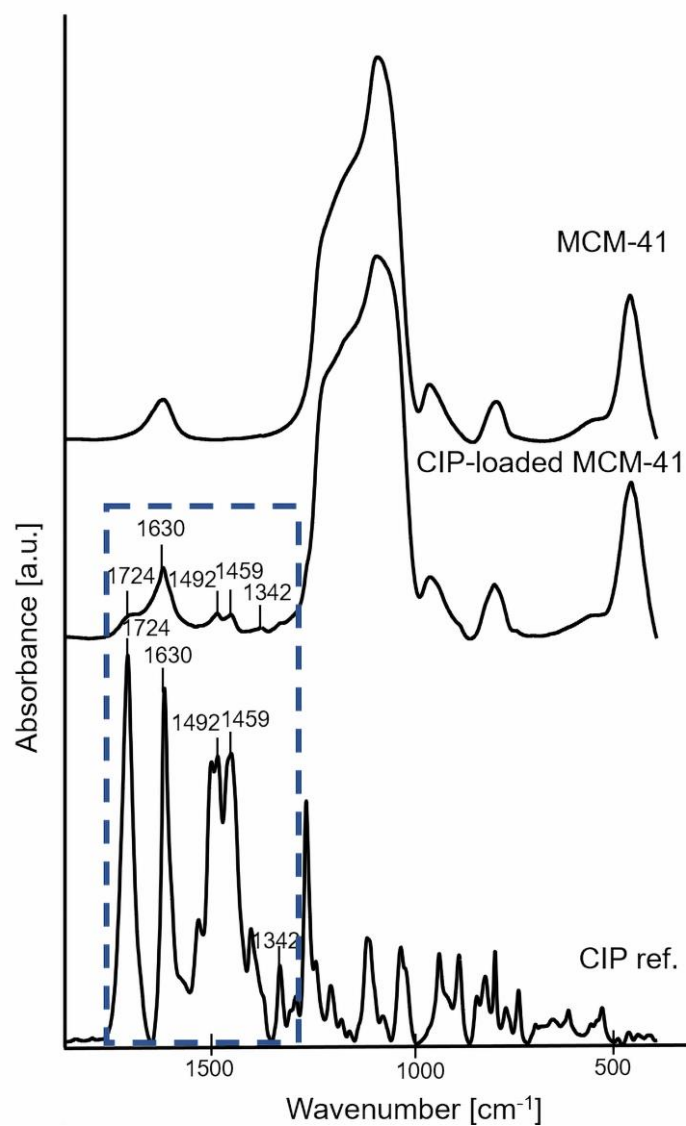
43. Jones, D.S.; Medlicott, N.J. Casting solvent controlled release of chlorhexidine from ethylcellulose films prepared by solvent evaporation. *Int. J. Pharm.* **1995**, *114*, 257–261. [[CrossRef](#)]
44. Prokopowicz, M. Atomic force microscopy technique for the surface characterization of sol–gel derived multi-component silica nanocomposites. *Colloids Surfaces A Physicochem. Eng. Asp.* **2016**, *504*, 350–357. [[CrossRef](#)]
45. Kim, H.J.; Matsuda, H.; Zhou, H.; Honma, I. Ultrasound-triggered smart drug release from a poly(dimethylsiloxane)- mesoporous silica composite. *Adv. Mater.* **2006**, *18*, 3083–3088. [[CrossRef](#)]
46. Popova, M.; Trendafilova, I.; Zgureva, D.; Kalvachev, Y.; Boycheva, S.; Novak Tušar, N.; Szegedi, A. Polymer-coated mesoporous silica nanoparticles for controlled release of the prodrug sulfasalazine. *J. Drug Deliv. Sci. Technol.* **2018**, *44*, 415–420. [[CrossRef](#)]



© 2019 by the authors. Licensee MDPI, Basel, Switzerland. This article is an open access article distributed under the terms and conditions of the Creative Commons Attribution (CC BY) license (<http://creativecommons.org/licenses/by/4.0/>).

Supplementary data

A. Skwira, A. Szewczyk, M. Prokopowicz, The Effect of Polydimethylsiloxane-Ethylcellulose Coating Blends on the Surface Characterization and Drug Release of Ciprofloxacin-Loaded Mesoporous Silica, *Polymers (Basel)*. 11 (2019) 1450.



Supplementary Fig. 1. FTIR spectra of MCM-41 before and after ciprofloxacin adsorption (CIP-loaded MCM-41) together with ciprofloxacin reference sample (CIP ref.).

Publikacja 2. A. Skwira, A. Szewczyk, A. Konopacka, M. Górską, D. Majda, R. Sądej, M. Prokopowicz, *Silica-polymer composites as the novel antibiotic delivery systems for bone tissue infection, Pharmaceutics. 12 (2020) 28.*

Głównym celem badań opublikowanych w drugim artykule było poszerzenie charakterystyki fizykochemicznej oraz przeprowadzenie analizy mikrobiologicznej i biologicznej kompozytów otrzymanych z formułacji wytypowanych na podstawie wyników opisanych w publikacji pierwszej. Wśród nich znalazły się: *MCM-F1*, *MCM-F3*, *CIP-F3* oraz dodatkowo *CIP-F1* (liofilizowana cyprofloksacyna fizycznie zdyspergowana w matrycy etylocelulozowej, bez dodatku PDMS-u). Dla kompozytów tych przyjęto następujące nazwy: *EC/MCM-41-CIP*, *EC/PDMS/MCM-41-CIP*, *EC/PDMS/CIP* oraz *EC/CIP*.

W niniejszym artykule, w celu scharakteryzowania kompozytów w zakresie właściwości fizykochemicznych, oprócz standardowych analiz przeprowadzonych za pomocą technik FTIR i SEM-EDX, przeprowadzono także, istotną dla biomateriałów przeznaczonych do implantacji do tkanki kostnej, ocenę parametrów tekstury przy użyciu analizatora tekstury TA.XTplusC. Za pomocą metody termogravimetrii (TGA) oraz skaningowej kalorymetrii różnicowej (DSC) określono wpływ powlekania materiałów krzemionkowych mieszaninami polimerowymi na stabilność termiczną cyprofloksacyny. Ponownie wyznaczono profile uwalniania antybiotyku z poszczególnych kompozytów na podstawie wyników badania dostępności farmaceutycznej. W celu poszerzenia analizy badanie prowadzono 30 dni. Aktywność przeciwdrobnoustrojową uwalnianego z otrzymanych kompozytów antybiotyku zweryfikowano wykorzystując szczep referencyjny *Staphylococcus aureus* (ATCC 6538) za pomocą zmodyfikowanej metody dyfuzyjnej. Analizę cytotoksyczności otrzymanych kompozytów przeprowadzono za pomocą rekomendowanego przez część piątą normy ISO 10993 (*Biological evaluation of medical devices — Part 5: Tests for in vitro cytotoxicity*) testu kontaktu bezpośredniego z wykorzystaniem linii komórkowej ludzkich osteoblastów hFOB 1.19.

Analiza tekstury wykazała, że dodatek PDMS-u do kompozytów wpłynął na zwiększenie elastyczności (ang. *elasticity*), siły potrzebnej do pęknięcia próbki (ang. *rupture force*) i twardości, będącej miarą odporności na odkształcenia (ang. *firmness*). Jest to znane zjawisko wynikające z właściwości elastomerowych PDMS-u. W literaturze odnotowano poprawę elastyczności i sprężystości w wyniku dodatku zakończonych grupami hydroksylowymi PDMS-u do powłok złożonych z żywic

epoksydowych i grafenu [100] oraz powłok zawierających nanocząstki krzemionki i tlenku tytanu [101]. Na podstawie analizy termicznej TGA i DSC wykazano, że wśród kompozytów najwyższą stabilnością termiczną charakteryzował się *EC/PDMS/MCM-41-CIP*. Potwierdziło to korzystny wpływ adsorpcji cyprofloksacyny na mezoporowatym materiale krzemionkowym oraz procesu powlekania mieszaniną złożoną z etylocelulozy i PDMS-u na stabilność termiczną antybiotyku. Obserwacja ta jest zgodna z potwierdzoną w literaturze odpornością termiczną obu polimerów [104,105].

Przeprowadzone badanie dostępności farmaceutycznej potwierdziło wcześniejsze obserwacje dotyczące modyfikacji uwalniania cyprofloksacyny z kompozytów. Największe zmniejszenie początkowego uwolnienia cyprofloksacyny obserwowano dla kompozytów *EC/PDMS/MCM-41-CIP* (Tabela 3). Kompozyty te oraz kompozyty *EC/MCM-41-CIP* wykazały również znaczne przedłużenie uwalniania, w stosunku do pozostałych kompozytów, charakteryzujące się uwolnieniem odpowiednio 21% i 75% całkowitej ilości cyprofloksacyny w czasie badania trwającego 30 dni. Analiza kinetyki procesu uwalniania ponownie wskazała na mechanizm dyfuzyjny.

Tabela 3. Procentowa ilość uwolnionej cyprofloksacyny z poszczególnych kompozytów.

Nazwa kompozytu	Procentowa ilość cyprofloksacyny uwolnionej po pierwszych 24 godzinach badania	Procentowa ilość cyprofloksacyny uwolnionej po całkowitym czasie badania – 30 dniach
<i>MCM-41-CIP</i>	80%	97%*
<i>EC/MCM-41-CIP</i>	39%	75%
<i>EC/PDMS/MCM-41-CIP</i>	9%	21%
<i>EC/PDMS/CIP</i>	86%	98%**
<i>EC/CIP</i>	89%	97%*

* uwolnienie całkowitej ilości antybiotyku po 6 dniach badania; ** uwolnienie całkowitej ilości antybiotyku po 7 dniach badania

Ważnym aspektem niniejszego artykułu była również ocena działania przeciwdrobnoustrojowego uwalnianego z kompozytów antybiotyku. Za pomocą testu aktywności przeciwbakteryjnej wykazano znaczący wpływ obecności PDMS-u w kompozycie na wielkość strefy zahamowania wzrostu *S. aureus*. Po upływie pierwszych 24 godzin eksperymentu największą strefę zahamowania wzrostu wyznaczono dla kompozytów *EC/CIP* (Tabela 4). W przypadku kompozytów

EC/PDMS/CIP obserwowano zmniejszenie powierzchni strefy zahamowania wzrostu bakterii o około 20%. Podobną powierzchnię strefy zahamowania wzrostu wyznaczono dla kompozytów *EC/MCM-41-CIP*. Dodatek PDMS-u do tych kompozytów (*EC/PDMS/MCM-41-CIP*) spowodował ok. 3-krotne zmniejszenie pola powierzchni strefy zahamowania wzrostu *S. aureus*. Ponadto kompozyty zawierające liofilizowany antybiotyk (*EC/CIP* i *EC/PDMS/CIP*) charakteryzowały się maksymalnie 7-dniową aktywnością przeciwdrobnoustrojową, natomiast kompozyty zawierające antybiotyk zaadsorbowany na MCM-41 wykazywały działanie przeciwbakteryjne do 20. (*EC/MCM-41-CIP*) i 30. (*EC/PDMS/MCM-41-CIP*) dnia eksperymentu.

Tabela 4. Powierzchnia strefy zahamowania wzrostu bakterii wyznaczona dla poszczególnych kompozytów po pierwszych 24 godzinach badania oraz czas aktywności przeciwbakteryjnej.

Nazwa kompozytu	Powierzchnia strefy zahamowania wzrostu bakterii [cm ²]	Czas aktywności przeciwbakteryjnej [dni]
<i>EC/CIP</i>	48,5 ± 8,42	6
<i>EC/PDMS/CIP</i>	37,8 ± 7,23	7
<i>EC/MCM-41-CIP</i>	36,2 ± 6,8	20
<i>EC/PDMS/MCM-41-CIP</i>	12,7 ± 2,59	30

Na podstawie uzyskanych wyników badania dostępności farmaceutycznej oraz oceny mikrobiologicznej stwierdzono, że zarówno adsorpcja cyprofloksacyny na MCM-41, jak i obecność PDMS-u w formulacji są kluczowe dla uzyskania oczekiwanej długotrwałej aktywności przeciwbakteryjnej w warunkach *in vitro*.

Za pomocą testu cytotoksyczności oceniono wpływ na żywotność osteoblastów zarówno bezpośredniego oddziaływania kompozytów, jak również uwalnianej do pożywki komórkowej cyprofloksacyny. Oba aspekty są kluczowe dla implantowanych do tkanki kostnej systemów dostarczających antybiotyki. Potwierdzono w ten sposób biogodność poszczególnych komponentów otrzymanych kompozytów (etylocelulozy, PDMS-u, MCM-41) na poziomie komórkowym oraz wykazano zależną od stężenia cytotoksyczność cyprofloksacyny ($IC_{50} = 79 \mu\text{g/ml}$). Kompozyty zawierające cyprofloksacynę zaadsorbowaną na mezoporowatym materiale krzemionkowym (*EC/MCM-41-CIP* i *EC/PDMS/MCM-41-CIP*) wykazały całkowitą biogodność z ludzkimi osteoblastami, natomiast obecność w hodowli komórkowej kompozytów

zawierających liofilizowany antybiotyk, niezaadsorbowany na MCM-41 (*EC/CIP* i *EC/PDMS/CIP*) spowodowała spadek żywotności komórek. Obserwacje te dowiodły, że zmniejszenie żywotności osteoblastów związane było z uwalnianym do pożywki komórkowej antybiotykiem.

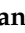


Badania opisane w niniejszym artykule potwierdziły, w aspekcie mikrobiologicznym i biologicznym, słusność i skuteczność modyfikacji uwalniania antybiotyku za pomocą zaproponowanej mieszaniny polimerowej. Najlepsze właściwości mechaniczne, termiczne, największe zmniejszenie początkowego wyrzutu substancji leczniczej oraz najdłużej utrzymującą się aktywność przeciwdrobnoustrojową, przy zachowanej całkowitej biogodności z ludzkimi osteoblastami, wykazano dla kompozytów formulacji o najwyższej zawartości PDMS-u (*EC/PDMS/MCM-41-CIP*).

Podsumowując wyniki badań opisanych w powyższych artykułach naukowych (publikacje 1 i 2) można stwierdzić, iż zastosowanie PDMS-u w mieszaninie polimerowej skutkuje:

- oczekiwaną modyfikacją profilu uwalniania cyprofloksacyny (zmniejszenie początkowego wyrzutu oraz przedłużenie całkowitego czasu uwalniania),
- poprawą właściwości mechanicznych kompozytów,
- zwiększeniem stabilności termicznej antybiotyku w kompozytach,
- wydłużeniem czasu trwania aktywności przeciwdrobnoustrojowej kompozytów,
- zwiększeniem biogodności otrzymywanych kompozytów na poziomie komórkowym.

Article

Silica-Polymer Composites as the Novel Antibiotic Delivery Systems for Bone Tissue Infection

Adrianna Skwira ¹, Adrian Szewczyk ¹, Agnieszka Konopacka ², Monika Górka ³, Dorota Majda ⁴, Rafał Sądej ³ and Magdalena Prokopowicz ^{1,*}

¹ Department of Physical Chemistry, Faculty of Pharmacy, Medical University of Gdańsk, Hallera 107, 80-416 Gdańsk, Poland; adrianna.skwira@gumed.edu.pl (A.S.); adrian.szewczyk@gumed.edu.pl (A.S.)

² Department of Pharmaceutical Microbiology, Faculty of Pharmacy, Medical University of Gdańsk, Hallera 107, 80-416 Gdańsk, Poland; agnieszka.konopacka@gumed.edu.pl

³ Department of Molecular Enzymology and Oncology, Intercollegiate Faculty of Biotechnology, University of Gdańsk and Medical University of Gdańsk, 80-210 Gdańsk, Poland; monika.gorska@gumed.edu.pl (M.G.); rsadej@gumed.edu.pl (R.S.)

⁴ Faculty of Chemistry, Jagiellonian University, Gronostajowa 2, 30-387 Kraków, Poland; majda@chemia.uj.edu.pl

* Correspondence: magdalena.prokopowicz@gumed.edu.pl

Received: 29 November 2019; Accepted: 25 December 2019; Published: 30 December 2019



Abstract: Bone tissue inflammation, *osteomyelitis*, is commonly caused by bacterial invasion and requires prolonged antibiotic therapy for weeks or months. Thus, the aim of this study was to develop novel silica-polymer local bone antibiotic delivery systems characterized by a sustained release of ciprofloxacin (CIP) which remain active against *Staphylococcus aureus* for a few weeks, and do not have a toxic effect towards human osteoblasts. Four formulations composed of ethylcellulose (EC), polydimethylsiloxane (PDMS), freeze-dried CIP, and CIP-adsorbed mesoporous silica materials (MCM-41-CIP) were prepared via solvent-evaporation blending method. All obtained composites were characterized in terms of molecular structure, morphological, and structural properties by using Fourier Transform Infrared Spectroscopy (FTIR), scanning electron microscopy equipped with energy-dispersive X-ray spectroscopy (SEM/EDX), and X-ray diffraction (XRD), thermal stability by thermogravimetric analysis (TGA) and differential scanning calorimetry (DSC), and in vitro antibiotic release. The antibacterial activity against *Staphylococcus aureus* (ATCC 6538) as well as the in vitro cytocompatibility to human osteoblasts of obtained composites were also examined. Physicochemical results confirmed the presence of particular components (FTIR), formation of continuous polymer phase onto the surface of freeze-dried CIP or MCM-41-CIP (SEM/EDX), and semi-crystalline (composites containing freeze-dried CIP) or amorphous (composites containing MCM-41-CIP) structure (XRD). TGA and DSC analysis indicated the high thermal stability of CIP adsorbed onto the MCM-41, and higher after MCM-41-CIP coating with polymer blend. The release study revealed the significant reduction in initial burst of CIP for the composites which contained MCM-41-CIP instead of freeze-dried CIP. These composites were also characterized by the 30-day activity against *S. aureus* and the highest cytocompatibility to human osteoblasts in vitro.

Keywords: drug delivery system; mesoporous silica; silica-polymer; ciprofloxacin; polydimethylsiloxane; composites; coating blend

1. Introduction

Surgical site infection, bone fracture, or trauma may lead to severe bone inflammation such as *osteomyelitis* [1]. Treatment with systemic delivery of antibiotics usually lasts from 4 to 6 weeks,

and requires an administration of high dosages to achieve a sufficient concentration at the site of infection. Moreover, it may be unachievable in patients with poorly vascularized infected tissue and osteonecrosis, which are common symptoms accompanying *osteomyelitis* [2].

Therefore, local bone antibiotic delivery systems (LBADS) have gained an increasing interest in the treatment of bone tissue infections, as an alternative method to the systemic therapy [3,4], that provide the release of antibiotics in controlled and sustained manner directly in infected bone site. Therapy with the use of LBADS has been found as safe and effective due to limiting its action only to desired site. Local concentrations of antibiotics that have been released from implantable LBADS are many times higher than minimal inhibitory concentration (MIC). Thus, LBADS provide the efficient antibacterial activity and decrease the risk of bacterial resistance at the site of infection. However, the maintenance of antibiotics at high concentrations in bone tissue for a long time may lead to significant impairment of bone cells functions or cytotoxic effect [5,6]. Duewelhenke et al. [7] and Rathbone et al. [8] examined the influence of antimicrobial agents on human osteoblasts activity and viability. The authors presented a concentration-dependent cytotoxicity of antibiotics towards human osteoblasts. Therefore, the greatest challenge for LBADS is to provide the antibiotic at effective, bactericidal levels which are not toxic to human tissues.

Among LBADS, mesoporous silica materials (MSM) have received considerable attention, due to their unique properties, such as high surface area, controlled mesopore size, tunable pore diameter, thermal stability, biocompatibility, and modified release profile of active substance [9–11]. However, the release profiles of water-soluble drug, such as antibiotics, loaded into MSM have usually presented high-level burst release [12] which may be difficult to control and lead to cytotoxic effect. Therefore, the development of antibiotic-loaded mesoporous silica characterized by a sustained release with reduced initial burst has constituted a major challenge. Various methods of chemical drug release modification have been described [13–16]. They have been mainly focused on mesoporous silica surface functionalization by the reaction of silanols with the amino-propyl [17], carboxylic [18] groups, or organic chains [19,20]. These processes may slow down the release rate but usually the time of drug release does not exceed a few days [21,22]. However, due to the long duration of *osteomyelitis* treatment, there is a need to provide the local system which releases the antibacterial agents for at least a few weeks. Presently, a great attention has been paid to fabrication of silica-based composites [23,24] which exhibit both the significantly prolonged release of drug and good biocompatibility [25,26]. Advanced silica-polymer composites have been mainly prepared by the blending method combined with the solvent evaporation [27].

Therefore, the main objective of this study was to design the silica-polymer composites characterized by (i) reduced initial burst, (ii) sustained release of antibiotic, which remain active for a few weeks against bacteria that commonly cause *osteomyelitis*, and (iii) do not have a toxic effect towards human osteoblasts. *Staphylococcus aureus* strains have been the most frequently isolated pathogens from the site of infection in bone tissue [28]. These strains are sensitive to fluoroquinolones which present essential characteristics for the use in local drug delivery systems e.g., favorable penetration into the bone tissue and stability at body temperature [29,30]. Among fluoroquinolones, ciprofloxacin presents one of the highest activity against strains of *Staphylococcus aureus* and *Pseudomonas aeruginosa* [31]. Therefore, ciprofloxacin was chosen as an active component loaded onto MSM, type of MCM-41. The coating blend was composed of ethylcellulose (EC) and polydimethylsiloxane (PDMS). EC as the most stable, non-toxic cellulose derivative with modifiable viscosity has been broadly used in pharmaceuticals as a good film forming agent [32]. Moreover, one of the widely known applications of EC is film coating in dosage forms with controlled drug release [33,34]. PDMS was chosen due to its biocompatibility, bioinertness, and documented applicability in implantable materials [35,36]. Additionally, unique physicochemical properties such as high elasticity (flexibility), adhesion and hydrophobicity play a crucial role in considering PDMS as valuable excipient for drug release modification from dosage forms [37,38]. Nahrup et al. [39] indicated that the usage of PDMS as

a pharmaceutical tablet coating may provide a possible zero-order release (highly desirable delivery of a constant amount of drug per unit of time).

In this paper, synthesized MSM, type MCM-41, adsorbed with ciprofloxacin (MCM-41-CIP) were coated either with EC or blend of EC and PDMS. All the composites were evaluated in terms of physicochemical properties, release study in vitro, antimicrobial activity (against *Staphylococcus aureus*), and cytocompatibility in vitro (osteoblastic cell line) to assess their potential applicability in vivo.

2. Materials and Methods

2.1. Materials

Tetraethyl orthosilicate (TEOS), cetyltrimethylammonium bromide (CTAB), ethanol, aqueous ammonia (25%), hydroxyl-terminated polydimethylsiloxane (PDMS, 150 cSt, $d = 0.97 \text{ mg/mL}$) were purchased from Sigma-Aldrich (Saint Louis, MO, USA). Ethylcellulose (EC, Ethocel 20 cP, molecular weight: 454 g/mol, ethoxyl content: 48.0%–49.5% wt.) was obtained from Dow Chemical (Midland, MI, USA). Acidic solution of ciprofloxacin (pH = 3.5, 10 mg/mL, Proxacin) was obtained from Polfa S.A. (Warsaw, Poland). Mueller Hinton Broth, 1:1 mixture of Ham's F12 Medium Dulbecco's Modified Eagle's Medium, 10% fetal bovine serum, and penicillin/streptomycin (10,000 U/mL/10 mg/mL), DNA staining with 4,6-diamidino-2-phenylindole dihydrochloride (DAPI) were purchased from Sigma-Aldrich. MycoAlert™ Mycoplasma Detection Kit was obtained from Lonza (Basel, Switzerland). Human fetal osteoblastic cell line (hFOB 1.19) was obtained from American Type Culture Collection (cat. no. CRL-11372), pLVTHM was a gift from Didier Trono (Addgene plasmid # 12247).

2.2. Synthesis of Mesoporous Silica Materials (MCM-41)

The synthesis of MCM-41 was performed using sol–gel method as previously described [40] with the usage of TEOS as a silica source and cetyltrimethylammonium bromide (CTAB) cationic surfactant as a structure directing agent [36]. The water, ethanol, aqueous ammonia (25%), and CTAB in the amounts of 125, 12.5, 9.18 and 2.39 g, respectively, were mixed together in polypropylene beaker by stirring for 10 min (300 rpm, 25 °C) until complete dissolution of surfactant. Then, TEOS in amount of 10.03 g was added, and the resulting mixture was continuously stirred for 2 h. Next, the mixture was aging at 90 °C for 5 days without stirring. Once the solid product occurred, it was washed with absolute ethanol and dried at 40 °C for 1 h. To remove CTAB, the calcination process was performed (550 °C, 6 h, heating rate of 1 °C/min) in a muffle furnace (FCF 7SM, CZYLOK, Jastrzebie-Zdroj, Poland). The final MSM MCM-41 were micronized (50 rpm, 10 min, Mortar Grinder Pulverisette 2, Fritsch, Weimar, Germany) to obtain the fraction size ranging from 200–500 μm for further experiments.

2.3. Ciprofloxacin Adsorption

The ciprofloxacin (CIP) adsorption onto the mesoporous silica MCM-41 was carried out by using previously optimized procedure [40]. Briefly, MCM-41 material (particles fraction in the range of 200–500 μm) was suspended in the 10 mg/mL CIP lactate solution (pH = 3.5) using 50:1 mass to volume ratio. Then, CIP-loaded MCM-41 material (MCM-41-CIP) was centrifuged, separated from supernatant, and freeze-dried (−52 °C, 0.1 mBar, 24 h). The concentration of the CIP remaining in the supernatant was calculated spectrophotometrically at 278 nm (model UV-1800 UV–Vis spectrophotometer, Shimadzu, Kyoto, Japan), whereas the amount of CIP adsorbed onto MCM-41 at equilibrium state and adsorption efficiency were calculated using Equations (1) and (2), respectively:

$$Q_e = \frac{(C_0 - C_e) \cdot V}{m}, \quad (1)$$

$$\%Ads = \frac{C_0 - C_e}{C_e} \times 100\%, \quad (2)$$

Q_e [mg/g]—an amount of CIP adsorbed onto MCM-41 at the equilibrium state; %*Ads* [%]—an adsorption efficiency coefficient; C_0 [mg/mL]—an initial CIP concentration; C_e [mg/mL]—a CIP concentration at equilibrium state; V [mL]—a volume of CIP solution, m [g]—a mass of MCM-41.

The adsorption process was repeated 6 times and both the amount of CIP adsorbed and the adsorption efficiency were expressed as the mean values \pm SD. The charge change of MCM-41 surface after adsorption process of CIP was performed by using the zeta potential analysis (Litesizer 500, Anton-Paar, Graz, Austria). To measure the zeta potential the samples of both the MCM-41 (before CIP adsorption) and the MCM-41-CIP (after CIP adsorption) were immersed in HCl solution (pH = 3.5) at concentration of 1 mg/mL and dispersed in ultrasonic bath for 5 min. The zeta potential values were expressed as a mean \pm SD calculated from 10 measurements. The parameters characterizing the porosity of the MCM-41 before and after CIP adsorption were determined by the measurements of low-temperature nitrogen adsorption–desorption at -196 °C using a volumetric adsorption analyzer ASAP 2405 (Micromeritics, Norcross, GA, USA). Prior to the experiment, all the samples were dried overnight at 25 °C under vacuum. The specific surface areas were calculated using the standard Brunauer–Emmett–Teller (BET) equation for nitrogen adsorption data acquired in the range of relative pressure p/p_0 in the range from 0.05 to 0.25. The total pore volumes were estimated from a single point adsorption at 0.993 p/p_0 . The average pore size was determined from the desorption branch of the nitrogen isotherm using the Barrett–Joyner–Halenda (BJH) procedure.

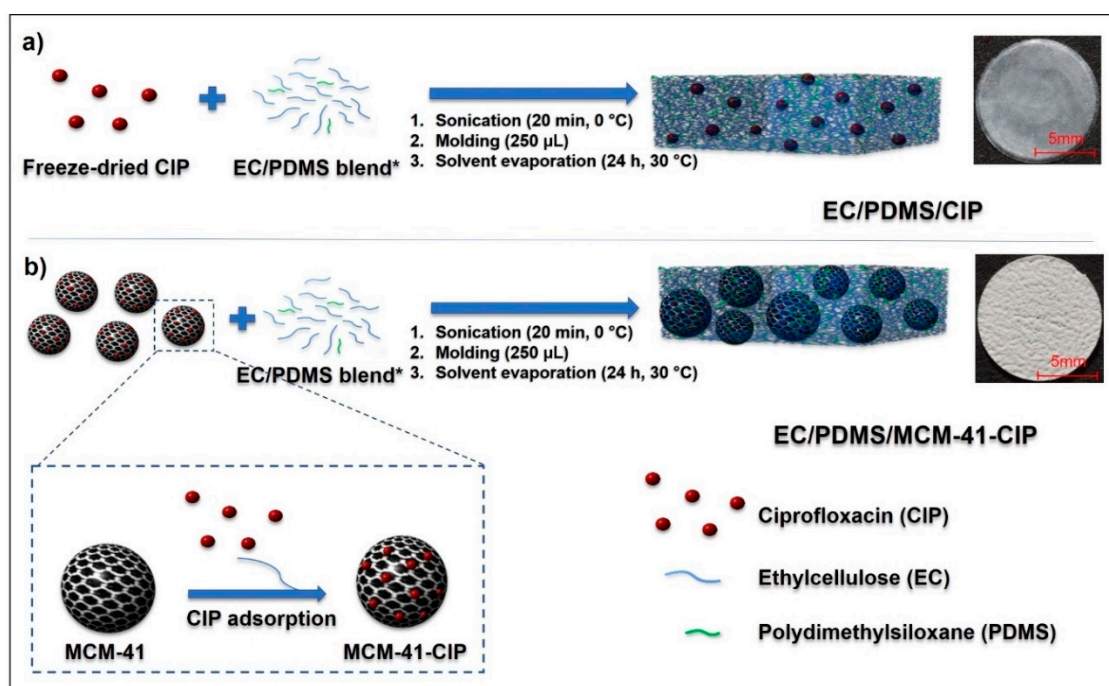
2.4. Composites Fabrication

Consecutive stages of composites fabrication were presented in Scheme 1. The composites named respectively EC/CIP, EC/PDMS/CIP, EC/MCM-41-CIP, and EC/PDMS/MCM-41-CIP were prepared via solvent-evaporation blending method. The qualitative and quantitative composition data of each composite were presented in Table 1. In brief, to prepare EC/PDMS/CIP composites (Scheme 1a), PDMS in the volume of 5 μ L was mixed with 245 μ L of EC ethanolic solution (5% (*w/w*)). Then, 0.79 ± 0.05 mg of freeze-dried CIP in quantity corresponding to the amount of CIP adsorbed onto 6 ± 0.02 mg of MCM-41-CIP was added into the sol of EC/PDMS at dynamic viscosity of $\sim 49 \pm 4$ mPa·s, 24 °C (Rotational Viscometer V2-L, Conbest, Krakow, Poland). Composites containing MCM-41-CIP (EC/PDMS/MCM-41-CIP) were fabricated in the same manner but instead of freeze-dried CIP, 6 mg \pm 0.02 mg of MCM-41-CIP (corresponding to 0.79 mg of adsorbed drug) was added into the EC/PDMS sol (Scheme 1b). In case of composites without PDMS (EC/CIP, EC/MCM-41-CIP), freeze-dried CIP or MCM-41-CIP were added directly to 250 μ L of EC ethanolic solution (5% (*w/w*)) at dynamic viscosity of $\sim 44 \pm 3$ mPa·s, 24 °C. All obtained suspensions were sonicated in ice bath for 20 min, poured into the polypropylene molds, and incubated at 30 ± 0.5 °C till complete ethanol evaporation (24 h). Composites were then removed from the molds, weighted (Quintix 1250, Sartorius Lab, Goettingen, Germany), and stored in the desiccator (25 °C). The amount of CIP was 0.79 ± 0.05 mg per each composite.

Table 1. The qualitative and quantitative composition data of composites.

Name of Composite	¹ EC Content [μ L]	PDMS Content [μ L]	² MCM-41-CIP Content [mg]	² CIP Content [mg]
EC/CIP	250	-	-	
EC/PDMS/CIP	245	5	-	0.79 ± 0.05
EC/MCM-41-CIP	250	-		
EC/PDMS/MCM-41-CIP	245	5	6.0 ± 0.02	

¹ EC ethanolic solution (5% (*w/w*)); ² mean value.



Scheme 1. Schematic diagram of consecutive stages of the composite fabrication. Composites containing freeze-dried CIP: EC/CIP, EC/PDMS/CIP (a); Composites containing MCM-41-CIP: EC/MCM-41-CIP, EC/PDMS/MCM-41-CIP (b). * for the composites without PDMS, EC ethanolic solution (5% (*w/w*)) was used instead of EC/PDMS blend.

2.5. Composites Physicochemical Characterization

All obtained composites were investigated in terms of molecular structure with the use of Fourier Transform Infrared Spectroscopy (FTIR, Jasco FT/IR-4200, Jasco, Pfungstadt, Germany) in the range of 4000–400 cm^{-1} . Surface morphology and elemental analysis of composites were investigated using a scanning electron microscope with energy-dispersive X-ray spectroscopy (SEM/EDX, Hitachi SU-70, Tokyo, Japan). The results were obtained by using electron microscope at an acceleration voltage of 3 kV. The crystallinity of composites was characterized by X-ray diffraction analysis (XRD, Empyrean PANalytical, Malvern, UK). The diffractometer was operated using Cu $K\alpha$ radiation beam at 40 kV and 40 mA, in the 2θ range between 5 and 40° with the following parameters: a step width of 0.020° and a scanning rate of 0.5°/min. The texture properties were determined by TA. XTplusC Texture Analyzer (Godalming, UK). TGA characterization was performed using a Mettler Toledo TGA/SDTA 851e apparatus (Warsaw, Poland), calibrated with indium, zinc, and aluminum (accuracy equal to 10^{-6} g). The samples were placed in alumina crucible and heated from 25 to 1000 °C with rate of 10 K min^{-1} , in argon atmosphere (60 $\text{cm}^3 \text{min}^{-1}$). The DSC measurements were performed using Mettler Toledo apparatus DSC 821e (Warsaw, Poland) equipped with the IntraCooler system. Calibration for the heat flux and temperature was done with indium and zinc standards. The sample was placed in aluminum pan and heated from –40 to 300 °C in the Ar (60 $\text{cm}^3 \text{min}^{-1}$).

2.6. Ciprofloxacin In Vitro Release

For the drug release study, each composite containing 0.79 ± 0.05 mg of CIP was immersed in 2 mL of distilled water (pH = 7.0), and continuously shaken at 37 ± 0.5 °C (80 rpm). The theoretical highest concentration of drug after complete CIP release into the medium was below the 10% drug aqueous solubility (solubility of ciprofloxacin lactate around 100 mg/mL [41]) providing sink conditions. The amounts of CIP released were measured every 24 h for 30 days. The whole release medium was replaced after each measurement to simulate dynamic fluid conditions in the body. Quantitative

determinations of the amount of CIP released was based on pre-calibration of the spectrometer at 278 nm wavelength using standard solutions of the CIP. The release study was repeated 6 times and values were given as mean \pm SD.

2.7. Composites Biological Evaluation

2.7.1. Composites Sterilization

The composites intended for the biological evaluation were prepared via aseptic assembly [42], which is a pharmacopeial method dedicated for the materials that cannot be terminally sterilized, such as antibiotic-loaded systems. MCM-41 was sterilized by the heating in air for a period of 3 h at 300 °C in a muffle furnace (FCF 7SM, CZYLOK, Jastrzebie-Zdroj, Poland). The CIP solution used to adsorption process was sterilized by producer. Additionally, the sterility of the composites was provided by the usage of the ethanolic solution (96% (*w/w*)) as a solvent which is classified as sterilization agent [43]. All the composites fabrication stages were conducted using conditions and facilities designed to prevent microbial contamination. The sterility of the composites was verified via membrane filtration test [44]. No growth of bacteria confirmed the sterility of the composites.

2.7.2. Antimicrobial Activity

Modified agar diffusion test [45] was performed to verify the ciprofloxacin potency against *Staphylococcus aureus* (ATCC 6538) released from the composites (EC/CIP, EC/PDMS/CIP, EC/MCM-41-CIP, EC/PDMS/MCM-41-CIP) over time. All composites were examined in triplicates. To confirm *Staphylococcus aureus* susceptibility to CIP, MIC, and minimal bactericidal concentration (MBC) were determined via serial dilution method [46]. The composites were placed onto the surface of Petri dishes (one composite per dish), then completely covered with a liquefied Mueller-Hinton (MH) agar (45 °C), and pre-incubated for 1 h at 37 °C. Then, a thin layers of liquefied MH agar (45 °C) inoculated with a suspension of *S. aureus* at density of 10⁶ CFU/mL were poured onto the surface of MH agar plates and incubated for another 24 h at 37 °C. Bacterial growth zones of inhibition (ZOI) were measured and photographed, then the composites were transferred aseptically into the new Petri dish and the whole procedure was repeated. After each 24 h of incubation the composites were transferred to the new Petri dish and covered with a freshly prepared MH agar inoculated with *S. aureus*, then incubated according to the description above. The procedure was repeated each day until the ZOI disappeared. The areas of ZOI were calculated using the image processing program (Image J).

2.7.3. Cytotoxicity Assay

Human fetal osteoblastic cell line was cultured in 1:1 mixture of Ham's F12 Medium Dulbecco's Modified Eagle's Medium (DMEM/F12), with 2.5 mM L-glutamine (without phenol red), 15 mM HEPES, and sodium bicarbonate, supplemented with 10% fetal bovine serum and penicillin/streptomycin (100 U/mL/100 µg/mL) at 34 °C in a humidified atmosphere of 5% CO₂. Medium was replaced every 2–3 days. Cells were passaged for a maximum of 3–4 months post resuscitation and regularly tested for mycoplasma contamination by the two methods: DNA staining with 4,6-diamidino-2-phenylindole dihydrochloride (DAPI) and MycoAlert™ Mycoplasma Detection Kit. Cells were transduced for stable expression of enhanced GFP (eGFP) with pLVTHM plasmid (Addgene, Watertown, MA, USA).

The *in vitro* cytotoxicity of the composites (EC/CIP, EC/PDMS/CIP, EC/MCM-41-CIP, EC/PDMS/MCM-41-CIP) was examined by direct contact test, according to the ISO Standard 10993-5 [47], which is focused on the physical interaction between examined materials and the cell monolayer. However, in case of drug delivery systems, the results may be also related to the drug released into the cell culture medium. Therefore, CIP-free analogues such as EC#, EC/PDMS# and EC/PDMS/MCM-41# and various concentration of CIP aqueous solutions (10, 20, 40, 80, 160 µg/mL) were also examined for comparative purposes. The frequently used proliferation tests based on addition of dyes (such

as MTT or WST-1) may lead to false negative results due to unspecific interaction of the dye with tested material (e.g. dye adsorption onto the material surface) [48]. Thus, we decided to perform eGFP fluorescence-based assay. Since the eGFP fluorescence is lost after the cell death, the cells viability may be evaluated as fluorescence intensity [49].

According to the ISO Standard 10993-5 the specimen of analyzed material should cover one tenth of cell layer surface, thus the composites were cut into the circle-shaped samples with the diameter of 3.5 mm. For the test, cells were seeded in 48-well plate at a concentration of 3×10^4 per well. After 24 h of incubation (34 °C, 5% CO₂), the medium from each well was removed, specimens of composites were carefully placed onto the cell layer, 500 µL of fresh medium was added into each well and incubated for 72 h (34 °C, 5% CO₂). Cells cultured without any specimen were used as a control. Images were obtained with Axiovert 200 fluorescent microscope equipped with AxioCam MRm digital camera (Zeiss, Oberkochen, Germany). Before the quantitative determination of cells viability, specimens were removed from each well and the conditioned medium was replaced with the fresh one. Fluorescence intensity was measured with excitation/emission at 485/528 nm using Synergy H1 microplate reader (BioTek, Winooski, VT, USA). Evaluation of the influence of CIP solutions on osteoblasts viability was performed in the same manner using the increasing concentration of drug instead of the specimens of composites.

Data was presented as the mean \pm standard deviation for three independent experiments. Statistical analysis was performed by Student's *t*-test using STATISTICA 13.3 software (Statsoft, Kraków, Poland). The results were considered to be statistically significant when *p* value was <0.05 vs. control.

3. Results and Discussion

3.1. The Synthesis of MCM-41 and CIP Adsorption onto Its Surface

MCM-41 in the powder form was successfully synthesized by using structure directing sol-gel method [50]. The mean amount of CIP adsorbed onto each 1 g of MCM-41 was 131 ± 5 mg that corresponded to $65 \pm 2.5\%$ adsorption efficiency. The adsorption of positively charged CIP onto negatively charged surface of MCM-41 [51] resulted in the change of zeta potential value from -12.02 ± 0.91 mV to 11.04 ± 0.04 mV for MCM-41 and MCM-41-CIP, respectively. The change of the surface zeta potential after drug adsorption onto the mesoporous silica is well-known phenomenon [52,53]. The negative charge of MCM-41 was caused by the dissociation of residual surface silanols ($\equiv\text{Si}-\text{OH} \rightleftharpoons \text{SiO}^- + \text{H}^+$) in HCl solution (pH = 3.5) which acted as the adsorption sites for positively charged CIP molecules.

The changes in the mesoporous structure of MCM-41 and MCM-41 after CIP adsorption were also confirmed by the nitrogen adsorption-desorption data (Table S1—Supplementary Material). The decrease in the surface area, pore diameter, and pore volume of MCM-41 material by the factors of 1.22, 1.19 and 1.30, respectively, was observed. This phenomenon resulted from the pore blocking by the adsorbed drug molecules.

3.2. Fabrication of Composites

The composites were successfully fabricated via solvent-evaporation blending method. All of the composites were characterized by the diameter of 11 ± 1 mm. For the composites containing of 0.79 ± 0.05 mg freeze-dried CIP (Table 1: EC/CIP and EC/PDMS/CIP) the thickness was in the range of 40–45 µm, whereas, for the composites containing MCM-41-CIP in amount of 6.0 ± 0.02 mg corresponding to 0.79 of CIP (Table 1: EC/MCM-41-CIP and EC/PDMS/MCM-41-CIP), the thickness increased up to 50–55 µm. The observed increase of thickness composite was related to the addition of MCM-41.

3.3. Composites Physicochemical Properties

3.3.1. Molecular Structure

The molecular structure of composites was investigated by FTIR technique. Figure 1 shows the spectra of precursors (EC, PDMS, freeze-dried CIP, MCM-41, MCM-41-CIP) as well as the spectra of the final composites: EC/CIP, EC/PDMS/CIP, EC/MCM-41-CIP, EC/PDMS/MCM-41-CIP. For the MCM-41 typical vibrations modes of Si–O–Si at 1097 cm^{-1} and 802 cm^{-1} , Si–OH at 969 cm^{-1} , and Si–O at 463 cm^{-1} were observed [54]. In comparison to the MCM-41 spectrum, the spectrum of MCM-41-CIP presented additional bands at 1715 cm^{-1} , 1494 cm^{-1} , and 1459 cm^{-1} , which were also observed in the spectrum of freeze-dried CIP confirming the drug adsorption onto the MCM-41. These three bands were respectively attributed to the stretching vibrations of C=O, C–H, and aromatic C=C of CIP [55].

The well-defined peak of CIP at 1722 cm^{-1} was observed in the spectra of both EC/CIP and EC/PDMS/CIP composites (Figure 1). These spectra also presented bands characteristic for EC (2972 cm^{-1} (C–H), 1375 cm^{-1} (C–H), and 1052 cm^{-1} (C–O–C) for EC/CIP composite, and 2964 cm^{-1} (C–H), 1377 cm^{-1} (C–H) for EC/PDMS/CIP) [56]. The presence of PDMS in EC/PDMS/CIP composite was confirmed by the characteristic peaks at 1261 cm^{-1} and 802 cm^{-1} corresponding to the stretching vibrations of Si–C, and 1024 cm^{-1} attributed to stretching vibration of Si–O [57]. The spectra of composite containing adsorbed CIP onto MCM-41: EC/MCM-41-CIP and EC/PDMS/MCM-41-CIP showed the bands specific for all the components presented in the composites, excluding bands characteristic for CIP. It was explained by the CIP amount below the *detection limit* of FTIR method. However, the identification of CIP in MCM-41-CIP after the adsorption process (MCM-41-CIP spectrum, Figure 1) confirmed the CIP loading in the more complex composites.

3.3.2. Morphological and Structural Analysis

To characterize morphology and structural composition of obtained composites the SEM/EDX and XRD analyses were performed (Figure 2). To better visualize the alteration of morphology and crystallinity before and after polymer coating, the SEM/EDX images and XRD patterns of uncoated freeze-dried CIP and MCM-41-CIP were also presented. The morphological structure of freeze-dried CIP was highly heterogenous with observed irregularities in the crystals size and shape, whereas the MCM-41-CIP presented more homogeneous size distribution of spherical-shaped particles (the detailed particle size analysis of MCM-41-CIP was presented in Figure S1—Supplementary Material). After coating, the SEM images of composites containing freeze-dried CIP (EC/CIP, EC/PDMS/CIP) revealed elongated crystals with the sharp edges of CIP distributed in polymer blends (Figure 2c,e). However, the composites containing MCM-41-CIP (EC/MCM-41-CIP and EC/PDMS/MCM-41-CIP) showed the formation of compact and continuous polymer phase with homogeneously distributed MCM-41-CIP particles (Figure 2d,f). The significant differences in surface morphology between the composites with PDMS (EC/PDMS/CIP and EC/PDMS/MCM-41-CIP) and without PDMS (EC/CIP and EC/MCM-41-CIP) were observed (Figure 2, insets I–IV). As previously reported [40], based on the optical profilometry results, the surface roughness of these composites increases as function of PDMS. Therefore, this phenomenon explained the differences in SEM surface results.

The EDX spectrum of freeze-dried CIP (Figure 2a) presented the relatively high peak of fluorine (F) - element characteristic for this molecule. After coating the freeze-dried CIP using EC the peak derived from F was still observed confirming the presence of drug in the EC/CIP composites (Figure 2c). After addition of PDMS (EC/PDMS/CIP, Figure 2e) the EDX profile showed additional peak of silicon (Si) element. Thus, the EDX spectra of the composites containing freeze-dried CIP confirmed the presence of particular components (EC, CIP, and PDMS). In the EDX spectra of composites containing MCM-41-CIP (Figure 2d,f) peaks of Si and O may be also attributed to MCM-41 (Figure 2b). There was no peak corresponding to CIP observed in these spectra which may be explained by fact that drug molecules were loaded into the mesopores that were additionally coated with the EC/PDMS blend.

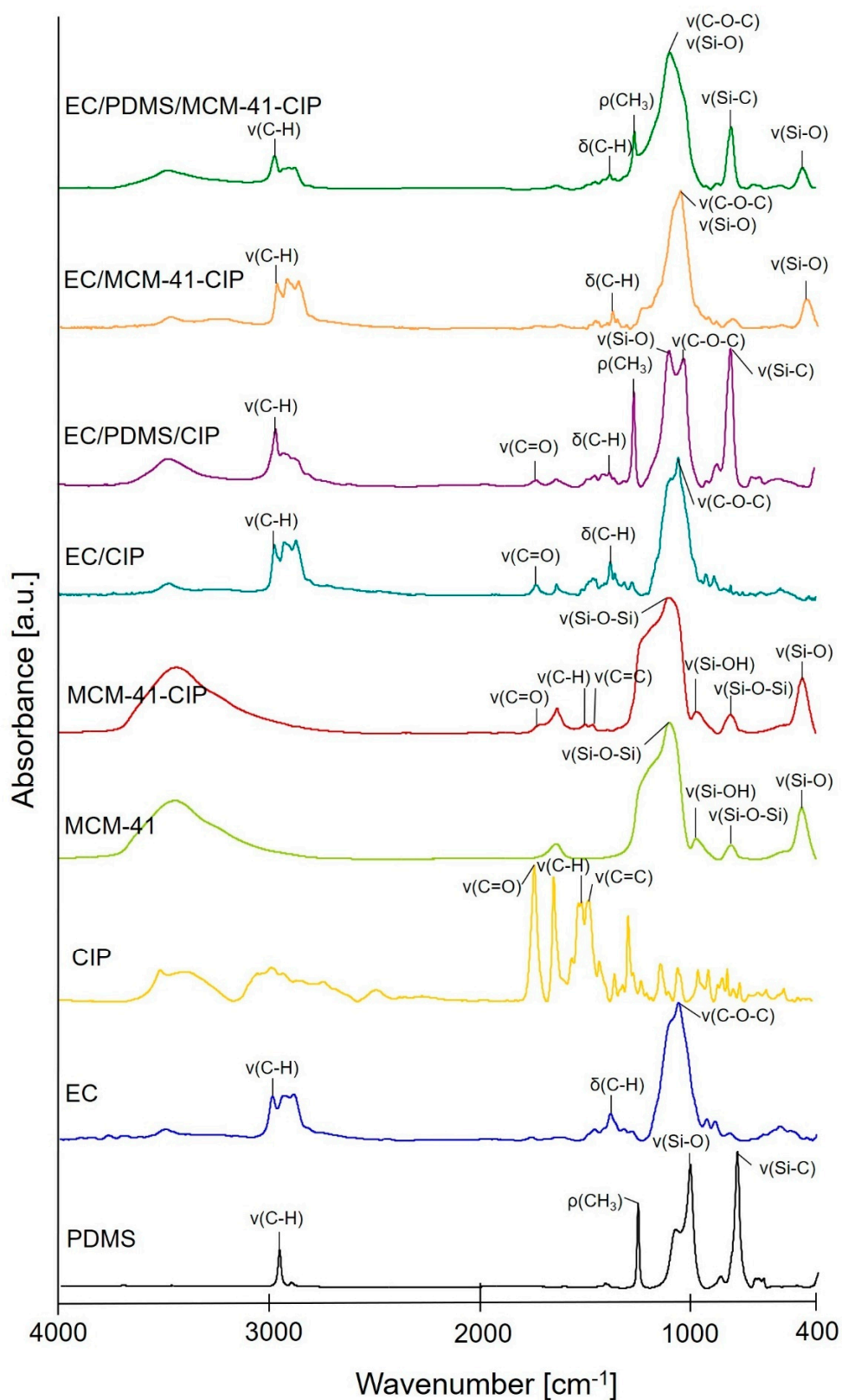


Figure 1. The FTIR spectra of composites: EC/CIP, EC/PDMS/CIP, EC/MCM-41-CIP, EC/PDMS/MCM-41-CIP and precursors: PDMS, EC, freeze-dried CIP, MCM-41, MCM-41-CIP (types of vibration: ν —stretching, δ —bending, ρ —rocking).

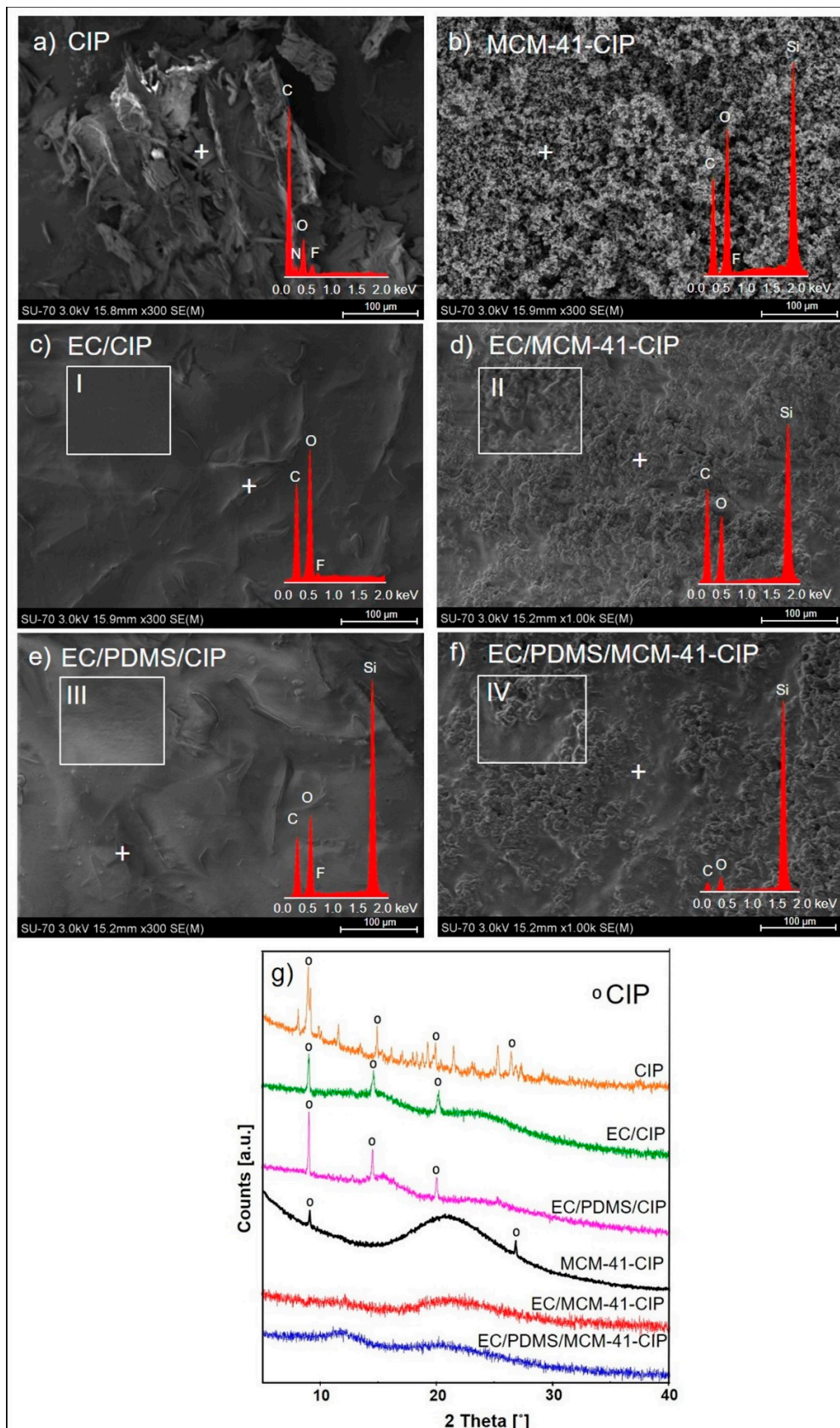


Figure 2. The SEM-EDX images of: freeze-dried CIP, MCM-41-CIP in the form of powders (a,b), SEM-EDX images of final composites: EC/CIP, EC/MCM-41-CIP, EC/PDMS/CIP, EC/PDMS/MCM-41-CIP (c–f) with high-magnification of composites surfaces (insets I–IV), and XRD patterns of each sample (g).

To examine the crystallinity of the composites, the XRD patterns of freeze-dried CIP and MCM-41-CIP before and after polymer coating were compared (Figure 2g). The XRD pattern of freeze-dried CIP showed highly crystalline structure with characteristic, more intense peaks at 8° , 15° , 21° and 27° 2θ . The XRD pattern of MCM-41-CIP presented the broad halo in the range of 15 – 35° derived from the amorphous silica [58] with two well-defined peaks at 8 and 27° 2θ characteristic for the CIP, suggesting a semi-crystalline structure of CIP adsorbed onto MCM-41. On the other hand, after MCM-41-CIP coating with EC or EC/PDMS blend, the EC/MCM-41-CIP and EC/PDMS/MCM-41-CIP composites were characterized by two diffraction haloes in the 2θ range of 10 – 15° and 15 – 30° derived from the amorphous polymer blends and silica, respectively, with no diffraction peaks derived from CIP. It suggested that the MCM-41-CIP was successfully coated with amorphous polymer blend. After the coating of CIP with EC or EC/PDMS blend the significant reduction in CIP crystallinity was observed revealing semi-crystalline nature of CIP in the EC/CIP and EC/PDMS/CIP composites, most probably as a consequence of the changes in overall background scattering of X-rays due to the presence of amorphous polymer coating blend. It should be noted that there were no significant differences in XRD patterns between composites with PDMS and PDMS-free composites.

3.3.3. Texture Analysis

The texture properties were examined for all the final composites (EC/CIP, EC/PDMS/CIP, EC/MCM-41-CIP, EC/PDMS/MCM-41-CIP). For comparative purpose, the analogues without CIP and MCM-41-CIP, such as EC and EC/PDMS, were also tested. The values of rupture force, elasticity, firmness, weight, and thickness were presented in Table 2. The results were expressed as the means of 6 measurements with standard deviations. Rupture force referred to the force required to produce a major break of a sample, whereas the elasticity defined the distance at break. Based on these parameters, the values of firmness were calculated. The EC/CIP was characterized by relatively low rupture force (0.48 ± 0.16 N) and elasticity (0.58 ± 0.12 mm) which resulted in the low firmness (0.68 ± 0.22 N mm $^{-1}$). Addition of PDMS (EC/PDMS/CIP) resulted in the increase of firmness to 0.97 ± 0.41 N mm $^{-1}$. The same phenomenon was observed for the composites containing MCM-41-CIP. Thus, EC/MCM-41-CIP was characterized by the value of 2.5 ± 0.76 N mm $^{-1}$, whereas for the composites with PDMS (EC/PDMS/MCM-41-CIP) the significant increase was observed (3.22 ± 0.81 N mm $^{-1}$). The results of texture study were in good accordance with the values of weight and thickness. The firmness increased with the increase of the weight and thickness.

Table 2. The rupture force, elasticity, and firmness of obtained composites EC/CIP, EC/PDMS/CIP, EC/MCM-41-CIP, EC/PDMS/MCM-41-CIP and solid films of EC/PDMS blend and EC.

Name of Composite	Rupture Force [N]	Elasticity [mm]	Firmness [N mm $^{-1}$]	Weight [mg]	Thickness [μ m]
EC/CIP	0.48 ± 0.16	0.58 ± 0.12	0.68 ± 0.22	10.84 ± 0.16	42 ± 2
EC/PDMS/CIP	0.66 ± 0.06	0.80 ± 0.33	0.97 ± 0.41	14.81 ± 0.18	44 ± 1
EC/MCM-41-CIP	1.25 ± 0.34	0.50 ± 0.21	2.5 ± 0.76	16.12 ± 0.22	52 ± 3
EC/PDMS/MCM-41-CIP	1.97 ± 0.21	0.62 ± 0.14	3.22 ± 0.81	20.58 ± 0.32	53 ± 2
EC	0.54 ± 0.28	0.80 ± 0.18	0.67 ± 0.18	10.02 ± 0.11	38 ± 2
EC/PDMS	0.71 ± 0.14	1.03 ± 0.22	0.72 ± 0.01	14.64 ± 0.28	40 ± 4

3.3.4. Thermal Analysis

To determine the effect of polymer coating on thermal stability, the TG curves and DSC profiles of uncoated freeze-dried CIP and MCM-41-CIP, and final composites (EC/CIP, EC/PDMS/CIP, EC/MCM-41-CIP, EC/PDMS/MCM-41-CIP) were compared (Figure 3). MCM-41 was also examined for comparative purpose. The thermal decomposition of ciprofloxacin (Figure 3a) was characterized by two mass losses, first in the temperature range of 25 – 250° C (23% of its mass) and, the second, between 250 – 550° C (51%). The detailed description of this process can be found in the literature [59]. On the

other hand, the total weight loss of MCM-41-CIP was 17% what confirmed the calculated amount of drug adsorbed onto MCM-41. Pure MCM-41 was characterized by the high thermal stability with small mass loss (3%) below 100 °C which may result from the evaporation of water absorbed in the silica channels [60].

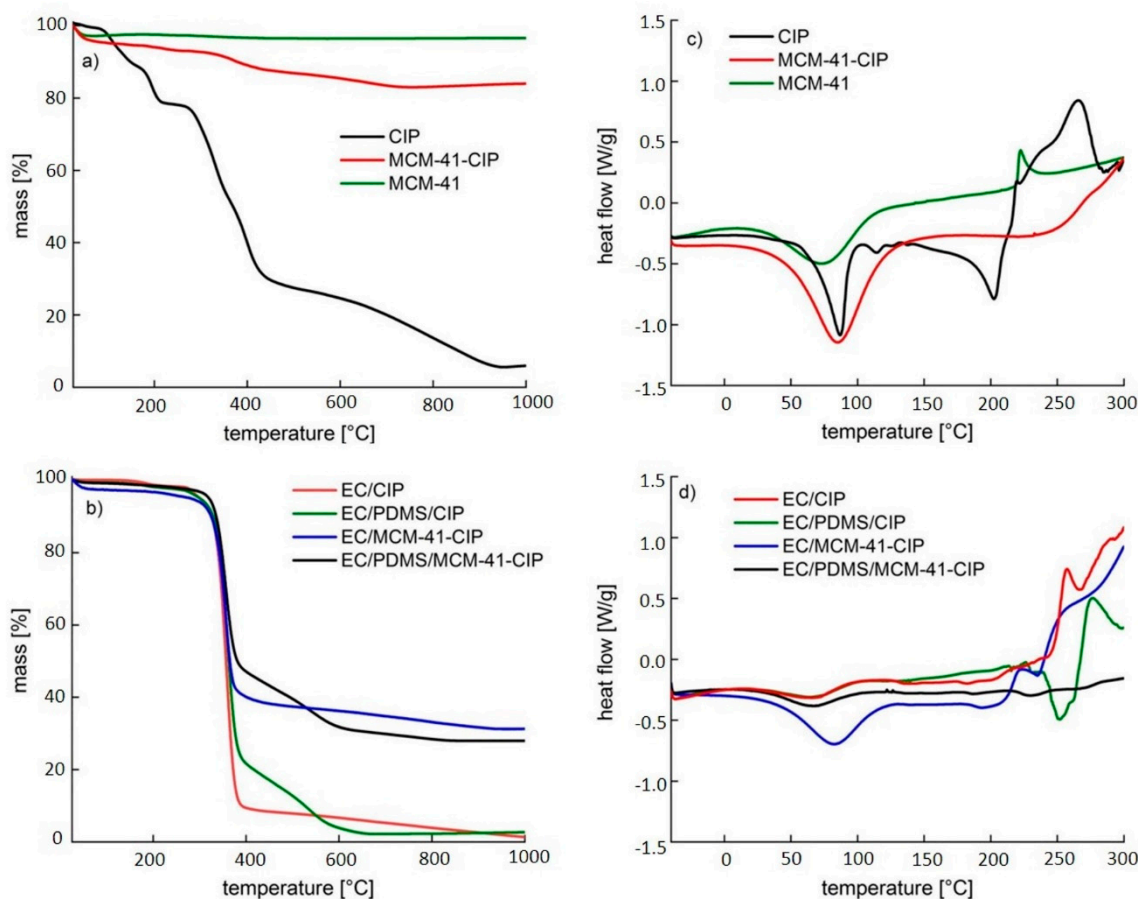


Figure 3. TG profiles normalized to the initial weight of freeze-dried CIP, MCM-41-CIP, and MCM-41 (a), TG normalized to the initial weight of the final composites: EC/CIP, EC/PDMS/CIP, EC/MCM-41-CIP, EC/PDMS/MCM-41-CIP (b), DSC curves normalized to the initial weight of freeze-dried CIP, MCM-41-CIP, and MCM-41 (c), DSC curves normalized to the initial weight of the final composites: EC/CIP, EC/PDMS/CIP, EC/MCM-41-CIP, EC/PDMS/MCM-41-CIP (d).

All final composites were stable in the temperature range of 25–330 °C (Figure 3b). Mass loss of EC/CIP was observed above 330 °C, and was equal to 98%, whereas in case of EC/MCM-41-CIP decrease to 69%. Addition of PDMS to the composites slightly changed their thermal stability. Heating the EC/PDMS/CIP and EC/PDMS/MCM-41-CIP above 330 °C resulted in mass loss of 99% and 72%, respectively.

The DSC profiles (Figure 3c,d) were in accordance with the observations described above. The profile of freeze-dried CIP (Figure 3c) presented the endothermic peak ca. 90 °C which probably resulted from the evaporation of water, whereas, the endothermal decomposition started above 150 °C. This decomposition was not observed in the curve of MCM-41-CIP indicating the increase of drug thermal stability after its adsorption onto MCM-41.

The DSC profiles presented in Figure 3d confirmed the high thermal stability of the composites. There was no peak attributed to CIP decomposition noticed up to 250 °C. Above this temperature small phase transition changes were observed, especially for the composites without MCM-41, suggesting the beginning of the decomposition process. It is not seen for EC/PDMS/MCM-41/CIP, thus this composite

seemed to be the most stable. The difference in the stability temperature obtained from TG and DSC (330 °C and 250 °C, respectively) results from the differences in the measurement conditions.

3.3.5. In Vitro Ciprofloxacin Release

The CIP release profiles of obtained composites and MCM-41-CIP before coating were presented in Figure 4. Both the EC/CIP and EC/PDMS/CIP composites were characterized by the high burst release ($89.0 \pm 2.5\%$ and $85.4 \pm 0.8\%$, respectively) of CIP after first 24 h of release study. Comparatively, the $80 \pm 3.2\%$ of adsorbed CIP was released from MCM-41-CIP during the first 24 h (Figure 4b). These three samples (MCM-41-CIP, EC/CIP and EC/PDMS/CIP) were characterized by complete drug release after 6–7 days with no significant differences between them. The use of CIP adsorbed onto MCM-41 in EC/MCM-41-CIP composite instead of freeze-dried CIP resulted in reduction of burst release by the factor of 2.2 from $89.0 \pm 2.5\%$ (for EC/CIP) to $38.8 \pm 3.1\%$ (for EC/MCM-41-CIP) after first 24 h (Figure 4a). Moreover, the addition of PDMS into the polymer blend in EC/PDMS/MCM-41-CIP resulted in higher reduction of CIP burst release by the factor of 4.4 compared to EC/MCM-41-CIP (from $38.8 \pm 3.1\%$ to $8.8 \pm 1.2\%$) (Figure 4a). As described in our previous studies [38,40], the PDMS addition into the composites resulted in a prolonged drug release due to the occlusion of mesopores of drug-loaded silica particles by hydrophobic PDMS chains. The PDMS-occluded silica particles impeded the penetration of dissolution medium into the composites, and hence the further dissolution and release of drug loaded into the pores were slowed down.

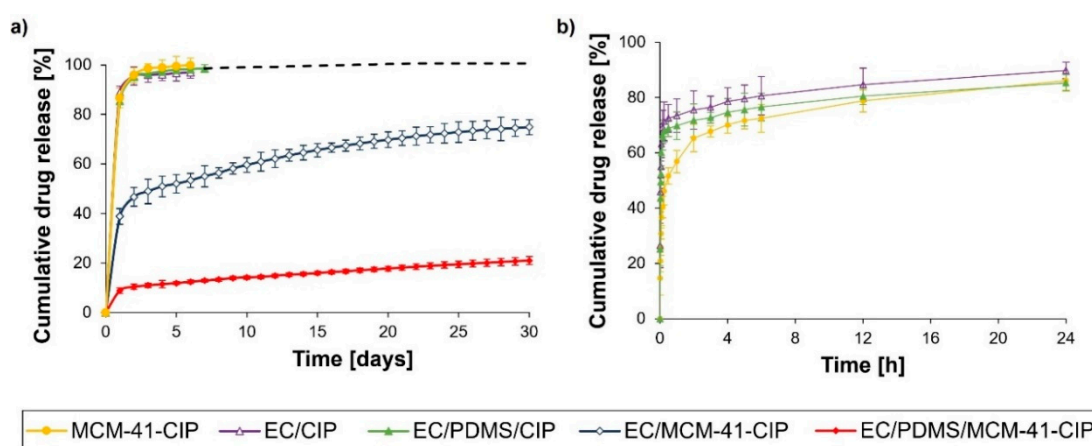


Figure 4. The CIP release profiles of obtained composites: EC/CIP, EC/PDMS/CIP, EC/MCM-41-CIP, EC/PDMS/MCM-41-CIP and MCM-41-CIP sample (a), and first 24 h release profiles of MCM-41-CIP, EC/CIP, EC/PDMS/CIP samples (b).

As previously reported [40], based on Higuchi and Korsmeyer–Peppas models, the CIP release from proposed non-disintegrating ethylcellulose-based composites was diffusion-controlled and followed zero-order kinetics after the burst stage. Consequently, the composites obtained in this study were characterized by both high R^2 for Higuchi model (from 0.936 to 0.993) and by Korsmeyer–Peppas release exponent n in the range of 0.17 to 0.54 proving a simple diffusion or quasi-diffusion-controlled drug release mechanism (Table S2—Supplementary Material).

The kinetic parameters of the zero-order release for all obtained composites were also calculated using Equation (3) and presented in Table 3.

$$Q = Q_0 + k_0t \quad (3)$$

Q [%]—the fraction released by time t [days], Q_0 [%]—the initial fraction of released drug in burst stage, k_0 —zero-order release constant [% of dose released per day].

The release data confirmed that the prolonged release of CIP with negligible burst was presumably associated with the drug entrapment into the pores of MCM-41 which were additionally coated by EC/PDMS blend [40]. Thus, the presence of PDMS and MCM-41-CIP seemed to be a crucial factor for ensuring the zero-order release with highly reduced burst stage what was further correlated in both the microbiological and cytotoxicity assays.

Table 3. The zero-order kinetics of obtained composites.

Name of Composite	Linear Regression Equation	R ²	k ₀ (%/day)	¹ Estimated Dose of Drug Released (µg/day)
EC/CIP	$y = 0.35x + 94.9$	0.919	0.35	2.8
EC/PDMS/CIP	$y = 0.64x + 94.4$	0.932	0.64	5.1
EC/MCM-41-CIP	$y = 0.99x + 48.6$	0.954	0.99	7.8
EC/PDMS/MCM-41-CIP	$y = 0.73x + 10.2$	0.995	0.73	5.8

R²—coefficient of determination, k₀—zero-order release constant, ¹ did not include the amounts of drug released during the burst stage (initial 24 h).

3.4. Composites Biological Evaluation

3.4.1. Bacterial Growth Inhibition Assay

The modified agar diffusion test was performed for all obtained composites. To verify antimicrobial activity of antibiotic released from the composites the areas of ZOI were determined. The susceptibility of *Staphylococcus aureus* (ATCC 6538) to CIP was expressed by MIC and MBC values which were 0.125 µg/mL and 0.25 µg/mL, respectively. In Figure 5, the average areas of ZOI with standard deviations and corresponding representative images were presented. The areas of resulting ZOI corresponded to the amounts of antibiotic diffused into the MH agar and indicated that the value of MIC was reached. After first 24 h of incubation the composites containing freeze-dried CIP, such as EC/CIP and EC/PDMS/CIP, were characterized by the ZOI area of 48.5 ± 8.42 cm² and 37.8 ± 7.23 cm², respectively. Similar area of ZOI (36.2 ± 6.8 cm²) was observed for the PDMS-free composites containing MCM-41-CIP (EC/MCM-41-CIP). The addition of PDMS to the composites containing MCM-41-CIP reduced ZOI to 12.66 ± 2.59 cm² which was in good accordance with the significantly reduced initial burst in the in vitro release results (Figure 4).

The EC/CIP and EC/PDMS/CIP composites lost the antimicrobial activity against *S. aureus* after day 6 and 7, respectively. It was considered to be not sufficient duration of antimicrobial activity in context of the treatment of *osteomyelitis* using bone antibiotic drug delivery systems. By contrast, the ZOI determined for the composites containing MCM-41-CIP occurred after each cycle of incubation until day 20 (EC/MCM-41-CIP) and day 30 (EC/PDMS/MC-41-CIP). The results of bacterial growth inhibition were in good accordance with the in vitro release results (Figure 4). In both studies, the EC/PDMS/MCM-41-CIP was recognized as the most promising candidate for local bone antibiotic delivery system characterized by release the smallest amount of CIP in the burst stage and significantly sustained release. The occurrence of ZOI after each cycle of incubation confirmed that the amount of CIP released from the composites sufficiently exceeded MIC, thus, EC/PDMS/MCM-41-CIP remained active against *S. aureus* for 30 days. The discrepancy between zero-order release kinetics (Table 3, 21% of cumulative drug amount released after 30 days) and the loss of ZOI after 30 days of incubation may be explained by high viscosity of MH agar medium that might have clogged both the nanopores in ethylcellulose structure and the CIP-loaded mesopores in MCM-41 particles which inhibits the further drug release to MH agar.

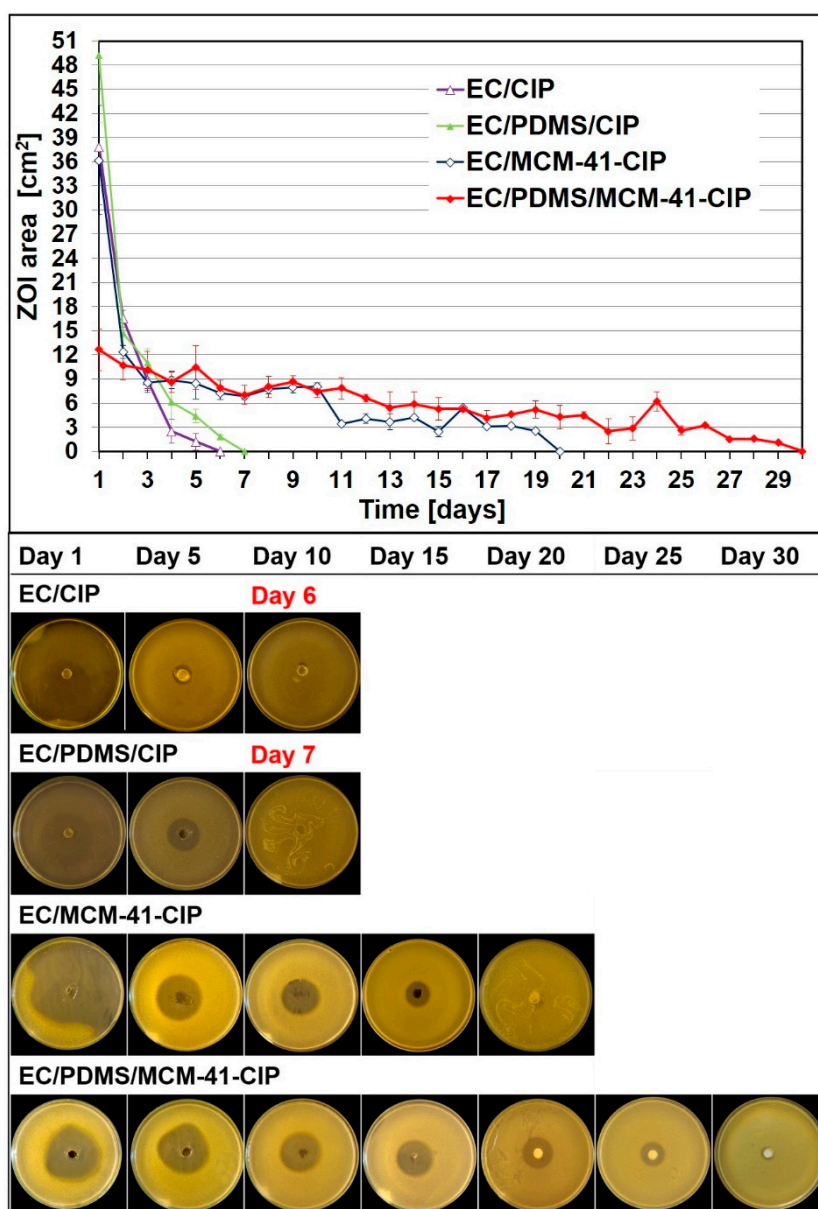


Figure 5. Modified agar diffusion test for composites (EC/CIP, EC/PDMS/CIP, EC/MCM-41-CIP, EC/PDMS/MCM-41-CIP) with the mean values of areas of ZOI [cm²] with standard deviations and representative images of ZOI for particular composites.

3.4.2. Cytotoxicity Assay

The quantitative results and representative images of cytotoxicity assay against human fetal osteoblasts of all obtained composites with drug (EC/CIP, EC/PDMS/CIP, EC/MCM-41-CIP, EC/PDMS/MCM-41-CIP) were presented in Figure 6. The tested circle-shaped specimens which covered 10% of cell layer surface contained approx. 60 µg of CIP. Cytotoxicity of various concentration of referenced CIP aqueous solutions and the CIP-free analogues such as EC#, EC/PDMS#, and EC/PDMS/MCM-41# was also shown for comparative purposes.

The CIP cytotoxicity assay revealed the concentration-dependent effect (Figure 6b), with the calculated IC₅₀ at concentration of 79 µg/mL. The statistically significant reduction in cell viability to 75 ± 7.4% and 86 ± 6.3% ($p < 0.05$) was observed for the MCM-41-free composites containing freeze-dried CIP: EC/CIP and EC/PDMS/CIP, respectively (Figure 6a). It was well correlated with the in vitro release results which revealed the highest burst release of CIP for EC/CIP and

EC/PDMS/CIP composites (approx. 89.0% and 85.0%, respectively, Figure 4). There was no significant cytotoxic effect observed for the composites containing MCM-41-CIP (Figure 6a, EC/MCM-41-CIP and EC/PDMS/MCM-41-CIP) which were characterized by significantly reduced initial burst release (Figure 4) suggesting that the amounts of CIP released into the culture medium were non-toxic to osteoblast. The CIP-free analogues (EC#, EC/PDMS#, and EC/PDMS/MCM-41#) did not impede the osteoblasts growth as well (Figure 6a). Therefore, the negative impact on osteoblasts viability observed for EC/CIP and EC/PDMS/CIP was possibly related to the initial release of higher dose of drug into the medium (compared to the others composites) what also correlated with drug release profiles (Figure 4).

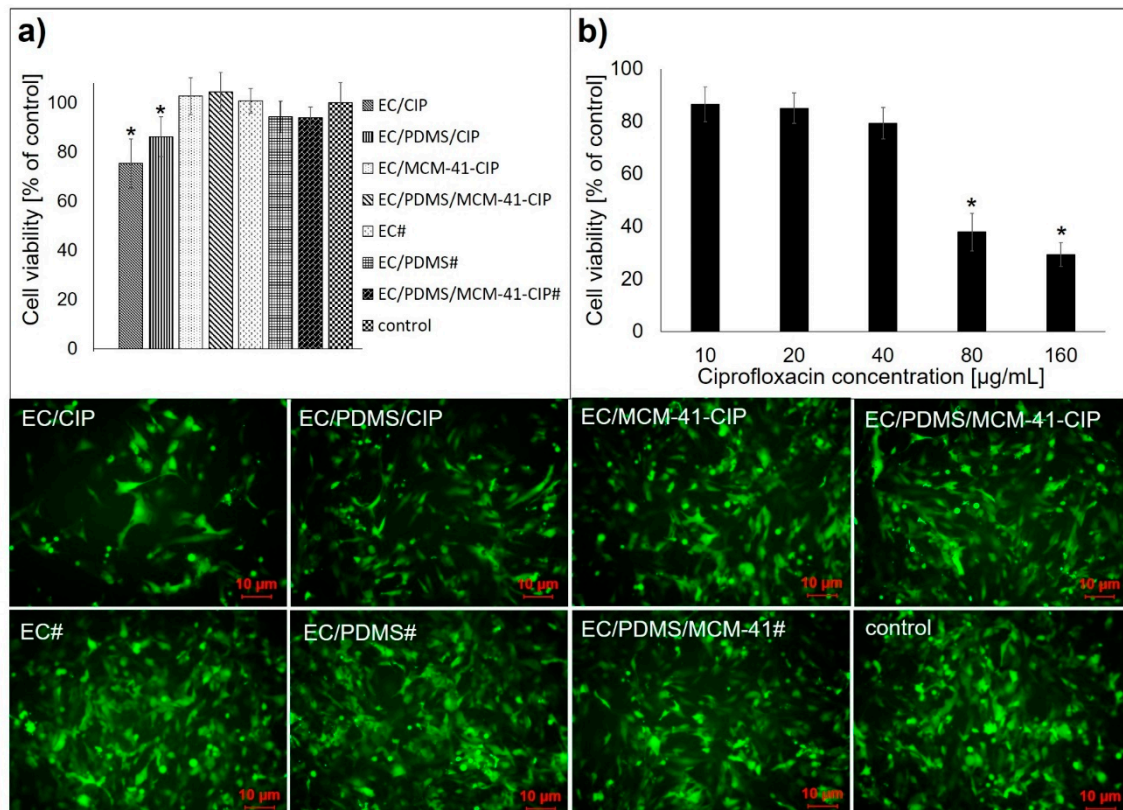


Figure 6. The effect of the composites (EC/CIP, EC/PDMS/CIP, EC/MCM-41-CIP, EC/PDMS/MCM-41-CIP) and CIP-free analogues (EC#, EC/PDMS#, EC/PDMS/MCM-41#) on osteoblasts viability (a); the effect of the various concentrations of CIP on osteoblasts viability (b). Data is represented as mean \pm SD ($n = 3$). * $p < 0.05$ was considered statistically significant.

4. Conclusions

Herein, the composites composed of freeze-dried CIP or MCM-41-CIP coated with EC or EC/PDMS blend were successfully obtained via solvent-evaporation blending method. The physicochemical properties, drug release profiles, antibacterial activity and cytocompatibility with osteoblasts of the prepared composites were assessed to select the most promising candidate for further in vivo evaluation as implantable self-contained antibiotic delivery system or functional coating for implant surfaces.

The most beneficial properties were reported for the formulation composed of ciprofloxacin adsorbed onto MCM-41 coated with blend of ethylcellulose and polydimethylsiloxane (EC/PDMS/MCM-41-CIP). It presented significantly higher thermal stability than the composites containing freeze-dried CIP (instead of MCM-41-CIP) and composites not containing PDMS. Moreover, EC/PDMS/MCM-41-CIP was characterized by sustained release rate with the lowest initial burst of ciprofloxacin. The microbiological and biological evaluation was in correlation to the in vitro release

results, revealing the 30-day maintenance of antimicrobial activity and excellent cytocompatibility with human fetal osteoblasts.

Supplementary Materials: The following are available online at <http://www.mdpi.com/1999-4923/12/1/28/s1>, Table S1: Surface area, pore diameter and pore volume of MCM-41 and MCM-41-CIP powders, Figure S1: Particle size of MCM-41-CIP powder, Table S2: The kinetic parameters of fitted experimental data for MCM-41-CIP sample and EC/CIP, EC/PDMS/CIP, EC/MCM-41-CIP and EC/PDMS/MCM-41-CIP composites.

Author Contributions: Conceptualization, M.P.; Formal analysis, M.P.; Funding acquisition, A.S. (Adrianna Skwira) and M.P.; Investigation, A.S. (Adrianna Skwira), A.S. (Adrian Szewczyk), M.P., D.M., A.K.; Methodology, A.S. (Adrianna Skwira), A.S. (Adrian Szewczyk), M.P., D.M., A.K., M.G., R.S.; Supervision, M.P.; Writing—original draft, A.S. (Adrianna Skwira), A.S. (Adrian Szewczyk), M.P., D.M., A.K. All authors have read and agreed to the published version of the manuscript.

Funding: The study was supported by the project OPUS 15 (2018/29/B/NZ7/00533) co-financed by National Science Centre, and partially supported by the project POWR.03.02.00-00-I035/16-00 co-financed by the European Union through the European Social Fund under the Operational Program Knowledge Education Development 2014–2020.

Acknowledgments: pLVTHM was a gift from Didier Trono (Addgene plasmid # 12247).

Conflicts of Interest: The authors declare no conflict of interest. The funders had no role in the design of the study; in the collection, analyses, or interpretation of data; in the writing of the manuscript, or in the decision to publish the results.

References

- Shah, M.Q.; Zardad, M.S.; Khan, A.; Ahmed, S.; Awan, A.S.; Mohammad, T. Surgical site infection in orthopaedic implants and its common bacteria with their sensitivities to antibiotics, in open reduction internal fixation. *J. Ayub Med. Coll. Abbottabad* **2017**, *29*, 50–53.
- Tsourvakas, S. Local antibiotic therapy in the treatment of bone and soft tissue infections. In *Selected Topics in Plastic Reconstructive Surgery*; Danilla, S., Ed.; IntechOpen: London, UK, 2012; pp. 17–46.
- Zalavras, C.G.; Patzakis, M.J.; Holtom, P. Local antibiotic therapy in the treatment of open fractures and osteomyelitis. *Clin. Orthop. Relat. Res.* **2004**, *427*, 86–93. [[CrossRef](#)]
- Soundrapandian, C.; Basu, D.; Sa, B.; Datta, S. Local drug delivery system for the treatment of osteomyelitis: In vitro evaluation. *Drug Dev. Ind. Pharm.* **2011**, *37*, 538–546. [[CrossRef](#)]
- Thabit, A.K.; Fatani, D.F.; Bamakhrama, M.S.; Barnawi, O.A.; Basudan, L.O.; Alhejaili, S.F. Antibiotic penetration into bone and joints: An updated review. *Int. J. Infect. Dis.* **2019**, *81*, 128–136. [[CrossRef](#)] [[PubMed](#)]
- Mantripragada, V.P.; Jayasuriya, A.C. Effect of dual delivery of antibiotics (vancomycin and cefazolin) and BMP-7 from chitosan microparticles on Staphylococcus epidermidis and pre-osteoblasts in vitro. *Mater. Sci. Eng. C* **2016**, *67*, 409–417. [[CrossRef](#)] [[PubMed](#)]
- Duewelhenke, N.; Krut, O.; Eysel, P. Influence on mitochondria and cytotoxicity of different antibiotics administered in high concentrations on primary human osteoblasts and cell lines. *Antimicrob. Agents Chemother.* **2007**, *51*, 54–63. [[CrossRef](#)] [[PubMed](#)]
- Rathbone, C.R.; Cross, J.D.; Brown, K.V.; Murray, C.K.; Wenke, J.C. Effect of various concentrations of antibiotics on osteogenic cell viability and activity. *J. Orthop. Res.* **2011**, *29*, 1070–1074. [[CrossRef](#)]
- Martínez-Carmona, M.; Gunko, Y.K.; Vallet-Regí, M. Mesoporous silica materials as drug delivery: “The nightmare” of bacterial infection. *Pharmaceutics* **2018**, *10*, 279. [[CrossRef](#)]
- Beck, G.R.; Ha, S.W.; Camalier, C.E.; Yamaguchi, M.; Li, Y.; Lee, J.K.; Weitzmann, M.N. Bioactive silica-based nanoparticles stimulate bone-forming osteoblasts, suppress bone-resorbing osteoclasts, and enhance bone mineral density in vivo. *Nanomed. Nanotechnol. Biol. Med.* **2012**, *8*, 793–803. [[CrossRef](#)]
- Nairi, V.; Medda, L.; Monduzzi, M.; Salis, A. Adsorption and release of ampicillin antibiotic from ordered mesoporous silica. *J. Colloid Interface Sci.* **2017**, *497*, 217–225. [[CrossRef](#)]
- Shi, X.; Wang, Y.; Ren, L.; Zhao, N.; Gong, Y.; Wang, D.A. Novel mesoporous silica-based antibiotic releasing scaffold for bone repair. *Acta Biomater.* **2009**, *5*, 1697–1707. [[CrossRef](#)]
- Narayan, R.; Nayak, U.Y.; Raichur, A.M.; Garg, S. Mesoporous silica nanoparticles: A comprehensive review on synthesis and recent advances. *Pharmaceutics* **2018**, *10*, 118. [[CrossRef](#)]

14. Izquierdo-Barba, I.; Sousa, E.; Doadrio, J.C.; Doadrio, A.L.; Pariente, J.P.; Martínez, A.; Babonneau, F.; Vallet-Regí, M. Influence of mesoporous structure type on the controlled delivery of drugs: Release of ibuprofen from MCM-48, SBA-15 and functionalized SBA-15. *J. Sol-Gel Sci. Technol.* **2009**, *50*, 421–429. [[CrossRef](#)]
15. Natarajan, S.K.; Selvaraj, S. Mesoporous silica nanoparticles: Importance of surface modifications and its role in drug delivery. *RSC Adv.* **2014**, *4*, 14328–14334. [[CrossRef](#)]
16. Gounani, Z.; Asadollahi, M.A.; Pedersen, J.N.; Lyngsø, J.; Skov Pedersen, J.; Arpanaei, A.; Meyer, R.L. Mesoporous silica nanoparticles carrying multiple antibiotics provide enhanced synergistic effect and improved biocompatibility. *Colloids Surf. B Biointerfaces* **2019**, *175*, 498–508. [[CrossRef](#)]
17. Szewczyk, A.; Prokopowicz, M.; Sawicki, W.; Majda, D.; Walker, G. Aminopropyl-functionalized mesoporous silica SBA-15 as drug carrier for cefazolin: Adsorption profiles, release studies, and mineralization potential. *Microporous Mesoporous Mater.* **2019**, *274*, 113–126. [[CrossRef](#)]
18. Varache, M.; Bezverkhyy, I.; Weber, G.; Saviot, L.; Chassagnon, R.; Baras, F.; Bouyer, F. Loading of cisplatin into mesoporous silica nanoparticles: Effect of surface functionalization. *Langmuir* **2019**, *35*, 8984–8995. [[CrossRef](#)]
19. Yang, H.; Cheng, B.; Li, Z.; Su, K.; Guo, Q.; Han, P. Organically modified MCM-type material preparation and its usage in controlled ibuprofen delivery. *Adv. Mater. Res.* **2010**, *342*, 607–613. [[CrossRef](#)]
20. Doadrio, J.C.; Sousa, E.M.B.; Izquierdo-Barba, I.; Doadrio, A.L.; Perez-Pariente, J.; Vallet-Regí, M. Functionalization of mesoporous materials with long alkyl chains as a strategy for controlling drug delivery pattern. *J. Mater. Chem.* **2006**, *16*, 462–466. [[CrossRef](#)]
21. Martín, A.; Morales, V.; Ortiz-Bustos, J.; Pérez-Garnes, M.; Bautista, L.F.; García-Muñoz, R.A.; Sanz, R. Modelling the adsorption and controlled release of drugs from the pure and amino surface-functionalized mesoporous silica hosts. *Microporous Mesoporous Mater.* **2018**, *262*, 23–34. [[CrossRef](#)]
22. Maria, G.; Stoica, A.I.; Luta, I.; Stirbet, D.; Radu, G.L. Cephalosporin release from functionalized MCM-41 supports interpreted by various models. *Microporous Mesoporous Mater.* **2012**, *162*, 80–90. [[CrossRef](#)]
23. Zhou, X.; Weng, W.; Chen, B.; Feng, W.; Wang, W.; Nie, W.; Chen, L.; Mo, X.; Su, J.; He, C. Mesoporous silica nanoparticles/gelatin porous composite scaffolds with localized and sustained release of vancomycin for treatment of infected bone defects. *J. Mater. Chem. B* **2018**, *6*, 740–752. [[CrossRef](#)]
24. Chen, X.; Xu, C.; He, H. Electrospinning of silica nanoparticles-entrapped nanofibers for sustained gentamicin release. *Biochem. Biophys. Res. Commun.* **2019**, *516*, 1085–1089. [[CrossRef](#)] [[PubMed](#)]
25. Xue, J.M.; Shi, M. PLGA/mesoporous silica hybrid structure for controlled drug release. *J. Control. Release* **2004**, *98*, 209–217. [[CrossRef](#)] [[PubMed](#)]
26. Zanjanzadeh Ezazi, N.; Shahbazi, M.A.; Shatalin, Y.V.; Nadal, E.; Mäkilä, E.; Salonen, J.; Kemell, M.; Correia, A.; Hirvonen, J.; Santos, H.A. Conductive vancomycin-loaded mesoporous silica polypyrrole-based scaffolds for bone regeneration. *Int. J. Pharm.* **2018**, *536*, 241–250. [[CrossRef](#)]
27. Lee, D.W.; Yoo, B.R. Advanced silica/polymer composites: Materials and applications. *J. Ind. Eng. Chem.* **2016**, *38*, 1–12. [[CrossRef](#)]
28. Masters, E.A.; Trombetta, R.P.; de Mesy Bentley, K.L.; Boyce, B.F.; Gill, A.L.; Gill, S.R.; Nishitani, K.; Ishikawa, M.; Morita, Y.; Ito, H.; et al. Evolving concepts in bone infection: Redefining “biofilm”, “acute vs. chronic osteomyelitis”, “the immune proteome” and “local antibiotic therapy”. *Bone Res.* **2019**, *7*, 20.
29. Nandi, S.K.; Mukherjee, P.; Roy, S.; Kundu, B.; De, D.K.; Basu, D. Local antibiotic delivery systems for the treatment of osteomyelitis—A review. *Mater. Sci. Eng. C* **2009**, *29*, 2478–2485. [[CrossRef](#)]
30. Nayak, A.K.; Bhattacharyya, A.; Sen, K.K. In Vivo ciprofloxacin release from hydroxyapatite-based bone implants in rabbit tibia: A preliminary study. *ISRN Orthop.* **2011**, *2011*, 420549. [[CrossRef](#)]
31. Dajcs, J.J.; Thibodeaux, B.A.; Marquart, M.E.; Girgis, D.O.; Traidej, M.; O’Callaghan, R.J. Effectiveness of ciprofloxacin, levofloxacin, or moxifloxacin for treatment of experimental *Staphylococcus aureus* keratitis. *Antimicrob. Agents Chemother.* **2004**, *48*, 1948–1952. [[CrossRef](#)]
32. Tran, T.T.D.; Tran, P.A. Controlled release film forming systems in drug delivery: The potential for efficient drug delivery. *Pharmaceutics* **2019**, *11*, 290. [[CrossRef](#)] [[PubMed](#)]
33. Adeleke, O.A. Premium ethylcellulose polymer based architectures at work in drug delivery. *Int. J. Pharm. X* **2019**, *1*, 100023. [[CrossRef](#)] [[PubMed](#)]
34. Regdon, G.; Hegyesi, D.; Pintye-Hódi, K. Thermal study of ethyl cellulose coating films used for modified release (MR) dosage forms. *J. Therm. Anal. Calorim.* **2012**, *108*, 347–352. [[CrossRef](#)]

35. Kim, S.H.; Moon, J.H.; Kim, J.H.; Jeong, S.M.; Lee, S.H. Flexible, stretchable and implantable PDMS encapsulated cable for implantable medical device. *Biomed. Eng. Lett.* **2011**, *1*, 199–203. [[CrossRef](#)]
36. Raczowska, J.; Prauzner-Bechcicki, S.; Lukes, J.; Sepitka, J.; Bernasik, A.; Awsiuk, K.; Paluszkiwicz, C.; Pabijan, J.; Lekka, M.; Budkowski, A. Physico-chemical properties of PDMS surfaces suitable as substrates for cell cultures. *Appl. Surf. Sci.* **2016**, *389*, 247–254. [[CrossRef](#)]
37. Prokopowicz, M.; Szewczyk, A.; Lunio, R.; Sawicki, W. Monolithic polydimethylsiloxane-modified silica composites prepared by a low-temperature sol-gel micromolding technique for controlled drug release. *React. Funct. Polym.* **2017**, *114*, 136–145. [[CrossRef](#)]
38. Prokopowicz, M. Correlation between physicochemical properties of doxorubicin-loaded silica/polydimethylsiloxane xerogel and in vitro release of drug. *Acta Biomater.* **2009**, *5*, 193–207. [[CrossRef](#)]
39. Nahrup, J.S.; Gao, Z.M.; Mark, J.E.; Sakr, A. Poly(dimethylsiloxane) coatings for controlled drug release—Polymer modifications. *Int. J. Pharm.* **2004**, *270*, 199–208. [[CrossRef](#)]
40. Skwira, A.; Szewczyk, A.; Prokopowicz, M. The effect of polydimethylsiloxane-ethylcellulose coating blends on the surface characterization and drug release of ciprofloxacin-loaded mesoporous silica. *Polymers* **2019**, *11*, 1450. [[CrossRef](#)]
41. Mesallati, H.; Umerska, A.; Paluch, K.J.; Tajber, L. Amorphous polymeric drug salts as ionic solid dispersion forms of ciprofloxacin. *Mol. Pharm.* **2017**, *14*, 2209–2223. [[CrossRef](#)]
42. Council of Europe. Methods of preparation of sterile products. In *European Pharmacopoeia*, 9th ed.; Council of Europe: Strasbourg, France, 2017; pp. 4333–4336.
43. White, J.F.; Verma, S.K. Isolation of endophytic microbes. In *Seed Endophytes*; Springer: Cham, Switzerland, 2019; pp. 57–63.
44. Council of Europe. Biological tests. In *European Pharmacopoeia*, 9th ed.; Council of Europe: Strasbourg, France, 2017; pp. 185–188.
45. Howlin, R.P.; Brayford, M.J.; Webb, J.S.; Cooper, J.J.; Aiken, S.S.; Stoodley, P. Antibiotic-loaded synthetic calcium sulfate beads for prevention of bacterial colonization and biofilm formation in periprosthetic infections. *Antimicrob. Agents Chemother.* **2015**, *59*, 111–120. [[CrossRef](#)] [[PubMed](#)]
46. Wiegand, I.; Hilpert, K.; Hancock, R.E.W. Agar and broth dilution methods to determine the minimal inhibitory concentration (MIC) of antimicrobial substances. *Nat. Protoc.* **2008**, *3*, 163–175. [[CrossRef](#)] [[PubMed](#)]
47. International Organization for Standardization. *Biological Evaluation of Medical Devices—Part 5: Tests for In Vitro Cytotoxicity*; ISO 10993-5:2009; ISO: Geneva, Switzerland, 2012.
48. Qi, R.; Shen, M.; Cao, X.; Guo, R.; Tian, X.; Yu, J.; Shi, X. Exploring the dark side of MTT viability assay of cells cultured onto electrospun PLGA-based composite nanofibrous scaffolding materials. *Analyst* **2011**, *136*, 2897–2903. [[CrossRef](#)] [[PubMed](#)]
49. Miller, F.; Hinze, U.; Chichkov, B.; Leibold, W.; Lenarz, T.; Paasche, G. Validation of eGFP fluorescence intensity for testing in vitro cytotoxicity according to ISO 10993-5. *J. Biomed. Mater. Res. B Appl. Biomater.* **2017**, *105*, 715–722. [[CrossRef](#)] [[PubMed](#)]
50. Kecht, J.; Bein, T. Oxidative removal of template molecules and organic functionalities in mesoporous silica nanoparticles by H₂O₂ treatment. *Microporous Mesoporous Mater.* **2008**, *116*, 123–130. [[CrossRef](#)]
51. Roik, N.V.; Belyakova, L.A.; Dziacko, M.O. Adsorption of antitumor antibiotic doxorubicin on MCM-41-type silica surface. *Adsorpt. Sci. Technol.* **2017**, *35*, 1–16. [[CrossRef](#)]
52. Moodley, T.; Singh, M. Polymeric mesoporous silica nanoparticles for enhanced delivery of 5-Fluorouracil in vitro. *Pharmaceutics* **2019**, *11*, 288. [[CrossRef](#)]
53. Hung, C.C.; Huang, W.C.; Lin, Y.W.; Yu, T.W.; Chen, H.H.; Lin, S.C.; Chiang, W.H.; Chiu, H.C. Active tumor permeation and uptake of surface charge-switchable theranostic nanoparticles for imaging-guided photothermal/chemo combinatorial therapy. *Theranostics* **2016**, *6*, 302–317. [[CrossRef](#)]
54. Li, X.; Han, C.; Zhu, W.; Ma, W.; Luo, Y.; Zhou, Y.; Yu, J.; Wei, K. Cr(VI) removal from aqueous by adsorption on amine-functionalized mesoporous silica prepared from silica fume. *J. Chem.* **2014**, *2014*, 765856. [[CrossRef](#)]
55. Durgapal, S.; Mukhopadhyay, S.; Goswami, L. Preparation, characterization and evaluation of floating microparticles of ciprofloxacin. *Int. J. Appl. Pharm.* **2017**, *9*, 1–8. [[CrossRef](#)]

56. Trivedi, M.K.; Branton, A.; Trivedi, D.; Nayak, G.; Mishra, R.K.; Jana, S. Characterization of physicochemical and thermal properties of biofield treated ethyl cellulose and methyl cellulose. *Int. J. Biomed. Mater. Res.* **2015**, *3*, 83–91.
57. Hanoosh, W.S.; Abdelrazaq, E.M. Polydimethyl siloxane toughened epoxy resins: Tensile strength and dynamic mechanical analysis. *Malays. Polym. J.* **2009**, *4*, 52–61.
58. Siddiqui, S.; Siddiqui, Z.N. Strontium doped MCM-41: A highly efficient, recyclable and heterogeneous catalyst for the synthesis of phenoxy pyrazolyl pyrazolines. *Catal. Lett.* **2018**, *148*, 3628–3645. [[CrossRef](#)]
59. Turel, I.; Bukovec, P. Comparison of the thermal stability of ciprofloxacin and its compounds. *Thermochim. Acta* **1996**, *287*, 311–318. [[CrossRef](#)]
60. Galarneau, A.; Nader, M.; Guenneau, F.; Di Renzo, F.; Gedeon, A. Understanding the stability in water of mesoporous SBA-15 and MCM-41. *J. Phys. Chem. C* **2007**, *111*, 8268–8277. [[CrossRef](#)]



© 2019 by the authors. Licensee MDPI, Basel, Switzerland. This article is an open access article distributed under the terms and conditions of the Creative Commons Attribution (CC BY) license (<http://creativecommons.org/licenses/by/4.0/>).

Supplementary Materials: Silica-Polymer Composites as the Novel Antibiotic Delivery Systems for Bone Tissue Infection

Adrianna Skwira, Adrian Szewczyk, Agnieszka Konopacka, Monika Górka, Dorota Majda, Rafał Sądej and Magdalena Prokopowicz

Table S1. Surface area, pore diameter and pore volume of MCM-41 and MCM-41-CIP powders.

Sample	Surface Area (S_{BET}) (m^2/g)	Pore Diameter (nm)	Pore Volume (cm^3/g)
MCM-41	720	3.55	0.61
MCM-41-CIP	590	2.98	0.47

Note: calculated from the desorption branch of the nitrogen adsorption-desorption isotherm using the Barrett–Joyner–Halenda (BJH) method.

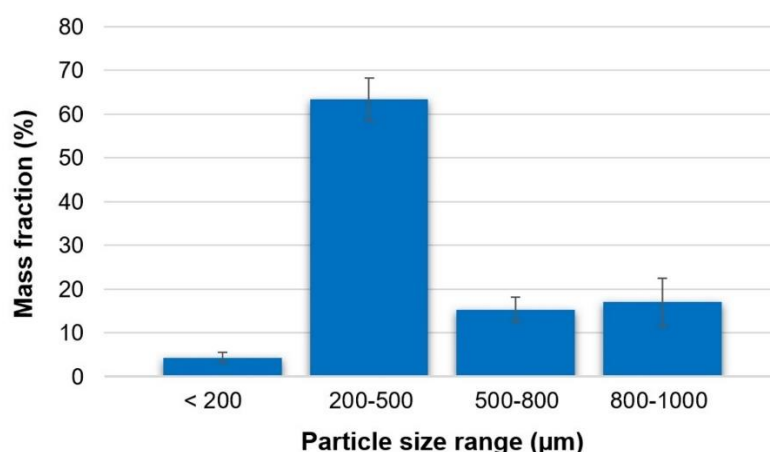


Figure S1. Particle size of MCM-41-CIP powder.

Table S2. The kinetic parameters of fitted experimental data for MCM-41-CIP sample and EC/CIP, EC/PDMS/CIP, EC/MCM-41-CIP and EC/PDMS/MCM-41-CIP composites.

Sample	Higuchi Model		Korsmeyer-Peppas Model	
	k_H	R^2	n	R^2
MCM-41-CIP ¹	7.44	0.882	0.42	0.911
EC/CIP ¹	27.6	0.952	0.50	0.954
EC/PDMS/CIP ¹	30.4	0.936	0.54	0.951
EC/MCM-41-CIP ²	7.39	0.992	0.17	0.979
EC/PDMS/MCM-41-CIP ³	2.68	0.993	0.26	0.866

R^2 —coefficient of determination, n —release exponent in Korsmeyer-Peppas model, k_H —Higuchi dissolution constant ($min^{-1/2}$; $day^{-1/2}$). ¹ calculated for 60% of cumulative amount of released CIP; ² calculated for first 11 days of release study (60% of cumulative amount of released CIP); ³ calculated for 30 days of release study (21% of cumulative amount of released CIP).

3.2. Otrzymanie i charakterystyka bioszklą jako materiału o potencjalnych właściwościach regenerujących tkankę kostną

Publikacja 3. A. Skwira, A. Szewczyk, R. Sądej, M. Prokopowicz, *Bioglass obtained via one-pot synthesis as osseointegrative drug delivery system, Int. J. Pharm.* 633 (2023) 122610.

W trzecim artykule zaprezentowano etapy badawcze zrealizowane w celu oceny zdolności do osseointegracji otrzymanego przez nasz zespół badawczy bioszklą. Ważną cechą biomateriałów jest ich biozgodność, jednakże biomateriały stosowane w celu uzupełniania ubytków kości, nie tylko powinny być biozgodne, ale również powinny stymulować odbudowę uszkodzonej lub utraconej tkanki kostnej.

W niniejszej publikacji bioszklą o wyjściowym składzie masowym SiO₂ (70%) CaO-P₂O₅ (30%) otrzymano na drodze modyfikacji klasycznego procesu zol-żel. Metoda ta pozwoliła na uzyskanie produktu końcowego w jednym etapie, w czasie nieprzekraczającym 24 godzin. Jako prekursorzy jonów osteogenicznych zastosowano ortokrzemian tetraetylu (TEOS), fosforan trietylu (TEP) oraz dwuwodny chlorek wapnia (CaCl₂·2H₂O). Otrzymane bioszklą, o wielkości cząstek < 100 μm, oceniono w zakresie zdolności do osseointegracji w porównaniu z dwoma komercyjnie dostępnymi, wyprodukowanymi za pomocą klasycznej metody zol-żel, materiałami: bioszklą 45S i bioszklą 85S.

Zgodnie z zaleceniami części piątej normy ISO 10993, przeprowadzono dwa rodzaje testów wykorzystując linię komórkową ludzkich osteoblastów hFOB 1.19 jako model *in vitro* – testy kontaktu bezpośredniego oraz testy z zastosowaniem ekstraktów z bioszkieł. Komórki tej linii wykazują cechy komórek osteoprogenitorowych, a więc posiadają zdolność do różnicowania w kierunku dojrzałych osteoblastów, które aktywnie wytwarzają tkankę kostną. Testy kontaktu bezpośredniego posłużyły zbadaniu oddziaływania osteoblastów z bioszklami (analiza właściwości osteokondukcyjnych). W tym celu komórki obserwowano za pomocą mikroskopii fluorescencyjnej oraz techniki SEM-EDX. Testy z zastosowaniem ekstraktów z bioszkieł pozwoliły na ocenę wpływu uwalnianych do pożywki komórkowej jonów wapnia oraz ortokrzemianów na żywotność, różnicowanie i regulowany przez osteoblasty proces mineralizacji (analiza właściwości osteoindukcyjnych). Do przeprowadzenia tych analiz wykorzystano następujące techniki badawcze: kolorymetryczny test cytotoksyczności (*WST-1*); ilościową reakcję

łańcuchowej polimerazy (*qRT-PCR*), oznaczanie kolorymetryczne aktywności enzymatycznej fosfatazy alkalicznej, barwienie białek macierzy zewnątrzkomórkowej metodą immunofluorescencyjną, barwienie zlokalizowanych zewnątrzkomórkowo soli wapnia za pomocą czerwieni alizarynowej S, ilościowe oznaczenie wapnia wewnątrzkomórkowego metodą pomiaru intensywności fluorescencji (*Rhod-4 Calcium Assay Kit*) oraz obserwację przyżyciową z wykorzystaniem mikroskopii holotomograficznej. W celu oceny wpływu ekstraktu z otrzymanego bioszkiełka na poszczególne etapy różnicowania osteoblastów, przeprowadzono pomiar ekspresji wybranych genów, uznawanych za markery wczesnych etapów tego procesu: gen kodujący czynnik transkrypcyjny RUNX2 (*RUNX2*), gen kodujący łańcuch alfa 1 kolagenu typu I (*COL1A1*) i gen kodujący fosfatazę alkaliczną (*ALPL*) oraz późnych etapów tego procesu: gen kodujący osteopontynę (*OPN*), gen kodujący osteokalcynę (*OCN*).

Analiza biozgodności *in vitro*, przeprowadzona za pomocą testu kontaktu bezpośredniego, wykazała najsilniejszą adhezję osteoblastów do powierzchni cząstek otrzymanego bioszkiełka oraz bioszkiełka komercyjnego 45S. Wyjaśniono to prawdopodobnym efektem chemotaktycznym wapnia uwalnianego ze struktury bioszkiełka. Przeprowadzony dla ekstraktów test cytotoksyczności wykazał niewielki spadek proliferacji osteoblastów hodowanych w obecności ekstraktu z otrzymanego bioszkiełka. Jednocześnie odnotowano cytotoksyczne działanie ekstraktu z bioszkiełka komercyjnego 45S. Efekt ten uzasadniono wysoką wartością pH (10,14) ekstraktu oraz prawie 4-krotnie wyższym stężeniem krzemianów w porównaniu z ekstraktem z otrzymanego bioszkiełka. Ekstrakt z bioszkiełka komercyjnego 45S został wykluczony z dalszych etapów badawczych.

Uważa się, że komórki osteoprogenitorowe wykazują wysoką ekspresję genu czynnika transkrypcyjnego RUNX1, który jest zaangażowany w progresję cyklu komórkowego i proliferację. Następnie czynnik transkrypcyjny RUNX2, uznawany za nadrzędny regulator procesu kościotworzenia, indukuje przejście komórek w fazę dojrzewania. Na tym etapie, ekspresji ulegają geny docelowe czynnika transkrypcyjnego RUNX2, do których należą m.in. gen *COL1A1* i gen *ALPL*. Przeprowadzona analiza wpływu ekstraktów z bioszkiełek na wczesne etapy różnicowania komórkowego wykazała istotnie wyższą ekspresję genu *RUNX2* w osteoblastach hodowanych w obecności ekstraktu z otrzymanego bioszkiełka w porównaniu z osteoblastami hodowanymi w obecności ekstraktu z bioszkiełka komercyjnego 85S oraz kontrolą (osteoblasty hodowane

z pożywką komórkową). W przeprowadzonym badaniu nie stwierdzono wpływu ekstraktu z otrzymanego bioszkiełka na ekspresję genu *COL1A1*. Interesującej obserwacji dokonano natomiast dla genu *ALPL*. Odnotowano spadek jego ekspresji w komórkach hodowanych w obecności ekstraktu z otrzymanego bioszkiełka i ekstraktu z bioszkiełka 85S w porównaniu z kontrolą. Podobny efekt obu ekstraktów wykazano dla równocześnie przeprowadzonego badania aktywności enzymatycznej fosfatazy alkalicznej. Stwierdzono, iż najprawdopodobniej spadek ekspresji genu oraz zmniejszenie aktywności enzymatycznej fosfatazy alkalicznej wynikały z szybszego rozpoczęcia fazy mineralizacji przez komórki hodowane w obecności ekstraktu z otrzymanego bioszkiełka. Powyższą hipotezę zweryfikowano dodatkowo za pomocą analizy obecności zlokalizowanych zewnątrzkomórkowo soli wapnia. Za pomocą barwienia czerwienią alizarynową S oraz obrazowania przyżyciowego potwierdzono stopniowe odkładanie soli wapnia w czasie przez osteoblasty. Początek tego procesu przypadający na 7. dobę badania pozostawał w korelacji czasowej ze spadkiem ekspresji genu *ALPL* i obniżoną aktywnością enzymatyczną fosfatazy alkalicznej. Dane te były zgodne z doniesieniami literaturowymi opisującymi molekularne mechanizmy różnicowania i mineralizacji komórkowej, w których wskazano na istnienie odwrotnej korelacji mineralizacji komórkowej z aktywnością enzymatyczną fosfatazy alkalicznej [106,107]. Na podstawie wyników przeprowadzonych analiz potwierdzono, że aktywność fosfatazy alkalicznej może być obniżona, gdy komórki rozpoczęły mineralizację – kluczowy etap w procesie kościotworzenia. Z drugiej strony wysoka aktywność fosfatazy alkalicznej, dotychczas określana jako pozytywny marker procesu kościotworzenia, może świadczyć o różnicowaniu komórek do dojrzałych osteoblastów, które jednak, przy braku odpowiednich bodźców molekularnych, mogą nigdy nie rozpocząć mineralizacji. Dlatego też analiza właściwości osteoindukcyjnych biomateriałów *in vitro* zawsze powinna opierać się o ocenę więcej niż jednego parametru, uznawanego za wskaźnik formowania nowej tkanki kostnej na poziomie komórkowym.

Analiza wpływu ekstraktów z bioszkiełek na późne etapy różnicowania nie wykazała istotnych statystycznie różnic w ekspresji genu *OPN*. Natomiast w komórkach traktowanych ekstraktem z otrzymanego bioszkiełka potwierdzono znacznie wyższą ekspresję genu *OCN* w porównaniu z komórkami hodowanymi z ekstraktem z bioszkiełka 85S i kontrolą. Produktem genu *OCN* jest białko, którego główną rolą jest wiązanie jonów wapniowych i stymulowanie mineralizacji kości. Przeprowadzone badania pozwoliły

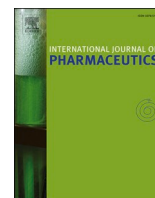
na obserwację korelacji czasowej pomiędzy wzrostem ekspresji genu *OCN* i nasileniem odkładania soli wapnia przez osteoblasty.

W związku z odnotowanymi w literaturze naukowej próbami zastosowania bioszkle jako nośników substancji leczniczych, zweryfikowano również możliwości adsorpcyjne otrzymanego bioszkle. Przeprowadzono adsorpcję modelowego antybiotyku – doksycykliny. Obecność zaadsorbowanego antybiotyku na powierzchni bioszkle potwierdzono za pomocą technik FTIR oraz DSC. Wydajność procesu adsorpcji wynosiła około 10%, co odpowiadało adsorpcji 2,2 mg doksycykliny na 100 mg otrzymanego bioszkle. Przeprowadzone badanie dostępności farmaceutycznej wykazało dwufazowy profil uwalniania doksycykliny. Charakteryzował się on wysokim początkowym wyrzutem antybiotyku w pierwszych 24 godzinach badania (na poziomie 70%) i następnie jego wolniejszym uwalnianiem do 5 dni.

Wyniki szczegółowych analiz, zaprezentowane w niniejszym artykule, potwierdziły biogodność otrzymanego przez nas bioszkle na poziomie komórkowym. Ponadto wykazano korzystny wpływ uwalnianych z otrzymanego bioszkle jonów wapnia i ortokrzemianów na różnicowanie osteoblastów i regulowany przez nie proces mineralizacji. Warto zauważyć, że efekty biologiczne otrzymanego bioszkle zweryfikowane za pomocą dwóch rodzajów testów były znacznie korzystniejsze niż bioszkieł komercyjnych 45S i 85S. W związku z tym, stwierdzono, że zrealizowane etapy badawcze pozwoliły na potwierdzenie przydatności otrzymanego bioszkle jako materiału o potencjalnych właściwościach regeneracyjnych. Mimo wykazanej możliwości adsorpcji doksycykliny na otrzymanym bioszkle, uznano, że kilkudniowy czas uwalniania antybiotyku nie spełniał rekomendacji leczenia zakażeń bakteryjnych tkanki kostnej oraz założeń pracy doktorskiej.

Oprócz otrzymania bioszkle o potwierdzonych właściwościach osteokonducyjnych i osteoindukcyjnych przewyższających analizowane bioszkieł komercyjne, niniejsza praca stanowi zbiór zoptymalizowanych procedur umożliwiający przeprowadzenie kompleksowej oceny biomateriałów degradowalnych zgodnie z normą ISO 10993. Ponadto wyniki badań zaprezentowanych w niniejszym artykule pozwoliły na pogłębienie wiedzy na temat molekularnych i komórkowych aspektów procesu mineralizacji, który do dziś nie został w pełni poznany. Dowiedziono, iż analizie aktywności enzymatycznej fosfatazy alkalicznej zawsze powinna towarzyszyć ocena dodatkowych markerów procesu różnicowania osteoblastów i regulowanej przez nie mineralizacji. Obserwacja ta jest szczególnie ważna w obliczu tego, że wzrost aktywności

enzymatycznej fosfatazy alkalicznej jest często wskazywany jako jedyny marker procesu kościotworzenia, a więc służy potwierdzeniu pozytywnego efektu wywieranego przez testowany biomateriał na osteoblasty. Tymczasem, przeprowadzone badania wskazują, iż sama weryfikacja aktywności enzymatycznej fosfatazy alkalicznej może prowadzić do uzyskania wyników fałszywie ujemnych, zwłaszcza, gdy osteoblasty na etapie analizy znajdują się już w fazie mineralizacji.



Bioglass obtained via one-pot synthesis as osseointegrative drug delivery system

Adrianna Skwira^a, Adrian Szewczyk^a, Rafał Sądej^b, Magdalena Prokopowicz^{a,*}

^a Department of Physical Chemistry, Faculty of Pharmacy, Medical University of Gdansk, Hallera 107, 80-416 Gdansk, Poland

^b Department of Molecular Enzymology and Oncology, Intercollegiate Faculty of Biotechnology, University of Gdańsk and Medical University of Gdańsk, Dębinki 1, 80-211 Gdańsk, Poland

ARTICLE INFO

Keywords:

Bioglass
Osseointegration
Osteoblasts
Bone tissue
Local drug delivery

ABSTRACT

Osseointegration is a fundamental process during which implantable biomaterial integrates with host bone tissue. The surgical procedure of biomaterial implantation is highly associated with the risk of bacterial infection. Thus, the research continues for biodegradable bone void fillers which are able to stimulate the bone tissue regeneration and locally deliver the antibacterial agent. Herein, we obtained bifunctional bioglass (BG) using novel, preoptimized, rapid one-pot synthesis. Following the ISO Standards, the influence of the obtained BG on osteoblast-mediated phenomena, such as osteoconduction and osteoinduction was assessed and compared to two commercial materials: bioactive glass powder 45S and bioactive glass powder 85S. Direct-contact tests revealed osteoblast adhesion to BG particles; whereas, tests on extracts confirmed high viability of cells incubated with BG extract. Analyses of gene expression, alkaline phosphatase activity, and calcium phosphates deposition confirmed the stimulation of early and late stages of osteoblast differentiation and mineralization. Additionally, an extended evaluation of intracellular calcium fluctuations revealed a possible correlation between osteoblast calcium uptake and extracellular matrix mineralization. Moreover, proposed bioglass exhibited satisfactory doxycycline adsorption capacity and release profile. The obtained results confirmed the bifunctionality of the proposed BG and indicated its potential as osseointegrative bone drug delivery system.

1. Introduction

Biomaterials are substances engineered to interact with the host tissue for therapeutic or diagnostic purposes (Hudecki et al., 2018). The fundamental property of a biomaterial is its biocompatibility, i.e., each potentially implantable material must not trigger any harmful effect on the tissues and organs adjacent to the site of application or those located elsewhere in the body. However, biomaterials used in bone tissue engineering as bone fillers or bone substitutes should not only be biocompatible but also enhance bone tissue regeneration. To effectively support the formation of new bone, a stable structural and functional connection between the implant surface and host bone should be developed. This process is called osseointegration (Brauer, 2015) and depends on two cell-mediated phenomena—osteoconduction and osteoinduction (Albrektsson and Johansson, 2001; Vaidya et al., 2017). Osteoconduction refers to the ability of osteoblasts to move across an implantable material through cell adhesion and growth (Wypych,

2018). Osteoinduction is defined as the recruitment of bone progenitors and their differentiation during which the extracellular matrix is deposited and mineralized (Rutkovskiy et al., 2016).

The application of biomaterials into the bone site is frequently associated with orthopedic bacterial infections (Inzana et al., 2016). An acute bone infection may develop into chronic osteomyelitis associated with high mortality. The gold standard for osteomyelitis prophylaxis and treatment is non-biodegradable polymethyl methacrylate (PMMA) bone cement impregnated with gentamycin (van Vugt et al., 2019). Although the PMMA beads are effective in prevention of implant-associated osteomyelitis, they have to be removed after the release of total drug content since they do not integrate with the bone tissue. The subsequent surgical procedure carries significant risk of secondary bacterial infection. Contrarily to PMMA, biodegradable materials do not need to be removed after infection management. Therefore, the scientific findings are focused on designing of biodegradable bifunctional bone void fillers which not only stimulate the tissue regeneration, but also deliver the

* Corresponding author.

E-mail addresses: adrianna.skwira@gumed.edu.pl (A. Skwira), adrian.szewczyk@gumed.edu.pl (A. Szewczyk), rafal.sadej@gumed.edu.pl (R. Sądej), magdalena.prokopowicz@gumed.edu.pl (M. Prokopowicz).

<https://doi.org/10.1016/j.ijpharm.2023.122610>

Received 6 November 2022; Received in revised form 3 January 2023; Accepted 11 January 2023

Available online 18 January 2023

0378-5173/© 2023 The Authors. Published by Elsevier B.V. This is an open access article under the CC BY-NC-ND license (<http://creativecommons.org/licenses/by-nc-nd/4.0/>).

antibiotic at the affected site to prevent bacterial infection after surgery (Amarnath Praphakar et al., 2019; Coelho et al., 2019; Ene et al., 2021; Radwan et al., 2021; Wassif et al., 2021).

Amongst biodegradable materials, bioglasses are recognized as the most bioactive materials which are able to induce the formation of bone-like apatite (Vallet-Regi and Salinas, 2021). The inventor of 45S5 Bioglass®, Larry Hench, proved that the deposition of carbonate hydroxyapatite is detectable four days after implantation; however, the formation of the apatite layer characterized by Ca/P ratio equivalent to human bone tissue apatite required approximately two weeks (Hench, 1991). The significance of semi-crystalline carbonate apatite formed on bioglass surfaces during osseointegration processes was confirmed by both *in vitro* and *in vivo* studies (Souza et al., 2018). Apart from the calcium ions and orthophosphates released from hydroxyapatites or calcium phosphates, bioglasses release silicates that are involved in the early stages of bone tissue formation and mineralization at relatively low concentrations (Götz et al., 2019).

Nowadays, various modifications of bioglasses are produced to increase their bioactivity (Furlan et al., 2018; Schmitz et al., 2020; Schumacher et al., 2021). There are two principal methods of bioglasses synthesis. The first one, developed by Hench, relies on the melting of oxides (SiO₂, Na₂O, CaO, and P₂O₅) at temperatures > 1300 °C (Hench, 2006). Bioglass synthesized in this manner has a dense structure, smooth texture, and low specific surface area that results in decreased biodegradability and bioactivity (Sepulveda et al., 2001). The sol-gel-derived bioglasses are characterized by higher porosity in the mesoporous range and a significantly larger specific surface area. They are more bioactive than melt-derived ones. However, the multi-stage sol-gel method requires optimization of many steps, such as hydrolysis and condensation of molecular precursors of calcium ions, phosphates, and silicates; aging; drying; stabilizing; and calcining to efficiently form a gel and then transform it to glass (Dang et al., 2020; Sepulveda et al., 2001). Although the qualitative and quantitative composition may suggest high bioactivity of obtained material, the biological properties should be preliminarily assessed every time.

ISO 10993 Standards (Biological evaluation of medical devices) provide the scheme for testing implantable materials. For cytotoxicity evaluation, three types of tests are used: direct-contact test, test on extracts, and indirect-contact test (Biological evaluation of medical devices, Part 5: Tests for *in vitro* cytotoxicity). The most appropriate tests should be selected according to the potential manner and site of application of the examined materials. As bioglasses are directly implanted into the bone tissue and belong to the group of degradable biomaterials, the two following types of tests were selected, 1) the direct-contact test, which evaluates the interaction between cells and biomaterial surface (osteoconductive properties), and 2) the test on extracts, which is used to verify the effect of the degradable products on cellular differentiation and mineralization (osteoinductive properties). Each assay should simulate the conditions of use as closely as possible (ISO 10993-12, Biological evaluation of medical devices, Part 12: Sample preparation and reference materials). Thus, the extraction conditions, such as time, temperature, extraction vehicle, agitation, and the surface area or mass/volume ratio should be chosen according to the nature of the material and its potential application. Moreover, for the materials that dissolve or degrade after application, such as bioglasses, ISO 10993-12 Standard recommends performing a more exaggerated extraction to release a greater amount of extracts into the medium than under conditions simulated during the application. The exaggerated conditions can identify the potential hazards and risks of using the biomaterial. Unfortunately, in previous studies, *in vitro* assessments applied the mass/volume ratios that gave favored concentrations of osteogenic ions in the examined extracts and provided expected results during extraction (Tsigkou et al., 2009; Xynos et al., 2000; Yan et al., 2020). Furthermore, the observed positive effects of the examined materials on cell metabolism, functioning, and differentiation frequently required specific conditions of pretreatment prior to the direct-contact test (Tsigkou et al.,

2009; Xynos et al., 2001). Nevertheless, according to the ISO 10993-12 Standard, samples should be examined in the form they are intended to be administered (without any additional preconditioning, such as changing particle size, micronizing, or diluting parent extract) for reliable results.

The aims of this project were to evaluate our newly proposed bioglass synthesized via a preoptimized one-pot sol-gel method in terms of: osseointegration capacity in comparison to commercial reference materials (i) and capacity of drug adsorption and delivery (ii). Frequently, the standard way of bone drug delivery systems assessment consisted of a preliminary determination of physicochemical parameters, drug adsorption efficiency, and bioactivity demonstrated as hydroxyapatite (HA) formation onto the material surface during incubation in simulated body fluid (SBF) (Geuli et al., 2017; Tabia et al., 2019; Yan et al., 2006). According to the relevant findings (Bellucci et al., 2019; Pan et al., 2010), there is a lack of correlation between the results of physicochemical analysis, such as incubation of biomaterial in SBF and biological assessment simulating *in vivo* conditions. Thus, we decided to examine biomaterials in reverse order starting from the evaluation of cellular response. All the biological assays were designed to simulate clinical use and provide the most reliable results according to the rigorous procedures described in ISO 10993-5 and ISO 10993-12 Standards. To verify the ability of our bioglass to serve as drug delivery system which may reduce the bacteriological implant-associated risk, we performed the adsorption and release studies for doxycycline hyclate, as a model drug used in treatment and prophylaxis of bacterial bone infections (Spellberg and Lipsky, 2012).

2. Materials and methods

2.1. One-pot synthesis of bioglass

The rapid synthesis of bioglass powder (BG_p) was carried out using preoptimized sol-gel method. First, 10.4 g of tetraethyl orthosilicate (TEOS, 98% purity, Sigma-Aldrich, USA) was poured into a polypropylene beaker and mixed with 4.55 g of purified water (Millipore Direct-Q 3 UV, Merck, Germany) and 200 µL of 1.0 M HCl (500 rpm, 30 min). Next, 0.65 g of triethyl phosphate (TEP, 99.8% purity, Sigma-Aldrich, USA) was added, and the mixture was stirred for 2 h under the same conditions. Thereafter, 0.99 g of calcium chloride dihydrate (CaCl₂·2H₂O, 99.0% purity, Sigma-Aldrich, USA) was weighed and dissolved, and the mixture was left for an additional 1.5 h with stirring. Finally, the obtained sol was poured into the crucible and calcined at 600 °C for 4 h in the muffle furnace (1 °C/min heating rate, FCF 7SM, Czylok). The obtained bioglass was powdered in the mortar, homogenized through a 100 µm sieve, and stored in the desiccator prior to further analyses.

2.2. Cell culture

Human fetal osteoblastic cell line (hFOB 1.19) was obtained from the American Type Culture Collection (Cat. No. CRL-11372™). hFOB 1.19 cell line comprises conditionally immortalized human fetal osteoblasts with a temperature-sensitive mutant of the SV40 large T antigen (tsSV40LTA) gene. At the permissive temperature of 33.5 °C, the tsSV40LTA is active, and the hFOB 1.19 cells exhibit rapid cell division. At the restrictive temperature of 39.5 °C, the tsSV40LTA becomes inactive, slowing the cell division and increasing differentiation so that the cells display a mature osteoblast phenotype (Harris et al., 1995; Yen et al., 2007). The cell line displays phenotypic markers specific for osteoblasts and deposits extracellular matrix proteins (Subramaniam et al., 2002). Osteoblasts were cultured in a 1:1 mixture of Ham's F12 Medium Dulbecco's Modified Eagle's Medium (DMEM/F12) with 2.5 mM L-glutamine (without phenol red), 15 mM HEPES, and sodium bicarbonate, supplemented with 10% fetal bovine serum and penicillin/streptomycin (100 U/mL/100 µg/mL) at 33.5 °C in a humidified atmosphere of

5% CO₂. The medium was replaced every 2–3 days. Cells were passaged for a maximum of 3–4 months post-resuscitation and regularly tested for mycoplasma contamination. For qualitative evaluation of cell morphology in the direct-contact test, human fetal osteoblasts hFOB 1.19 were transduced with eGFP using a lentiviral vector before the assays. Since osteoblasts are not fast responders and the synthesis of bone matrix by the cells usually takes several weeks (Rutkovskiy et al., 2016), the incubation time for the following assays was prolonged to 14 days.

2.3. Sample preparation

Assays were performed for one-pot-derived bioglass and two reference sol–gel-derived materials: bioactive glass powder 45S (Cat. No. 915084, Sigma-Aldrich, USA) and bioactive glass powder 85S (Cat. No. 916072, Sigma-Aldrich, USA). According to the ISO 10993–5 Standard, the assessment of *in vitro* cytotoxicity of implantable materials should verify the biological response of mammalian cells incubated with the analyzed material (direct-contact test) and incubated with an extract from the materials (test on extracts). Therefore, the samples for the tests were prepared under aseptic conditions according to the ISO 10993-12 Standard “Biological evaluation of medical devices, Part 12: Sample preparation and reference materials”. For the direct-contact test, examined materials were weighted, sterilized with UV light for one hour, and used. The samples in powder form with < 500 μm grain size were named BG_p (bioglass synthesized via one-pot synthesis; specific surface area: ~20 m²/g), BG45S_p (bioglass Cat. No. 915084, Sigma-Aldrich, USA, specific surface area: ~0.2 m²/g), and BG85S_p (bioglass Cat. No. 916072, Sigma-Aldrich, USA; specific surface area: ~200 m²/g). For the test on extracts, 100 mg/mL of each bioglass was immersed into the cell culture medium in sterile polypropylene centrifuge tubes and incubated with agitation (140 rpm) for 24 h at 37 °C. Then, the extracts were separated from the bioglass through centrifugation at 5000 min⁻¹ for 5 min. The extracts of samples were named BG_e (extract from bioglass obtained via one-pot synthesis), BG45S_e (extract from bioglass Cat. No. 915084, Sigma-Aldrich, USA), and BG85S_e (extract from bioglass Cat. No. 916072, Sigma-Aldrich, USA). The concentration of osteogenic ions: calcium (Ca), phosphates (P), and silicates (Si) in the obtained extracts were measured spectrophotometrically using colorimetric assays according to the manufacturer’s protocol (Spectroquant®, Supelco, Merck, Germany). Analytical measurements were conducted following the requirements for quantitative analyses, calibrating the UV–Vis detector with standard solutions of Ca, P, and Si ions. The concentration of Ca, P, and Si ions in a pristine cell culture medium was determined for comparison. The pH value and osmolality of the extracts and pristine cell culture medium were determined with pH-meter LAB 860 (SI Analytics GmbH, Mainz, Germany) and Osmometer OS 3000 (Marcel, Merzet, Poznan, Poland), respectively.

2.4. Evaluation of cell viability

2.4.1. Direct-contact test

To evaluate the cytocompatibility of BG_p, osteoblasts expressing eGFP were seeded in a 96-well plate at 5000 cells/well and incubated for cell adhesion for 24 h (33.5 °C, 5% CO₂). According to ISO 10993–5 Standard for the direct-contact test, the material should cover one-tenth of the cell layer surface. Thus, an appropriate amount of material per well was determined using stereoscopic analysis. The suspensions of each material (0.1–2.0 mg/mL) in the cell culture medium were obtained and poured into the wells. After sedimentation, the pictures of the wells’ bottom were taken, and the percentage of coverage was calculated using ImageJ software (Schneider et al., 2012). Next, the calibration curves of surface area coverage (%) as the function of suspension concentration (mg/mL) were plotted, and an appropriate concentration of each material was selected for the direct-contact test (0.5, 1.0, and 0.1 mg/mL for BG_p, BG45S_p, and BG85S_p, respectively). After 24 h of

osteoblast incubation, the pristine culture medium was replaced with a suspension of BG_p, BG45S_p, and BG85S_p in a fresh cell culture medium at the abovementioned concentrations or only fresh medium (control). The plates were incubated at 33.5 °C, and after 1, 3, 7, and 14 days the cell morphology was observed and recorded using Axiovert 200 fluorescent microscope equipped with AxioCam MRm digital camera (Zeiss, Germany). To verify the BG_p element that induced the observed chemotactic effect, the analogs consisting of silicon and calcium (SiCa_p), silicon and phosphate (SiP_p), and silicon (Si_p) at concentrations corresponding to that of BG_p were prepared via the one-pot synthesis and examined according to the procedure described above. The amounts of substrates used in the synthesis of BG_p and its analogs are presented in Table S1 (Supplementary materials). Moreover, to verify the probable adhesion of osteoblast on bioglass surface, BG_p samples were analyzed using scanning electron microscopy equipped with energy-dispersive X-ray spectroscopy (SEM/EDX, Hitachi SU-70, Japan) after 14 days of incubation with the cell culture. Before SEM/EDX analysis, samples were carefully rinsed thrice with 100 μL of PBS and then fixed with 50 μL of 4% paraformaldehyde (20 min, room temperature). Next, the samples were dehydrated with the graded series of ethanol: 30%, 50%, 75%, and 96% and then freeze-dried (–52 °C, 0.1 mBar, 24 h). Prepared samples were sputter-coated with gold and observed at an accelerating voltage of 5 kV.

2.4.2. Test on extracts

For the test, cells were seeded in the 96-well plate at 5000 cells/well. After 24 h of incubation (33.5 °C, 5% CO₂), the culture medium was replaced with bioglasses extracts or fresh medium (control) and incubated under the cell culture conditions. During the incubation, the morphological traits of the cells in each well were examined with an inverted microscope (Olympus, Japan). After 1, 3, 7, and 14 days of incubation, WST-1 assay was performed according to the manufacturer’s protocol. In brief, the culture medium was removed from the wells, and 100 μL of fresh medium was added to each well and incubated for 1 h (33.5 °C, 5% CO₂). Then 10 μL of tetrazolium salt, WST-1 reagent, was added to each well and incubated for another 3 h (33.5 °C, 5% CO₂). Subsequently, 100 μL from each well was transferred to the new sterile plate, and the absorbance was measured with a microplate reader (Synergy H1 microplate reader, BioTek, Winooski) at 450 nm (the reference wavelength was 630 nm). Additionally, to verify if the observed effects were caused by the osteogenic ions released from BG_p, the reference solutions of cell culture medium containing calcium and silicate ions at concentrations corresponding to the ones measured in BG_e were obtained. Ca reference solution (Ca_{ref}) at a concentration of 5.4 mM was prepared by dissolving calcium chloride dihydrate, the calcium precursor used during bioglass synthesis, in the cell culture medium. Si reference solution (Si_{ref}) was prepared by extracting silicates from 100% SiO₂ bioglass (Si_p) using 100 mg of powder per 1 mL of cell culture medium, determining the silicates concentration using colorimetric assays (Spectroquant®, Supelco, Merck, Germany), and further diluting it to 1.4 mM. Due to the decrease in phosphate concentrations after BG_p extraction, the P reference solution was not examined.

2.5. Osteoblast differentiation and mineralization

Since the results of the WST-1 assay obtained for BG45S_e confirmed the negative impact on osteoblasts viability (shown in Fig. 2C), this material was excluded from subsequent evaluation. Thus, further analyses of osteoblast differentiation (gene expression, alkaline phosphatase (ALP) enzymatic activity, and immunofluorescence staining) and mineralization (extracellular calcium deposit and intracellular calcium assays) were conducted for BG_e and BG85S_e samples.

2.5.1. Real-time polymerase chain reaction (RT-PCR)

For the assay, human fetal osteoblasts were seeded into a 24-well

plate at a density of 50,000 cells/well and incubated for cell adhesion for 24 h (33.5 °C, 5% CO₂). Thereafter, the culture medium was replaced with BG_e, BG85S_e, or fresh culture medium (control) and incubated at 39.5 °C and 5% CO₂ for 1, 3, and 7 days (for the analysis of differentiation at early stages) and for 7 and 14 days (for the analysis of differentiation at late stages). After each incubation interval, the conditioned extracts or the medium (control) were discarded, and total RNA was isolated with PureLink™ RNA Mini Kit (ThermoFisher Scientific, USA) according to the manufacturer's protocol. To analyze the osteoblast differentiation on the level of mRNA expression, the following target genes were selected: Runt-related transcription factor 2 (*RUNX2*), collagen type 1 alpha 1 (*COL1A1*), alkaline phosphatase (*ALPL*) (Weng and Su, 2013), secreted phosphoprotein 1, also called osteopontin (*OPN*), and bone gamma-carboxyglutamate protein, also called osteocalcin (*OCN*) (Rutkovskiy et al., 2016). Reverse transcription was performed with LunaScript RT SuperMix Kit (Cat. No. E3010, New England Biolabs, USA) with Eppendorf Mastercycler (Hamburg, Germany). For gene expression analysis, the Luna Universal Probe qPCR Master Mix (Cat. No. M3004, New England Biolabs, USA), and the following TaqMan probes: Hs01587814_g1, Hs00959010_m1, Hs01047973_m1, Hs00164004_m1, Hs01029144_m1 (ThermoFisher Scientific, USA) were used. Reactions were performed in duplicates with an inter-run calibrator, a set of non-template controls, and controls for genomic DNA contamination. Real time-PCR was performed using CFX96 Touch Real-Time PCR Detection System (Bio-Rad, California, USA). The expression of each gene was normalized to the reference genes: β -actin and *GADPH* ($\Delta\Delta Cq$).

2.5.2. Determination of alkaline phosphatase (ALP) enzymatic activity

To determine the ALP enzymatic activity, human fetal osteoblasts were seeded into a 24-well plate at a density of 50,000 cells/well and incubated for cell adhesion for 24 h (33.5 °C, 5% CO₂). Thereafter, the culture medium was replaced with BG_e, BG85S_e, or fresh culture medium (control) and incubated for 1, 3, and 7 days at 39.5 °C and 5% CO₂. After each incubation interval, the conditioned extracts or the medium (control) were discarded and cells were lysed by incubation with ice-cold RIPA buffer (5 min, 4 °C). The lysates were quick-frozen and clarified using centrifugation at 5000 min⁻¹ for 10 min at 4 °C prior to use. Lysates (30 μ L) were carefully transferred to a 96-well plate, and 100 μ L of the substrate of alkaline phosphatase, p-nitrophenyl phosphate, was added to each well. The plate was incubated for 40 min (39.5 °C, 5% CO₂). To stop the reaction 100 μ L of 1 M NaOH was added, and the ALP activity was measured. The absorbance of alkaline phosphatase product, p-nitrophenol, was measured at 405 nm (the reference wavelength was 655 nm) with a microplate reader (Synergy H1 microplate reader, Bio-Tek, USA). The calibration curve for the p-nitrophenol as a standard was prepared. ALP enzymatic activity was normalized to total protein content determined using the DC protein assay (Bio-Rad, UK) with 5 μ L of each lysate and bovine serum albumin (BSA) as a standard. Alkaline phosphatase activity was expressed as nmol p-nitrophenol/mg of protein. The assay was performed thrice as independent experiments, each performed in triplicates.

2.5.3. Immunofluorescence staining

For immunofluorescence staining of late-stage extracellular matrix proteins, osteopontin (*OPN*) and osteocalcin (*OCN*), human fetal osteoblasts were seeded into an 8-well Lab-Tek Chamber Slide™ (Nunc, USA) at a density of 50,000 cells/well and incubated for cell adhesion for 24 h (33.5 °C, 5% CO₂). Thereafter, the culture medium was replaced with BG_e, BG85S_e, or fresh culture medium (control) and incubated for 7 and 14 days at 39.5 °C and 5% CO₂. After each incubation interval, the conditioned extracts or the medium (control) were discarded, cells were washed thrice with PBS, and fixed with 150 μ L of 4% paraformaldehyde (20 min, room temperature). Then, the cells were permeabilized with 0.1% TritonX-100 in PBS and blocked with 3% BSA and 3% filtered FBS in PBS overnight at 4 °C in a humidity chamber with primary antibodies:

mouse monoclonal anti-OPN (1:50, Cat. No. sc-365797, Santa Cruz Biotechnology, USA) and mouse monoclonal anti-OCN (1:50, Cat. No. sc-21742, Santa Cruz Biotechnology, USA). Thereafter, cells were rinsed thrice with PBS and incubated with DyLight™ 549-conjugated AffiniPure sheep anti-mouse (1:800, Cat. No. 111-485-003, Jackson Immuno Research, USA) at 37 °C for 1 h. Nuclei were counterstained with Duolink® In Situ Mounting Medium with DAPI (Sigma-Aldrich, USA). Before observation, cells were rinsed with PBS and images were recorded under an Axiovert 200 fluorescent microscope equipped with AxioCam MRm digital camera (Zeiss, Germany).

2.5.4. Extracellular calcium deposit

To verify the extracellular mineralization, human fetal osteoblasts were seeded into a 96-well plate at a density of 5000 cells/well and incubated for cell adhesion for 24 h (33.5 °C, 5% CO₂). Thereafter, the culture medium was replaced with BG_e, BG85S_e, or fresh culture medium (control) and incubated for 1, 3, 7, and 14 days at 39.5 °C and 5% CO₂. The presence of mineralized calcium nodules was visualized using Alizarin Red S reagent (Cat. No. TMS-008-C Sigma-Aldrich, USA) that reacts with calcium to form a red-colored chelate. Before staining, the cells were fixed with 4% paraformaldehyde (20 min, room temperature). Next, the cells were carefully washed twice with deionized water. We added 100 μ L Alizarin Red S reagent into each well and incubated the plate for 40 min at room temperature. Then, the reagent was discarded, and cells were washed thrice with deionized water. The images of mineralized calcium nodules were taken with an inverted light microscope (Olympus, Japan). To verify how the osteogenic ions present in extracts affect the deposition of calcium nodules by osteoblasts, the reference solutions of calcium ions and silicates were also tested for comparison.

2.5.5. Intracellular calcium assay

For the assay, human fetal osteoblasts were seeded into a 96-well plate at a density of 5000 cells/well and incubated for cell adhesion for 24 h (33.5 °C, 5% CO₂). Thereafter, the culture medium was replaced with BG_e, BG85S_e, or fresh culture medium (control) and incubated for 1, 3, 7, and 14 days at 39.5 °C and 5% CO₂. Intracellular calcium was determined with fluorescence-based assay Rhod-4 Calcium Assay Kit (Abcam, England). After crossing the cell membrane, Rhod-4 is transformed by cell esterase into the negatively charged fluorescent dye that stays inside the cell. The Rhod-4 fluorescence intensity increases proportionally with increasing intracellular calcium concentration. Thus, it can be used to monitor intracellular calcium fluctuations. After each incubation interval, the conditioned extracts or medium (control) were replaced with 100 μ L of HHBS (1X Hank's with 20 mM HEPES Buffer, pH 7.0). Then, 100 μ L of Rhod-4 dye-loading solution was added to each well and incubated for 30 min at 39.5 °C and 5% CO₂. The intracellular calcium flux was monitored by measuring fluorescence intensity (Ex/Em = 540/590 nm). The images were taken after replacing the cell culture medium with HHBS using Axiovert 200 fluorescent microscope equipped with AxioCam MRm digital camera (Zeiss, Germany).

2.5.6. Live-cell 3D-holotomographic microscopy and image analysis

For 3D holotomography, eGFP-transduced osteoblasts in the amount of 50,000 were seeded onto the low walls μ -Dish 35 mm (Ibidi®, Germany) and incubated for adhesion for 24 h (33.5 °C, 5% CO₂). Next, the culture medium was replaced with BG_e or fresh culture medium (control) and incubated for 7 days (39 °C, 5% CO₂). Then, the μ -Dish with cells treated with BG_e extract was transferred to the Nanolive-ibidi top-stage incubator (39 °C, 5% CO₂) and monitored for 24 h using 3D Cell Explorer. 3D holotomographic images and videos were acquired using a 3D Cell Explorer-Fluo microscope (Nanolive®, Switzerland) equipped with 60 \times magnification (λ = 520 nm, sample exposure 0.2 mW/mm², depth of field = 30 μ m) and a fluorescence unit (CoolLED pE-300ultra). Images were acquired every 30 min in both refractive index (RI) and fluorescence channel (FITC) and analyzed using Steve® software v.2.6

(Nanolive®, Switzerland).

2.6. Adsorption of DOX onto BG

2.6.1. Adsorption studies

The adsorption of doxycycline hyclate (DOX, A&A Biotechnology) onto BG samples was carried out using adsorption from a concentrated solution. Each 2 mL of 10 mg/mL DOX aqueous solution was poured into polypropylene tubes. Next, 100 mg of BG sample was added and the suspension was stirred for 24 h (50 rpm, room temperature), in the absence of light. Then, the suspension was centrifuged (9200 rpm, 5 min), the supernatant was collected, diluted, and the DOX concentration was analyzed using the UV–Vis spectrophotometer (Shimadzu UV-1800, Japan) at 347 nm. Analytical measurements were conducted following the requirements for quantitative analyses, calibrating the detector with standard aqueous solutions of DOX ($R^2 = 0.9999$). The adsorption efficiency (%Ads) together with the amount of drug adsorbed onto BG (m_{Ads}) and drug loading percentage (DL) were calculated using Eqs 1–3, respectively.

$$\%Ads = \left(\frac{C_0 - C_e}{C_0} \right) \cdot 100\% \quad (1)$$

$$m_{Ads} = (C_0 - C_e) \cdot V \quad (2)$$

$$DL = \left(\frac{m_{Ads}}{m_{Ads} + m_{BG}} \right) \cdot 100\% \quad (3)$$

where: C_0 and C_e (mg/mL) correspond to the initial and equilibrium concentration of DOX, respectively; V – the volume of DOX solution used (mL); m_{BG} – the mass of bioglass used.

The experiment was performed in three replicates and the results were expressed as mean \pm standard deviation. The obtained DOX-loaded BG samples (BG-DOX) were freeze-dried and stored in sealed amber glass tubes before further use.

2.6.2. FTIR and DSC analyses

In order to confirm the presence of drug adsorbed onto bioglass, the BG-DOX samples were analyzed using Fourier transform infrared spectroscopy (FTIR, Jasco 4700) and differential scanning calorimetry (DSC). In brief, 1 mg of sample was powdered with 100 mg of KBr, compressed into the tablet, and analyzed with FTIR in the range of 4000–400 cm^{-1} . The DSC experiments were carried out using the DSC 822e Mettler Toledo instrument in the temperature range of 25–300 °C (10 °C heating rate per min) under a nitrogen atmosphere (30 mL/min flow rate) with an approx. 5 mg samples placed in a 40 μL aluminum pan with a hole in the lid. For comparative purposes, the reference drug sample together with the pristine BG sample were analyzed in the same manner.

2.6.3. DOX release studies

The drug release was performed following the already reported procedure (Prokopowicz, 2010). Briefly, 56 mg of DOX-BG powders (equal to 1.2 mg of DOX) were suspended in 50 mL of purified water (Milipore) in a polypropylene flask placed in a planar shaking water bath (50 rpm, 37 °C) and kept out of the light. At various time intervals, the suspension was left for sedimentation at 4 °C and next, 1-mL aliquots of the solution were analyzed using the UV–Vis spectrophotometer to calculate the amount of drug released. The total volume of the release medium was replaced with a 25 mL of pre-thermostated purified water every 24 h during the test. After the test, the residual powders were analyzed using the FTIR and DSC methods to verify the presence of the drug in the material.

2.7. Statistical analysis

Data are expressed as mean \pm standard deviation of three

independent experiments. Comparative data were analyzed with the unpaired Student's t -test using the STATISTICA 13.3 software (Statsoft, Kraków, Poland). P values ≤ 0.05 were considered statistically significant.

3. Results and discussion

3.1. One-pot-derived bioglass particles presented similar shape and roughness to reference materials

BG_p was successfully synthesized via the rapid sol–gel method. The SEM-EDX micrographs of BG_p and commercially available bioglasses (BG85S_p and BG45S_p) are presented in Fig. 1.

All investigated samples were characterized by angular and irregularly-shaped particles of diverse sizes. The finest particles of BG85S_p differed from those of BG_p and BG45S_p by their increased tendency to form agglomerates. Based on the SEM images, all types of bioglasses revealed intrinsically rough surfaces characteristic of sol–gel-derived materials (Faure et al., 2015; Prokopowicz, 2009). The EDX profiles confirmed the expected content (wt.%) of compounds in synthesized BG_p (SiO₂: 83%, CaO: 10%, P₂O₅: 7%) and the declared content of compounds in commercially available bioglasses: BG85S_p (SiO₂: 86%, CaO: 6.5%, P₂O₅: 7.5%) and BG45S_p (SiO₂: 42.5%, CaO: 25%, Na₂O: 25%, P₂O₅: 7.5%).

3.2. Extract from one-pot-derived bioglass contained calcium ions at high concentration

The mean concentrations of calcium ions (Ca), phosphates (P), and silicates (Si), together with the pH and osmotic pressure of pristine cell culture medium and obtained bioglass extracts are presented in Table 1. The measured concentrations of Ca and P in pristine cell culture medium (1.1 ± 0.10 and 1.3 ± 0.06 mM, respectively) agreed with the literature (Schäck et al., 2013) and specifications provided by the supplier. Compared to the pristine cell culture medium, the Ca concentrations in the extracts of BG_e and BG85S_e were 5 times higher (5.40 ± 0.16 and 5.00 ± 0.09 mM, respectively) suggesting the rapid release of Ca ions from the bioglasses structure. Contrarily, the Ca concentrations for BG45S_e were notably lower (0.54 ± 0.05 mM) than that of the control, possibly due to the deposition of Ca ions onto the bioglass surface (Theodorou et al., 2011). The concentration of P ions in all obtained extracts was lower compared with the control (0.99 ± 0.08 mM (BG_e); 0.28 ± 0.02 mM (BG85S_e); and 0.45 ± 0.09 mM (BG45S_e)). The reduction of P content in the culture medium after immersion of bioglasses was likely due to the initial formation of the apatite layer onto the bioglass surfaces, a well-known phenomenon (Xynos et al., 2001). To preliminarily verify this hypothesis, a sample of each bioglass powder after the extraction procedure was analyzed using Fourier-transform infrared spectroscopy (FTIR, Jasco 4700, Japan). Compared to pristine materials, the spectra of BG_p and BG85S_p samples after their immersion in the cell culture medium revealed new bands at 566 and 601 cm^{-1} , attributed to phosphate groups of newly-formed apatite layer (Prokopowicz et al., 2014) (Supplementary Fig. S1). In the case of the BG45S_p sample, an increase in the intensity of ν_3 PO₄³⁻ vibrational mode was manifested by a sharp peak at 1040 cm^{-1} , confirming the formation of the apatite layer as well. No presence of Si ions was noticed in the pristine cell culture medium, whereas their detectable concentration was confirmed in all obtained extracts. Moreover, the Si concentration in BG45S_e was almost 4 times higher (5.30 ± 0.11 mM) than in BG_e and BG85S_e (~ 1.40 mM). The highest concentration of released Si ions caused drastic changes in the pH value of BG45S_e. Significant alkalization (pH = 10.14 ± 0.08) in the BG45S_e was observed; whereas no significant change of pH for BG_e (pH = 8.13 ± 0.06) and a slight pH increase for BG85S_e (pH = 8.61 ± 0.09) compared with the cell culture medium (pH = 8.10 ± 0.06) were observed. This phenomenon might be related to both the partial dissolution of silica and the rapid exchange of

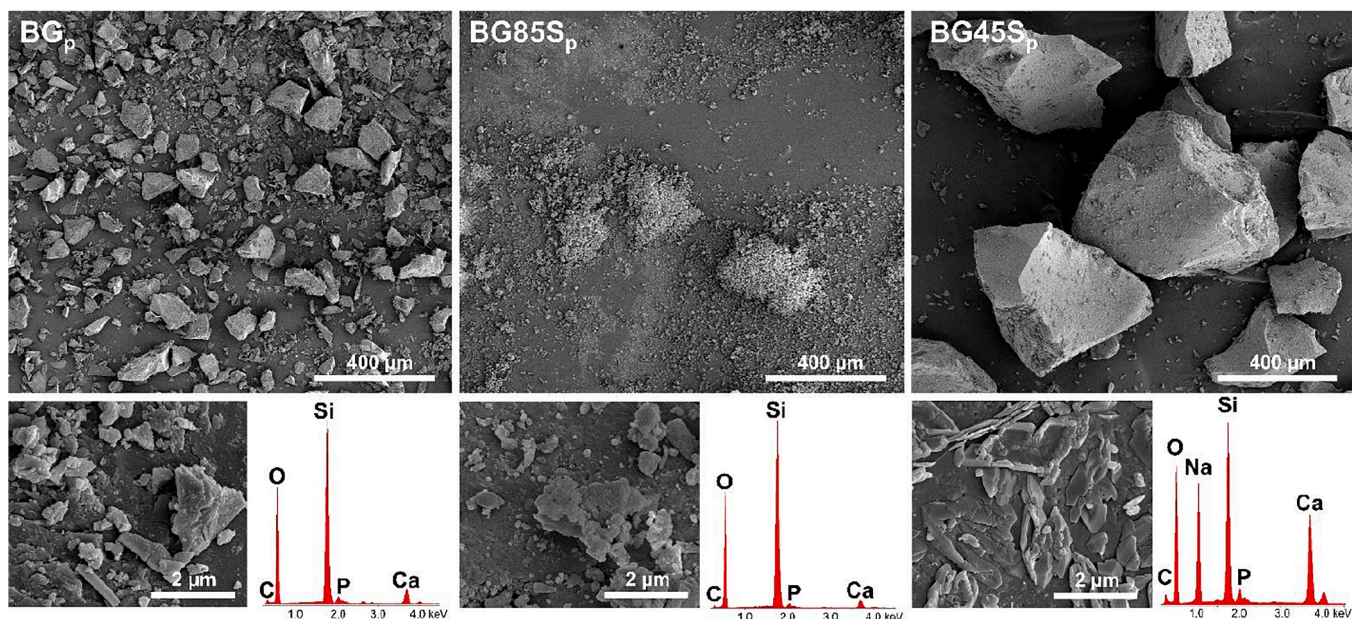


Fig. 1. Morphology and composition of bioglass particles. SEM images of BG_p, BG85S_p, and BG45S_p, together with EDX micrographs.

Table 1

Ionic composition, pH, and osmolality of extracts and cell culture medium.

	Cell culture medium	BG _e	BG85S _e	BG45S _e
Ca [mM]	1.1 ± 0.10	5.40 ± 0.16	5.00 ± 0.09	0.54 ± 0.05
P [mM]	1.3 ± 0.06	0.99 ± 0.08	0.28 ± 0.02	0.45 ± 0.09
Si [mM]	0	1.40 ± 0.09	1.40 ± 0.12	5.30 ± 0.11
pH	8.10 ± 0.06	8.13 ± 0.06	8.61 ± 0.09	10.14 ± 0.08
Osmotic pressure [mOsm/kg]	344 ± 12	348 ± 9	331 ± 8	368 ± 14

alkali-metal cations (e.g., Ca²⁺) with H⁺ from the solution (Yousefi et al., 2014). The release of silicon from the bioglasses after their immersion in physiological solutions was previously reported by Silver et al., who showed that the released silicates immediately form a silicic acid with simultaneous consumption of H⁺ from the solution causing its alkalization (Silver et al., 2001). Extracellular osmolality is an important factor that affects cell viability, metabolic activity, and gene expression (Finan and Guilak, 2010; Taieb et al., 2021). The osmolality of all extracts remained comparable to that of the cell culture medium (~350 mOsm/kg). Thus, no potential influence on osteoblast viability was considered.

3.3. Osteoblasts exhibited high viability in the presence of one-pot-derived bioglass

The effect of obtained bioglass on cell viability was evaluated by both direct-contact test and test on extracts according to the ISO 10993–5 and ISO 10993–12 Standards (Fig. 2). The cells incubated directly with BG_p and BG45S_p revealed the strongest adhesion to the materials over time (Fig. 2A). To further confirm this observation, the BG_p sample after 14 days of the direct-contact test was examined using SEM-EDX. Both SEM micrographs and EDX spectrum with the peak of carbon, nitrogen, and sodium confirmed the osteoblast adhesion to the surface of BG_p particles after 14-day incubation (Fig. 2B). The cellular adhesion to bioglasses was probably related to the chemotactic effect of released calcium or silicates (Supplementary Fig. S2). More importantly, considering *in vivo*

conditions, the bone remodeling process relies on the correct balance between bone formation by osteoblasts and resorption by osteoclasts (Olszta et al., 2007). Bone tissue dissolution produces a locally high concentration of calcium ions, inducing the osteoblast chemotaxis to the site of resorption (Aquino-Martínez et al., 2019; Chai et al., 2012). The calcium-dependent chemotactic effect was also demonstrated for other calcium-containing biomaterials (Aquino-Martínez et al., 2017). Moreover, Yan et al. proved that lower concentrations of silicates increase the membrane fluidity, stimulating cellular chemotaxis and differentiation (Yan et al., 2020). There was a modest chemotactic effect observed for BG85S_p on day 3; however, it disappeared during further incubation.

Surface morphology of implantable materials has a significant impact on osseointegration processes. Gough et al. presented the differences in osteoblast attachment and spreading on rough and smooth monolith of bioglass 45S5S. The osteoblasts attached to the rough surface presented three-dimensional morphology which promoted extracellular mineralization (Gough et al., 2004). According to Bigerelle et al., the material surface should be relatively flat at the material scale and rough at the cellular scale for effective cell adhesion (Bigerelle et al., 2002). Thus, the various cell adhesion to examined bioglasses may also result from considerable differences in morphology and specific surface area of BG85S_p, BG_p, and BG45S_p. The above-mentioned physical properties of bioglasses that may affect the cell adhesion should be investigated in detail in further research as the knowledge about this phenomenon has been evolving. Osteoblasts incubated without any material (control) expressed regular morphology and growth.

Cell viability in the presence of bioglass extracts was examined with WST-1 assay. It revealed a modest decrease in proliferation for cells incubated with BG_e. Surprisingly, the highest decrease was observed for BG45S_e (Fig. 2C). It may be caused by the rapid release of silicates into the medium resulting in their excess at 5.30 mM or alkaline pH (Table 1). Due to the biodegradability of bioglasses, their chemical composition significantly affects the osteogenic activity (Fernandes et al., 2018). The release of calcium ions plays a crucial role in osteoblast mineralization through inducing their chemotaxis and differentiation (An et al., 2012); whereas, silicon ions at suitable concentration may promote metabolic activity and proliferation (Zou et al., 2009). The bioglass compositions were previously examined in the terms of the impact of released ions and subsequent changes in local pH on osteoblast behavior. Valerio et al. observed the increase in osteoblast collagen

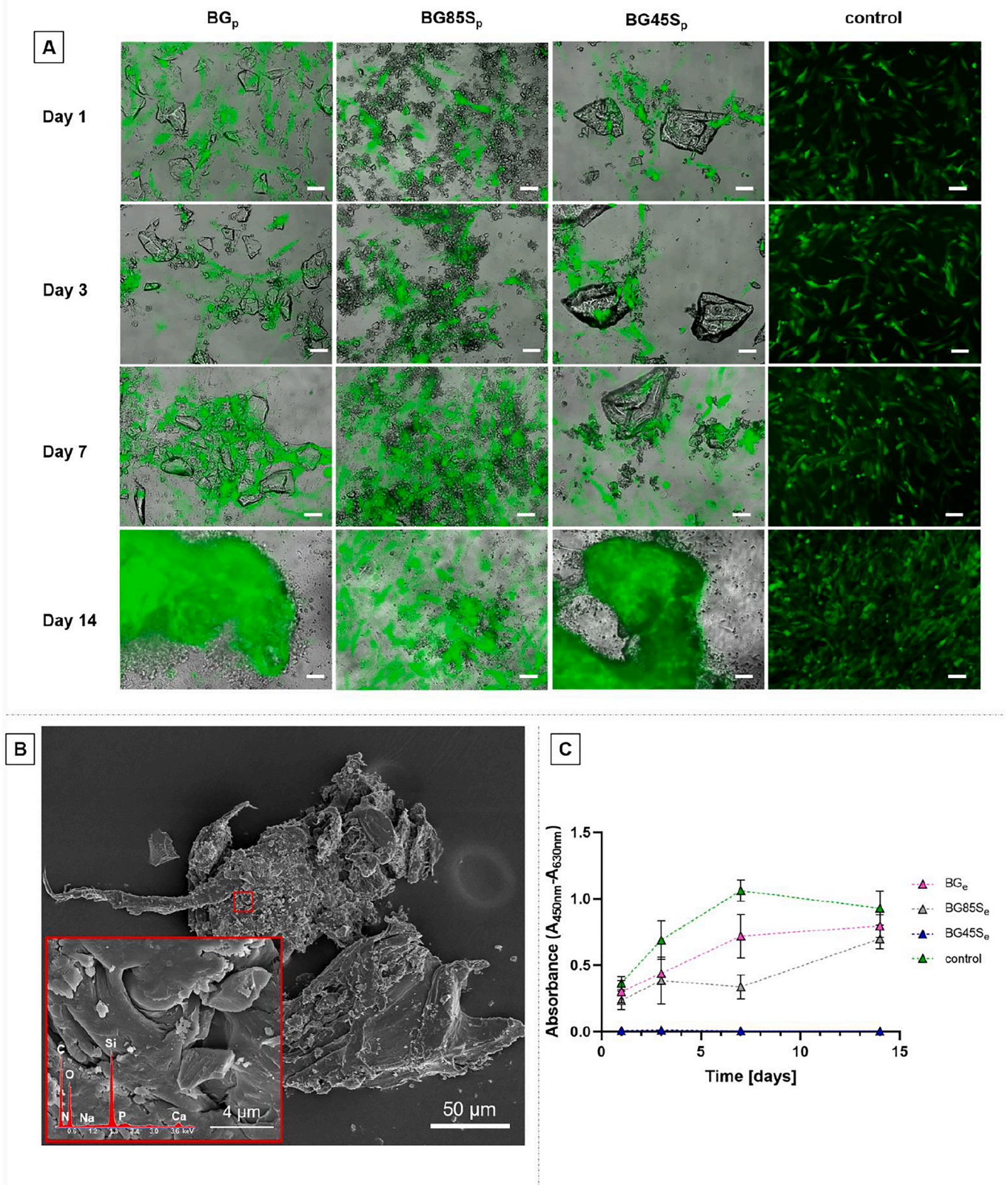


Fig. 2. Cell viability at the permissive temperature of 33.5 °C. Merged fluorescent and bright field images of eGFP osteoblasts incubated in direct contact with BG_p, BG85S_p, BG45S_p, or cell culture medium (control) for 1, 3, 7, and 14 days; scale bar = 100 μm (A); SEM-EDX micrographs of osteoblast attached to BG_p after 14 days of incubation (B); viability of osteoblasts incubated with BG_e, BG85S_e, BG45S_e, and cell culture medium (control) for 1, 3, 7, and 14 days measured with WST-1 assay (C).

production caused by the release of silicates from bioglass 60S that was followed by cell culture medium alkalinization (Valerio et al., 2004). Similar findings were made by Silver et al. who examined bioglasses 45S5, 58S, and 77S and noticed that the alterations of osteoblast were accompanied by rise in intracellular calcium ions concentration and pH (Silver et al., 2001). Importantly, there is no simple correlation between the content of particular elements in bioglass composition and release rate of its ions. In the case of sol-gel-derived bioglasses, the incorporation of alkaline earth ions (e.g. Na^+ , K^+ , Ca^{2+}) into the silica network results in the higher mobility of ions that promotes ion exchange and bioglass activity (Santos et al., 2018; Serra et al., 2002). Moreover, in the case of silicates, their release from bioglasses decreases with a decreasing amount of alkaline earth ions content. Silica-rich bioglasses (>60 wt%) are characterized by higher network connectivity and lower amount of non-bridging oxygens; thus, chemical stability of silica matrix is increased causing an impaired dissolution of silicates (Jones and Clare, 2012). This phenomenon was also observed in the present work, where the concentration of silicates in the cell culture medium after incubation with BG45S_e was 4 times higher compared with the cell culture medium after incubation with BG85S_p and proposed BG_p (Table 1). Since not only the composition of bioglass but also method of synthesis, structure, texture (surface area and porosity) may affect the release rate of ions (Lin et al., 2009), biological properties of each material should be examined experimentally.

Although the osteoblastic cell lines revealed increased activity at slightly elevated pH (up to 8.4), when the pH goes above 9.0, the cell metabolism radically declined (Galow et al., 2017). The high reduction in cell viability and a change in pH were not observed for BG_e. This indicates that alkalinization by the released silicon caused cytotoxicity. To verify the effect of the calcium and silicates on osteoblasts growth, the cell culture medium with concentrations relevant to ones

determined for BG_e was examined in the same way after 3 days of incubation (Supplementary Fig. S3). These results showed a significant reduction of cells proliferation for Ca at 5.4 mM and Si at 1.4 mM. Surprisingly, the cell culture medium containing either Ca or Si caused a higher reduction in osteoblast viability compared with BG_e. This observation might suggest that BG_e in which Ca and Si ions are combined acts as a more preferable environment for osteoblast proliferation compared with an enriched cell culture medium where these ions are administrated separately.

3.4. One-pot-derived bioglass induced osteoblasts differentiation in early stages

Since the previous results obtained for BG45S_e confirmed the negative impact on osteoblast activity (Fig. 2C), this material was excluded from further analyses. To evaluate the impact on the early stages of osteoblast differentiation of BG_e compared with BG85S_e and control, the expression of the following genes was assessed: runt-related transcription factor 2 (*RUNX2*), collagen type I alpha 1 (*COL1A1*), and alkaline phosphatase (*ALPL*). The obtained results were normalized using ($\Delta\Delta\text{Cq}$) the relative quantities of the reference genes (β -actin and GADPH). According to Stein et al., the early stages of osteoblast growth and differentiation might be described as follows. Osteoprogenitors predominantly express runt-related transcription factor 1 (*RUNX1*), involved in the progression of the cell cycle and proliferation. Subsequently, *RUNX2* suppresses growth and induces a transition from proliferation to the maturation stage as a 'master switch'. During maturation, *RUNX2* target genes, such as collagen type I alpha 1 (*COL1A1*) and alkaline phosphatase (*ALPL*) are expressed (Stein et al., 2004). In our study, the RT-PCR analysis revealed that *RUNX2* was significantly upregulated in osteoblasts incubated with BG_e on day 1 and

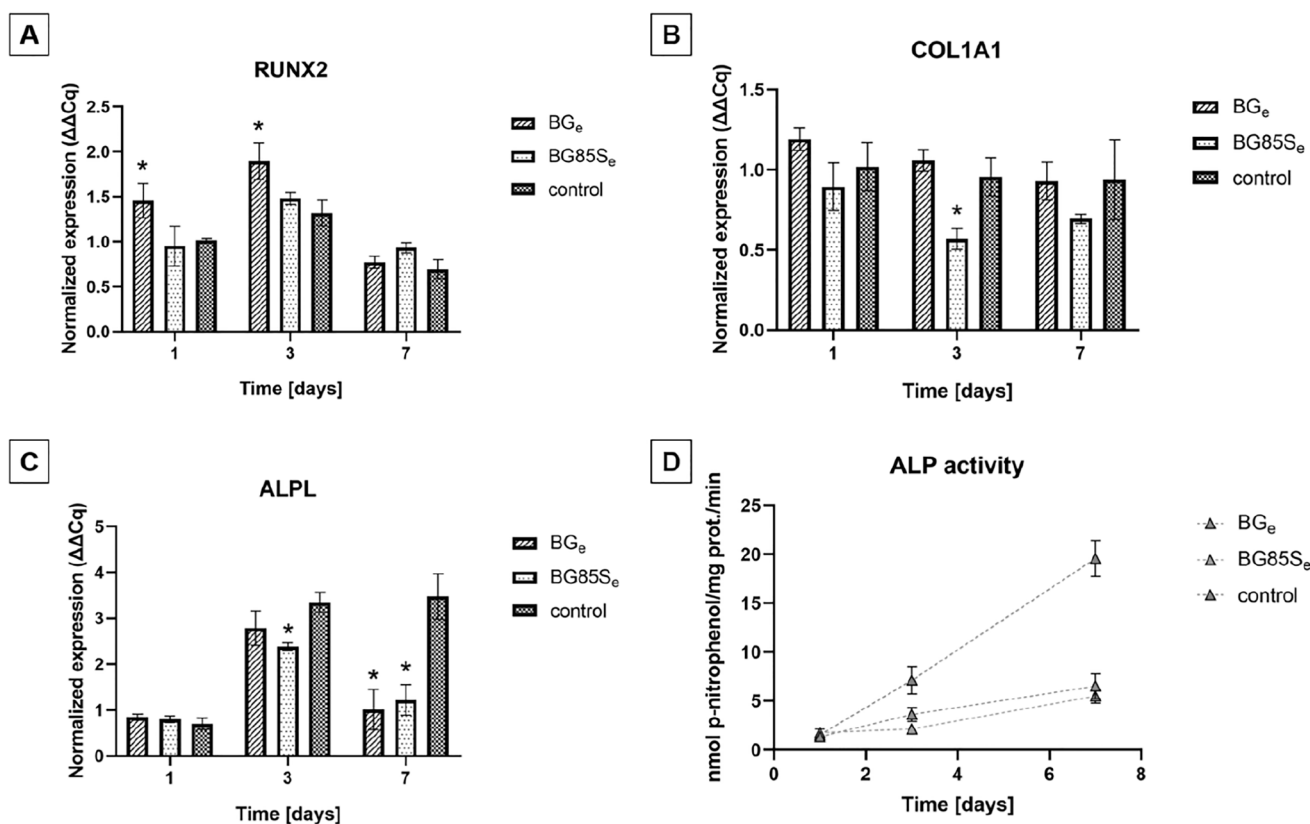


Fig. 3. Effect of bioglass extracts on early stages of osteoblast differentiation. Graphs of normalized expression of *RUNX2* (A), *COL1A1* (B), and *ALPL* (C) genes in osteoblasts determined after 1, 3, and 7 days of incubation with BG_e, BG85S_e, or cell culture medium (control). Graph of osteoblast ALP activity (D) measured after 1, 3, and 7 days of incubation with BG_e, BG85S_e, and cell culture medium (control). *Significant difference between analyzed sample and control ($p < 0.05$).

3 compared with the control (Fig. 3A). The subsequent decrease of *RUNX2* expression on day 7 indicated the progression to the maturation phase. There was no effect of BG_e on *COL1A1* expression; whereas, a statistically significant decrease was observed for $BG85S_e$ on day 3 (Fig. 3B). Similar gene expression profiles over time were previously reported (Setzer et al., 2009; Westhauser et al., 2020). Alkaline phosphatase produces phosphates from pyrophosphates, especially during the early stages of differentiation (Rutkovskiy et al., 2016). It reaches maximal mRNA expression and activity at the maturation phase. There was significant *ALPL* downregulation on day 7 for cells incubated with BG_e and $BG85S_e$; whereas, it kept increasing for the cells incubated with cell culture medium (control) up to day 7 (Fig. 3C). ALP activity assay (Fig. 3D) also demonstrated a slightly lower enzyme activity in cells incubated with BG_e and $BG85S_e$ compared with the control at day 3 that became significantly lower on day 7. The negative effect of bioglass extracts on ALP expression and activity was previously noted and attributed to the high concentration of calcium (Matsuoka et al., 2013; Ojansivu et al., 2018; Takagishi et al., 2006). Besides, An et al. observed the highest decrease of ALP activity (coded by *ALPL*) for Ca^{2+} concentration of 5.4 mM (An et al., 2012). Nonetheless, the extensive calcium

deposition accompanying high Ca^{2+} concentration was also observed (Fig. 5). This is because ALP acts exactly at the site of mineralization. Thus, once calcification starts, the enzyme active site adsorbs or/and is occluded by the newly deposited minerals resulting in loss of ALP activity (Genge et al., 1988). It explains why the highest decrease of alkaline phosphatase expression and activity is observed on day 7 – the time of the calcium nodules occurrence (Subsection 3.5.). Since the ALP activity is inversely correlated to mineralization, the decrease in *ALPL* expression and activity may indicate the high osteogenic potential leading to new bone formation. Therefore, increased *ALPL* expression and ALP activity cannot always be recognized as positive osteogenic markers. Moreover, a rapid and steep decrease in ALP activity may reflect swift and substantial mineralization. According to the obtained results, the osteogenic activity should not be judged based on this parameter alone but always in relation to the time of calcium nodules formation.

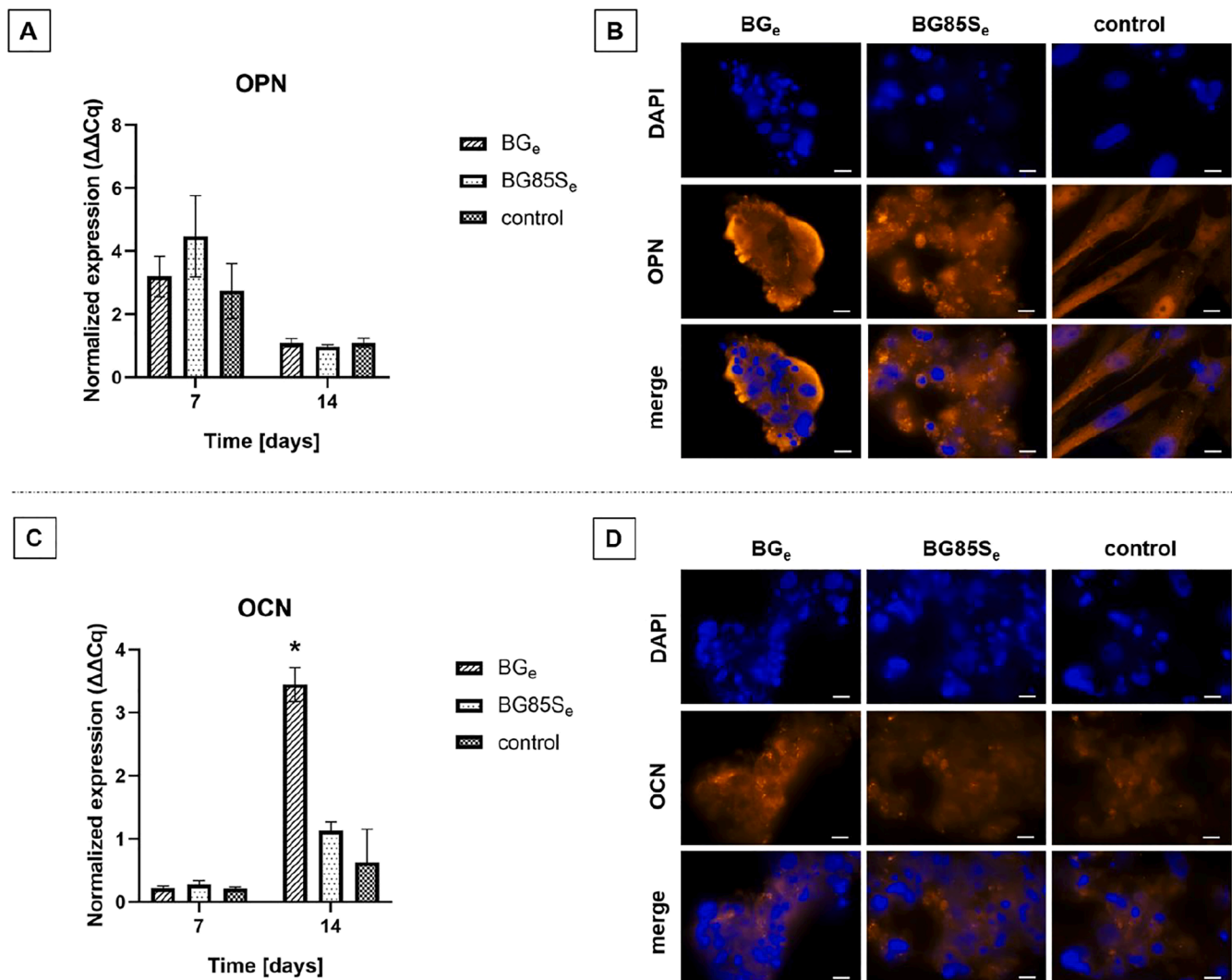


Fig. 4. Effect of bioglass extracts on late stages of osteoblast differentiation. Graphs of normalized expression of *OPN* gene in osteoblasts after 7 and 14 days of incubation with BG_e , $BG85S_e$, or cell culture medium (control) (A), together with the images of immunofluorescence staining with anti-osteopontin antibody (orange) and DAPI staining of nuclei (blue) at day 7 (B). Graphs of normalized expression of *OCN* gene in osteoblasts after 7 and 14 days of incubation with BG_e , $BG85S_e$, or cell culture medium (control) (C), together with the images of immunofluorescence staining with anti-osteocalcin antibody (orange) and DAPI staining of nuclei (blue) at day 14 (D). *Significant difference between analyzed sample and control ($p < 0.05$). Scale bar = 50 μm . (For interpretation of the references to colour in this figure legend, the reader is referred to the web version of this article.)

3.5. One-pot-derived bioglass promoted osteoblast differentiation in late stages

The late stages of osteoblast differentiation involve the transition of mature osteoblasts to osteocytes. During this phase, cells secrete extracellular matrix proteins, amongst which osteopontin (OPN) and osteocalcin (OCN) are the most abundant and used as markers of late-term osteoblast differentiation (Huang et al., 2007). OCN, also called the calcium-binding protein, can tightly bind synthesized hydroxyapatite and form a complex with collagen through OPN (Zoch et al., 2016). Therefore, OCN-OPN complexes play a crucial role in the nucleation of hydroxyapatite and bind the mineral and organic phase (osteoid) (Nikel et al., 2013). The results of RT-PCR analysis and immunofluorescence staining of OPN and OCN after 7-day and 14-day incubations are shown in Fig. 4.

There were no significant differences in OPN mRNA expression between the cells incubated with the studied extracts and cell culture medium (Fig. 4A). Contrarily, OCN was significantly upregulated in osteoblasts incubated with BG_e after two weeks (Fig. 4C). During the normal osteoblast differentiation, OPN appears before OCN (Banijamali et al., 2020). Thus, the obtained results confirmed the appropriate order

of osteogenic markers occurrence. Moreover, the OCN upregulation occurred simultaneously with calcium nodules deposition (Fig. 5A). Immunofluorescence staining results showed OPN and OCN with DAPI nuclear counterstain after 7 and 14 days of incubation (Fig. 4B, D). The images were correlated to mRNA expression results, confirming the extracellular matrix proteins synthesis by differentiated osteoblasts.

3.6. One-pot-derived bioglass increased extracellular matrix mineralization

To this day, little is known about the process of osteoblasts-mediated bone apatite formation. For years, various hypothetical mechanisms of mineral phase formation have been proposed; from those independent of cellular activity processes (Glimcher, 1984) to highly cell-controlled ones (Boonrungsiman et al., 2012). Mahamid et al. observed using cryo-SEM that the osteoblasts concentrate ions intracellularly in the form of granules (Mahamid et al., 2011). Similarly, Boonrungsiman et al. hypothesized that bone mineral formation starts from the intracellular storage of amorphous calcium phosphate by the mitochondria (Boonrungsiman et al., 2012). Thereafter, calcium salts are transferred to vesicles that are transported through the cellular membrane to the

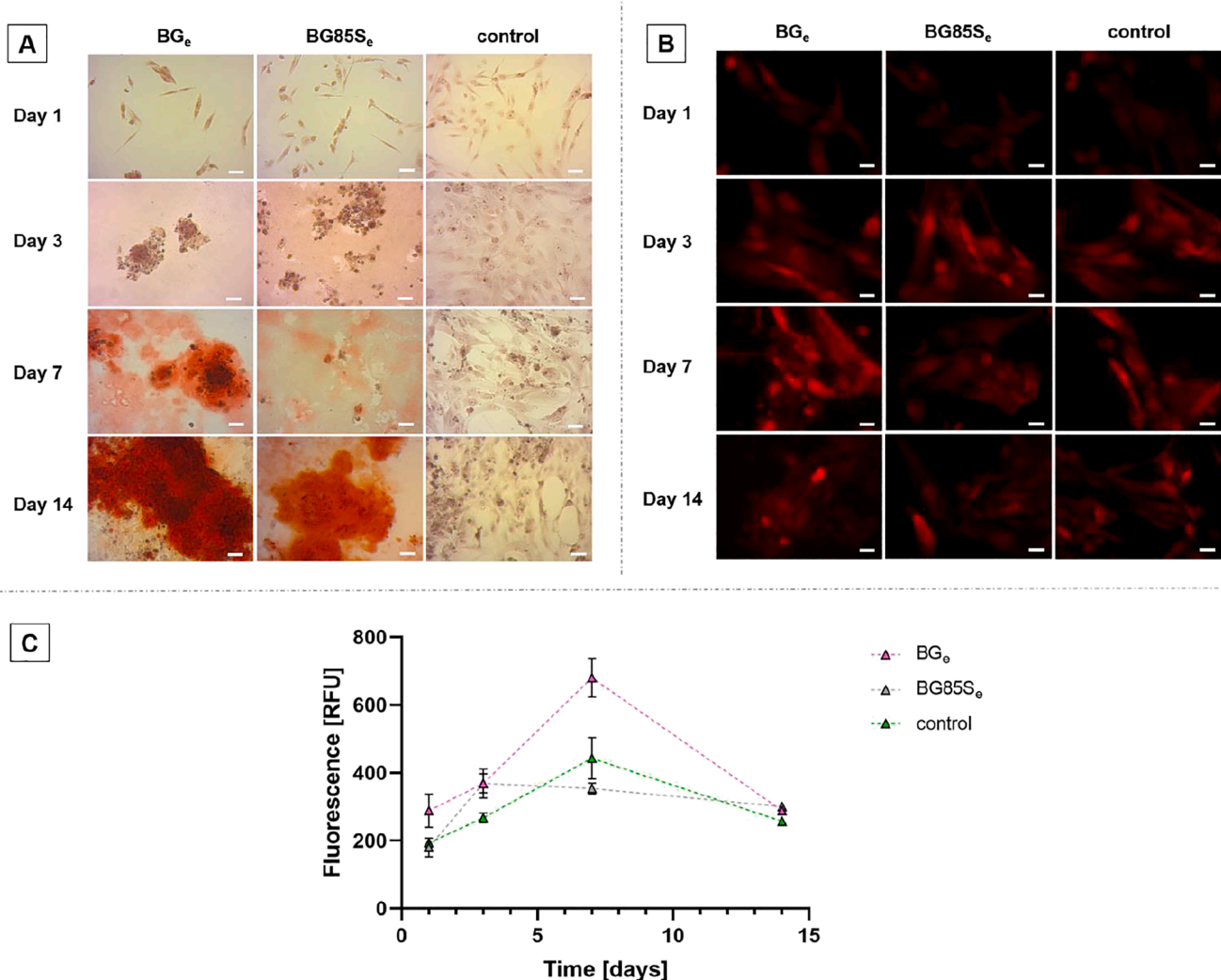


Fig. 5. Effect of bioglass extracts on osteoblast mineralization. Images of calcium nodules extracellularly deposited by osteoblasts incubated with BG_e, BG85S_e, and cell culture medium (control) for 1, 3, 7, and 14 days; scale bar = 100 μm (A). Images of intracellular calcium stained with Rhod-4 in osteoblasts incubated with BG_e, BG85S_e, or cell culture medium (control) for 1, 3, 7, and 14 days; scale bar = 50 μm (B). Graph of fluorescence intensity of Rhod-4-stained osteoblasts incubated with BG_e, BG85S_e, and cell culture medium (control) for 1, 3, 7, and 14 days (C).

extracellular matrix to be deposited on collagen fibrils, which then convert to a more crystalline structure, and initiate further deposition of minerals (Silver et al., 2001). Therefore, we decided to evaluate the effect of the extracts on the mineralization phase in two ways: calcium nodule staining and intracellular calcium fluctuations. Fig. 5 shows the images of osteoblasts stained with Alizarin Red S taken with an inverted light microscope after 1, 3, 7, and 14 days of incubation with BG_e, BG85S_e, or cell culture medium (control) (Fig. 5A), and the images of intracellular calcium stained with Rhod-4 (Fig. 5B), together with their quantitative analysis (Fig. 5C). The calcium nodules were visualized as bright red areas. For the cells exposed to BG_e, extracellular calcium nodules were detected after 7 days of incubation (39.5 °C) and the deposition increased over time (Fig. 5A). The areas of stained calcified nodules were substantially smaller after 7 days of incubation with BG85S_e than those exposed to BG_e. This was consistent with the almost 2-fold lower fluorescence of intracellular calcium in osteoblasts exposed to BG85S_e compared with those exposed to BG_e (Fig. 5B).

3.7. 3D live-cell holotomography of osteoblast calcium nodules deposition in the presence of one-pot-derived bioglass

3D live-cell holotomography and RI-based digital staining images, together with z-stacks after a 7-day incubation with BG_e and cell culture medium (control) are presented in Fig. 6. The cells incubated with BG_e displayed the morphological alteration during 24-hour recording in a Nanolive-ibidi top-stage incubator. The recording is available in [Supplementary Materials \(Supplementary video 2\)](#). The change of osteoblast shape from the spindle-like to cuboidal (Fig. 6A, D) is a known marker of osteogenic differentiation (Neve et al., 2011). Moreover, the high refractive index registered in the digital-stained images and z-stacks for the cells incubated with BG_e indicates a higher density in these areas that may be attributed to extracellular calcium phosphate deposition (Fig. 6B, C). Furthermore, the increase in the number and size of bright spots located around the cell attributed to calcium phosphates is strong evidence that bone tissue formation is highly dependent on osteoblast activity. Notably, similar effects were not observed for the control. These observations confirm the results of the extracellular mineralization assay.

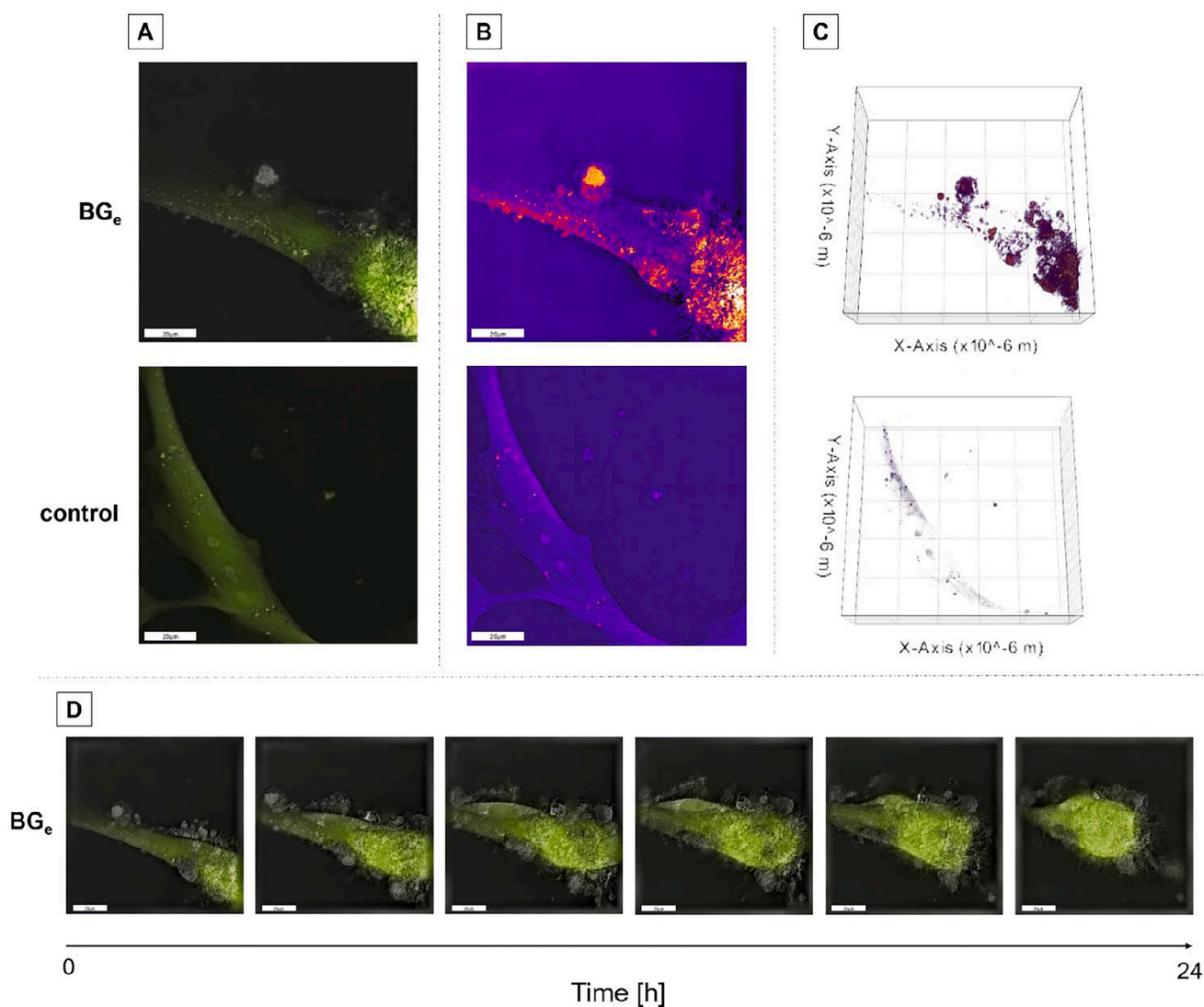


Fig. 6. Live-cell imaging of mineralized osteoblasts incubated with the extract from one-pot-derived bioglass. 3D holotomography images of osteoblasts after 7 days of incubation with BG_e and cell culture medium (control) (A). Digital staining (B), together with z-stacks based on the refractive index of osteoblasts after 7 days of incubation with BG_e or cell culture medium (control) (C). Time-lapse images of osteoblasts incubated with BG_e from day 7 to 8 (D). Scale bar = 20 μm.

3.8. One-pot-derived bioglass presented biphasic and prolonged release profile of doxycycline

The adsorption efficiency (%Ads) of DOX onto BG was $10.19 \pm 0.16\%$ which corresponded to 2.22 ± 0.04 mg of DOX adsorbed per each 100 mg of bioglass (equal to $2.17 \pm 0.03\%$ drug loading). Similar results were reported by Soriano-Souza et al. who observed 2% doxycycline loading onto hydroxyapatite-based microspheres as a consequence of doxycycline affinity to calcium ions that is a well-known phenomenon (Soriano-Souza et al., 2020). Despite the common use of drug adsorption from concentrated solution, this method of adsorption is characterized by several limitations such as the presence of residual solvents (both water and organic) and potential interactions between solvent and adsorbate that reduce the drug loading efficiency (Van Speybroeck et al., 2011). Thus, novel methods of adsorption might be considered in terms of obtaining drug-loaded delivery systems to bone tissue (i.e. incipient wetness impregnation (Cerruti et al., 2003) or spray-drying (Shen et al., 2011)). A promising technique for increasing adsorption efficiency is the impregnation of drugs by using supercritical CO₂ due to its increased diffusibility and high dissolving capacity (Wang et al., 2013). For example, the potential application of the above-mentioned method was proposed by Oparin et al. who obtained carbamazepine-loaded poly (methyl methacrylate – a widely used bone cement material (Oparin et al., 2021)). In the case of DOX, Rui et al. proposed DOX-loaded sodium

alginate and sodium hyaluronate-based hydrogels as wound dressings in which the drug was also impregnated using supercritical CO₂ method. Interestingly, after 3 h of impregnation using supercritical CO₂ a drug-loading equal to 1.4% was achieved and considered as sufficient to provide the antimicrobial activity of final hydrogel. Thus, in further studies on the drug-loading capacity of our proposed BG, the impregnation method using supercritical CO₂ will be implemented to compare it in the terms of adsorption efficiency with DOX adsorption from concentrated solution method.

The presence of DOX adsorbed onto the BG sample was also confirmed using FTIR and DSC analyses (Fig. 7A, B). In the case of FTIR, the bands characteristic for the drug in BG-DOX samples were observed at 3500–3300; 2900; 1620; 1505; 1460 cm⁻¹ which corresponded to N–H and O–H stretching; C–H stretching; C=O stretching, N–H bending; and C–H bending vibrations, respectively (Junejo and Safdar, 2019; Szweczyk et al., 2021). The DSC analysis of the DOX reference sample revealed an endothermic peak at 171 °C followed by an exothermic peak at 226 °C characteristic for melting point and thermal decomposition of the drug, respectively (de Freitas et al., 2022; Szweczyk et al., 2021). In the case of the BG-DOX sample, the endothermic peak was shifted towards a higher temperature (from 170 to 192 °C) and the sharp exothermic peak at 226 °C was not present suggesting the possible interaction between DOX molecules and BG surface. De Cicco et al. also observed the same phenomenon in which the DOX loading into the

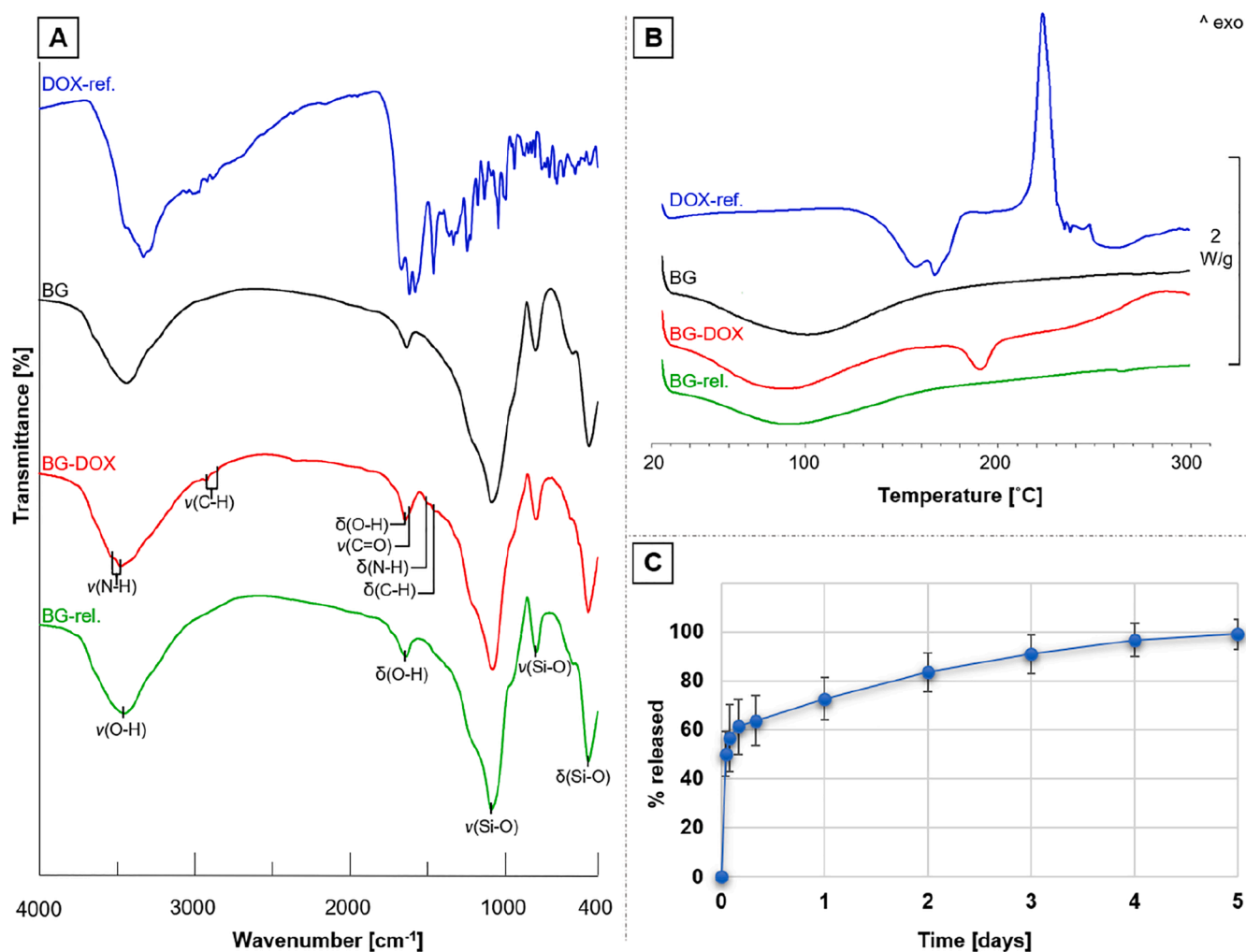


Fig. 7. Drug adsorption and release studies of one-pot-derived bioglass. FTIR spectra (A) and DSC thermographs (B) of the drug reference sample (DOX-ref., blue), pristine bioglass (BG, black), DOX-loaded bioglass (BG-DOX, red), and bioglass sample after drug release (BG-rel., green) together with DOX release profile (C) (ν – stretching vibrations, δ – bending vibrations). (For interpretation of the references to colour in this figure legend, the reader is referred to the web version of this article.)

calcium pectinate core-shell beads caused the shift of melting peak to a higher temperature as a consequence of complex formation between the drug and polymer matrix (De Cicco et al., 2016). The DOX release from BG is presented in Fig. 7C. The obtained drug release is characterized by a biphasic profile: a burst release stage, in which 70% of the drug adsorbed during released during the first 8 h, followed by a 5-day prolonged release stage. Moreover, the prolonged drug release followed the zero-order kinetics ($R^2 = 0.9464$, 6.6% of adsorbed dose released every 24 h (80 µg/day)) what suggested the controlled drug release via elution mechanism driven by diffusion (Prokopowicz, 2010). Such biphasic drug release was also observed and emphasized in the case of DOX-loaded: hydroxyapatite ceramics (Soriano-Souza et al., 2020), biphasic calcium phosphates-based ceramics (Victor and Kumar, 2008), and brushite cements (Tamimi et al., 2008) dedicated for the treatment of bone infections and periodontal diseases. After drug release studies, the samples of bioglass (BG-rel.) were analyzed using FTIR and DSC (Fig. 7A, B). No signals derived from DOX confirmed the complete drug release what is an additional desirable feature, especially when insufficient and incomplete drug release may cause the development of antibiotic resistant strains (Barth et al., 2011).

4. Conclusions

In this study, we analyzed the bifunctionality of bioactive glass synthesized via the rapid sol-gel method in terms of its osseointegration and drug delivery system for doxycycline. The results of *in vitro* assays on human fetal osteoblasts confirmed that our material complies with the fundamental requirements for implantable biomaterials, such as cytocompatibility, cell adhesion, and growth. Moreover, extracts of one-pot-derived bioglass better stimulated osteoblast differentiation and extracellular matrix mineralization than the reference materials. The drug adsorption and release studies revealed the satisfactory adsorption capacity and biphasic release profile of doxycycline. These promising results suggest the ability of the proposed bioglass to serve as osseointegrative local bone drug delivery system and allow for its further investigation. Additionally, this project presents not only a pathway for consistent evaluation of biomaterials according to ISO Standards 10993-5 and 10993-12 but also provides relevant details on human osteoblast differentiation. We noted a decrease in alkaline phosphatase activity during the extracellular mineralization. Frequently, ALP activity is measured as the only marker of osteogenic differentiation. According to our results, to receive reliable data on a materials osteoinductive properties, markers of early and late stages of osteoblasts differentiation should always be correlated to the final mineralization. Due to the extended mineralization analysis, we have also confirmed osteoblast involvement in mineralization and the possible interrelationship between the cellular calcium uptake and calcium nodules deposition.

CRedit authorship contribution statement

Skwira Adrianna: Writing – original draft, Methodology, Investigation, Data curation, Formal analysis, Validation, Software, Visualization. **Szewczyk Adrian:** Writing – review & editing, Methodology, Investigation, Validation, Software, Visualization. **Sądej Rafał:** Writing – review & editing, Methodology, Resources. **Prokopowicz Magdalena:** Writing – review & editing, Conceptualization, Supervision, Project administration, Methodology, Resources, Funding acquisition.

Declaration of Competing Interest

The authors declare that they have no known competing financial interests or personal relationships that could have appeared to influence the work reported in this paper.

Data availability

Data will be made available on request.

Acknowledgments

This work was supported by the National Science Centre Poland (project OPUS 15 no.2018/29/B/NZ7/00533 and partially supported by the project POWR.03.02.00-00-1035/16-00 co-financed by the European Union through the European Social Fund under the Operational Programme Knowledge Education Development 2014–2020.

Appendix A. Supplementary data

Supplementary data to this article can be found online at <https://doi.org/10.1016/j.ijpharm.2023.122610>.

References

- Albrektsson, T., Johansson, C., 2001. Osteoinduction, osteoconduction and osseointegration. *Eur. Spine J.* 10, 96–101. <https://doi.org/10.1007/s005860100282>.
- Amarnath Praphakar, R., Sumathra, M., Sam Ebenezer, R., Vignesh, S., Shakila, H., Rajan, M., 2019. Fabrication of bioactive rifampicin loaded κ-Car-MA-INH/Nano hydroxyapatite composite for tuberculosis osteomyelitis infected tissue regeneration. *Int. J. Pharm.* 565, 543–556. <https://doi.org/10.1016/j.ijpharm.2019.05.035>.
- An, S., Gao, Y., Ling, J., Wei, X., Xiao, Y., 2012. Calcium ions promote osteogenic differentiation and mineralization of human dental pulp cells: Implications for pulp capping materials. *J. Mater. Sci. Mater. Med.* 23, 789–795. <https://doi.org/10.1007/s10856-011-4531-0>.
- Aquino-Martínez, R., Angelo, A.P., Pujol, F.V., 2017. Calcium-containing scaffolds induce bone regeneration by regulating mesenchymal stem cell differentiation and migration. *Stem Cell Res. Ther.* 8, 1–10. <https://doi.org/10.1186/s13287-017-0713-0>.
- Aquino-Martínez, R., Monroe, D.G., Ventura, F., 2019. Calcium mimics the chemotactic effect of conditioned media and is an effective inducer of bone regeneration. *PLoS One* 14, 1–19. <https://doi.org/10.1371/journal.pone.0210301>.
- Banjamali, S., Heydari, M., Mozafari, M., 2020. Cellular response to bioactive glasses and glass-ceramics. In: *Handbook of Biomaterials Biocompatibility*. pp. 133–164. doi: 10.1016/B978-0-08-102967-1.00019-0.
- Barth, R.E., Vogely, H.C., Hoepelman, A.I.M., Peters, E.J.G., 2011. “To bead or not to bead?” Treatment of osteomyelitis and prosthetic joint-associated infections with gentamicin bead chains. *Int. J. Antimicrob. Agents* 38, 371–375. <https://doi.org/10.1016/j.ijantimicag.2011.03.008>.
- Bellucci, D., Salvatori, R., Anesi, A., Chiarini, L., Cannillo, V., 2019. SBF assays, direct and indirect cell culture tests to evaluate the biological performance of bioglasses and bioglass-based composites: three paradigmatic cases. *Mater. Sci. Eng. C* 96, 757–764. <https://doi.org/10.1016/j.msec.2018.12.006>.
- Bigerelle, M., Anselme, K., Noël, B., Ruderman, I., Hardouin, P., Iost, A., 2002. Improvement in the morphology of Ti-based surfaces: a new process to increase *in vitro* human osteoblast response. *Biomaterials* 23, 1563–1577. [https://doi.org/10.1016/S0142-9612\(01\)00271-X](https://doi.org/10.1016/S0142-9612(01)00271-X).
- Boonrungsiman, S., Gentleman, E., Carzaniga, R., Evans, N.D., McComb, D.W., Porter, A. E., Stevens, M.M., 2012. The role of intracellular calcium phosphate in osteoblast-mediated bone apatite formation. *Proc. Natl. Acad. Sci. U. S. A.* 109, 1–6. <https://doi.org/10.1073/pnas.1208916109>.
- Brauer, D.S., 2015. Bioactive glasses—Structure and properties. *Angew. Chemie - Int. Ed.* 54, 4160–4181. <https://doi.org/10.1002/anie.201405310>.
- Cerruti, M., Magnacca, G., Bolis, V., Morterra, C., 2003. Characterization of sol-gel bioglasses with the use of simple model systems: a surface-chemistry approach. *J. Mater. Chem.* 13, 1279–1286. <https://doi.org/10.1039/b300961k>.
- Chai, Y.C., Carlier, A., Bolander, J., Roberts, S.J., Geris, L., Schrooten, J., Van Oosterwyck, H., Luyten, F.P., 2012. Current views on calcium phosphate osteogenicity and the translation into effective bone regeneration strategies. *Acta Biomater.* 8, 3876–3887. <https://doi.org/10.1016/j.actbio.2012.07.002>.
- Coelho, C.C., Araújo, R., Quadros, P.A., Sousa, S.R., Monteiro, F.J., 2019. Antibacterial bone substitute of hydroxyapatite and magnesium oxide to prevent dental and orthopaedic infections. *Mater. Sci. Eng. C* 97, 529–538. <https://doi.org/10.1016/j.msec.2018.12.059>.
- Dang, T.H., Bui, T.H., Guseva, E.V., Ta, A.T., Nguyen, A.T., Hoang, T.T.H., Bui, X.V., 2020. Characterization of bioactive glass synthesized by sol-gel process in hot water. *Crystals* 10. <https://doi.org/10.3390/cryst10060529>.
- De Cicco, F., Russo, P., Reverchon, E., García-González, C.A., Aquino, R.P., Del Gaudio, P., 2016. Prilling and supercritical drying: a successful duo to produce core-shell polysaccharide aerogel beads for wound healing. *Carbohydr. Polym.* 147, 482–489. <https://doi.org/10.1016/j.carbpol.2016.04.031>.
- de Freitas, J., Ferreira, A.P.G., Cavalheiro, É.T.G., 2022. Investigating the thermal behavior of doxycycline and meclizine. *J. Therm. Anal.* 147, 13413–13423. <https://doi.org/10.1007/s10973-022-11596-x>.

- Ene, R., Nica, M., Ene, D., Cursaru, A., Cirstoiu, C., 2021. Review of calcium-sulphate-based ceramics and synthetic bone substitutes used for antibiotic delivery in PJI and osteomyelitis treatment. *EFORT Open Rev.* 6, 297–304. <https://doi.org/10.1302/2058-5241.6.200083>.
- Faure, J., Drevet, R., Lemelle, A., Ben Jaber, N., Tara, A., El Btaouri, H., Benhayoune, H., 2015. A new sol-gel synthesis of 45S5 bioactive glass using an organic acid as catalyst. *Mater. Sci. Eng. C* 47, 407–412. <https://doi.org/10.1016/j.msec.2014.11.045>.
- Fernandes, H.R., Gaddam, A., Rebelo, A., Brazete, D., Stan, G.E., Ferreira, J.M.F., 2018. Bioactive glasses and glass-ceramics for healthcare applications in bone regeneration and tissue engineering. *Materials (Basel)* 11, 1–54. <https://doi.org/10.3390/ma11122530>.
- Finan, J.D., Guilak, F., 2010. The effects of osmotic stress on the structure and function of the cell nucleus. *J. Cell. Biochem.* 109, 460–467. <https://doi.org/10.1002/jcb.22437>.
- Furlan, R.G., Correr, W.R., Russi, A.F.C., da Costa lemma, M.R., Trovatti, E., Pecoraro, E., 2018. Preparation and characterization of boron-based bioglass by sol–gel process. *J. Sol-Gel Sci. Technol.* 88, 181–191. <https://doi.org/10.1007/s10971-018-4806-8>.
- Galow, A.M., Rebl, A., Koczan, D., Bonk, S.M., Baumann, W., Gimsa, J., 2017. Increased osteoblast viability at alkaline pH in vitro provides a new perspective on bone regeneration. *Biochem. Biophys. Reports* 10, 17–25. <https://doi.org/10.1016/j.bbrep.2017.02.001>.
- Genge, B.R., Sauer, G.R., Wu, L.N.Y., McLean, F.M., Wuthier, R.E., 1988. Correlation between loss of alkaline phosphatase activity and accumulation of calcium during matrix vesicle-mediated mineralization. *J. Biol. Chem.* 263, 18513–18519. [https://doi.org/10.1016/s0021-9258\(19\)81388-1](https://doi.org/10.1016/s0021-9258(19)81388-1).
- Geuli, O., Metoki, N., Zada, T., Rechtes, M., Eliaz, N., Mandler, D., 2017. Synthesis, coating, and drug-release of hydroxyapatite nanoparticles loaded with antibiotics. *J. Mater. Chem. B* 5, 7819–7830. <https://doi.org/10.1039/c7tb02105d>.
- Glimcher, M.J., 1984. Recent studies of the mineral phase in bone and its possible linkage to the organic matrix by protein-bound phosphate bonds. *Philos. Trans. R. Soc. London Ser. B* 304, 479–508. <https://doi.org/10.1098/rstb.1984.0041>.
- Götz, W., Tobiasch, E., Witzleben, S., Schulze, M., 2019. Effects of silicon compounds on biomineralization, osteogenesis, and hard tissue formation. *Pharmaceutics* 11, 117. <https://doi.org/10.3390/pharmaceutics11030117>.
- Gough, J.E., Notingher, I., Hench, L.L., 2004. Osteoblast attachment and mineralized nodule formation on rough and smooth 45S5 bioactive glass monoliths. *J. Biomed. Mater. Res. - Part A* 68, 640–650. <https://doi.org/10.1002/jbm.a.20075>.
- Harris, S.A., Enger, R.J., Riggs, L.B., Spelsberg, T.C., 1995. Development and characterization of a conditionally immortalized human fetal osteoblastic cell line. *J. Bone Miner. Res.* 10, 178–186. <https://doi.org/10.1002/jbm.5650100203>.
- Hench, L.L., 2006. The story of Bioglass®. *J. Mater. Sci. Mater. Med.* 17, 967–978. <https://doi.org/10.1007/s10856-006-0432-z>.
- Hench, L.L., 1991. Bioceramics: from concept to clinic. *J. Am. Ceram. Soc.* 74, 1487–1510. <https://doi.org/10.1111/j.1151-2916.1991.tb07132.x>.
- Huang, W., Yang, S., Shao, J., Li, Y.P., 2007. Signaling and transcriptional regulation in osteoblast commitment and differentiation. *Front* 12, 3068–3092. <https://doi.org/10.2741/2296>.
- Hudecki, A., Kiryrczyński, G., Łos, M.J., 2018. Biomaterials, definition, overview. In: *Stem Cells and Biomaterials for Regenerative Medicine*. pp. 85–98. doi: 10.1016/B978-0-12-812258-7.00007-1.
- Inzana, J.A., Schwarz, E.M., Kates, S.L., Awad, H.A., 2016. Biomaterials approaches to treating implant-associated osteomyelitis. *Biomaterials* 81, 58–71. <https://doi.org/10.1016/j.biomaterials.2015.12.012>.
- Jones, J.R., Clare, A.G., 2012. Sol-Gel Derived Glasses for Medicine and Phosphate Glasses. In: *Bio-Glasses: An Introduction*. Wiley, pp. 29–64. <https://doi.org/10.1002/9781118346457>.
- Junejo, Y., Safdar, M., 2019. Highly effective heterogeneous doxycycline stabilized silver nanocatalyst for the degradation of ibuprofen and paracetamol drugs. *Arab. J. Chem.* 12, 2823–2832. <https://doi.org/10.1016/j.arabjoc.2015.06.014>.
- Lin, S., Ionescu, C., Pike, K.J., Smith, M.E., Jones, J.R., 2009. Nanostructure evolution and calcium distribution in sol-gel derived bioactive glass. *J. Mater. Chem.* 19, 1276–1282. <https://doi.org/10.1039/b814292k>.
- Mahamid, J., Sharir, A., Gur, D., Zelzer, E., Addadi, L., Weiner, S., 2011. Bone mineralization proceeds through intracellular calcium phosphate loaded vesicles: A cryo-electron microscopy study. *J. Struct. Biol.* 174, 527–535. <https://doi.org/10.1016/j.jsb.2011.03.014>.
- Matsuoka, F., Takeuchi, I., Agata, H., Kagami, H., Shiono, H., Kiyota, Y., Honda, H., Kato, R., 2013. Morphology-based prediction of osteogenic differentiation potential of human mesenchymal stem cells. *PLoS One* 8, e55082.
- Neve, A., Corrado, A., Cantatore, F.P., 2011. Osteoblast physiology in normal and pathological conditions. *Cell Tissue Res.* 343, 289–302. <https://doi.org/10.1007/s00441-010-1086-1>.
- Nikel, O., Laurencin, D., McCallum, S.A., Gundberg, C.M., Vashishth, D., 2013. NMR investigation of the role of osteocalcin and osteopontin at the organic-inorganic interface in bone. *Langmuir* 29, 13873–13882. <https://doi.org/10.1021/la403203w>.
- Ojansivu, M., Mishra, A., Vanhatupa, S., Juntunen, M., Larionova, A., Massera, J., Miettinen, S., 2018. The effect of S53P4-based borosilicate glasses and glass dissolution products on the osteogenic commitment of human adipose stem cells. *PLoS One* 13, 1–20. <https://doi.org/10.1371/journal.pone.0202740>.
- Olszta, M.J., Cheng, X., Jee, S.S., Kumar, R., Kim, Y.Y., Kaufman, M.J., Douglas, E.P., Gower, L.B., 2007. Bone structure and formation: a new perspective. *Mater. Sci. Eng. R Rep.* 58, 77–116. <https://doi.org/10.1016/j.mser.2007.05.001>.
- Oparin, R.D., Vaksler, Y.A., Krestyaninov, M.A., Idriissi, A., Kiselev, M.G., 2021. Possibility of dopant morphology control in the process of polymer impregnation with pharmaceuticals in a supercritical CO2 medium. *J. Mol. Liq.* 330, 115657. <https://doi.org/10.1016/j.molliq.2021.115657>.
- Pan, H., Zhao, X., Darvell, B.W., Lu, W.W., 2010. Apatite-formation ability - Predictor of “bioactivity”? *Acta Biomater.* 6, 4181–4188. <https://doi.org/10.1016/j.actbio.2010.05.013>.
- Prokopowicz, M., 2010. Synthesis and in vitro characterization of freeze-dried doxorubicin-loaded silica xerogels. *J. Sol-Gel Sci. Technol.* 53, 525–533. <https://doi.org/10.1007/s10971-009-2126-8>.
- Prokopowicz, M., 2009. Correlation between physicochemical properties of doxorubicin-loaded silica/polydimethylsiloxane xerogel and in vitro release of drug. *Acta Biomater.* 5, 193–207. <https://doi.org/10.1016/j.actbio.2008.07.027>.
- Prokopowicz, M., Szcwyczyk, A., Sawicki, W., 2014. The bioactivity studies of drug-loaded mesoporous silica- polydimethylsiloxane xerogels using FTIR and SEM/XEDS. *J. Mol. Struct.* 1056–1057, 262–266. <https://doi.org/10.1016/j.molstruc.2013.10.052>.
- Radwan, N.H., Nasr, M., Ishak, R.A.H., Awad, G.A.S., 2021. Moxifloxacin-loaded in situ synthesized Bioceramic/Poly(L-lactide-co-ε-caprolactone) composite scaffolds for treatment of osteomyelitis and orthopedic regeneration. *Int. J. Pharm.* 602, 120662. <https://doi.org/10.1016/j.ijpharm.2021.120662>.
- Rutkovskiy, A., Stenslokken, K.-O., Vaage, L.J., 2016. Osteoblast differentiation at a glance. *Med. Sci. Monit. Basic Res.* 2016, 95–106. doi: 10.12659/msmbr.901142.
- Santos, S.C., Lazaro, G.S., dos Santos, E.A., 2018. Ordering in sol-gel-derived bioactive glasses and its influence on the dissolution/precipitation behavior in a complex culture medium. *J. Non. Cryst. Solids* 494, 50–58. <https://doi.org/10.1016/j.jnoncrysol.2018.04.054>.
- Schäck, L.M., Noack, S., Winkler, R., Wißmann, G., Behrens, P., Wellmann, M., Jagodzinski, M., Krettek, C., Hoffmann, A., 2013. The phosphate source influences gene expression and quality of mineralization during in vitro osteogenic differentiation of human mesenchymal stem cells. *PLoS One* 8, 1–12. <https://doi.org/10.1371/journal.pone.0065943>.
- Schmitz, S.L., Widholz, B., Essers, C., Becker, M., Tulyaganov, D.U., Moghaddam, A., Gonzalo de Juan, I., Westhauser, F., 2020. Superior biocompatibility and comparable osteoinductive properties: Sodium-reduced fluoride-containing bioactive glass belonging to the CaO–MgO–SiO2 system as a promising alternative to 45S5 bioactive glass. *Bioact. Mater.* 5, 55–65. <https://doi.org/10.1016/j.bioactmat.2019.12.005>.
- Schneider, C.A., Rasband, W.S., Eliceiri, K.W., 2012. NIH Image to ImageJ: 25 years of image analysis. *Nat. Methods* 9, 671–675. <https://doi.org/10.1038/nmeth.2089>.
- Schumacher, M., Habibovic, P., van Rijt, S., 2021. Mesoporous bioactive glass composition effects on degradation and bioactivity. *Bioact. Mater.* 6, 1921–1931. <https://doi.org/10.1016/j.bioactmat.2020.12.007>.
- Sepulveda, P., Jones, J.R., Hench, L.L., 2001. Characterization of melt-derived 45S5 and sol-gel-derived 58S bioactive glasses. *J. Biomed. Mater. Res.* 58, 734–740. <https://doi.org/10.1002/jbm.10026>.
- Serra, J., González, P., Liste, S., Chiussi, S., León, B., Pérez-Amor, M., Ylänen, H.O., Hupa, M., 2002. Influence of the non-bridging oxygen groups on the bioactivity of silicate glasses. *J. Mater. Sci. Mater. Med.* 13, 1221–1225. <https://doi.org/10.1023/A:1021174912802>.
- Setzer, B., Bächle, M., Metzger, M.C., Kohal, R.J., 2009. The gene-expression and phenotypic response of hFOB 1.19 osteoblasts to surface-modified titanium and zirconia. *Biomaterials* 30, 979–990. <https://doi.org/10.1016/j.biomaterials.2008.10.054>.
- Shen, S.C., Ng, W.K., Chia, L., Hu, J., Tan, R.B.H., 2011. Physical state and dissolution of ibuprofen formulated by co-spray drying with mesoporous silica: Effect of pore and particle size. *Int. J. Pharm.* 410, 188–195. <https://doi.org/10.1016/j.ijpharm.2011.03.018>.
- Silver, I.A., Deas, J., Erećiška, M., 2001. Interactions of bioactive glasses with osteoblasts in vitro: effects of 45S5 Bioglass®, and 58S and 77S bioactive glasses on metabolism, intracellular ion concentrations and cell viability. *Biomaterials* 22, 175–185. [https://doi.org/10.1016/S0142-9612\(00\)00173-3](https://doi.org/10.1016/S0142-9612(00)00173-3).
- Soriano-Souza, C., Valiense, H., Mavropoulos, E., Martinez-Zelaya, V., Costa, A.M., Alves, A.T., Longuinho, M., Resende, R., Mourão, C., Granjeiro, J., Rocha-Leao, M. H., Rossi, A., Calasans-Maia, M., 2020. Doxycycline containing hydroxyapatite ceramic microspheres as a bone-targeting drug delivery system. *J. Biomed. Mater. Res. - Part B Appl. Biomater.* 108, 1351–1362. <https://doi.org/10.1002/jbm.b.34484>.
- Souza, L., Lopes, J.H., Encarnação, D., Mazali, I.O., Martin, R.A., Camilli, J.A., Bertran, C. A., 2018. Comprehensive in vitro and in vivo studies of novel melt-derived Nb-substituted 45S5 bioglass reveal its enhanced bioactive properties for bone healing. *Sci. Rep.* 8, 12808. <https://doi.org/10.1038/s41598-018-31114-0>.
- Spellberg, B., Lipsky, B.A., 2012. Systemic antibiotic therapy for chronic osteomyelitis in adults. *Clin. Infect. Dis.* 54, 393–407. <https://doi.org/10.1093/cid/cir842>.
- Stein, G.S., Lian, J.B., Van Wijnen, A.J., Stein, J.L., Montecino, M., Javed, A., Zaidi, S.K., Young, D.W., Choi, J.Y., Pockwinse, S.M., 2004. Runx2 control of organization, assembly and activity of the regulatory machinery for skeletal gene expression. *Oncogene* 23, 4315–4329. <https://doi.org/10.1038/sj.onc.1207676>.
- Subramaniam, M., Jalal, S.M., Rickard, D.J., Harris, S.A., Bolander, M.E., Spelsberg, T.C., 2002. Further characterization of human fetal osteoblastic hFOB 1.19 and hFOB/ERα cells: bone formation in vivo and karyotype analysis using multicolor fluorescent in situ hybridization. *J. Cell. Biochem.* 87, 9–15. <https://doi.org/10.1002/jcb.10259>.
- Szcwyczyk, A., Skwira, A., Konopacka, A., Sadej, R., Prokopowicz, M., 2021. Mesoporous silica-bioglass composite pellets as bone drug delivery system with mineralization potential. *Int. J. Mol. Sci.* 22, 4708. doi: 10.3390/ijms22094708.
- Tabia, Z., El Mabrouk, K., Briche, M., Nouneh, K., 2019. Mesoporous bioactive glass nanoparticles doped with magnesium: drug delivery and acellular. In vitro bioactivity. *RSC Adv.* 9, 12232–12246. <https://doi.org/10.1039/c9ra01133a>.

- Taieb, H.M., Garske, D.S., Contzen, J., Gossen, M., Bertinetti, L., Robinson, T., Cipitria, A., 2021. Osmotic pressure modulates single cell cycle dynamics inducing reversible growth arrest and reactivation of human metastatic cells. *Sci. Rep.* 11, 13455. <https://doi.org/10.1038/s41598-021-92054-w>.
- Takagishi, Y., Kawakami, T., Hara, Y., Shinkai, M., Takezawa, T., Nagamune, T., 2006. Bone-like tissue formation by three-dimensional culture of MG63 osteosarcoma cells in gelatin hydrogels using calcium-enriched medium. *Tissue Eng.* 12, 927–937. <https://doi.org/10.1089/ten.2006.12.927>.
- Tamimi, F., Torres, J., Bettini, R., Ruggera, F., Rueda, C., López-Ponce, M., Lopez-Cabarcos, E., 2008. Doxycycline sustained release from brushite cements for the treatment of periodontal diseases. *J. Biomed. Mater. Res. - Part A* 85, 707–714. <https://doi.org/10.1002/jbm.a.31610>.
- Theodorou, G., Goudouri, O.M., Kontonasaki, E., Chatzistavrou, X., Papadopoulou, L., Kantiranis, N., Paraskevopoulos, K.M., 2011. Comparative bioactivity study of 45S5 and 58S bioglasses in organic and inorganic environment. *Bioceram. Dev. Appl.* 1, 1–4. <https://doi.org/10.4303/bda/d110154>.
- Tsigkou, O., Jones, J.R., Polak, J.M., Stevens, M.M., 2009. Differentiation of fetal osteoblasts and formation of mineralized bone nodules by 45S5 Bioglass® conditioned medium in the absence of osteogenic supplements. *Biomaterials* 30, 3542–3559. <https://doi.org/10.1016/j.biomaterials.2009.03.019>.
- Vaidya, P., Mahale, S., Kale, S., Patil, A., 2017. Osseointegration- a review. *IOSR J. Dent. Med. Sci.* 16, 45–48. <https://doi.org/10.9790/0853-1601014548>.
- Valerio, P., Pereira, M.M., Goes, A.M., Leite, M.F., 2004. The effect of ionic products from bioactive glass dissolution on osteoblast proliferation and collagen production. *Biomaterials* 25, 2941–2948. <https://doi.org/10.1016/j.biomaterials.2003.09.086>.
- Vallet-Regi, M., Salinas, A.J., 2021. Mesoporous bioactive glasses for regenerative medicine. *Mater. Today Bio* 11, 100121. <https://doi.org/10.1016/j.mtbio.2021.100121>.
- Van Speybroeck, M., Mellaerts, R., Martens, J.A., Annaert, P., Van den Mooter, G., Augustijns, P., 2011. Ordered mesoporous silica for the delivery of poorly soluble drugs. In: *Controlled Release in Oral Drug Delivery*. pp. 203–219. doi: 10.1007/978-1-4614-1004-1_10.
- van Vugt, T.A.G., Arts, J.J., Geurts, J.A.P., 2019. Antibiotic-loaded polymethylmethacrylate beads and spacers in treatment of orthopedic infections and the role of biofilm formation. *Front. Microbiol.* 10, 1626. <https://doi.org/10.3389/fmicb.2019.01626>.
- Victor, S.P., Kumar, T.S.S., 2008. BCP ceramic microspheres as drug delivery carriers: Synthesis, characterisation and doxycycline release. *J. Mater. Sci. Mater. Med.* 19, 283–290. <https://doi.org/10.1007/s10856-006-0044-7>.
- Wang, L.H., Che, X., Xu, H., Zhou, L.L., Han, J., Zou, M.J., Liu, J., Liu, Y., Liu, J.W., Zhang, W., Cheng, G., 2013. A novel strategy to design sustained-release poorly water-soluble drug mesoporous silica microparticles based on supercritical fluid technique. *Int. J. Pharm.* 454, 135–142. <https://doi.org/10.1016/j.ijpharm.2013.07.027>.
- Wassif, R.K., Elkayal, M., Shamma, R.N., Elkheshen, S.A., 2021. Recent advances in the local antibiotics delivery systems for management of osteomyelitis. *Drug Deliv.* 28, 2392–2414. <https://doi.org/10.1080/10717544.2021.1998246>.
- Weng, J.J., Su, Y., 2013. Nuclear matrix-targeting of the osteogenic factor Runx2 is essential for its recognition and activation of the alkaline phosphatase gene. *Biochim. Biophys. Acta - Gen. Subj.* 1830, 2839–2852. <https://doi.org/10.1016/j.bbagen.2012.12.021>.
- Westhauser, F., Hohenbild, F., Arango-Ospina, M., Schmitz, S.I., Wilkesmann, S., Hupa, L., Moghaddam, A., Boccaccini, A.R., 2020. Bioactive glass (Bg) icie16 shows promising osteogenic properties compared to crystallized 45s5-bg. *Int. J. Mol. Sci.* 21, 1–12. <https://doi.org/10.3390/ijms21051639>.
- Wypych, G., 2018. 6 - Functional Fillers – Applications. In: *Functional Fillers: Chemical Composition, Morphology, Performance, Applications*. pp. 153–179.
- Xynos, I.D., Edgar, A.J., Buttery, L.D.K., Hench, L.L., Polak, J.M., 2001. Gene-expression profiling of human osteoblasts following treatment with the ionic products of Bioglass® 45S5 dissolution. *J. Biomed. Mater. Res.* 55, 151–157. [https://doi.org/10.1002/1097-4636\(200105\)55:2<151::AID-JBMT1001>3.0.CO;2-D](https://doi.org/10.1002/1097-4636(200105)55:2<151::AID-JBMT1001>3.0.CO;2-D).
- Xynos, I.D., Hukkanen, M.V.J., Batten, J.J., Buttery, L.D., Hench, L.L., Polak, J.M., 2000. Bioglass®45S5 stimulates osteoblast turnover and enhances bone formation in vitro: implications and applications for bone tissue engineering. *Calcif. Tissue Int.* 67, 321–329. <https://doi.org/10.1007/s002230001134>.
- Yan, L., Li, H., Xia, W., 2020. Bioglass could increase cell membrane fluidity with ion products to develop its bioactivity. *Cell Prolif.* 53, 1–16. <https://doi.org/10.1111/cpr.12906>.
- Yan, X., Huang, X., Yu, C., Deng, H., Wang, Y., Zhang, Z., Qiao, S., Lu, G., Zhao, D., 2006. The in-vitro bioactivity of mesoporous bioactive glasses. *Biomaterials* 27, 3396–3403. <https://doi.org/10.1016/j.biomaterials.2006.01.043>.
- Yen, M., Chien, C.-C., Chiu, I., Huang, H.-I., Chen, Y.-C., Hu, H.-I., Yen, B.L., 2007. Multilineage differentiation and characterization of the human fetal osteoblastic 1.19 cell line: a possible in vitro model of human mesenchymal progenitors. *Stem Cells* 25, 125–131. <https://doi.org/10.1634/stemcells.2006-0295>.
- Yousefi, A.M., Oudadesse, H., Akbarzadeh, R., Wers, E., Lucas-Girot, A., 2014. Physical and biological characteristics of nanohydroxyapatite and bioactive glasses used for bone tissue engineering. *Nanotechnol. Rev.* 3, 527–552. <https://doi.org/10.1515/ntrev-2014-0013>.
- Zoch, M.L., Clemens, T.L., Riddle, R.C., 2016. New insights into the biology of osteocalcin. *Bone* 82, 42–129. <https://doi.org/10.1016/j.bone.2015.05.046>.
- Zou, S., Ireland, D., Brooks, R.A., Rushton, N., Best, S., 2009. The effects of silicate ions on human osteoblast adhesion, proliferation, and differentiation. *J. Biomed. Mater. Res. - Part B Appl. Biomater.* 90 B, 123–130. <https://doi.org/10.1002/jbm.b.31262>.

Supplementary data

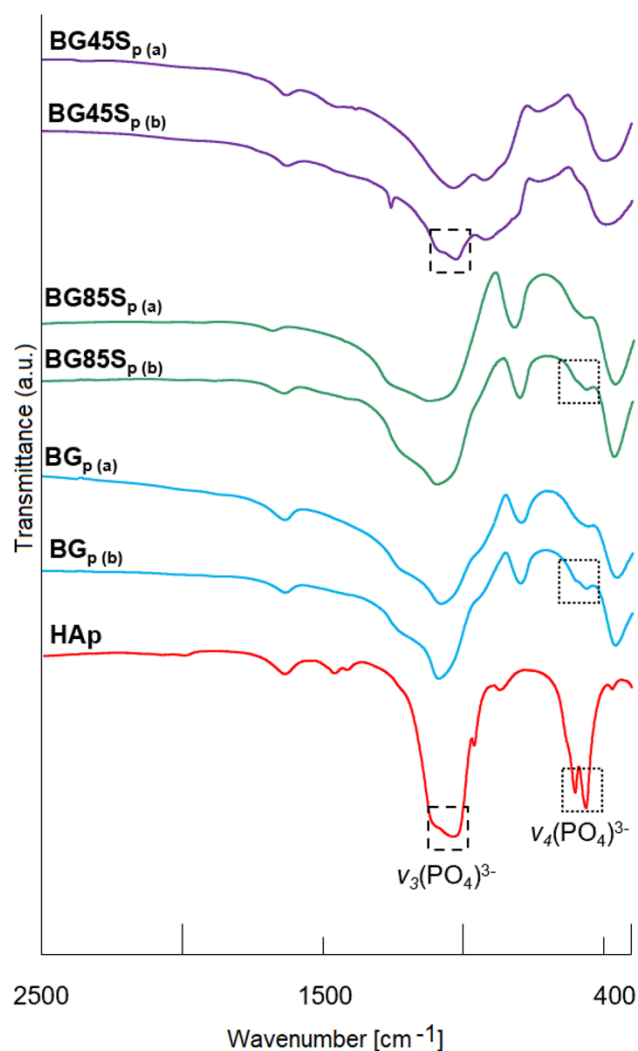
Bioglass obtained via one-pot synthesis as osseointegrative drug delivery system

Skwira Adrianna¹, Szewczyk Adrian¹, Sądej Rafał², Prokopowicz Magdalena^{1*}

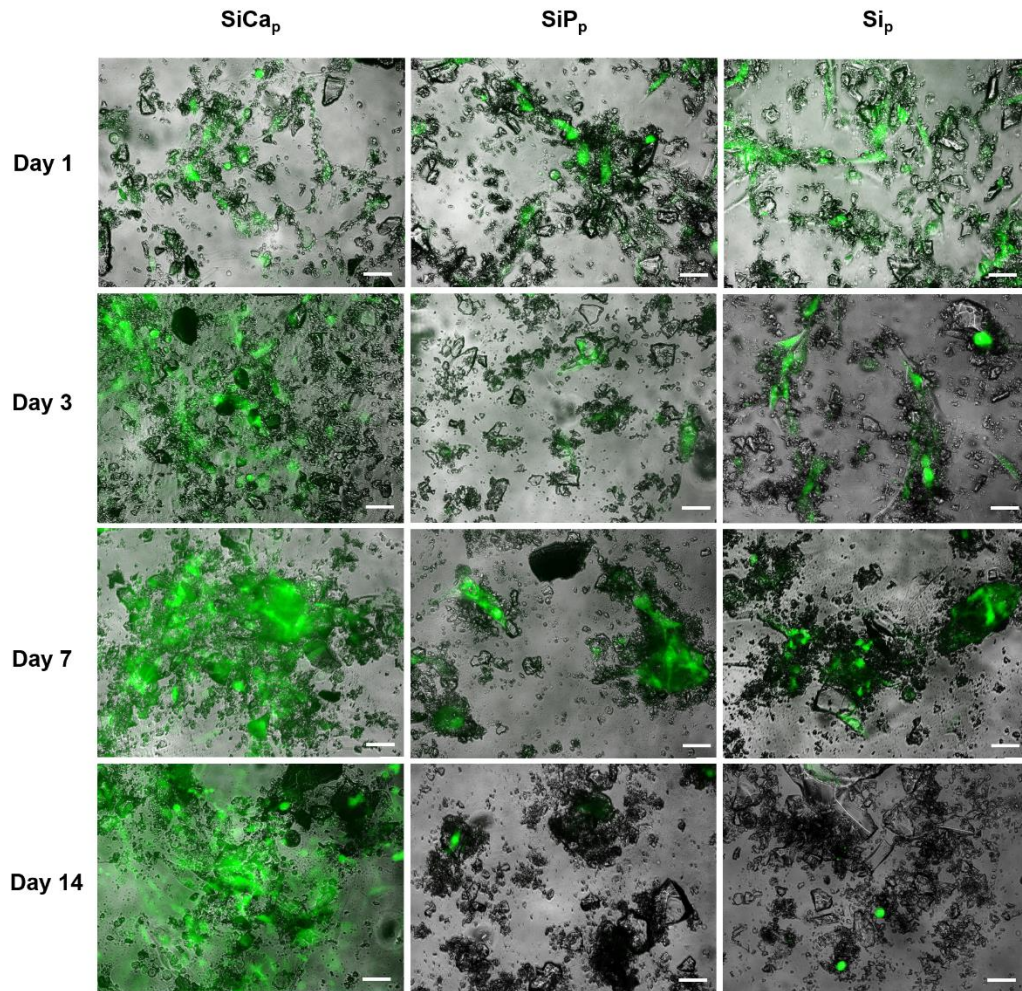
¹Department of Physical Chemistry, Faculty of Pharmacy, Medical University of Gdańsk, Hallera 107, 80-416 Gdańsk, Poland; adrianna.skwira@gumed.edu.pl; adrian.szewczyk@gumed.edu.pl

²Department of Molecular Enzymology and Oncology, Intercollegiate Faculty of Biotechnology, University of Gdańsk and Medical University of Gdańsk, Dębinki 1, 80-211 Gdańsk, Poland; rafal.sadej@gumed.edu.pl

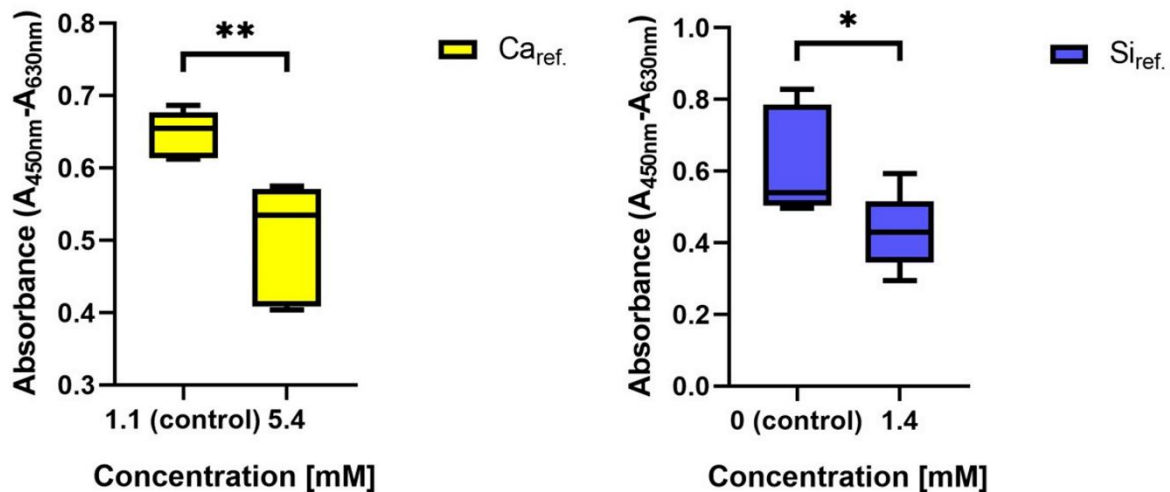
*Correspondence: magdalena.prokopowicz@gumed.edu.pl



Supplementary Fig. S1. **Apatite layer formation onto the surface of bioglasses during 24-hour extraction with cell culture medium.** FTIR spectra of BG_p, BG85S_p, and BG45S_p before (a) and after (b) extraction together with a hydroxyapatite reference sample (HAp). Types of vibrational modes: ν_2 (bending), ν_3 (stretching) of $(\text{CO}_3)^{2-}$; ν_3 (stretching), ν_4 (bending) of $(\text{PO}_4)^{3-}$.



Supplementary Fig. S2. **Cell viability evaluation at the permissive temperature of 33.5 °C for the analogues composed of silicon and calcium (SiCa), silicon and phosphate (SiP) and silicon (Si).** Merged fluorescent and bright field images of eGFP osteoblasts incubated in direct contact with SiCa, SiP, Si, and cell culture medium (control) for 1, 3, 7, and 14 days. Scale bar = 100 μm.



Supplementary Fig. S3. **Cell viability evaluation at the permissive temperature of 33.5 °C for reference solutions.** Metabolic activity measured with WST-1 assay of osteoblasts incubated with reference solutions composed of cell culture medium and calcium or silicate ions at concentrations relevant to the ones measured in BG_e (5.4 and 1.4 mM, respectively) for 3 days. *Significant difference between analyzed sample and control ($p < 0.05$); **significant difference between analyzed sample and control ($p < 0.01$).

Table S1. The amounts of substrates used in the rapid synthesis of bioglass (BG_p) and its analogues (Si_p, SiCa_p, SiP_p).

Composition	TEOS [g]	CaCl ₂ ×2H ₂ O [g]	TEP [g]	H ₂ O [g]	1 M HCl [μL]
BG _p	10.4	0.99	0.65	4.55	200
SiCa _p	10.4	0.86	-	4.55	200
SiP _p	10.4	-	0.60	4.55	200
Si _p	10.4	-	-	4.55	200

3.3. Otrzymanie i charakterystyka rusztowań kolagenowo-krzemionkowych jako potencjalnych systemów dostarczających substancję leczniczą i regenerujących tkankę kostną

Publikacja 4. A. Skwira, A. Szewczyk, J. Barros, M. Laranjeira, F.J. Monteiro, R. Sądej, M. Prokopowicz. Biocompatible antibiotic-loaded mesoporous silica/bioglass/collagen-based scaffolds as bone drug delivery systems – w trakcie recenzji na dzień złożenia pracy doktorskiej w czasopiśmie *Int. J. Pharm.* (IF: 6,510; MNiSW: 100,000).

W ostatniej pracy będącej przedmiotem rozprawy doktorskiej opisano etapy badawcze prowadzące do zrealizowania celu nadrzędnego – otrzymania biozgodnych nośników substancji leczniczej do tkanki kostnej o potencjalnym działaniu leczniczym i regeneracyjnym. Założeniem niniejszej pracy było zaprojektowanie i otrzymanie cylindrycznych rusztowań kolagenowo-krzemionkowych o odpowiednich parametrach strukturalnych, teksturalnych, zachowanej aktywności przeciwbakteryjnej oraz pożądanymi właściwościami biologicznymi.

W celu uzyskania oczekiwanej wielofunkcyjności rusztowań, do ich otrzymania wykorzystano opisane w poprzednich artykułach naukowych materiały na bazie krzemionki. Założono, że modyfikowany mezoporowaty materiał krzemionkowy z zaadsorbowaną cyprofloksacyną będzie pełnił funkcję nośnika substancji leczniczej o przedłużonym uwalnianiu, a bioszkieło, o potwierdzonej w modelu *in vitro* zdolności do osseointegracji, będzie stanowił komponent stymulujący regenerację tkanki kostnej.

Bazując na opisanych w pierwszej i drugiej publikacji wynikach oraz wyznaczonych zależnościach pomiędzy składem mieszaniny polimerowej (zawartością PDMS-u) a modyfikacją uwalniania, otrzymano pięć formułacji, których składy jakościowe i ilościowe są przedstawione w Tabeli 4. Pierwszą formułację (*Formulacja 1*) stanowił niemodyfikowany mezoporowaty materiał krzemionkowy MCM-41 zawierający cyprofloksacynę (*MCM-41-CIP*). Następne formułacje stanowił *MCM-41-CIP* z mieszaninami powlekającymi złożonymi z PDMS-u i 5% etanolowego roztworu etylocelulozy (*Formulacje 2 i 3*) oraz formułacje złożone z MCM-41 i samego PDMS-u (*Formulacje 4 i 5*). Stosunek masowy *MCM-41-CIP* do mieszaniny powlekającej w *Formulacjach 2 i 3* wynosił 1:4 przed odparowaniem rozpuszczalnika (oznaczało to, że do każdej partii *MCM-41-CIP* o masie 100 mg dodano mieszaninę PDMS-u i etylocelulozy o masie 400 mg), a stosunek masowy *MCM-41-CIP*

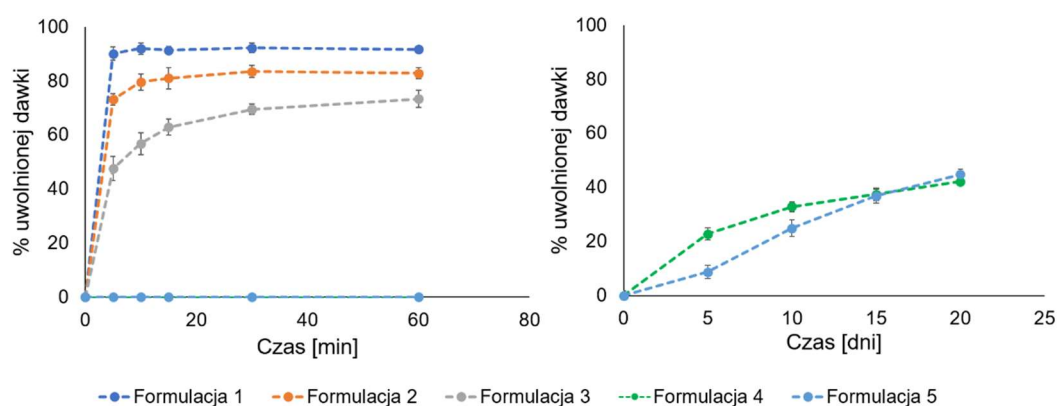
do PDMS-u w *Formulacjach 4 i 5* wynosił 2:1 i 1:1 (do każdej partii *MCM-41-CIP* o masie 100 mg dodano odpowiednio 50 mg i 100 mg PDMS-u).

Tabela 4. Składy jakościowe i ilościowe otrzymanych formułacji w postaci proszków (*badania wstępne*).

Nazwa formułacji	MCM-41-CIP [mg]	PDMS [mg]	EC [mg]
<i>Formulacja 1</i>	100	-	-
<i>Formulacja 2</i>	100	16,0	19,2*
<i>Formulacja 3</i>	100	32,0	18,4*
<i>Formulacja 4</i>	100	50,0	-
<i>Formulacja 5</i>	100	100,0	-

*masa po odparowaniu rozpuszczalnika

Na podstawie otrzymanych profili uwalniania (Rycina 3) zaobserwowano, iż dodatek mieszanin polimerowych w *Formulacjach 2 i 3* skutkowało zależnym od zawartości PDMS-u zmniejszeniem ilości antybiotyku uwolnionego w ciągu pierwszej godziny badania w porównaniu z materiałem niemodyfikowanym (*Formulacja 1*). Znaczne zmniejszenie początkowego wyrzutu substancji leczniczej do około 5% w ciągu pierwszych 24 godzin badania wykazano dla *Formulacji 4*, w której to dodatek PDMS-u wynosił 50 mg na 100 mg *MCM-41-CIP*. W przypadku *Formulacji 5* ilość uwolnionej substancji leczniczej powyżej granicy oznaczalności zastosowanej metody analitycznej odnotowano dopiero po 48 godzinach badania i wynosiła ok. 3% ilości całkowitej antybiotyku. Na tej podstawie, do otrzymania rusztowań kolagenowo-krzemionkowych, wytypowano *Formulację 4*.



Rycina 3. Profile uwalniania cyprofloksacyny z otrzymanych formułacji (*badania wstępne*).

Trójwymiarowe rusztowania otrzymano za pomocą zoptymalizowanej metody wylewania do form oraz liofilizacji. W badaniach pilotażowych, na podstawie wyników analiz opisanych we wcześniejszych artykułach, wytypowano ilościowe zawartości poszczególnych składników, stężenie roztworu kolagenu typu I, objętość mieszaniny dozowanej do form, czas żelowania i parametry liofilizacji. W celu otrzymania partii dziesięciu rusztowań kolagenowo-krzemionkowych, *MCM-CIP-PDMS* o masie 60 mg oraz bioszkło o masie 100 mg dodano do 9,8 ml roztworu kolagenu typu I w kwasie octowym o stężeniu 3,875 mg/ml. Następnie dodano 0,2 ml roztworu NaOH o stężeniu 1 M i mieszano przez 10 minut w temperaturze 25°C. Zawiesinę w objętości 1 ml dozowano do form polistyrenowych i pozostawiono w celu żelowania kolagenu przez 8 godzin w temperaturze 25°C. Następnie powstałe żełe kolagenowo-krzemionkowe poddano liofilizacji (24 godziny, 1 mBar, -55°C). Otrzymano cylindryczne rusztowania kolagenowo-krzemionkowe o średniej masie wynoszącej 22,2 mg oraz średniej wysokości i średnicy równych odpowiednio 10 mm i 7 mm.

Strukturę rusztowań oceniono za pomocą techniki SEM oraz mikrotomografii komputerowej. Analizę właściwości mechanicznych (twardości, plastyczności i wytrzymałości na ściskanie) przeprowadzono za pomocą analizatora tekstury TA.XTplusC w odniesieniu do rusztowań kolagenowych placebo, otrzymanych w analogiczny sposób, lecz bez dodatku materiałów krzemionkowych i bioszka. Celem weryfikacji właściwości mineralizacyjnych, rusztowania kolagenowo-krzemionkowe zanurzone w płynie symulującym ludzkie osocze (ang. *simulated body fluid*, SBF), a obecność hydroksyapatytu na ich powierzchni weryfikowano przy użyciu technik FTIR, SEM-EDX oraz XRD. W niniejszym artykule przeprowadzono również badanie dostępności farmaceutycznej cyprofloksacyny zawartej w rusztowaniach kolagenowo-krzemionkowych. Skuteczność przeciwbakteryjną, wyrażoną jako zapobieganie tworzeniu się biofilmu bakteryjnego oraz hamowanie wzrostu bakterii w otaczającym środowisku, oceniono za pomocą metody zliczania jednostek tworzących kolonie bakteryjne (ang. *colony forming unit*, CFU) z wykorzystaniem szczepu referencyjnego *Staphylococcus aureus* ATCC 25923. Właściwości biologiczne rusztowań zostały zbadane w warunkach *in vitro* oraz *in vivo*. Ocenę biogodności *in vitro* przeprowadzono za pomocą testu resazuryнового, techniki SEM oraz mikroskopii konfokalnej wykorzystując linię komórkową ludzkich osteoblastów hFOB 1.19. Natomiast analizę biogodności *in vivo* przeprowadzono za pomocą techniki *in vivo*

CAM (ang. *Chick Chorioallantoic Membrane*, błona kosmówkowo-omoczeniowa), która w wysokim stopniu spełnia kryteria etyczne zasady 3R (ang. *Replacement, Reduction, Refinement*). Została ona uznana za wiarygodną i wszechstronną metodę służącą wstępnej ocenie biomateriałów. Warto zauważyć, że CAM stanowi przedkliniczny model doświadczalny pozwalający na dobrą wizualizację początkowej odpowiedzi tkanki na implantowany biomateriał, podobnej do odpowiedzi obserwowanej w modelach ssaczy. W celu oceny biogodności rusztowań, analizie poddano żywotność zarodków kurzych, proces angiogenezy, zmiany morfologiczne i naczyniowe w CAM (przebarwienia, obecność zakrzepów lub krwotoków). Natomiast, aby ocenić początkową odpowiedź tkankową na rusztowania kolagenowo-krzemionkowe, wykonano barwienie hematoksyliną i eozyną wyizolowanych fragmentów CAM.

Strukturę rusztowań kolagenowo-krzemionkowych scharakteryzowano jako heterogeniczną z licznymi otwartymi i połączonymi wzajemnie makroporami o średnicy w zakresie 45-292 μm i średniej całkowitej porowatości równej 45,81%. Otrzymane wartości odniesiono do danych literaturowych, które wskazywały zakres wielkości porów od 100 do 300 μm jako optymalny [108], a wzajemne połączenia porów jako wspomagające proces osteokondukcji [109]. Na tej podstawie parametry porowatości rusztowań kolagenowo-krzemionkowych uznano za zadowalające i potencjalnie korzystne dla integracji z tkanką kostną. Za pomocą mikrotomografii komputerowej zidentyfikowano poszczególne komponenty krzemionkowe i potwierdzono ich równomierne rozmieszczenie w matrycy kolagenowej. Dodatkowo odnotowano występowanie *MCM-CIP-PDMS* w postaci aglomeratów. Obserwowane zjawisko uzasadniono hydrofobowym charakterem cząstek i ich prawdopodobnym łączeniem się w większe skupiska w trakcie mieszania z hydrofilowym roztworem kolagenu typu I. Za pomocą analizy tekstury wykazano porównywalne wartości parametrów plastyczności i twardości wyznaczone dla rusztowań kolagenowo-krzemionkowych oraz rusztowań kolagenowych. Natomiast rusztowania kolagenowo-krzemionkowe, w przeciwieństwie do rusztowań kolagenowych, zachowały swoją przestrzenną strukturę i kształt podczas prowadzonych analiz fizykochemicznych, mikrobiologicznych i biologicznych, potwierdzając w ten sposób, korzystny wpływ obecności materiałów krzemionkowych na stabilność struktury liofilizowanego kolagenu.

Znaczne właściwości mineralizacyjne rusztowań kolagenowo-krzemionkowych, wyrażone poprzez stopniowe formowanie się na ich powierzchni warstwy hydroksyapatytowej o morfologii i składzie pierwiastkowym zbliżonymi do apatytu

kostnego, uzasadniono faktem, iż w procesie mineralizacji kości oprócz jonów wapnia i ortokrzemianów, kluczową rolę odgrywa również makroporowata struktura kolagenu typu I. Miejsca nukleacji hydroksyapatytu znajdują się wewnątrz włókien kolagenowych, których specyficzne ułożenie sprzyja przepływowi jonów wapnia i fosforanów. Następnie w trakcie procesu mineralizacji, włókna kolagenu stanowią matrycę, na której osadzają się kryształy hydroksyapatytu.

Analiza dostępności farmaceutycznej potwierdziła przedłużone uwalnianie cyprofloksacyny aż do 80 dni, a początkowy jej wyrzut w ciągu pierwszych 24 godzin wynosił 44% całkowitej jej ilości. Dwufazowy profil uwalniania wyjaśniono w oparciu o badania opisane w poprzednich artykułach oraz wyniki uzyskane dla testu degradacji rusztowań w warunkach *in vitro*. Początkowe uwolnienie substancji czynnej związane było prawdopodobnie z częściową hydrolizą rusztowań kolagenowo-krzemionkowych, dla których oznaczono 20-procentowy ubytek masy początkowej w ciągu pierwszych 24 godzin badania. Natomiast przedłużenie uwalniania wynikało z omawianej już funkcji PDMS-u oraz zjawiska łączenia się cząstek mezoporowatego materiału krzemionkowego w aglomeraty podczas sporządzania rusztowań.

Ważnym aspektem implantów jest ich podatność na kolonizację przez mikroorganizmy. Odnosi się to w szczególności do materiałów charakteryzujących się wysoką hydrofilowością, których przykładem są matryce kolagenowe. Przeprowadzona ilościowa analiza mikrobiologiczna wykazała działanie bakteriobójcze zarówno wobec populacji *S. aureus* tworzących biofilm, jak również populacji planktonicznej. Brak obecności mikroorganizmów na powierzchni rusztowań kolagenowo-krzemionkowych potwierdzono także za pomocą techniki SEM. Uzyskane wyniki dowiodły zapobiegania adhezji bakterii do powierzchni rusztowań kolagenowo-krzemionkowych, a tym samym przeciwdziałania tworzeniu się biofilmu bakteryjnego, w przeciwieństwie do rusztowań kolagenowych placebo. Ponadto, udowodniono w ten sposób, iż proces otrzymywania rusztowań nie wpłynął na aktywność przeciwdrobnoustrojową antybiotyku względem testowanego szczepu.

Analiza właściwości biologicznych *in vitro* potwierdziła biogodność rusztowań kolagenowo-krzemionkowych z ludzkimi osteoblastami. Wykazano obecność komórek na powierzchni rusztowań i wewnątrz ich porowatej struktury, natomiast za pomocą testu resazurynowego dowiedziono ich proliferacji. W trakcie analizy biogodności *in vivo*, wskaźnik żywotności zarodków kurzych wynosił ponad 90%, dowodząc

tym samym braku toksyczności rusztowań kolagenowo-krzemionkowych. Nie wykryto również żadnych zmian morfologicznych i naczyniowych w obrębie błony kosmówkowo-omoczniowej zarodków inkubowanych z rusztowaniami kolagenowo-krzemionkowymi. Ponadto liczba naczyń krwionośnych utworzonych podczas inkubacji z rusztowaniami nie różniła się znacząco od wartości wyznaczonych dla kontroli (zarodki kurze inkubowane z roztworem PBS lub rusztowaniami kolagenowymi placebo). Wynik ten zinterpretowano jako brak wpływu obecności rusztowań kolagenowo-krzemionkowych na proces angiogenezy. Analiza mikroskopowa potwierdziła wnikanie komórek mezenchymalnych błony kosmówkowo-omoczniowej w głąb rusztowań, jak również obecność czerwonych krwinek i drobnych naczyń krwionośnych. Udowodniono w ten sposób wysoką biogodność rusztowań kolagenowo-krzemionkowych oraz ich potencjalną zdolność do integracji z tkanką pacjenta. W nielicznych obszarach bezpośredniego kontaktu błony z rusztowaniami stwierdzono występowanie pojedynczych komórek prekursorowych układu immunologicznego, co przypisano naturalnemu rozwojowi układu odpornościowego w zarodkach kurzych w czasie prowadzonego doświadczenia.

Podsumowując, w niniejszym artykule przedstawiono sposób otrzymywania rusztowań kolagenowo-krzemionkowych i ich kompleksową ocenę w celu określenia potencjalnej przydatności w miejscowym leczeniu *osteomyelitis*. Połączenie otrzymanych i scharakteryzowanych materiałów: modyfikowanego mezoporowatego materiału krzemionkowego MCM-41 zawierającego cyprofloksacynę oraz bioszklę pozwoliło na otrzymanie nośników o właściwościach wysoce pożądanym w inżynierii tkanki kostnej. Na podstawie uzyskanych wyników stwierdzono, że proponowane rusztowania kolagenowo-krzemionkowe mogą służyć jako wielofunkcyjne nośniki, które nie tylko uwalniają antybiotyk w sposób przedłużony, ale również stymulują regenerację tkanki kostnej. Jednakże, aby w pełni określić możliwości aplikacyjne rusztowań kolagenowo-krzemionkowych, konieczne jest przeprowadzenie dalszych długookresowych badań *in vivo* z wykorzystaniem ssaczych modeli zwierzęcych.

Biocompatible antibiotic-loaded mesoporous silica/bioglass/collagen-based scaffolds as bone drug delivery systems

Adrianna Skwira^a, Adrian Szewczyk^a, Joana Barros^{c,d,f}, Marta Laranjeira^{c,d,e}, Fernando Jorge Monteiro^{c,d,e,f}, Rafał Sądej^b, Magdalena Prokopowicz^a

^a*Department of Physical Chemistry, Faculty of Pharmacy, Medical University of Gdańsk, Hallera 107, 80-416 Gdańsk, Poland; adrianna.skwira@gumed.edu.pl; adrian.szewczyk@gumed.edu.pl*

^b*Department of Molecular Enzymology and Oncology, Intercollegiate Faculty of Biotechnology, University of Gdańsk and Medical University of Gdańsk, Dębinki 1, 80-211 Gdańsk, Poland; rafal.sadej@gumed.edu.pl*

^c*i3S – Instituto de Investigação e Inovação em Saúde, Universidade do Porto, Rua Alfredo Allen 208, 4200-135 Porto, Portugal; joana.barros@ineb.up.pt, msl@ineb.up.pt, fjmont@fe.up.pt*

^d*INEB – Instituto de Engenharia Biomédica, Universidade do Porto, Rua Alfredo Allen 208, 4200-135 Porto, Portugal*

^e*Porto Comprehensive Cancer Center Raquel Seruca (P.CCC), R. Dr. António Bernardino de Almeida, 4200-072 Porto, Portugal*

^f*FEUP-Faculdade de Engenharia, Departamento de Engenharia Metalúrgica e de Materiais, Universidade do Porto, Rua Dr. Roberto Frias, s/n 4200-465, Porto, Portugal*

**Correspondence: magdalena.prokopowicz@gumed.edu.pl*

Abstract

Local delivery of antibiotics has gained increasing interest in the treatment of osteomyelitis due to its effectiveness and safety. Since the regeneration of bone tissue at the site of infection is as important as bacterial eradication, implantable drug delivery systems should not only release the drug in a proper manner but also exert the osseointegration capability. Herein, we present an implantable drug delivery system in a scaffold form with a unique set of features for bone tissue regeneration and osteomyelitis treatment. For the first time, collagen type I, ciprofloxacin-loaded mesoporous silica, and bioglass were combined to obtain scaffolds using the molding method. Drug-loaded mesoporous silica was blended with polydimethylsiloxane to prolong a drug release. Bioglass served as remineralization agent. Collagen-silica scaffolds were evaluated in terms of physicochemical properties, drug release rate, mineralization potential, osteoblast response *in vitro*, antimicrobial activity, and biological properties using an *in vivo* preclinical model – chick embryo chorioallantoic membrane (CAM). The desirable multifunctionality of the proposed collagen-silica scaffolds was confirmed. They released the ciprofloxacin for 80 days, prevented biofilm development, and induced hydroxyapatite formation. Moreover, the resulting macroporous structure of the scaffolds promoted osteoblasts attachment, infiltration, and proliferation. Collagen-silica scaffolds were also biocompatible and effectively integrated with CAM.

Keywords: scaffolds, drug delivery, collagen, mesoporous silica, bioglass

1. Introduction

Osteomyelitis is defined as a bone or bone marrow inflammation caused by pyogenic organisms (bacteria, fungi, or mycobacteria), and characterized by acute or chronic tissue inflammatory destruction (osteolysis) (Wassif et al., 2021). About 60-70% of diagnosed cases is caused by *Staphylococcus aureus*. Treatment of osteomyelitis remains a clinical challenge in orthopedic surgery. Currently, oral or intravenous administration of antibiotics is recognized as the most efficient therapy for acute osteomyelitis. The success of antibiotic-based treatment depends on two main factors: the susceptibility of bacteria that colonized bone tissue to the administered drug (i) and the local antibiotic concentration at the site of infection (ii). Due to the low penetration of applied drugs into the bone tissue (bone to serum concentration ratio for most antibiotics is approx. 0.3 (Landersdorfer et al., 2015)) and poor vascularization of inflamed (often partially necrotic) area, systemic routes require an administration of high doses of antibacterial agents to provide an effective concentration at the site of infection. This strategy leads to severe systemic toxicity, significantly affecting the patients' overall condition (Tsourvakas, 2012). Therefore, local administration of antibiotics directly to the bone tissue has gained an increasing interest in the treatment of bone tissue infections as effective and relatively safe adjuvant therapy (Gogia et al., 2009; Liu et al., 2022; Nandi et al., 2016). As the regeneration of bone tissue after surgical debridement is as important as bacterial eradication, the implantable biomaterial should be characterized by not the sustained release of antibacterial agent (i) and bone-regenerative potential (ii).

Local treatment of bacterial bone tissue infection is commonly performed with commercially available gentamicin-loaded polymethyl methacrylate (PMMA) beads (Septopal™; U.S. Pat. No. 6m155, 812). Septopal™ is applied subsequently to tissue debridement and was found to effectively provide antibiotics directly to the site of infection for at least 14 days at a significantly higher level than minimal inhibitory concentrations determined for most osteomyelitis pathogens (Blaha et al., 1990; Patzakis et al., 1993; Walenkamp et al., 1986). However, due to the exothermic polymerization of PMMA which generates a temperature of around 90 °C, the application of beads is limited to only thermally-stable antibiotics. Furthermore, since PMMA beads are not biodegradable and do not integrate with host bone tissue, they need to be removed in a second surgical procedure, increasing the risk of reinfections. Therefore, PMMA beads may serve as an effective delivery system but do not comply with the second condition of implantable biomaterial referred to as the enhancement of bone tissue regeneration. That is why various modern biomaterials have been designed and considered not only as bone drug delivery systems but also as regenerative agents. Collagen fibers constitute a structural scaffold for hydroxyapatite deposition that mechanically reinforces bone tissue (Murshed, 2018; Olszta et al., 2007). Therefore, attention has been focused on freeze-dried scaffolds based on purified type-I collagen as bone substitutes (Li et al., 2021). They are characterized by biocompatibility, low immunogenicity, biodegradability, plasticity, well-established chemical structure, and textural properties, such as high specific surface area and pore size preferred for osteoblast adhesion, growth, proliferation, and differentiation (Murphy and O'Brien, 2010; Nijssure and Kishore, 2018). Nowadays, there are two commercially

available antibiotic-loaded collagen scaffolds which effectiveness was verified in the treatment of patients with osteomyelitis (Van Vugt et al., 2018). Collagen implants in the form of sponges impregnated with gentamicin sulfate (Sulmycin®) or a combination of gentamicin sulfate and gentamicin crobefate (Septocoll®) were reported to be less effective than PMMA beads. The lower effectiveness of collagen implants compared to PMMA may result from their unfavorable pharmacokinetics of drug release. They released approximately 95% of the total gentamicin load in the first hours after implantation, resulting in high local concentrations and leading to fistulas and prolonged wound drainage.

As mineralized collagen fibrils are the main structural unit of the bone-implant interface (Shah et al., 2019), various bioactive ceramics, such as calcium phosphates (CaP), hydroxyapatite (HA), or silica-based materials have been incorporated into collagen (Zhang et al., 2018). The bioactivity of these materials (also called mineralization potential) is demonstrated by the formation of an apatite layer onto their surface in contact with physiological fluids after implantation (Vallet-Regí and Balas, 2008). This process was found to be essential to provide a stable interface between bone tissue and implanted biomaterial (Wahl and Czernuszka, 2006). The formation of either an amorphous or semi-crystalline apatite layer depends on material composition, degradability, and release of osteogenic ions into the adjacent environment. To date, FDA has approved several collagen-ceramic materials applicable as fillers or scaffolds for bone tissue regeneration. Collagraft™, the first approved bone-grafting material, is a composite of porous calcium phosphate ceramic (hydroxyapatite and tricalcium phosphate) suspended in fibrillar collagen matrix which is soaked in the patient's freshly-aspirated bone marrow shortly before implantation (Cornell et al., 1991). Other similar composites are Healos® and OssiMend®. These collagen-ceramic composites are effective in bone tissue regeneration; however, they cannot be applied to patients with any active infection at the operative site due to a lack of antibacterial activity.

Silica materials have attracted enormous interest due to their wide medical applications e.g. as bone-repairing devices or drug delivery systems. Among them, bioglasses are classified as one of the most bioactive silica derivatives (Vallet-Regí and Balas, 2008), which can form a layer of bone-like apatite. Apart from the calcium ions and orthophosphates, which are released from hydroxyapatites or calcium phosphates, bioglasses release the silicates involved in the early stages of bone tissue formation and mineralization (Götz et al., 2019). Thus, the addition of bioglass into the bone drug delivery system is being used to increase the mineralization properties of final composites. Another type of silica materials, ordered mesoporous silica material (MSM), has been broadly applied in bone drug delivery systems as drug carriers (Gisbert-Garzarán et al., 2020). The ordered structure, volume, and size of the pores, as well as the large specific surface area, result in the high adsorption capacity of MSM. However, the drug release profile is characterized by an initial burst related to the dissolution of the drug portion located on or near the entrances of pores, which may be undesirable in the application directly to bone tissue. However, it was confirmed that a wide range of simple methods, e.g. chemical surface functionalization (Izquierdo-Barba et al., 2009; Prokopowicz et al., 2019; Szewczyk et al., 2020, 2019) or blending with polymers (Lee and Yoo, 2016; Narayan et al., 2018; Skwira et al., 2020, 2019) may successfully modify the kinetics of the release.

To the best of our knowledge, there is no commercially available implantable collagen-based composite that releases the drug in a prolonged manner and at the same time enhances bone tissue regeneration. Therefore, this work aimed to obtain the drug delivery system in the form of a collagen-based scaffold that fulfills both the requirements mentioned above. In our preliminary studies, we successfully modified the release rate of the model drug, ciprofloxacin hydrochloride (CIP), from the polydimethylsiloxane (PDMS)-blended mesoporous silica (Skwira et al., 2020, 2019). Moreover, the bioglass (BG) developed by our research team via the rapid sol-gel method was characterized by significantly higher osseointegration capability *in vitro* than commercially available ones (Skwira et al., 2023). Therefore, we combined the above-mentioned silica materials into a collagen type I (COL) matrix in this study. The obtained collagen-silica scaffolds were evaluated in terms of physicochemical properties, such as morphology, porosity, and textural properties. The release profile of the antibiotic and its antimicrobial activity against *Staphylococcus aureus* was also determined. Next, osseointegration capability was evaluated by verifying hydroxyapatite formation onto the scaffolds' surface and osteoblast-scaffold interactions (cellular attachment, infiltration, and proliferation). Finally, to verify collagen-silica scaffolds biocompatibility and initial tissue response, the CAM (chick chorioallantoic membrane) assays were used. The *in vivo* CAM technique was established as a reliable and versatile alternative for biomaterials evaluation which highly meets the ethical criteria – principles of 3Rs (Replacement, Reduction, Refinement) compared to conventional animal models. Importantly, CAM provides a preclinical model for the excellent visualization of tissue response to implantable biomaterials, similar to the tissue response observed in mammalian models (Valdes et al., 2002).

2. Materials and methods

2.1. Mesoporous silica synthesis

Mesoporous silica type MCM-41 was synthesized using a sol-gel method as previously described (Skwira et al., 2020). Tetraethyl orthosilicate (TEOS, Sigma-Aldrich, USA) was used as a silica source, and cetyltrimethylammonium bromide (CTAB, Sigma-Aldrich, USA) as a structure-directing agent. Briefly, water, ethanol, aqueous ammonia (25%), and CTAB in the following amounts of 125, 12.5, 9.18, and 2.39 g, respectively, were mixed in a polypropylene beaker (10 min, 300 rpm, 25 °C) until complete CTAB dissolution. Then, TEOS in the amount of 10.03 g was added and stirred for 2 h. Subsequently, the mixture was aged at 90 °C for 5 days (without stirring). The powder was washed with absolute ethanol, dried (40 °C, 1 h), and calcined at 550 °C, for 6 h (FCF 7SM, Czylok, Poland). MCM-41 powder was micronized in a mortar and sieved through the sieves to obtain a fraction in the range of 200-500 µm.

2.2. Drug-loading and PDMS-modification of mesoporous silica

The ciprofloxacin hydrochloride (CIP, Sigma-Aldrich, USA) loading into the mesoporous silica MCM-41 was carried out by using a previously optimized procedure (Skwira et al., 2020, 2019) with applied impregnation-drying modification. In brief, each 200 mg of MCM-41 material (particles fraction in the range of 200 µm – 500 µm) was impregnated with 2 mL of CIP (9.41 ± 0.56 mg/mL) incubated in a water bath (300 rpm) at room temperature for 30 min, and freeze-dried (-52 °C, 1 mBar, 24 h). The concentration of the CIP solution used in

the impregnation step was evaluated spectrophotometrically at 278 nm (UV-Vis spectrophotometer Shimadzu, model UV-1800). The drug-loading process was repeated 6 times. In the next step, each 100 mg of drug-loaded mesoporous silica (MCM-CIP) was blended with 50 mg of PDMS (65 cSt, $d = 0.97 \text{ mg/mL}$) in a mortar for 10 min and stored in the desiccator at room temperature before further use and named as MCM-CIP-PDMS ($58.93 \pm 4.47 \text{ mg of CIP per 1 g of final powder}$).

2.3. Bioglass synthesis

Bioglass (BG) was synthesized via the rapid one-pot sol-gel method previously described (Skwira et al., 2023). Briefly, 10.4 g of tetraethyl orthosilicate (TEOS, Sigma-Aldrich, USA) was poured into a polypropylene beaker and mixed with 4.55 g of purified water (Millipore Direct-Q 3 UV, Merck, Germany), and 200 μL of 1.0 M HCl (500 rpm, 30 min). Next, 0.65 g of triethyl phosphate (TEP, Sigma-Aldrich, USA) was added, and the mixture was stirred for 2 h under the same conditions. Thereafter, 0.99 g of calcium chloride dihydrate ($\text{CaCl}_2 \cdot 2\text{H}_2\text{O}$, 99.0% purity, Sigma-Aldrich, USA) was weighed and dissolved, and the mixture was left for an additional 1.5 h with stirring. Finally, the obtained sol was poured into the crucible and calcined at 600 $^\circ\text{C}$ for 4 h in the muffle furnace (1 $^\circ\text{C}/\text{min}$ heating rate, FCF 7SM, Czylok). The obtained BG was powdered in the mortar, homogenized through a 100 μm sieve, and stored in the desiccator at room temperature before further use.

2.4. Collagen-silica scaffolds fabrication

In the pilot studies, the formation process of the scaffold using the molding method was optimized. It included the selection of the quantitative contents of particular components, the concentration of collagen type-I solution, the time of vortexing, the volume of collagen-silica mixture dosed into each mold, the time of gelation, and the freeze-drying parameters. Our assumption was to design cylindrical-shaped scaffolds with satisfactory porosity and textural parameters, antimicrobial activity, and desirable biological properties. Herein, we demonstrate our approach for fabricating a formulation selected as the best one. To prepare a batch of ten collagen-silica scaffolds, preoptimized amounts of MCM-CIP-PDMS (60 mg mesoporous silica containing 0.35 mg of CIP and 2 mg of PDMS) and BG (100 mg) were added into 9800 μL of collagen type I in 0.02 M acetic acid at a concentration of 3.875 mg/mL (Skwira et al., 2020). Then, 200 μL of NaOH (1 M) was added and the suspension was vortexed for 10 min at room temperature. The resulting suspension in the volume of 1 mL was dosed into each polystyrene mold and incubated for 8 h (25 $^\circ\text{C}$) for the self-assembly of collagen fibrils, which lead to collagen gelation and embedding of the silica components. Thereafter, the collagen-silica gels were freeze-dried (24 h, 1 mBar, -55 $^\circ\text{C}$) and the final collagen-silica scaffolds were weighed, measured, and stored in the desiccator at room temperature before further analyses.

Additionally, the two following analogs were prepared in the same manner for comparative purposes in particular assays. Placebo collagen scaffolds without ciprofloxacin and silica materials (named collagen scaffolds) were fabricated to be comparatively analyzed in the mineralization study, microbiological, and biological assays. Collagen scaffolds containing CIP powder instead of MCM-CIP-PDMS (named CIP-loaded collagen scaffolds) were prepared for drug release studies. To fabricate one batch of CIP-loaded collagen

scaffolds (n=10), 3.5 mg of ciprofloxacin hydrochloride powder (Sigma-Aldrich, USA) was added to the collagen solution instead of 60 mg of MCM-CIP-PDMS.

2.5. Morphology and structure analyses

2.5.1. Scanning electron microscopy

The surface morphology and porosity of the collagen-silica scaffolds were determined using scanning electron microscopy combined with X-ray energy dispersive spectrometry (SEM-EDX; Hitachi SU-70 and Quanta 3D FEG). Samples were coated with a 10 nm gold layer and analyzed using a 5.0 kV operating voltage. The porosity and pore size were analyzed quantitatively with ImageJ software (National Institute of Health, Bethesda, MD, USA) (Schneider et al., 2012). Porosity measurement was performed using segmentation mode into a binary image with scaffolds material and pores based on the flowchart (Hojat et al., 2023). The pore size was measured by manual mode as mean diameters of at least 25 randomly selected pores at five SEM images.

2.5.2. X-ray micro-computed tomography (micro-CT)

The collagen-silica scaffolds were analyzed in the dry state. Micro-CT scans were acquired using SkyScan1276 (Bruker, Belgium). All the scans were performed under the following parameters: 10 μm pixel size, source voltage 40 kV, frame averaging (4), rotation step 0.2° , and scanning time ~ 1 h. The images were reconstructed from projections with NRecon software (v.1.7.5.2, Bruker, Belgium) using the adequate setting of correction parameters (misalignment, ring artifact) to reduce the effect of artifacts. Visualizations were acquired with DataViewer (v.1.5.6.0) and CTVOx (1.5.2, Bruker, Belgium).

2.6. Texture analysis

The mechanical properties of collagen and collagen-silica scaffolds in terms of hardness, plasticity, and compressive modulus (apparent Young's modulus) were determined using XTplusC Texture Analyzer (Godalming, UK) following the procedure implemented by Luzardo-Álvarez et al. (Luzardo-Álvarez et al., 2011). Eight collagen-silica scaffolds and collagen scaffolds were placed vertically on the platform and compressed to 50% of the original height at a rate of 0.5 mm/s using a P/20 cylindrical probe. Next, the probe was immediately removed using the same speed. The mechanical properties were calculated based on stress-strain curves. Hardness was expressed as a maximum force recorded during scaffold compression. The compressive modulus was obtained from the slope of linear least squares regression from the first region of the stress-strain curves. The plasticity was calculated using Eq. 1 (Luzardo-Álvarez et al., 2011):

$$Plasticity = (Resilience + 1)^{-1} \quad (1)$$

where resilience is an area under the curve that corresponds to the decompression phase divided by the area under the curve of the compression phase.

2.7. Mineralization potential studies

The mineralization potential studies were carried out for collagen-silica scaffolds and collagen scaffolds (for comparative purposes) following the procedure proposed by Kokubo and Takadama (Kokubo and Takadama, 2006). Collagen-silica scaffolds were immersed in simulated body fluid (SBF) providing a 2:1 (mg/ml) ratio of

scaffolds' mass to SBF volume and incubated for 21 days. The experiment was performed in a water bath (Witeg WSB-30) at 37.0 °C under stirring (70 rpm). The SBF was exchanged every 7 days by simple decantation method. After 7, 14, and 21 days of mineralization potential studies, scaffolds were filtered, dried at 40 °C, weighed, and analyzed with Fourier-transform infrared spectroscopy (FTIR), scanning electron microscopy equipped with energy-dispersive X-ray spectroscopy (SEM-EDX), and powder X-ray diffraction (XRD).

2.7.1. Scanning electron microscopy/X-ray energy dispersive spectrometry

Scanning electron microscopy was performed together with X-ray energy dispersive spectrometry (SEM-EDX; Hitachi SU-70 and Quanta 3D FEG). Samples were coated with a 10 nm gold layer and analyzed using a 5.0 kV operating voltage. The average weight content of osteogenic elements (Ca and P) was calculated based on EDX spectra obtained for nine randomly selected micrographs (50 $\mu\text{m} \times 50 \mu\text{m}$, 20 kV operating voltage).

2.7.2. Fourier transform infrared spectroscopy

Fourier transform infrared spectroscopy (FTIR) measurements were performed on Jasco 4700 model. Each 1 mg of the sample was mixed with 100 mg of KBr, compressed into the tablet, and analyzed in the range of 4000–400 cm^{-1} .

2.8. Drug release studies

The drug release studies for collagen-silica scaffolds were carried out using USP II Paddle Apparatus (Copley DIS-6000) at 37.0 °C, 75 rpm. For comparative purposes, the release studies were also performed for CIP-loaded collagen scaffolds. Briefly, each collagen-silica scaffold and CIP-loaded collagen scaffold (each scaffold contained 0.35 mg of CIP mg) were immersed into 50 mL of distilled water (pH = 7.0) as dissolution medium providing sink conditions. At particular time points, 1 mL of solution was collected, filtered using membrane filters (0.22 μm), and analyzed spectrophotometrically at a wavelength of 272 nm using a UV-Vis spectrophotometer (V-530 Jasco, Japan). Analytical studies were conducted in agreement with the requirements for quantitative analyses, calibrating the detector with a standard solution of the tested CIP in distilled water. The constant volume of dissolution medium was provided without it exchanging during the studies (drug release data were plotted as the cumulative percent of released CIP as a function of time). The release studies were performed in 6 replicates.

To calculate the release kinetics parameters, linearized forms of Higuchi, Korsmeyer-Peppas, and zero-order models were used, respectively:

$$Q = k_H t^{\frac{1}{2}} \quad (2)$$

$$\log Q = n \log t + \log k \quad (3)$$

$$Q = Q_0 + k_0 t \quad (4)$$

where Q (%) denotes the fraction released by time t (day), k_H is a Higuchi dissolution constant ($\text{day}^{-1/2}$), n is an exponent related to the drug release mechanism, k (day^{-n}) is a rate constant, Q_0 (%) – the initial fraction of released drug, k_0 – zero-order release constant (%/day). In Eq. (3), $n < 0.45$ indicates a Fickian diffusion for

cylindrical matrices, $0.45 < n < 0.89$ corresponds to non-Fickian diffusion, $n > 0.89$ for super case II transport. In the case of Higuchi and Korsmeyer-Peppas model, the data for the first 60% of drug release fraction Q was fitted.

2.9. Antimicrobial activity

Staphylococcus aureus ATCC 25923 was used as the reference strain to assess the antimicrobial effectiveness of the collagen-silica scaffolds. Collagen scaffolds were also evaluated for comparative purposes. The quantification of sessile and planktonic populations was performed through the colony-forming unit (CFU) counting method. Thereby, UV-sterilized collagen-silica scaffolds and collagen scaffolds were placed into 48-well plates (Cat. No. 677102, CELLSTAR, Greiner Bio-One, USA). Then, bacterial suspension (at exponential phase) at 1.0×10^6 cells/mL in tryptic soy broth (TSB, Merck Millipore, Germany) was added (1 mL) into the wells, and the plates were incubated for 24 h (37 °C). Bacteria-free broth and bacterial broth without scaffolds were used as negative and positive controls, respectively. After incubation, the bacterial suspensions were collected to determine the planktonic bacteria density, which involves serial dilution and spread-plating in tryptic soy agar (TSA, Merck Millipore, Germany). For the sessile population quantification, the scaffolds were carefully transferred to a new 48-well plate, twice washed with sterile 0.9% (w/w) sodium chloride (NaCl, Merck Millipore, Germany) solution to remove non-adherent and weakly-adherent bacteria. Then, 1 mL of 0.9% NaCl was added to each well, and the plate containing scaffolds was sonicated for 10 min using an ultrasonic water bath (200 W, 40 kHz, BactoSonic Ultrasonic Bath BS14, Bandelin), to detach the sessile bacteria. The sessile density was determined by serial dilution and spread-plating in tryptic soy agar (TSA, Merck Millipore, Germany). The assay was performed thrice as independent experiments, each performed in triplicates. The data are reported as mean \pm standard deviation. The differences among groups were tested by one-way analysis of variance (ANOVA), followed by multiple comparisons among groups using the Tukey HSD post hoc test (IBM®SPSS® Statistics, versus 19.0). In all cases, $p < 0.05$ was considered to be statistically significant.

For direct observation of sessile bacteria, collagen-silica scaffolds and collagen scaffolds were fixed in 3% (v/v) glutaraldehyde (Fluka, Germany) at room temperature for 30 min and then gradually dehydrated in ethanol (50, 70, 90, and 96%) for 10 min each series. Then, the scaffolds were fixed on sample holders with double-sided carbon tape and sputter-coated (SPI-module) with a conductive gold-palladium film. The sessile bacteria were imaged using a FEI Quanta 400 FEG/ESEM microscope (FEI, Hillsboro, OR, USA) operated at 15 kV with magnifications between 5000 and 25000 \times .

2.10. Biological analyses

2.10.1. Cell culture

The human fetal osteoblastic cell line (hFOB 1.19) was obtained from the American Type Culture Collection (Cat. No. CRL-11372™). hFOB 1.19 cell line comprises conditionally immortalized human fetal osteoblasts with a temperature-sensitive mutant of the SV40 large T antigen (tsSV40LTA) gene. Osteoblasts were cultured in a 1:1 mixture of Ham's F12 Medium Dulbecco's Modified Eagle's Medium (DMEM/F12) with 2.5 mM L-glutamine (without phenol red), 15 mM HEPES, and sodium bicarbonate, supplemented with 10% fetal bovine

serum and penicillin/streptomycin (100 U/mL/100 µg/mL) at 33.5 °C in a humidified atmosphere of 5% CO₂. The medium was replaced every 2–3 days. Cells were passaged for a maximum of 3–4 months post-resuscitation and regularly tested for mycoplasma contamination.

2.10.2. Cell attachment

Cells were seeded onto the surface of collagen-silica scaffolds and collagen scaffolds at a density of $3 \cdot 10^4$ cells/well incubated for 24 h (34 °C, 5% CO₂). Then, the samples were fixed with 4% paraformaldehyde (20 min, room temperature) and dehydrated with the graded ethanol (30, 50, 75, and 96%) (3 min for each concentration, room temperature). Afterward, the samples were freeze-dried, sputter-coated with gold, and analyzed with SEM at an accelerating voltage of 5 kV.

2.10.3. Cell viability and proliferation

Cell viability and proliferation onto collagen-silica scaffolds were evaluated with resazurin assay. Non-fluorescent resazurin dye is reduced to fluorescent resorufin by mitochondrial oxidoreductase reactions in live cells. The fluorescence of produced resorufin is proportional to the number of living cells. For the test, collagen-silica and collagen scaffolds (for comparative purposes) were divided by mass into equal parts. Each part of the collagen-silica scaffold and collagen scaffold weighed 1.5 ± 0.2 mg and 0.8 ± 0.2 mg, respectively. Each piece of the scaffolds was inserted in each well of a non-treated 96-well plate (Cat. No. 734-2781, VWR, USA) and incubated in cell culture medium overnight (37 °C, 5% CO₂). Then, the cells at the density of $9.3 \cdot 10^4$ cells/mL were seeded onto each scaffold and incubated for 2, 7, and 14 days. In control conditions, cells were seeded directly onto the wells of TC-treated 96-well plate (Cat. No. 734-2327). To assess the background signal, parts of each scaffold were incubated in a cell culture medium without cells and underwent the same procedure. At each time point, the conditioned medium was replaced with 200 µL of medium supplemented with resazurin sodium salt at a concentration of 0.01 mg/mL (R7017, Sigma-Aldrich, USA). After 4-hour incubation (37 °C, 5% CO₂) 100 µL from each well was transferred to the new dark-wall plate. The fluorescence was measured with a microplate reader (Synergy Mx microplate reader, BioTek, Winooski, US) at Ex/Em of 535/590 nm. To evaluate the viability of the cell attached to the scaffolds, the fluorescence of the background (scaffolds without the cells) was subtracted from the fluorescence of scaffolds with cells. Three independent experiments were done, each performed in triplicates. Comparative data were analyzed with the unpaired Student's t-test using the STATISTICA 13.3 software (Statsoft, Cracow, Poland). P values < 0.05 were considered statistically significant.

2.10.4. Cell infiltration

Immunofluorescence staining was performed to verify the cellular infiltration into the collagen-silica and collagen scaffolds (for comparative purposes). Cells were seeded and incubated according to the procedure described in section 2.10.3. After each incubation interval, the conditioned medium was discarded, scaffolds were washed three times with PBS, and fixed with 150 µL of 4% paraformaldehyde (20 min, room temperature). Then, the cells were permeabilized with 0.2% TritonX-100 in PBS under stirring in an orbital shaker (50 rpm, room temperature, 20 min), blocked with 1% in PBS (50 rpm, room temperature, 30 min), and incubated with

Alexa Fluor 488 phalloidin (1:100, Cat. No. A12379, Invitrogen™) in BSA/PBS solution protected from light under stirring (50 rpm, room temperature, 20 min). Before visualization, cells were rinsed with PBS and z-stack image acquisition was performed with a confocal laser scanning microscope Leica TCS SP5 (Wetzlar, Germany).

2.10.5. *In vivo* Chorioallantoic Membrane (CAM) assay

A CAM assay was performed to verify the biocompatibility of collagen-silica scaffolds *in vivo*. The chicken eggs were prepared (window opening) at embryonic development day (EDD) 3, to allow the growth of the CAM detached from the shell. For the test, collagen-silica and collagen scaffolds (for comparative purposes) were divided by mass into equal parts. Each part of collagen silica and collagen scaffold weighed 1.5 ± 0.2 mg and 0.8 ± 0.2 mg, respectively. At EDD10, parts of collagen-silica scaffolds and collagen scaffolds were applied directly on the CAM inside a silicone ring, and subsequently hydrated with 50 μ L of PBS. The same volume of PBS was also used as a control. At the endpoint (EDD13), the presence of toxicity symptoms, such as CAM morphology and vascular changes (membrane discoloration, coagulation, hemorrhages, and ghost vessels – vessels devoid of blood), and lethal effects (embryo death) was analyzed *in ovo* under a stereoscope at 20 X magnification (Olympus, SZX16 coupled with a DP71 camera). To determine the effect of scaffolds on angiogenesis, the CAMs were fixed (10% neutral-buffered formalin), excised from the embryo, and photographed *ex ovo* (Olympus, SZX16 coupled with a DP71 camera). The number of new vessels growing towards the inoculation site, delimited by the ring mark was counted (less than 20 μ m in diameter) with the Cell^A Olympus program. Excised CAMs were paraffin-embedded for slide sections and stained with hematoxylin-eosin (H&E) for histological evaluation of CAM/collagen-silica scaffold interface in terms of cellularization and vascularization (Olympus IX83 coupled with DP74 camera). Assay was performed as two independent experiments of at least ten replicates per each condition. Comparative data were analyzed with the unpaired Student's t-test using the STATISTICA 13.3 software (Statsoft, Cracow, Poland). The p values ≤ 0.05 were considered statistically significant. The corresponding images were performed with The Leica TCS SP5 Confocal (Wetzlar, Germany).

3. Results and discussion

3.1. Collagen-silica scaffold characterization

Cylindrical-shaped collagen-silica scaffolds were successfully obtained (**Fig 1A, B**). The mean mass, height, and diameter, calculated for 10 samples, were 22.19 ± 0.12 mg, 10 ± 0.94 mm, and 7 ± 0.67 mm, respectively. The microstructure and surface morphology were evaluated by SEM. **Fig. 1C-E** shows the collagen-silica scaffold cross-section and the images of silica components: bioglass (BG) and drug-loaded mesoporous silica (MCM-PDMS-CIP). The porosity [%], minimum, maximum, and mean pore size [μ m] were measured quantitatively with ImageJ software by analyzing 5 cross-section images of collagen-silica scaffolds. Collagen-silica scaffolds texture was characterized as heterogenous with highly interconnected and open macropores. The porosity was $45.81 \pm 7.50\%$; whereas, the variability of pore diameters was determined in the range of 45.37-292.03 μ m with the mean pore size of 141.44 ± 12.64 μ m. Since natural bone exhibits variability in pore

diameter and structure, bone tissue biomaterials should exert heterogeneous and macroporous structures to provide cell infiltration, growth, migration, nutrients, and mass transport (Koons et al., 2020; Wei et al., 2010). The optimal width of pores in the three-dimensional scaffolds dedicated to bone tissue engineering is between 100 and 300 μm (Moncayo-Donoso et al., 2021). Zhang et al. indicated the range of 150-250 μm as the most favorable for cartilage regeneration based on the analysis of collagen scaffolds characterized by various ranges of pore size (Zhang et al., 2014). Moreover, the interconnectivity of pores enhances the osteoconduction process during which bone-forming cells penetrate the scaffold and replace it with new bone over time (Wypych, 2018). Therefore, the porosity parameters of our collagen-silica scaffolds were considered satisfactory and potentially favorable for bone tissue integration. Both MCM-CIP-PDMS and BG powders distribution inside collagen-silica scaffolds was analyzed with micro-CT scanning (**Fig. 1 F, G**). According to the scale bar, the lowest density phase is represented as black, and the highest density phase is represented as blue. Collagen fibers were invisible for micro-CT due to their low density and X-rays transparency, which is a well-known phenomenon (Zidek et al., 2016). The images and cross-sections revealed homogeneously distributed BG (blue) and MCM-CIP-PDMS particles (orange) in a three-dimensional collagen matrix as it is shown in **Fig. 1F**. BG particles were individually dispersed in the bulk; whereas, MCM-CIP-PDMS formed larger agglomerates. This was probably due to the hydrophobic nature of MCM-CIP-PDMS as the result of the blending of CIP-loaded MCM with hydrophobic PDMS and its further separation during suspending in the hydrophilic collagen solution. A similar phenomenon was observed in our previous studies (Skwira et al., 2020).

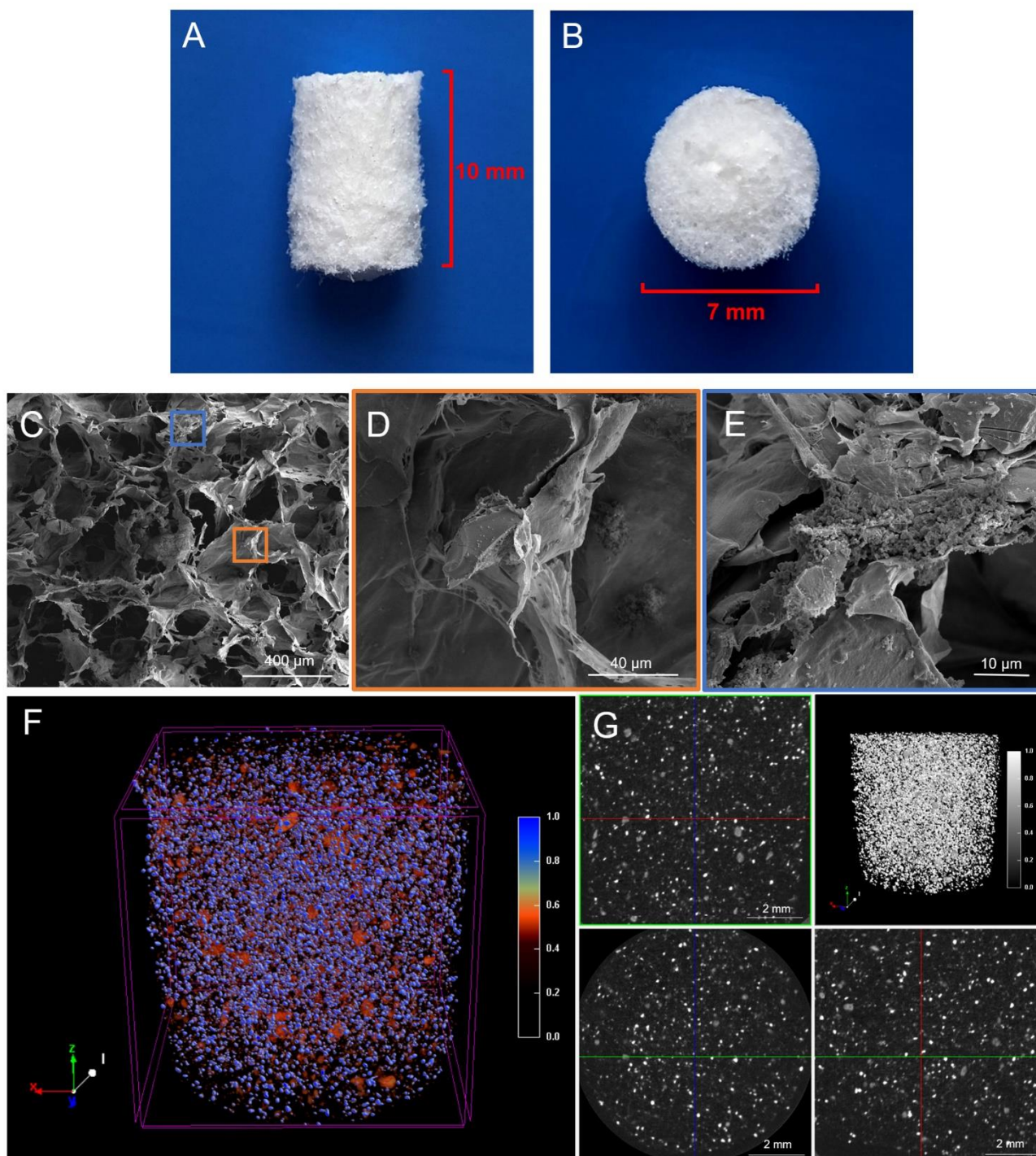


Fig. 1. Photographs of collagen-silica scaffolds: view from the side (A), and from the top (B). SEM images of collagen-silica scaffold cross-section (C), bioglass (D), and ciprofloxacin-loaded mesoporous silica (E). Three-dimensional micro-CT image of collagen-silica scaffold (F) together with cross-sections (G); cross-hair lines – each color matches the specific cutting line with the cross-section.

3.2. FTIR analysis of collagen-silica scaffolds

The FTIR spectra of collagen-silica scaffolds and pristine components, such as COL, BG, and MCM-CIP-PDMS were presented in **Fig. 2**. In the spectrum of the collagen-silica scaffold the following bands characteristic

for COL were observed. Stretching vibrations of **N-H** at 3430 cm^{-1} (amide A; overlapped with the band attributed to O-H), **N-H** at 3068 cm^{-1} , **C-H** at 2850 cm^{-1} , 2928 cm^{-1} , 2963 cm^{-1} (amide B), **C=O** at 1663 cm^{-1} (amide I), **N-H** at 1549 cm^{-1} (amide II), and **C-N** at 1340 cm^{-1} , and bending vibrations of **C-H** at 1445 and 1410 cm^{-1} (Belbachir et al., 2009; Douglas and Haugen, 2008). This spectrum also presented stretching vibrations of **Si-C** at 1260 cm^{-1} , **Si-O-Si** at 1092 cm^{-1} and 800 cm^{-1} , and bending vibrations of **O-Si-O** at 460 cm^{-1} typical for MCM-CIP-PDMS and BG (Skwira et al., 2020). There was no band in the spectrum of collagen-silica scaffold characteristic for CIP. It was explained by the CIP amount below the detection limit of the FTIR method. However, the spectrum of MCM-CIP-PDMS revealed characteristic bands for CIP at 1704 cm^{-1} , 1621 cm^{-1} , 1492 cm^{-1} , and 1451 cm^{-1} attributed to stretching vibrations of **C=O** (-COOH), **C=O**, **C-H**, and aromatic **C=C**, respectively (**Supplementary Material 1**) (Durgapal et al., 2017).

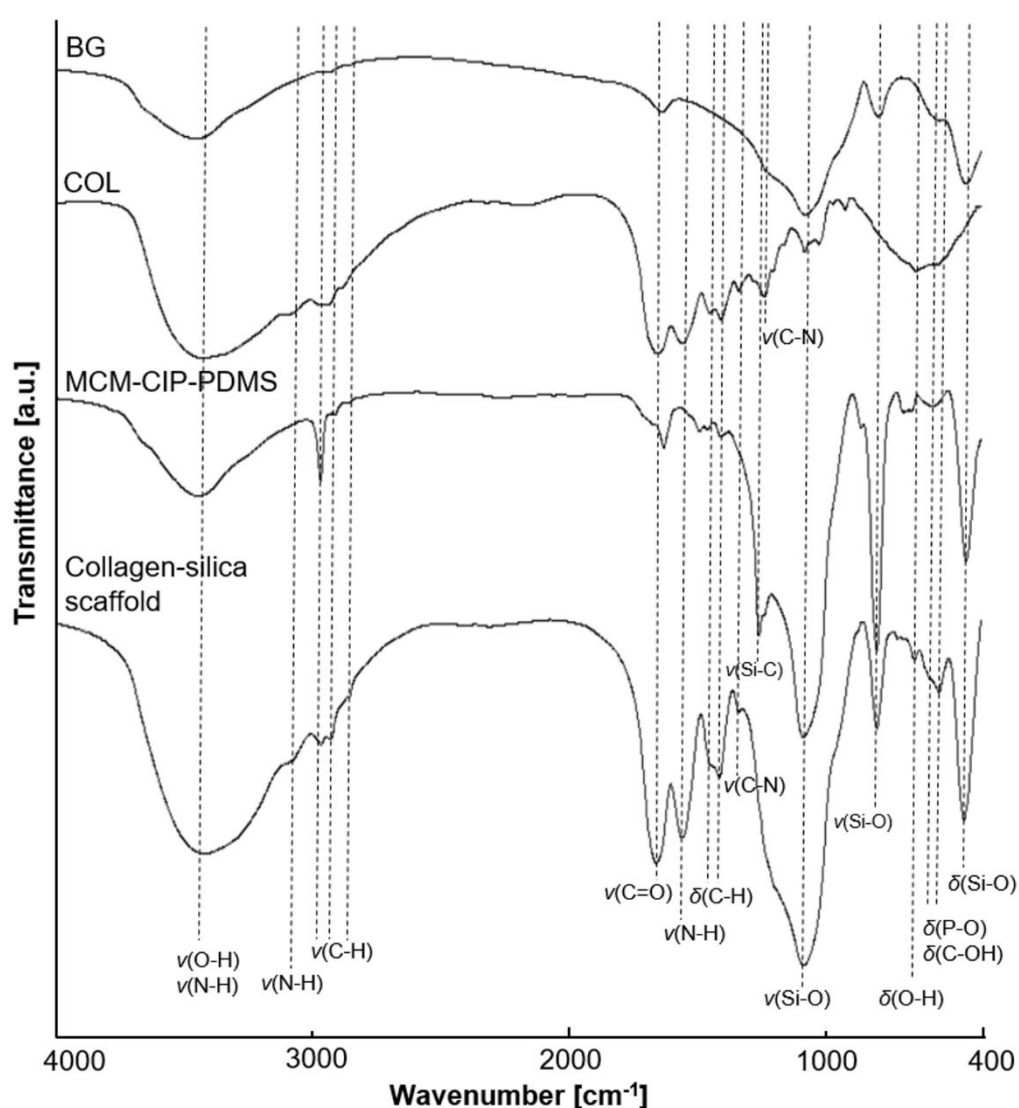


Fig. 2. FTIR spectra of collagen-silica scaffold and components: collagen (COL), bioglass (BG), and ciprofloxacin-loaded mesoporous silica blended with polydimethylsiloxane (MCM-CIP-PDMS); ν – stretching vibrations, δ – bending vibrations.

2.1. Texture analysis

The mechanical properties of the collagen-silica scaffolds and collagen scaffolds are presented in **Table 1**. To avoid the breaking-up of the porous structure after freeze-drying, the collagen scaffolds are often crosslinked with the usage of chemical crosslinkers, such as glutaraldehyde, N-hydroxysuccinimide, and 1-ethyl-3-(3-dimethylaminopropyl) (Nong et al., 2019; Tian et al., 2014). However, due to the cytotoxicity of chemical crosslinkers, this method requires a washing step to remove the residuals. In the case of our collagen-silica scaffolds, which are suspected to serve as drug delivery systems, the final washing cannot be performed to avoid the loss of drug content. Collagen blending with inorganic materials is one of the two methods of structure reinforcement commonly used in practical applications (Jiang et al., 2022). Indeed, when the collagen was freeze-dried without the addition of silica, the final product was irregular in shape and densely packed (**Supplementary material 2**) which might be the reason for the higher compressive modulus value compared to the collagen-silica scaffold. Interestingly, both collagen-silica scaffolds and collagen scaffolds were characterized by comparable plasticity and hardness. More importantly, the mechanical properties of collagen-silica scaffolds seemed to be sufficient to protect the scaffolds from fracture and rapid disintegration during further investigations. A similar conclusion was made in the previous studies (Antebi et al., 2013; Kane and Roeder, 2012) in which the compressive modulus in the range of 5-200 kPa of collagen-hydroxyapatite scaffolds for bone tissue engineering was considered satisfactory.

Table 1. Mechanical parameters of collagen-silica scaffolds and collagen scaffolds.

Sample	Hardness [N]	Compressive modulus [kPa]	Plasticity [%]
Collagen-silica scaffolds	0.39	11.4	75.9
Collagen scaffolds	0.35	17.7	76.3

2.2. Mineralization potential assay

During the preliminary studies, the 7-day mineralization potential assay was carried out in SBF for the collagen-silica scaffolds and collagen scaffolds for comparative purposes. Since collagen scaffolds did not exert an increase in band intensities attributed to HAp after 7 days of incubation (**Supplementary material 3**), they were excluded from further steps of this study.

In **Fig. 3** the progressive formation of hydroxyapatite (Hap) on the surface of collagen-silica scaffolds is presented. The FTIR spectra revealed the increasing intensity of the bands at 605 cm^{-1} and 566 cm^{-1} attributed to bending vibrations of $(\text{PO}_4)^{3-}$ characteristic for HAp. Moreover, the broadening of the band with a maximum peak at 1090 cm^{-1} towards lower wavelengths was observed during the time of incubation. It was attributed to the increase in the intensity of $(\text{PO}_4)^{3-}$ vibrational modes at 1040 cm^{-1} (Prokopowicz et al., 2020). The increase in the intensity of the band at 870 cm^{-1} , attributed to stretching vibrations of CO_3^{2-} , indicated the incorporation of carbonates into the formed hydroxyapatite structure (Prokopowicz et al., 2014). It is a desirable phenomenon as biological apatite is described as carbonated hydroxyapatite (Kono et al., 2022). Similarly, the increase in

intensity was also observed for bands at 1448 cm^{-1} and 1415 cm^{-1} in the spectra of scaffolds after 14 and 21 days. However, due to the overlapping of CO_3^{2-} and C-H bands (attributed to collagen), the initial decrease of these bands after 7 days might be associated with collagen degradation. Progressive degradation was also confirmed by changes in the intensity of bands typical for collagen. The decrease was observed in the case of bands at 2921 cm^{-1} , 2852 cm^{-1} attributed to C-H stretching modes, 1657 cm^{-1} , and 1558 cm^{-1} attributed to C=O and N-H, respectively. On the other hand, the increase of band attributed to C-N stretching mode (amide III) at 1240 cm^{-1} , which was not detected in the scaffold before incubation, was observed. Moreover, after 7 days of incubation, degradation of collagen structure revealed bands at 1260 cm^{-1} , and 800 cm^{-1} attributed to Si-C and O-Si-O modes of MCM-CIP-PDMS (**Fig. 2**). These observations agreed with the degradation results (**Supplementary Material 4**). They revealed 60.33% weight loss of collagen-silica scaffolds after 21 days of incubation in distilled water. Collagen degradability is a well-known phenomenon considered as a desirable feature of implantable bioactive materials. During implant degradation, newly-formed bone tissue grows into the biomaterial and progressively replaces it (Wei et al., 2020).

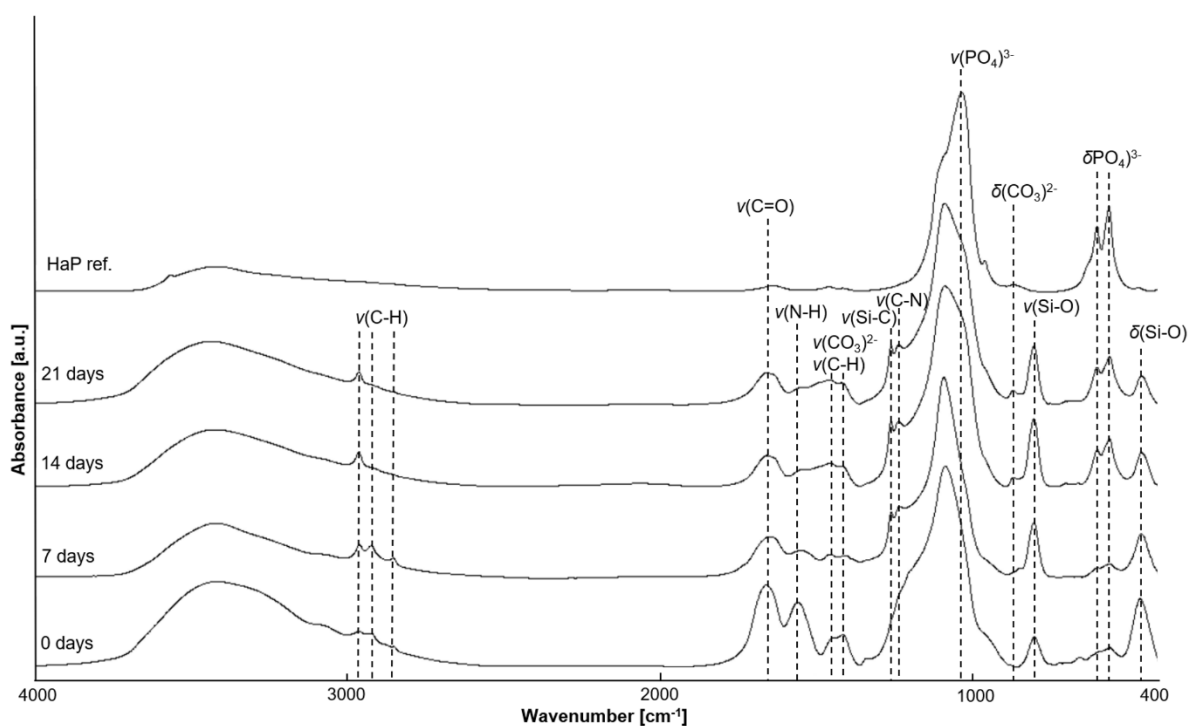


Fig. 3. FTIR spectra of collagen-silica scaffolds before (0 days) and after 7, 14, and 21 days of incubation in SBF together with a hydroxyapatite reference sample (HAp) (ν – stretching vibrations, δ – bending vibrations).

The progressive formation of HAp onto the surface of collagen-silica scaffolds was also confirmed with the SEM-EDX analysis (**Fig. 4**). Before immersion, the smooth surface of collagen may be noted. After 7 days of incubation, collagen-silica scaffolds were partially covered by spherical-shaped HAp. During the next days of incubation, the thickening, and spreading of the HAp layer were observed, with intermittent uncovered areas of collagen fibrils. After 21 days of immersion, a continuous layer of HAp was observed. It was further confirmed by X-ray diffraction analysis, in which diffraction peaks characteristic for the HAp phase were detected

(Supplementary material 5). These observations were in correspondence to the average weight content of osteogenic ions calculated from EDX spectra (**Table 2**). The weight contents of Ca and P in investigated SEM areas were increasing progressively in time (from 1.65 and 0.29% before incubation in SBF, up to 14.21 and 5.41% after 21 days of mineralization assay for Ca and P, respectively). The bone mineralization process is highly related to the structure of collagen type I. It plays a crucial role in HAp crystals depositing (Burger et al., 2008). Active sites of apatite nucleation are located in the interior of collagen fibers. A specific arrangement of collagen microfibrils creates microchannels that promote calcium and phosphate ions influx and nucleation of apatite (Wiesmann et al., 2004). Then, collagen fibrils constitute a template for the longitudinal HAp crystals growth (Zhang et al., 2003). The bioactivity of bioglasses is expressed as the induction of bone-like apatite formation due to their proven biodegradability (Skwira et al., 2023). Herein, collagen fibrils served as a scaffold for HAp deposition driven by osteogenic ions released from bioglass incorporated in collagen-silica scaffolds.

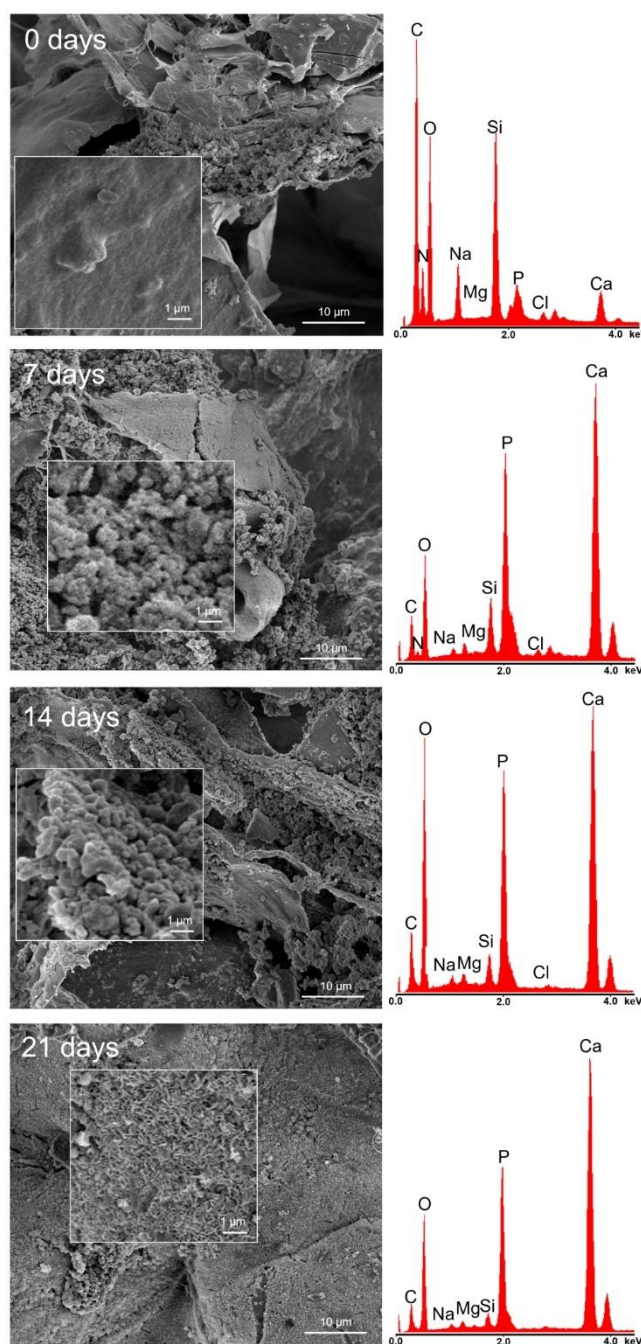


Fig. 4. SEM micrographs with corresponding EDX spectra of collagen-silica scaffolds before (0 days) and after 7, 14, and 21 days of incubation in SBF.

After 21 days of immersion, a continuous layer of HAP was observed. It was further confirmed by X-ray diffraction analysis, in which diffraction peaks characteristic for the HAP phase were detected (**Supplementary material 5**). These observations were in correspondence to the average weight content of osteogenic ions calculated from EDX spectra (**Table 2**). The weight contents of Ca and P in investigated SEM areas were increasing progressively in time (from 1.65 and 0.29% before incubation in SBF, up to 14.21 and 5.41% after 21 days of mineralization assay for Ca and P, respectively). The bone mineralization process is highly related to the structure of collagen type I. It plays a crucial role in HAP crystals depositing (Burger et al., 2008). Active

sites of apatite nucleation are located in the interior of collagen fibers. A specific arrangement of collagen microfibrils creates microchannels that promote calcium and phosphate ions influx and nucleation of apatite (Wiesmann et al., 2004). Then, collagen fibrils constitute a template for the longitudinal HAp crystals growth (Zhang et al., 2003). The bioactivity of bioglasses is expressed as the induction of bone-like apatite formation due to their proven biodegradability (Skwira et al., 2023). Herein, collagen fibrils served as a scaffold for HAp deposition driven by osteogenic ions released from bioglass incorporated in collagen-silica scaffolds.

Table 2. Average weight content [%] of Ca and P in collagen-silica scaffolds during incubation in SBF.

Time of incubation [days]	Weight content	
	Ca [%]	P [%]
0	1.65	0.29
7	5.73	1.84
14	10.71	4.32
21	14.21	5.41

2.3. Drug release studies

The drug release studies were performed for the collagen-silica scaffolds and the CIP-loaded collagen scaffolds (**Fig. 5**) with calculated kinetic parameters presented in **Table 3**. The CIP-loaded collagen scaffolds (blue graph) released the total amount of antibiotic within 2 h during the burst stage. In the case of collagen-silica scaffolds, the biphasic drug release profile was observed (green graph) with the initial release of ciprofloxacin equaling 44% during the first 24 h followed by a prolonged release up to 80 days. The reduced burst release of CIP from the collagen-silica scaffold was confirmed by the lower k_H value (20.97 and 653.77 $\text{day}^{-1/2}$ for collagen-silica and CIP-loaded collagen scaffolds, respectively). Moreover, the n values of the Kosmeyer-Peppas model were 0.7 for CIP-loaded collagen scaffolds and 0.3 for collagen-silica scaffolds denoting the non-Fickian and Fickian diffusion as dominant release mechanisms, respectively. After the first 24 h, the stage of prolonged release was observed in the release profile of the collagen-silica scaffold that followed the zero-order kinetics (0.69% of loaded CIP was released per day, $R^2=0.9394$). The micro-CT results (**Fig. 1 F, G**) revealed the homogenous distribution of MCM-CIP-PDMS in the bulk of collagen-silica scaffolds suggesting a matrix-type delivery system. It is known that in the case of hydrophilic matrices, the typical diffusion-controlled drug release might be affected by polymer degradation in time (Patel et al., 2011). It agreed with the results of the scaffold degradation assay which proved progressive collagen matrix degradation (**Supplementary Material 4**). The significant modification of drug release in the silica formulations containing PDMS was observed in our previous work (Skwira et al., 2020). We noted that the increase of PDMS content in the formulations had resulted in a decrease in initial burst release and an extension of the time of release (Skwira et al., 2019). Thus, herein, the content of PDMS was carefully selected to provide a relatively high initial dose of antibiotic followed by lower maintenance doses released during the next days. We explained the mechanism of drug release modification by PDMS occlusion of drug-loaded mesopores in silica particles (Skwira et al., 2020). Moreover,

the addition of PDMS to drug-loaded mesoporous silica resulted in drug entrapment within hydrophobic agglomerates formed during suspending of silica components in collagen type I aqueous solution (**Fig. 1E, F**).

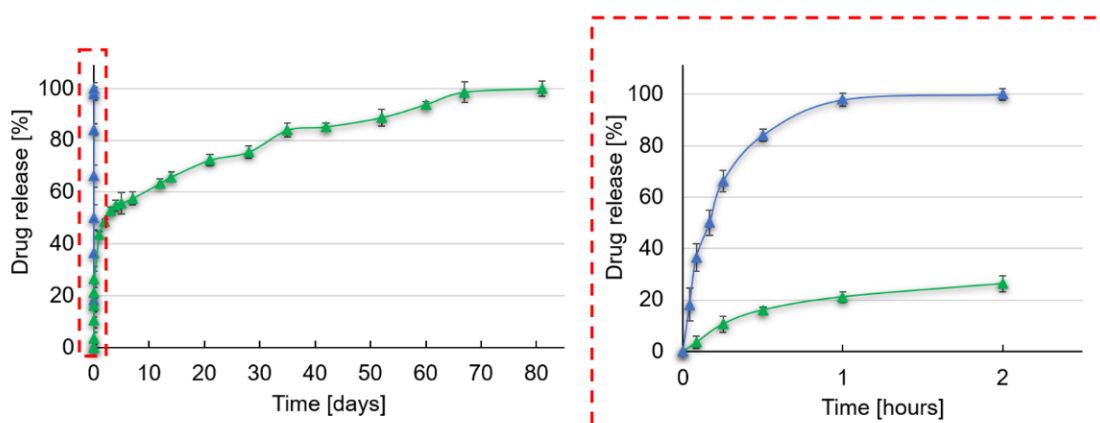


Fig. 5. Drug release profiles of collagen-silica scaffolds (green) and CIP-loaded collagen scaffolds (blue).

Currently, collagen-based drug delivery systems usually release antibiotics for only 10 days (Oshima et al., 2020; Roth et al., 2019). Herein, the significantly prolonged release of ciprofloxacin up to 80 days is possibly governed by a complex mechanism involving the degradation of the collagen matrix and the diffusion from MCM-CIP-PDMS.

Table 3. The kinetic parameters of fitted experimental data for CIP-loaded collagen scaffolds and collagen-silica scaffolds.

Sample	Higuchi model		Korsmeyer-Peppas model		Zero-order kinetics ^a	
	k_H	R^2	n	R^2	k_0	R^2
CIP-loaded collagen scaffolds	653.77	0.9797	0.70	0.9712	-	-
Collagen-silica scaffolds	20.97	0.8798	0.30	0.8865	0.69	0.9394

R^2 – coefficient of determination, k_H – Higuchi dissolution constant ($\text{day}^{-1/2}$), n – exponent related to the drug release mechanism, k_0 – zero-order release constant ($\%/ \text{day}$).

^a calculated excluding the first 24 h of CIP release

2.4. Antibacterial activity

In the present study, the antimicrobial effectiveness of collagen-silica scaffolds in terms of the ability to inhibit the development of biofilms (sessile population) and bacterial growth in the surrounding medium (planktonic population) was evaluated (**Fig. 6**). Antimicrobial evaluation test by CFUs counting method showed the collagen-silica scaffolds bactericidal activity on both sessile and planktonic populations of *S.aureus* (**Fig. 6A**); as opposed to collagen scaffolds. These results were in agreement with SEM imaging which revealed the presence of *S.aureus* biofilm onto the collagen scaffolds and the bacteria-free surface of collagen-silica scaffolds after 24-hour incubation (**Fig. 6B**). A susceptibility to microbial colonization is a crucial factor of implantable biomaterials, especially in the case of highly hydrophilic collagen matrices (Oliveira et al., 2010) which may be

avored for bacterial adhesion. It is noteworthy that the antibiotic tolerance of bacteria increases when they grow in the biofilm (Smith et al., 2022). The obtained results suggest that the released dose of ciprofloxacin protected the collagen-silica scaffolds from *S. aureus* attachment which is the first step of biofilm development. It is also important to note that the manufacturing process of collagen-silica scaffolds did not impair the pharmacological activity of a drug.

2.5. Osteoblast attachment, infiltration, and proliferation

Cell attachment was analyzed with SEM. After 24-hour incubation, osteoblasts were found to be distributed onto the surfaces of collagen-silica scaffolds and collagen scaffolds (for comparative purposes) presenting spread and elongated morphology (**Fig. 7A**). It is known that the shape of attached cells may differ considering the surface properties of investigated biomaterials. Rabel et al. demonstrated that the spreading and elongation of osteoblasts favor their proliferation and differentiation, contrarily to cellular roundness which decreases metabolic activity (Rabel et al., 2020). Moreover, as presented in **Fig. 7A**, the collagen structure also changed and revealed thin fibrils entangled into a tight network when compared to the primary microstructure observed in **Fig. 1A**. It may be caused by the modest increase of collagen hydrogel pH after incubation in the cell culture medium (pH = 8.13 (Skwira et al., 2023)). These observations corresponded to Achilli and Mantovani's results which pointed out the decrease in fibril diameter with an increase in pH (Achilli and Mantovani, 2010).

To evaluate the proliferation of attached cells, the resazurin assay was performed both for the cells seeded onto collagen-silica scaffolds and collagen scaffolds. The intensity of fluorescence corresponding to the metabolic activity of live cells was measured on days 2, 7, and 14. There were no significant differences found between the osteoblasts seeded onto both types of scaffolds during the whole period of incubation (**Fig. 7B**). The cells were metabolically active and proliferated over time until day 14 when they entirely covered the scaffolds with the monolayer. This indicates that the scaffolds did not exert cytotoxicity toward osteoblasts. Additionally, the immunofluorescent staining revealed cellular infiltration of the three-dimensional collagen-silica and collagen bulk (**Fig. 7C**). It confirmed that collagen macroporous structure, preferred by osteoblasts, has not been impaired by the incorporation of silica components.

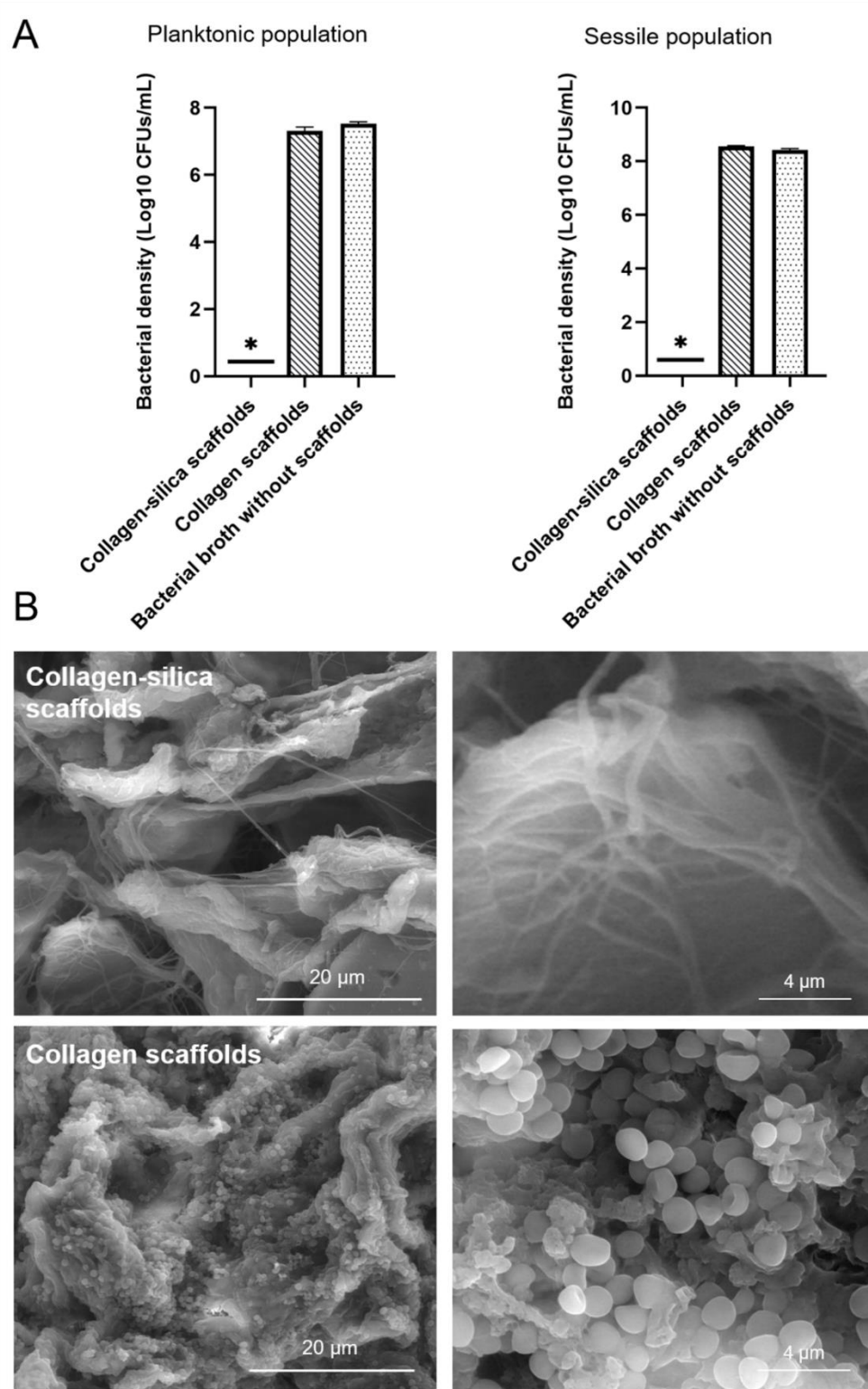


Fig. 6. Antibacterial activity of collagen-silica and collagen scaffolds (for comparative purposes) against the planktonic and sessile *S.aureus* population (A) together with SEM images of the sessile population onto collagen-silica and collagen scaffolds (B). * $p < 0.05$, significant differences compared to control positive (bacterial broth without scaffold).

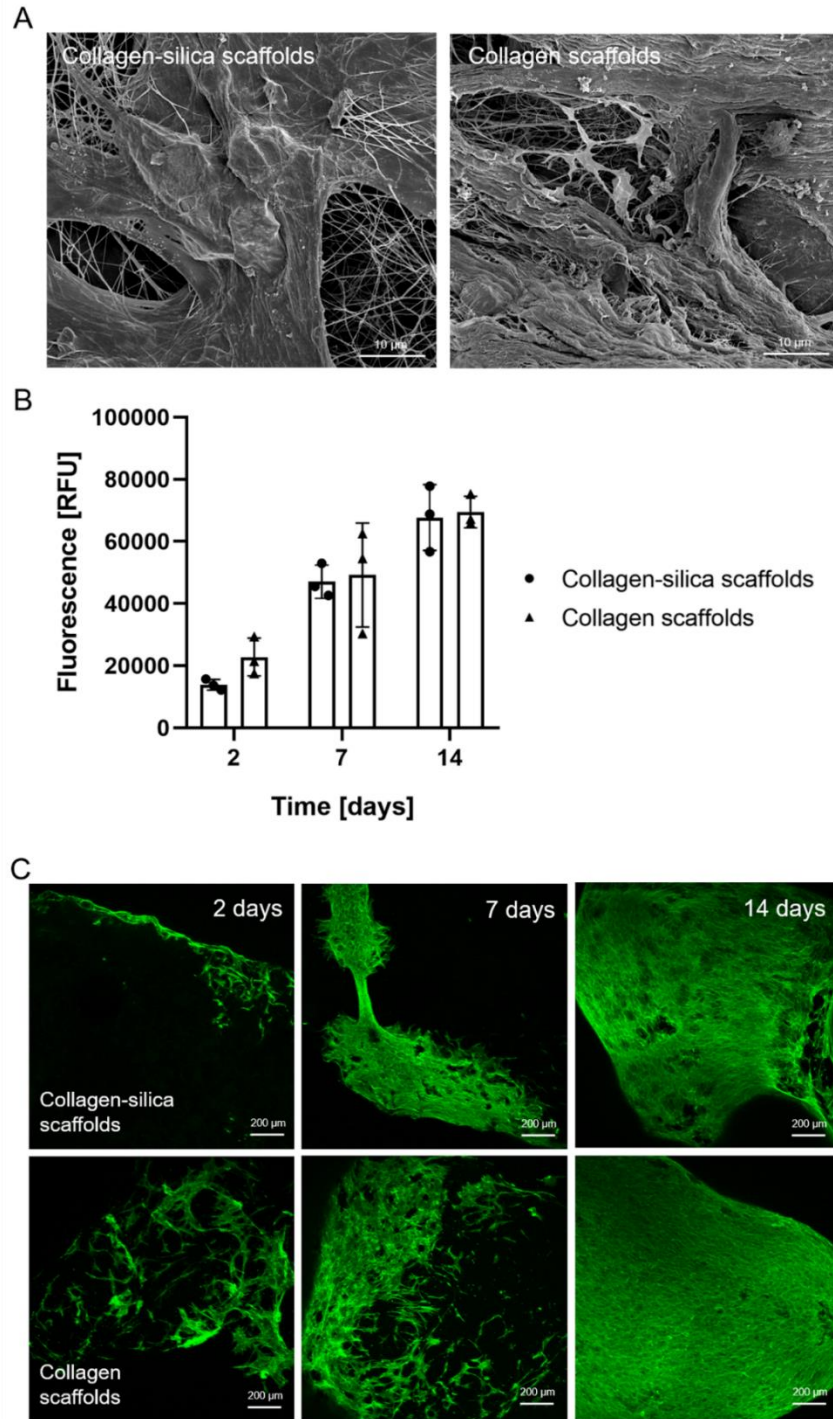


Fig. 7. SEM micrographs of osteoblasts attached to collagen-silica scaffolds and collagen scaffolds (A); osteoblast proliferation onto collagen-silica scaffolds and collagen scaffolds (B) together with immunofluorescent images of cellular infiltration (C).

2.6. *In vivo* chicken embryo chorioallantoic membrane (CAM) assay

The chorioallantoic membrane (CAM) assays were established as an alternative model to conventional *in vivo* experimentation, which highly meets the ethical criteria (principles of the 3Rs – Replacement, Reduction, Refinement) (Buhr et al., 2020). Since chicken embryos have a circulatory system and organic functions, they

have been used in versatile applications, e.g. evaluation of nanomaterials toxicity (Ahmad et al., 2016), screening of nanoparticles with anticancer activity (Mitrevska et al., 2023), determination of lethal dose of pharmaceuticals (Kue et al., 2014), or studies on human bone regeneration (Moreno-Jiménez et al., 2016). Since this method is comparable to mouse assays, it gains increasing interest as a valuable preclinical model for extensive testing of biomaterials biocompatibility (Giovannini et al., 2018; Vu et al., 2018). The main advantage of *in vivo* CAM method over other *in vivo* approaches is an excellent visualization of initial tissue response. Collagen-silica scaffold biocompatibility was assessed using *in vivo* CAM assay (Fig. 8). According to the literature the toxicity of substance may cause significant morphological and vascular changes in CAM. It was observed that tested material might cause coagulations, hemorrhages, membrane discolorations, and ghost vessels as a result of their toxicity (Ahmad et al., 2016; Rampino et al., 2013; Tang et al., 2018). Moreover, an important indicator of biomaterial toxicity is chick embryo mortality.

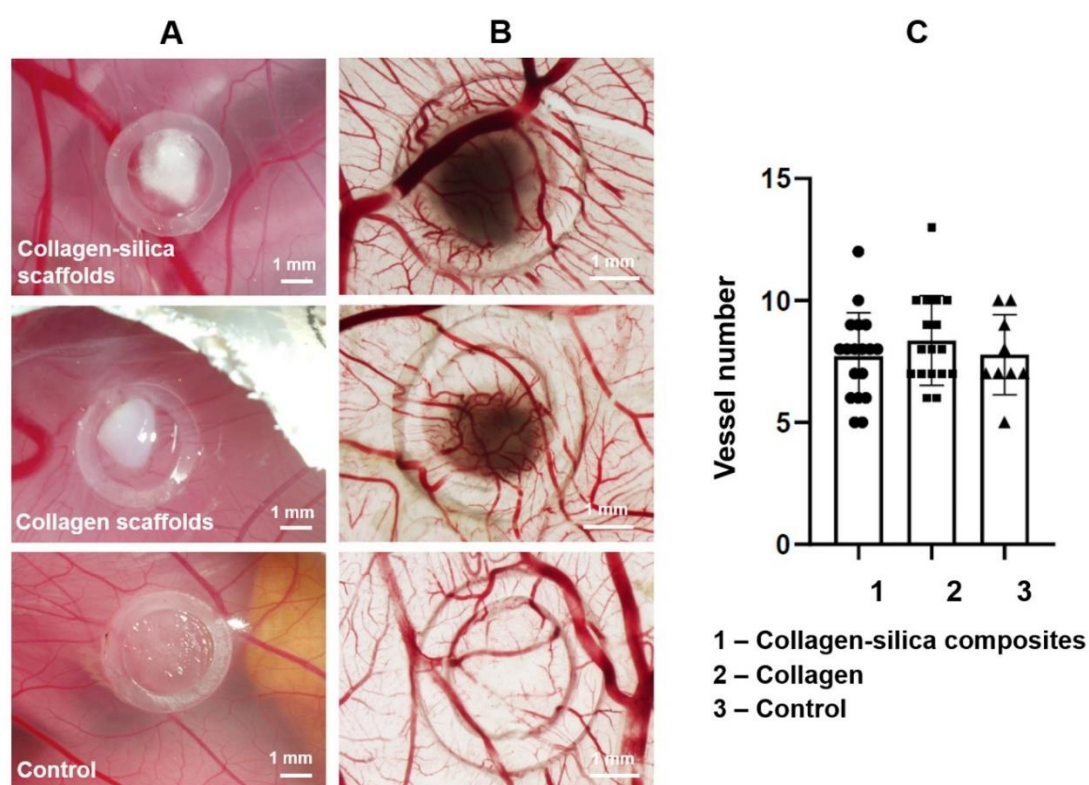


Fig. 8. *In vivo* CAM assay. Representative images used for the analysis of toxicity symptoms *in ovo* (A); the representative images (B) and graph (C) of the *ex ovo* analysis of angiogenesis.

No vascular changes were detected in the eggs inoculated with collagen-silica scaffolds, collagen scaffolds, and PBS (Fig. 8A). Moreover, the number of vessels created during incubation with collagen-silica scaffolds, collagen scaffolds, and PBS did not differ from each other (Fig. 8B). It suggests that the scaffolds did not affect the angiogenesis which is a natural process during embryo development. No death was observed for embryos incubated with collagen-silica scaffolds; whereas, two embryos died during incubation with collagen scaffolds and one during incubation with PBS. The overall viability of embryos during the experimental procedure should be around 90%. In this study, the mortality rate did not exceed 10% which was within the expected value.

Therefore, it may be stated that the scaffolds did not show toxicity in CAM. These results agreed with the *in vitro* cytotoxicity assay (Fig. 7).

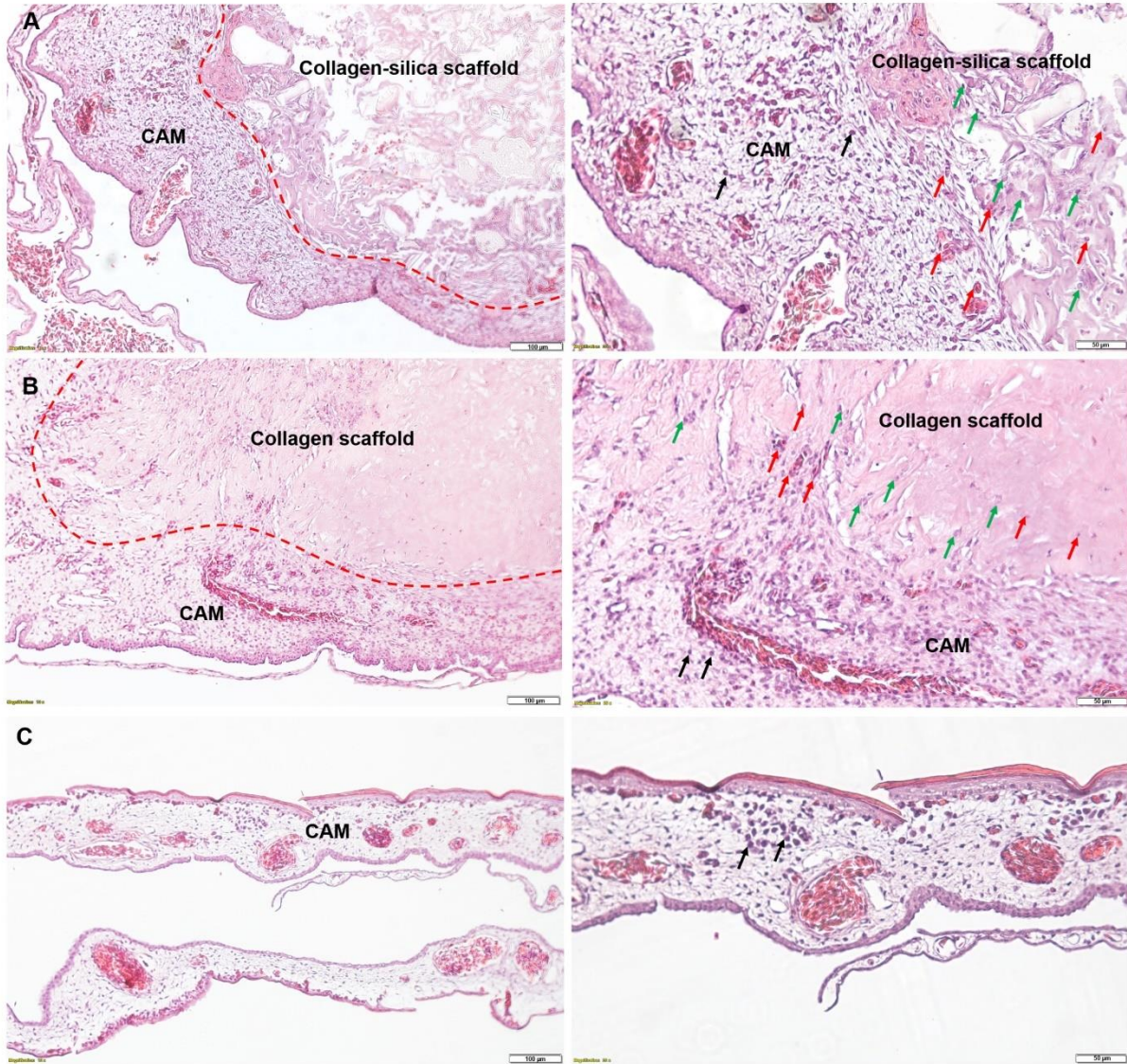


Fig. 9. H&E staining of excised CAM integrated with collagen-silica scaffold (A), collagen scaffold (B), and excised CAM incubated with PBS (C). CAM mesenchymal cells – green arrows; blood cells – red arrows; immune cell precursors – black arrows.

The integration with host tissue, expressed by cellularization and vascularization, is a critical factor in the clinical success of implantable biomaterials (Reis, 2014). Mangir et al. proved the usability of CAM in consideration of biomaterial/tissue integration (Mangir et al., 2019). To evaluate the initial tissue response to the collagen-silica scaffolds, collagen scaffolds, and PBS (control), H&E staining of excised CAM was performed. In Fig 9, green arrows indicate the CAM mesenchymal cells infiltration into the pores of the collagen-silica scaffold (Fig. 9A) as well as the collagen scaffold (Fig. 9B). Moreover, the analysis revealed the blood cells and microvasculature (red arrows) growth inside the scaffolds proving their high biocompatibility and capability to integrate with host bone tissue. Some immune cell precursors (blue arrows) were detected in

the images presented in the collagen-silica scaffold/CAM interface, collagen scaffold/CAM interface, and PBS (control). According to the literature, the CAM model might be considered immunocompetent only after EDD 18. Therefore, the occurrence of immune cell precursors may be attributed to the development of an immune system in chick embryos, which typically starts from EDD10 (Mangir et al., 2019).

3. Conclusions

Herein, three-dimensional collagen scaffolds were incorporated with silica components: drug-loaded mesoporous silica and bioglass. Since the implantable system dedicated to the treatment of osteomyelitis should not only release the drug in a proper manner but also stimulate bone tissue regeneration, the multifunctionality of the proposed scaffolds was verified. Collagen-silica scaffolds showed high mineralization potential manifested as progressive carbonated hydroxyapatite formation during incubation in simulated body fluid. The release of ciprofloxacin was prolonged to 80 days, and the released antibiotic was effective against the planktonic and sessile population of *Staphylococcus aureus*. Macro- and heterogenous structure of collagen-silica scaffolds structure was favored by osteoblasts which revealed excellent attachment, infiltration into the bulk, and proliferation over time. These results emphasize collagen-silica scaffolds' capability to stimulate both cellular-independent, e.g. physical apatite precipitation and strongly osteoblast-controlled osteogenesis processes. Moreover, a slow collagen-silica scaffold degradation with the simultaneous release of osteogenic ions from incorporated bioglass seems to provide excellent conditions for efficient bone tissue regeneration. Notably, proposed collagen-silica scaffolds exhibited high biocompatibility towards chick embryos and desirable integration with CAM (tissue ingrowth into the scaffold structure). To conclude, based on the obtained results proposed collagen-silica scaffolds may serve as multifunctional drug delivery systems which not only release the antibiotic in a prolonged manner but also promote bone tissue regeneration. Further *in vivo* assays are necessary to fully determine collagen-scaffolds applicability; however, we hope that the proposed collagen-silica scaffolds may provide a novel strategy for long-term local treatment of osteomyelitis.

Acknowledgments

This research and publication of the article were supported by the National Science Centre Poland (project Preludium 20 no. 2021/41/N/NZ7/01877). Publication of the article was also partially supported by the project POWR.03.02.00-00-I035/16-00 co-financed by the European Union through the European Social Fund under the Operational Programme Knowledge Education Development 2014–2020.

CRedit authorship contribution statement

Skwira Adrianna: Writing – original draft, Methodology, Investigation, Data curation, Formal analysis, Validation, Software, Visualization, Funding acquisition. **Szewczyk Adrian:** Writing – review & editing, Methodology, Investigation, Validation, Software, Visualization. **Joana Barros:** Methodology, Investigation, Writing – review & editing. **Marta Laranjeira:** Methodology, Writing – review & editing. **Fernando Jorge Monteiro:** Writing – review & editing, Resources. **Sądej Rafał:** Writing – review & editing, Methodology, Resources. **Prokopowicz Magdalena:** Writing – review & editing, Conceptualization, Supervision, Project administration, Methodology, Resources.

References

- Achilli, M., Mantovani, D., 2010. Tailoring mechanical properties of collagen-based scaffolds for vascular tissue engineering: The effects of pH, temperature and ionic strength on gelation. *Polymers (Basel)*. 2, 664–680. <https://doi.org/10.3390/polym2040664>
- Ahmad, K.A., Mohammed, A.S., Abas, F., 2016. Chitosan nanoparticles as carriers for the delivery of FKAZ14 bacteriophage for oral biological control of colibacillosis in chickens. *Molecules* 21, 256. <https://doi.org/10.3390/molecules21030256>
- Antebi, B., Cheng, X., Harris, J.N., Gower, L.B., Chen, X.D., Ling, J., 2013. Biomimetic collagen-hydroxyapatite composite fabricated via a novel perfusion-flow mineralization technique. *Tissue Eng. - Part C Methods* 19, 487–496. <https://doi.org/10.1089/ten.tec.2012.0452>
- Belbachir, K., Noreen, R., Gouspillou, G., Petibois, C., 2009. Collagen types analysis and differentiation by FTIR spectroscopy. *Anal. Bioanal. Chem.* 395, 829–837. <https://doi.org/10.1007/s00216-009-3019-y>
- Blaha, J.D., Nelson, C.L., Frevert, L.F., Henry, S.L., Seligson, D., Esterhai, J.L., Heppenstal, R.B., Calhoun, J., Cobos, J., Mader, J., 1990. The use of septopal (polymethylmethacrylate beads with gentamicin) in the treatment of chronic osteomyelitis. *Instr. Course Lect.* 39, 509–514.
- Buhr, C.R., Wiesmann, N., Tanner, R.C., Brieger, J., Eckrich, J., 2020. The chorioallantoic membrane assay in nanotoxicological research—an alternative for in vivo experimentation. *Nanomaterials* 10, 1–16. <https://doi.org/10.3390/nano10122328>
- Burger, C., Zhou, H.W., Wang, H., Sics, I., Hsiao, B.S., Chu, B., Graham, L., Glimcher, M.J., 2008. Lateral packing of mineral crystals in bone collagen fibrils. *Biophys. J.* 95, 1985–1992. <https://doi.org/10.1529/biophysj.107.128355>
- Cornell, C.N., Lane, J.M., Chapman, M., Merkow, R., Seligson, D., Henry, S., Gustilo, R., Vincent, K., 1991. Multicenter trial of collagraft as bone graft substitute. *J. Orthop. Trauma* 5, 1–8. <https://doi.org/10.1097/00005131-199103000-00001>
- Douglas, T., Haugen, H.J., 2008. Coating of polyurethane scaffolds with collagen: Comparison of coating and cross-linking techniques. *J. Mater. Sci. Mater. Med.* 19, 2713–2719. <https://doi.org/10.1007/s10856-008-3393-6>
- Durgapal, S., Mukhopadhyay, S., Goswami, L., 2017. Preparation, characterization and evaluation of floating microparticles of ciprofloxacin. *Int. J. Appl. Pharm.* 9, 1–8. <https://doi.org/10.22159/ijap.2017v9i1.14183>
- Giovannini, G., Warncke, P., Fischer, D., Stranik, O., Hall, A.J., Gubala, V., 2018. Improving colloidal stability of silica nanoparticles when stored in responsive gel: application and toxicity study. *Nanotoxicology* 12, 407–422. <https://doi.org/10.1080/17435390.2018.1457729>
- Gisbert-Garzarán, M., Manzano, M., Vallet-Regí, M., 2020. Mesoporous silica nanoparticles for the treatment of complex bone diseases: Bone cancer, bone infection and osteoporosis. *Pharmaceutics* 12, 83. <https://doi.org/10.3390/pharmaceutics12010083>
- Gogia, J., Meehan, J., Di Cesare, P., Jamali, A., 2009. Local Antibiotic Therapy in Osteomyelitis. *Semin.*

- Plast. Surg. 23, 100–107. <https://doi.org/10.1055/s-0029-1214162>
- Götz, W., Tobiasch, E., Witzleben, S., Schulze, M., 2019. Effects of silicon compounds on biomineralization, osteogenesis, and hard tissue formation. *Pharmaceutics* 11, 117. <https://doi.org/10.3390/pharmaceutics11030117>
- Hojat, N., Piergiorgio, G., Ferreira, A.M., Šiller, L., 2023. Automatic pore size measurements from scanning electron microscopy images of porous scaffolds. *J. Porous Mater.* 93–101.
- Izquierdo-Barba, I., Sousa, E., Doadrio, J.C., Doadrio, A.L., Pariente, J.P., Martínez, A., Babonneau, F., Vallet-Regí, M., 2009. Influence of mesoporous structure type on the controlled delivery of drugs: Release of ibuprofen from MCM-48, SBA-15 and functionalized SBA-15. *J. Sol-Gel Sci. Technol.* 50, 421–429. <https://doi.org/10.1007/s10971-009-1932-3>
- Jiang, Y.-H., Lou, Y.-Y., Li, T.-H., Liu, B.-Z., Chen, K., Zhang, D., Li, T., 2022. Cross-linking methods of type I collagen-based scaffolds for cartilage tissue engineering. *Am. J. Transl. Res.* 14, 1146–1159.
- Kane, R.J., Roeder, R.K., 2012. Effects of hydroxyapatite reinforcement on the architecture and mechanical properties of freeze-dried collagen scaffolds. *J. Mech. Behav. Biomed. Mater.* 7, 41–49. <https://doi.org/10.1016/j.jmbbm.2011.09.010>
- Kokubo, T., Takadama, H., 2006. How useful is SBF in predicting in vivo bone bioactivity? *Biomaterials* 27, 2907–2915. <https://doi.org/10.1016/j.biomaterials.2006.01.017>
- Kono, T., Sakae, T., Nakada, H., Kaneda, T., Okada, H., 2022. Confusion between Carbonate Apatite and Biological Apatite (Carbonated Hydroxyapatite) in Bone and Teeth. *Minerals* 12, 1–11. <https://doi.org/10.3390/min12020170>
- Koons, G.L., Diba, M., Mikos, A.G., 2020. Materials design for bone-tissue engineering. *Nat. Rev. Mater.* 5, pages584–603. <https://doi.org/10.1038/s41578-020-0204-2>
- Kue, C.S., Tan, K.Y., Lam, M.L., Lee, H.B., 2014. Chick embryo chorioallantoic membrane (CAM): An alternative predictive model in acute toxicological studies for anti-cancer drugs. *Exp. Anim.* 64, 129–138. <https://doi.org/10.1538/expanim.14-0059>
- Landersdorfer, C.B., Bulitta, J.B., Sörgel, F., 2015. Pharmacokinetics and Pharmacodynamics of Antibiotics in Bone, in: *Bone and Joint Infections: From Microbiology to Diagnostics and Treatment*. pp. 21–37. <https://doi.org/10.1002/9781118581742.ch3>
- Lee, D.W., Yoo, B.R., 2016. Advanced silica/polymer composites: Materials and applications. *J. Ind. Eng. Chem.* 38, 1–12. <https://doi.org/10.1016/j.jiec.2016.04.016>
- Li, Y., Liu, Y., Li, R., Bai, H., Zhu, Z., Zhu, L., Zhu, C., Che, Z., Liu, H., Wang, J., Huang, L., 2021. Collagen-based biomaterials for bone tissue engineering. *Mater. Des.* 210, 110049. <https://doi.org/10.1016/J.MATDES.2021.110049>
- Liu, Y., Li, X., Liang, A., 2022. Current research progress of local drug delivery systems based on biodegradable polymers in treating chronic osteomyelitis. *Front. Bioeng. Biotechnol.* 10.
- Luzardo-Álvarez, A., Blanco-Méndez, J., Varela-Patiño, P., Martín Biedma, B., 2011. Amoxicillin-loaded sponges made of collagen and poly[(methyl vinyl ether)-co-(maleic anhydride)] for root canal treatment:

- Preparation, characterization and in vitro cell compatibility. *J. Biomater. Sci. Polym. Ed.* 22, 329–342.
<https://doi.org/10.1163/092050610X486937>
- Mangir, N., Dikici, S., Claeysens, F., Macneil, S., 2019. Using ex Ovo Chick Chorioallantoic Membrane (CAM) Assay to Evaluate the Biocompatibility and Angiogenic Response to Biomaterials. *ACS Biomater. Sci. Eng.* 5, 3190–3200. <https://doi.org/10.1021/acsbiomaterials.9b00172>
- Mitrevska, K., Merlos Rodrigo, M.A., Cernei, N., Michalkova, H., Splichal, Z., Hynek, D., Zitka, O., Heger, Z., Kopel, P., Adam, V., Milosavljevic, V., 2023. Chick chorioallantoic membrane (CAM) assay for the evaluation of the antitumor and antimetastatic activity of platinum-based drugs in association with the impact on the amino acid metabolism. *Mater. Today Bio* 19, 100570.
<https://doi.org/10.1016/J.MTBIO.2023.100570>
- Moncayo-Donoso, M., Rico-Llanos, G.A., Garzón-Alvarado, D.A., Becerra, J., Visser, R., Fontanilla, M.R., 2021. The effect of pore directionality of collagen scaffolds on cell differentiation and in vivo osteogenesis. *Polymers (Basel)*. 13. <https://doi.org/10.3390/polym13183187>
- Moreno-Jiménez, I., Hulsart-Billstrom, G., Lanham, S.A., Janeczek, A.A., Kontouli, N., Kanczler, J.M., Evans, N.D., Oreffo, R.O.C., 2016. The chorioallantoic membrane (CAM) assay for the study of human bone regeneration: A refinement animal model for tissue engineering. *Sci. Rep.* 6, 1–12.
<https://doi.org/10.1038/srep32168>
- Murphy, C.M., O'Brien, F.J., 2010. Understanding the effect of mean pore size on cell activity in collagen-glycosaminoglycan scaffolds. *Cell Adhes. Migr.* <https://doi.org/10.4161/cam.4.3.11747>
- Murshed, M., 2018. Mechanism of Bone Mineralization. *Cold Spring Harb. Perspect. Med.* 8, 1–12.
<https://doi.org/10.1101/cshperspect.a031229>
- Nandi, S.K., Bandyopadhyay, S., Das, P., Samanta, I., Mukherjee, P., Roy, S., Kundu, B., 2016. Understanding osteomyelitis and its treatment through local drug delivery system. *Biotechnol. Adv.* 34, 1305–1317. <https://doi.org/10.1016/j.biotechadv.2016.09.005>
- Narayan, R., Nayak, U.Y., Raichur, A.M., Garg, S., 2018. Mesoporous silica nanoparticles: A comprehensive review on synthesis and recent advances. *Pharmaceutics* 10, 118.
<https://doi.org/10.3390/pharmaceutics10030118>
- Nijsure, M.P., Kishore, V., 2018. Collagen-based scaffolds for bone tissue engineering applications, in: *Orthopedic Biomaterials: Advances and Applications*. pp. 187–224. https://doi.org/10.1007/978-3-319-73664-8_8
- Nong, L.-M., Zhou, D., Zheng, D., Jiang, Y.-Q., Xu, N.-W., Zhao, G.-Y., Wei, H., Zhou, S.-Y., Han, H., Han, L., 2019. The effect of different cross-linking conditions of EDC/NHS on type II collagen scaffolds: an in vitro evaluation. *Cell Tissue Bank.* 20, 557–568. <https://doi.org/10.1007/s10561-019-09790-7>
- Oliveira, S.M., Ringshia, R.A., Legeros, R.Z., Clark, E., Yost, M.J., Terracio, L., Teixeira, C.C., 2010. An improved collagen scaffold for skeletal regeneration. *J. Biomed. Mater. Res. - Part A* 94, 371–379.
<https://doi.org/10.1002/jbm.a.32694>
- Olszta, M.J., Cheng, X., Jee, S.S., Kumar, R., Kim, Y.Y., Kaufman, M.J., Douglas, E.P., Gower, L.B., 2007.

- Bone structure and formation: A new perspective. *Mater. Sci. Eng. R Reports* 58, 77–116.
<https://doi.org/10.1016/j.mser.2007.05.001>
- Oshima, S., Sato, T., Honda, M., Suetsugu, Y., Ozeki, K., Kikuchi, M., 2020. Fabrication of gentamicin-loaded hydroxyapatite/collagen bone-like nanocomposite for anti-infection bone void fillers. *Int. J. Mol. Sci.* 21, 551. <https://doi.org/10.3390/ijms21020551>
- Patel, H., Panchal, D.R., Patel, U., Brahmabhatt, T., Suthar, M., 2011. Matrix Type Drug Delivery System : A Review. *J. Pharm. Sci. Biosci. Res.* 1, 143–151.
- Patzakis, M.J., Mazur, K., Wilkins, J., Sherman, R., Holtom, P., 1993. Septopal beads and autogenous bone grafting for bone defects in patients with chronic osteomyelitis, in: *Clinical Orthopaedics and Related Research*. pp. 112–118. <https://doi.org/10.1097/00003086-199310000-00016>
- Prokopowicz, M., Szewczyk, A., Sawicki, W., 2014. The bioactivity studies of drug-loaded mesoporous silica- polydimethylsiloxane xerogels using FTIR and SEM/XEDS. *J. Mol. Struct.* 1056–1057, 262–266.
<https://doi.org/10.1016/j.molstruc.2013.10.052>
- Prokopowicz, M., Szewczyk, A., Skwira, A., Sądej, R., Walker, G., 2020. Biphasic composite of calcium phosphate-based mesoporous silica as a novel bone drug delivery system. *Drug Deliv. Transl. Res.* 10, 455–470. <https://doi.org/10.1007/s13346-019-00686-3>
- Prokopowicz, M., Żeglinski, J., Szewczyk, A., Skwira, A., Walker, G., 2019. Surface-activated fibre-like SBA-15 as drug carriers for bone diseases. *AAPS PharmSciTech* 20, 17. <https://doi.org/10.1208/s12249-018-1243-5>
- Rabel, K., Kohal, R.J., Steinberg, T., Tomakidi, P., Rolauffs, B., Adolfsson, E., Palmero, P., Fürderer, T., Altmann, B., 2020. Controlling osteoblast morphology and proliferation via surface micro-topographies of implant biomaterials. *Sci. Rep.* 10. <https://doi.org/10.1038/s41598-020-69685-6>
- Rampino, A., Borgogna, M., Blasi, P., Bellich, B., Cesàro, A., 2013. Chitosan nanoparticles: Preparation, size evolution and stability. *Int. J. Pharm.* 455, 219–228. <https://doi.org/10.1016/j.ijpharm.2013.07.034>
- Reis, R.L., 2014. Bioinspired scaffold, hydrogel and stem cell based strategies for engineering distinct tissues. *Cell J.* 15, 1–22.
- Roth, K.E., Maier, G.S., Schmidtmann, I., Eigner, U., Hübner, W.D., Peters, F., Drees, P., Maus, U., 2019. Release of antibiotics out of a moldable collagen- β -Tricalciumphosphate-composite compared to two calcium phosphate granules. *Materials (Basel)*. 12, 4056. <https://doi.org/10.3390/ma1224056>
- Schneider, C.A., Rasband, W.S., Eliceiri, K.W., 2012. NIH Image to ImageJ: 25 years of image analysis. *Nat. Methods* 9, 671–675. <https://doi.org/10.1038/nmeth.2089>
- Shah, F.A., Thomsen, P., Palmquist, A., 2019. Osseointegration and current interpretations of the bone-implant interface. *Acta Biomater.* 84, 1–15. <https://doi.org/10.1016/j.actbio.2018.11.018>
- Skwira, A., Szewczyk, A., Konopacka, A., Górska, M., Majda, D., Sądej, R., Prokopowicz, M., 2020. Silica-polymer composites as the novel antibiotic delivery systems for bone tissue infection. *Pharmaceutics* 12. <https://doi.org/10.3390/pharmaceutics12010028>
- Skwira, A., Szewczyk, A., Prokopowicz, M., 2019. The Effect of Polydimethylsiloxane-Ethylcellulose

- Coating Blends on the Surface Characterization and Drug Release of Ciprofloxacin-Loaded Mesoporous Silica. *Polymers (Basel)*. 11, 1450. <https://doi.org/10.3390/polym11091450>
- Skwira, A., Szewczyk, A., Sądej, R., Prokopowicz, M., 2023. Bioglass obtained via one-pot synthesis as osseointegrative drug delivery system. *Int. J. Pharm.* 633. <https://doi.org/https://doi.org/10.1016/j.ijpharm.2023.122610>
- Smith, M., Roberts, M., Al-Kassas, R., 2022. Implantable drug delivery systems for the treatment of osteomyelitis. *DRUG Dev. Ind. Pharm.* 48, 511–527.
- Szewczyk, A., Prokopowicz, M., Sawicki, W., Majda, D., Walker, G., 2019. Aminopropyl-functionalized mesoporous silica SBA-15 as drug carrier for cefazolin: adsorption profiles, release studies, and mineralization potential. *Microporous Mesoporous Mater.* 274, 113–126. <https://doi.org/10.1016/j.micromeso.2018.07.046>
- Szewczyk, A., Skwira, A., Konopacka, A., Sądej, R., Walker, G., Prokopowicz, M., 2020. Mesoporous silica pellets as bifunctional bone drug delivery system for cefazolin. *Int. J. Pharm.* 588, 119718. <https://doi.org/10.1016/j.ijpharm.2020.119718>
- Tang, Y., Cai, R., Cao, D., Kong, X., Lu, Y., 2018. Photocatalytic production of hydroxyl radicals by commercial TiO₂ nanoparticles and phototoxic hazard identification. *Toxicology* 406–407, 1–8. <https://doi.org/10.1016/j.tox.2018.05.010>
- Tian, Z., Li, C., Duan, L., Li, G., 2014. Physicochemical properties of collagen solutions cross-linked by glutaraldehyde. *Connect. Tissue Res.* 55, 239–247. <https://doi.org/10.3109/03008207.2014.898066>
- Tsourvakas, S., 2012. Local antibiotic therapy in the treatment of bone and soft tissue infections, in: Danilla, S. (Ed.), *Selected Topics in Plastic Reconstructive Surgery*. IntechOpen, London, UK, pp. 17–46. <https://doi.org/10.5772/28833>
- Valdes, T.I., Kreutzer, D., Moussy, F., 2002. The chick chorioallantoic membrane as a novel in vivo model for the testing of biomaterials. *J. Biomed. Mater. Res.* 62, 273–282. <https://doi.org/10.1002/jbm.10152>
- Vallet-Regí, M., Balas, F., 2008. Silica Materials for Medical Applications. *Open Biomed. Eng. J.* 2, 1–9. <https://doi.org/10.2174/1874120700802010001>
- Van Vugt, T.A.G., Walraven, J.M.B., Geurts, J.A.P., Arts, J.J.C., 2018. Antibiotic-Loaded Collagen Sponges in Clinical Treatment of Chronic Osteomyelitis: A Systematic Review. *J. Bone Jt. Surg. - Am. Vol.* 100, 2153–2161. <https://doi.org/10.2106/JBJS.17.01140>
- Vu, B.T., Shahin, S.A., Croissant, J., Fatieiev, Y., Matsumoto, K., Le-Hoang Doan, T., Yik, T., Simargi, S., Conteras, A., Ratliff, L., Jimenez, C.M., Raehm, L., Khashab, N., Durand, J.O., Glackin, C., Tamanoi, F., 2018. Chick chorioallantoic membrane assay as an in vivo model to study the effect of nanoparticle-based anticancer drugs in ovarian cancer. *Sci. Rep.* 8, 8524. <https://doi.org/10.1038/s41598-018-25573-8>
- Wahl, D.A., Czernuszka, J.T., 2006. Collagen-hydroxyapatite composites for hard tissue repair. *Eur. Cells Mater.* 11, 43–56. <https://doi.org/10.22203/eCM.v011a06>
- Walenkamp, G.H.I.M., Vree, T.B., Van Rens, T.J.G., 1986. Gentamicin-PMMA beads. Pharmacokinetic and nephrotoxicological study. *Clin. Orthop. Relat. Res.* 205, 171–183. <https://doi.org/10.1097/00003086->

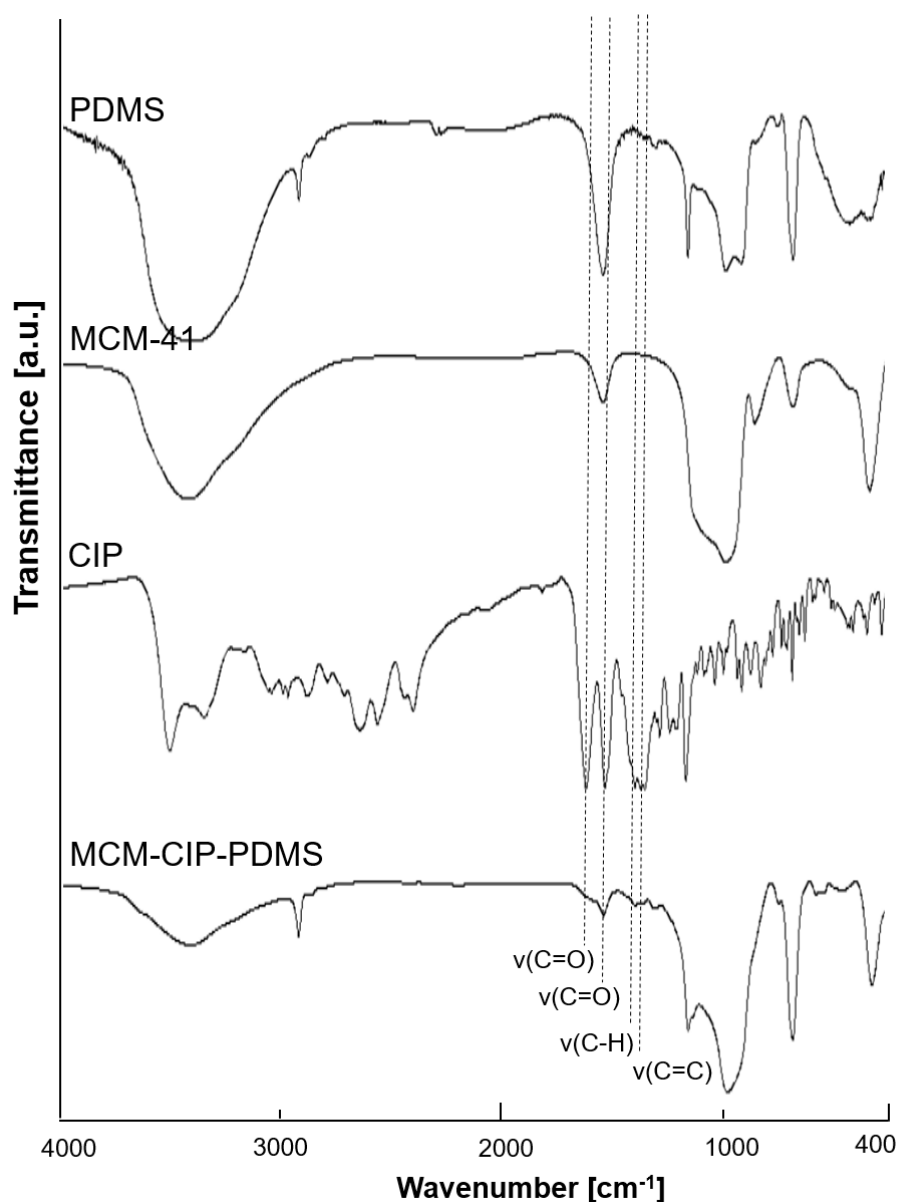
198604000-00021

- Wassif, R.K., Elkayal, M., Shamma, R.N., Elkheshen, S.A., 2021. Recent advances in the local antibiotics delivery systems for management of osteomyelitis. *Drug Deliv.* 28, 2392–2414. <https://doi.org/10.1080/10717544.2021.1998246>
- Wei, J., Jia, J., Wu, F., Wei, S., Zhou, H., Zhang, H., Shin, J.W., Liu, C., 2010. Hierarchically microporous/macroporous scaffold of magnesium-calcium phosphate for bone tissue regeneration. *Biomaterials* 31, 1260–1269. <https://doi.org/10.1016/j.biomaterials.2009.11.005>
- Wei, S., Ma, J.X., Xu, L., Gu, X.S., Ma, X.L., 2020. Biodegradable materials for bone defect repair. *Mil. Med. Res.* <https://doi.org/10.1186/s40779-020-00280-6>
- Wiesmann, H.P., Meyer, U., Plate, U., Höhling, H.J., 2004. Aspects of collagen mineralization in hard tissue formation. *Int. Rev. Cytol.* 242, 121–156. [https://doi.org/10.1016/S0074-7696\(04\)42003-8](https://doi.org/10.1016/S0074-7696(04)42003-8)
- Wypych, G., 2018. 6 - FUNCTIONAL FILLERS - APPLICATIONS, in: *Functional Fillers: Chemical Composition, Morphology, Performance, Applications.* pp. 153–179.
- Zhang, D., Wu, X., Chen, J., Lin, K., 2018. The development of collagen based composite scaffolds for bone regeneration. *Bioact. Mater.* <https://doi.org/10.1016/j.bioactmat.2017.08.004>
- Zhang, Q., Lu, H., Kawazoe, N., Chen, G., 2014. Pore size effect of collagen scaffolds on cartilage regeneration. *Acta Biomater.* 10. <https://doi.org/10.1016/j.actbio.2013.12.042>
- Zhang, W., Liao, S.S., Cui, F.Z., 2003. Hierarchical self-assembly of nano-fibrils in mineralized collagen. *Chem. Mater.* 15, 3221–3226. <https://doi.org/10.1021/cm030080g>
- Zidek, J., Vojtova, L., Abdel-Mohsen, A.M., Chmelik, J., Zikmund, T., Brtnikova, J., Jakubicek, R., Zubal, L., Jan, J., Kaiser, J., 2016. Accurate micro-computed tomography imaging of pore spaces in collagen-based scaffold. *J. Mater. Sci. Mater. Med.* 27, 1–18. <https://doi.org/10.1007/s10856-016-5717-2>

Supplementary material 1

Biocompatible antibiotic-loaded mesoporous silica/bioglass/collagen-based scaffolds as bone drug delivery systems

Aдриана Skwira, Adrian Szewczyk, Joana Barros, Marta Laranjeira, Fernando Jorge Monteiro, Rafał Sądej, Magdalena Prokopowicz



Supplementary material 1. FTIR spectra of modified ciprofloxacin-loaded mesoporous silica (MCM-CIP-PDMS), ciprofloxacin hydrochloride (CIP), mesoporous silica (MCM-41), and polydimethylsiloxane (PDMS).

Supplementary material 2

Biocompatible antibiotic-loaded mesoporous silica/bioglass/collagen-based scaffolds as bone drug delivery systems

Adrianna Skwira, Adrian Szewczyk, Joana Barros, Marta Laranjeira, Fernando Jorge Monteiro, Rafał Sądej, Magdalena Prokopowicz

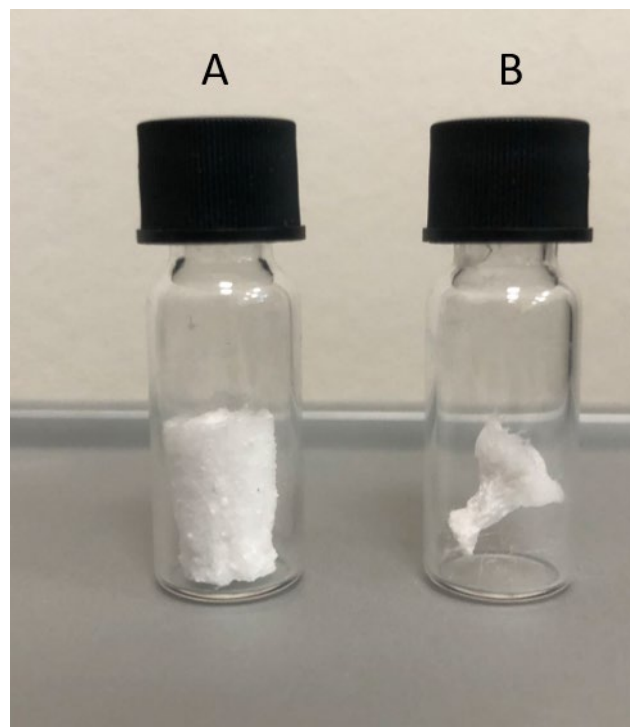


Fig. S2. Photos of an intact cylindrical shape of collagen-silica scaffold (A) and collapsed structure of placebo collagen scaffold (B) after the freeze-drying process.

Supplementary material 3

Biocompatible antibiotic-loaded mesoporous silica/bioglass/collagen-based scaffolds as bone drug delivery systems

Adrianna Skwira, Adrian Szewczyk, Joana Barros, Marta Laranjeira, Fernando Jorge Monteiro, Rafał Sądej, Magdalena Prokopowicz

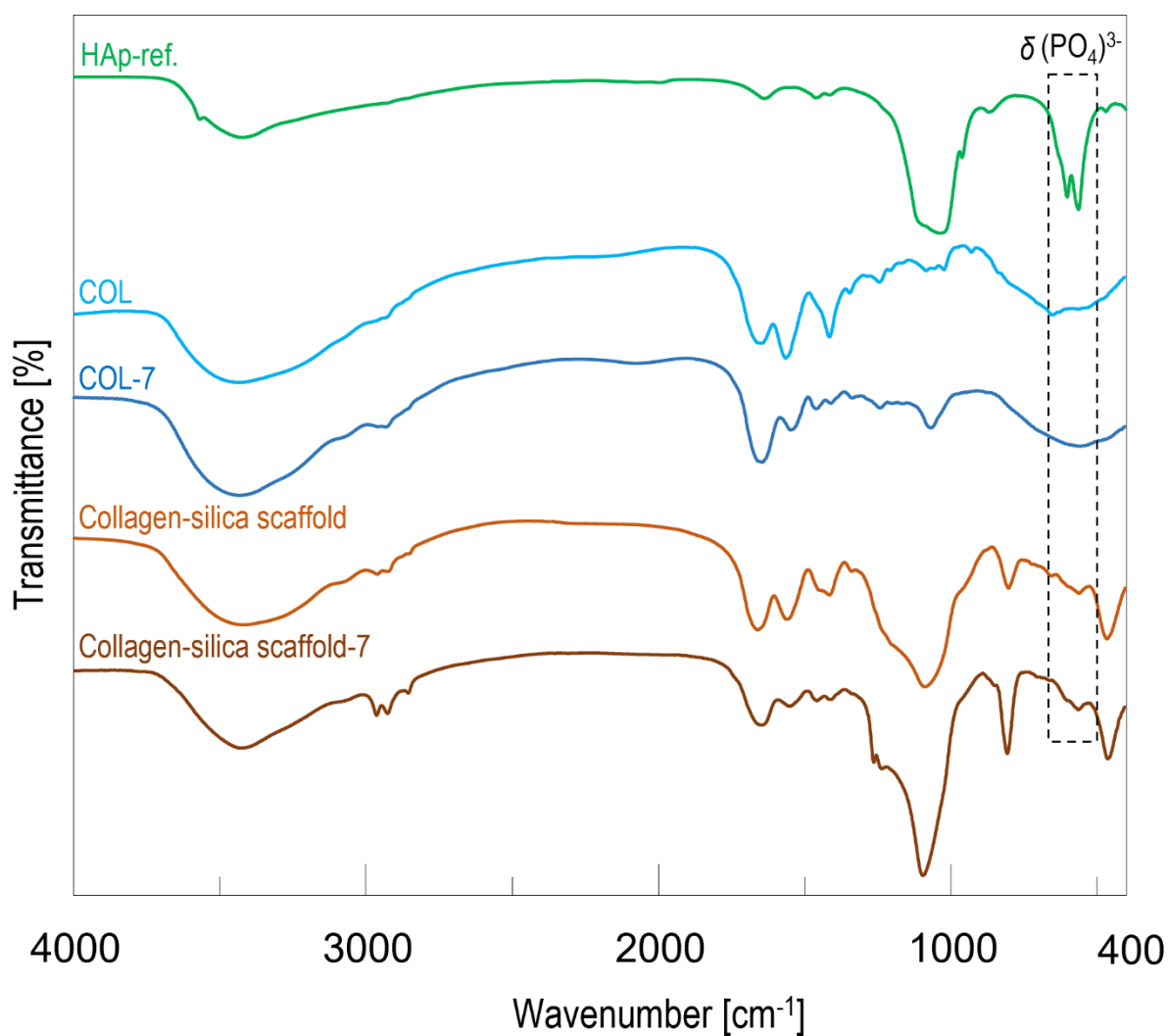


Fig. S3. FTIR spectra of both collagen and collagen-silica scaffold before and after 7 days of mineralization potential assay in SBF with increased intensity of δ (bending) mode of PO_4^{3-} observed in the collagen-silica scaffold.

Supplementary material 4

Biocompatible antibiotic-loaded mesoporous silica/bioglass/collagen-based scaffolds as bone drug delivery systems

Adrianna Skwira, Adrian Szewczyk, Joana Barros, Marta Laranjeira, Fernando Jorge Monteiro, Rafał Sądej, Magdalena Prokopowicz

Scaffold degradation test

The scaffold degradation test was performed based on *ISO 10993-13:2010(E) Biological evaluation of medical devices — Part 13: Identification and quantification of degradation products from polymeric medical devices* and *ISO 10993-14:2001(E) Biological evaluation of medical devices — Part 14: Identification and quantification of degradation products from ceramics*. Each collagen-silica scaffold (22.19 ± 0.12 mg) and collagen scaffold (5.11 ± 0.08 mg) was immersed into 10 mL of distilled water (pH = 7.0) and incubated under stirring (120 rpm, 37.0 °C). At particular time points, scaffolds were freeze-dried (24h, 1 mBar, -55 °C) and weighed. The experiment was carried on until the variation in mass loss between consecutive time points was below 1%. The weight loss of each material was calculated according to Eq. 1:

$$\text{Weight loss (\%)} = \frac{W_0 - W_t}{W_0} \cdot 100\%$$

where W_0 and W_t correspond to the initial and weight at each time point, respectively. The assay was performed in three replicates.

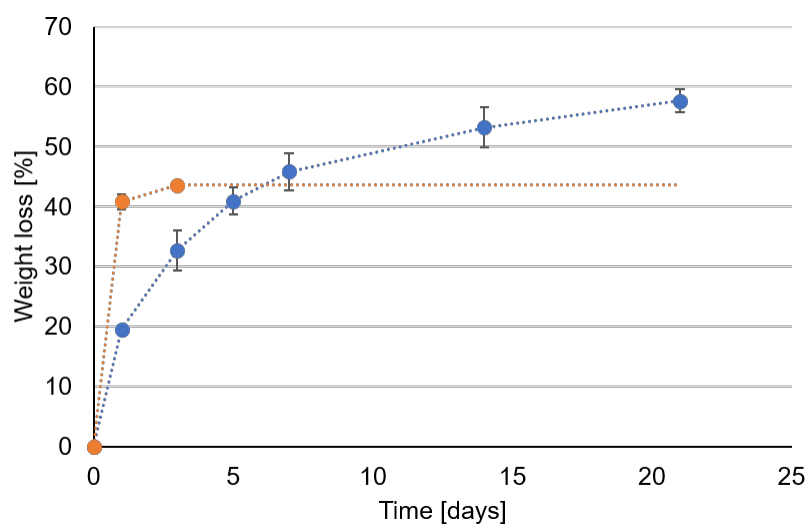


Fig. S4. Weight loss [%] of collagen-silica scaffolds (blue graph) and collagen scaffolds (orange graph) in time [days].

Supplementary material 5

Biocompatible antibiotic-loaded mesoporous silica/bioglass/collagen-based scaffolds as bone drug delivery systems

Adrianna Skwira, Adrian Szewczyk, Joana Barros, Marta Laranjeira, Fernando Jorge Monteiro, Rafał Sądej, Magdalena Prokopowicz

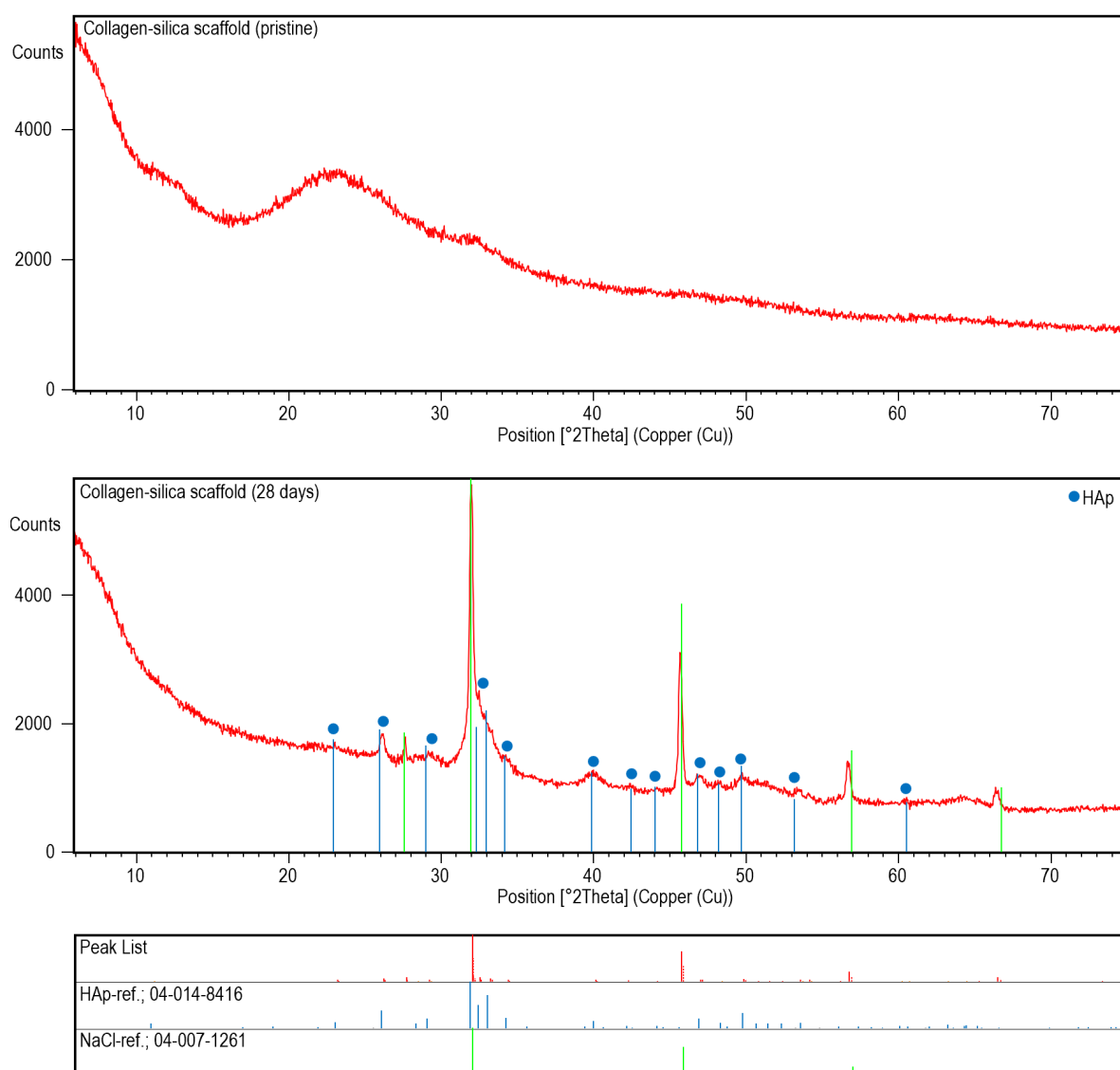


Fig. S5. XRD diffractograms of the collagen-silica scaffold before and after 21 days of incubation in SBF with present peaks of HAp phase after mineralization potential assay. Data were recorded on the Empyrean PANalytical diffractometer using CuK α radiation (40 kV and 25 mA) at a scanning rate of 1 deg/min with a step width of 0.02 in the 2θ range of 5–75. Before analysis, each scaffold was compressed using a hydraulic press to obtain a flat surface.

4. Podsumowanie i wnioski

Zrealizowane w ramach pracy doktorskiej zadania badawcze pozwoliły na osiągnięcie postawionego celu nadrzędnego – otrzymania biozgodnych nośników substancji leczniczej do tkanki kostnej na bazie mezoporowatych materiałów krzemionkowych. Postępowanie prowadzące do realizacji tego celu wiązało się z koniecznością wykonania etapów pośrednich, do których należały - otrzymanie mezoporowatego materiału krzemionkowego MCM-41, jego charakterystyka oraz modyfikacja profilu uwalniania substancji leczniczej; - otrzymanie i wykazanie potencjalnych właściwości regeneracyjnych bioszklą; - otrzymanie i ocena wielofunkcyjności rusztowań kolagenowo-krzemionkowych stanowiących połączenie kolagenu typu I, MCM-41 oraz bioszklą.

Poniżej przedstawiono najważniejsze wnioski wynikające z badań przeprowadzonych w ramach pracy doktorskiej:

- Oczekiwaną modyfikację profilu uwalniania substancji leczniczej z mezoporowatego materiału krzemionkowego MCM-41 można uzyskać na drodze jego powleczenia za pomocą mieszanin polimerowych złożonych z etylocelulozy i PDMS-u lub samego PDMS-u.
- Modyfikacja profilu uwalniania następuje zgodnie z następującą zależnością. Im wyższa jest zawartość PDMS-u w formulacji, tym większe jest zmniejszenie początkowego wyrzutu substancji leczniczej w czasie pierwszych 24 godzin badania oraz tym dłuższy jest całkowity czas uwalniania.
- Otrzymane za pomocą modyfikowanej metody zol-żel bioszklą charakteryzuje się potwierdzonymi w modelu *in vitro* właściwościami osteoindukcyjnymi oraz osteokondukcyjnymi, przewyższającymi analizowane bioszklą komercyjne, mogąc stanowić alternatywę dla biomateriałów obecnie stosowanych.
- Zaprezentowane w pracy zoptymalizowane procedury służące ocenie właściwości osseointegracyjnych w modelu *in vitro* mogą stanowić etapy postępowania w przeprowadzeniu kompleksowej oceny biomateriałów degradowalnych zgodnie z normą ISO 10993.
- Ocena właściwości osteoindukcyjnych zawsze powinna być dokonywana w oparciu o analizę więcej niż jednego markera molekularnego, ze szczególnym zwróceniem uwagi na możliwie fałszywe wyniki indywidualnie przeprowadzanej

analizy aktywności fosfatazy alkalicznej – najczęściej oznaczanego markera procesu kościotworzenia.

- Połączenie materiałów nieorganicznych (mezoporowatego materiału krzemionkowego MCM-41 oraz bioszklą) i kolagenu typu I może stanowić skuteczną metodę poprawy stabilności struktury powstałej po procesie liofilizacji.
- Zaproponowana metoda otrzymywania, skład jakościowy oraz ilościowy umożliwia otrzymanie wielofunkcyjnych rusztowań kolagenowo-krzemionkowych, charakteryzujących się zmniejszonym wyrzutem początkowym modelowej substancji przeciwbakteryjnej (cyprofloksacyny) oraz całkowitym czasem uwalniania przedłużonym do 80 dni; aktywnością przeciwbakteryjną; potencjalnymi właściwościami regeneracyjnymi wyrażonymi poprzez stopniowe narastanie warstwy hydroksyapatytu węglanowego w płynie symulującym osocze ludzkie oraz promowanie adhezji, wnikania i proliferacji osteoblastów umiejscowionych w rusztowaniach; biozgodnością i korzystną początkową odpowiedzią tkankową w modelu *in vivo* CAM.
- Otrzymane rusztowania kolagenowo-krzemionkowe wykazują potencjalną przydatność w miejscowym leczeniu *osteomyelitis*.

Zaprezentowane w ramach rozprawy doktorskiej badania stanowią próbę odpowiedzi na potrzebę poszukiwania nowych sposobów miejscowego leczenia zakażeń bakteryjnych tkanki kostnej. Na podstawie uzyskanych wyników można stwierdzić, iż otrzymane wielofunkcyjne rusztowania kolagenowo-krzemionkowe mogą w przyszłości stanowić atrakcyjną alternatywę dla obecnie stosowanych granulatów z polimetakrylanu metylu. Przede wszystkim, oprócz przedłużonego uwalniania antybiotyku posiadają właściwości osseointegracyjne, w przeciwieństwie do granulatów z PMMA. Wstępnie ocenione właściwości fizykochemiczne, mineralizacyjne, mikrobiologiczne oraz biologiczne dają podstawę dla rozpoczęcia kolejnych etapów badawczych. Szczegółowa ocena odczynu tkankowego, w tym zdolność do integracji i regeneracji tkanki kostnej, wymaga wykorzystania zwierząt doświadczalnych. W związku z tym, w celu oceny aplikacyjności proponowanych rusztowań kolagenowo-krzemionkowych w kolejnym etapie badań, stanowiącym kontynuację projektu prowadzonego w ramach pracy doktorskiej, planuje się przeprowadzenie długookresowej oceny odpowiedzi biologicznej *in vivo* z wykorzystaniem ssaczych modeli zwierzęcych. Dodatkowo planuje się również zbadanie przydatności rusztowań

kolagenowo-krzemionkowych jako nośników innych antybiotyków wykorzystywanych w leczeniu *osteomyelitis* (np. wankomycyny), jak również substancji leczniczych zalecanych w leczeniu osteoporozy (np. alendronianu sodu) oraz substancji przeciwnowotworowych stosowanych w leczeniu kostniakomięśaka (np. doksorubicyny).

5. Bibliografia

- [1] G. Cierny, J.T. Mader, J.J. Penninck, A clinical staging system for adult osteomyelitis., *Clin. Orthop. Relat. Res.* 414 (2003) 7–24. <https://doi.org/10.1097/01.blo.0000088564.81746.62>.
- [2] P.D.P. Lew, P.F.A. Waldvogel, Osteomyelitis, *Lancet.* 364 (2004) 369–379. [https://doi.org/10.1016/S0140-6736\(04\)16727-5](https://doi.org/10.1016/S0140-6736(04)16727-5).
- [3] S. Aytaç, M. Schnetzke, B. Swartman, P. Herrmann, C. Woelfl, V. Heppert, P.A. Gruetzner, T. Guehring, Posttraumatic and postoperative osteomyelitis: Surgical revision strategy with persisting fistula, *Arch. Orthop. Trauma Surg.* 134 (2014) 159–165. <https://doi.org/10.1007/s00402-013-1907-2>.
- [4] R.O. Darouiche, Treatment of Infections Associated with Surgical Implants, *N. Engl. J. Med.* 350 (2004) 1422–1429. <https://doi.org/10.1056/nejmra035415>.
- [5] H. Ben Ghazlen, H. Kaziz, F. Abid, Y. Zitoun, N. Sassi, Management of subacute acetabular osteomyelitis in a child, *Arch. Pediatr.* 22 (2015) 861–864. <https://doi.org/10.1016/j.arcped.2015.05.001>.
- [6] G. Walter, M. Kemmerer, C. Kappler, R. Hoffmann, Treatment algorithms for chronic osteomyelitis, *Dtsch. Arztebl. Int.* 109 (2012) 257–264. <https://doi.org/10.3238/arztebl.2012.0257>.
- [7] D.C. Bury, T.S. Rogers, M.M. Dickman, Osteomyelitis: Diagnosis and Treatment, *Am. Fam. Physician.* 104 (2021) 395–402.
- [8] H.M. Kremers, M.E. Nwojo, J.E. Ransom, C.M. Wood-Wentz, L. Joseph Melton, P.M. Huddleston, Trends in the epidemiology of osteomyelitis a population-based study, 1969 to 2009, *J. Bone Jt. Surg. - Am. Vol.* 97 (2015) 837–845. <https://doi.org/10.2106/JBJS.N.01350>.
- [9] Ø.R. Riise, E. Kirkhus, K.S. Handeland, B. Flatø, T. Reiseret, M. Cvancarova, B. Nakstad, K.O. Wathne, Childhood osteomyelitis-incidence and differentiation from other acute onset musculoskeletal features in a population-based study, *BMC Pediatr.* 8 (2008) 45. <https://doi.org/10.1186/1471-2431-8-45>.
- [10] M. Street, R. Puna, M. Huang, H. Crawford, Pediatric acute hematogenous osteomyelitis, *J. Pediatr. Orthop.* 35 (2015) 634–639. <https://doi.org/10.1097/BPO.0000000000000332>.
- [11] J.C. Arnold, J.S. Bradley, Osteoarticular Infections in Children, *Infect. Dis. Clin. North Am.* 29 (2015) 557–574. <https://doi.org/10.1016/j.idc.2015.05.012>.
- [12] A. Gigante, V. Coppa, M. Marinelli, N. Giampaolini, D. Falcioni, N. Specchia, Acute osteomyelitis and septic arthritis in children: A systematic review of systematic reviews, *Eur. Rev. Med. Pharmacol. Sci.* 23 (2019) 145–158. https://doi.org/10.26355/EURREV_201904_17484.
- [13] A.L. Gornitzky, A.E. Kim, J.M. O'Donnell, I. Swarup, Diagnosis and management of osteomyelitis in children: A critical analysis review, *JBJS Rev.* 8 (2020) e1900202. <https://doi.org/10.2106/JBJS.RVW.19.00202>.
- [14] T. Padrão, C.C. Coelho, P. Costa, N. Alegrete, F.J. Monteiro, S.R. Sousa,

Combining local antibiotic delivery with heparinized nanohydroxyapatite/collagen bone substitute: A novel strategy for osteomyelitis treatment, *Mater. Sci. Eng. C.* 119 (2021) 111329. <https://doi.org/10.1016/j.msec.2020.111329>.

- [15] L. Lazzarini, J.T. Mader, J.H. Calhoun, Osteomyelitis in long bones, *J. Bone Jt. Surg.* 86 (2004) 2305–2318. <https://doi.org/10.2106/00004623-200410000-00028>.
- [16] S.K. Nandi, S. Bandyopadhyay, P. Das, I. Samanta, P. Mukherjee, S. Roy, B. Kundu, Understanding osteomyelitis and its treatment through local drug delivery system, *Biotechnol. Adv.* 34 (2016) 1305–1317. <https://doi.org/10.1016/j.biotechadv.2016.09.005>.
- [17] H.-K. Li, I. Rombach, R. Zambellas, A.S. Walker, M.A. McNally, B.L. Atkins, B.A. Lipsky, H.C. Hughes, D. Bose, M. Kümin, C. Scarborough, P.C. Matthews, A.J. Brent, J. Lomas, R. Gundle, M. Rogers, A. Taylor, B. Angus, I. Byren, A.R. Berendt, S. Warren, F.E. Fitzgerald, D.J.F. Mack, S. Hopkins, J. Folb, H.E. Reynolds, E. Moore, J. Marshall, N. Jenkins, C.E. Moran, A.F. Woodhouse, S. Stafford, R.A. Seaton, C. Vallance, C.J. Hemsley, K. Bisnauthsing, J.A.T. Sandoe, I. Aggarwal, S.C. Ellis, D.J. Bunn, R.K. Sutherland, G. Barlow, C. Cooper, C. Geue, N. McMeekin, A.H. Briggs, P. Sendi, E. Khatamzas, T. Wangrangsimakul, T.H.N. Wong, L.K. Barrett, A. Alvand, C.F. Old, J. Bostock, J. Paul, G. Cooke, G.E. Thwaites, P. Bejon, M. Scarborough, Oral versus Intravenous Antibiotics for Bone and Joint Infection, *N. Engl. J. Med.* 380 (2019) 425–436. <https://doi.org/10.1056/nejmoa1710926>.
- [18] C.B. Landersdorfer, J.B. Bulitta, F. Sörgel, Pharmacokinetics and Pharmacodynamics of Antibiotics in Bone, in: *Bone Jt. Infect. From Microbiol. to Diagnostics Treat.*, 2015: pp. 21–37. <https://doi.org/10.1002/9781118581742.ch3>.
- [19] S. Tsourvakas, Local antibiotic therapy in the treatment of bone and soft tissue infections, in: S. Danilla (Ed.), *Sel. Top. Plast. Reconstr. Surg.*, IntechOpen, London, UK, 2012: pp. 17–46. <https://doi.org/10.5772/28833>.
- [20] A.J.T. Douglas R Osmon, Nonvertebral osteomyelitis in adults: Treatment, UpToDate. (2023). <http://www.uptodate.com>.
- [21] I.I. Momodu, V. Savaliya, Osteomyelitis, in: *StatPearls*, StatPearls Publishing, Treasure Island (FL), 2021.
- [22] M.A. Velasco, C.A. Narváez-Tovar, D.A. Garzón-Alvarado, Design, materials, and mechanobiology of biodegradable scaffolds for bone tissue engineering, *Biomed Res. Int.* 2015 (2015) 729076. <https://doi.org/10.1155/2015/729076>.
- [23] S. Błażewicz, L. Stoch, Biomateriały (Tom 4), in: M. Naęcz (Ed.), *Biocybernetyka i Inżynieria Biomed.* 2000, Akademicka Oficyna Wydawnicza EXIT, Warszawa, 2003.
- [24] T. Albrektsson, P.I. Brånemark, H.A. Hansson, J. Lindström, Osseointegrated titanium implants: Requirements for ensuring a long-lasting, direct bone-to-implant anchorage in man, *Acta Orthop.* 52 (1981) 155–170. <https://doi.org/10.3109/17453678108991776>.
- [25] S. Hanada, H. Matsumoto, S. Watanabe, Mechanical compatibility of titanium implants in hard tissues, *Int. Congr. Ser.* 1284 (2005) 239 – 247. <https://doi.org/10.1016/j.ics.2005.06.084>.

- [26] V. Karageorgiou, D. Kaplan, Porosity of 3D biomaterial scaffolds and osteogenesis, *Biomaterials*. 26 (2005) 5474–5491. <https://doi.org/10.1016/j.biomaterials.2005.02.002>.
- [27] C.L. Nelson, The current status of material used for depot delivery of drugs, *Clin. Orthop. Relat. Res.* 427 (2004) 72–78. <https://doi.org/10.1097/01.blo.0000143741.92384.18>.
- [28] G.H.I.M. Walenkamp, T.B. Vree, T.J.G. Van Rens, Gentamicin-PMMA beads. Pharmacokinetic and nephrotoxicological study, *Clin. Orthop. Relat. Res.* 205 (1986) 171–183. <https://doi.org/10.1097/00003086-198604000-00021>.
- [29] M.J. Patzakis, K. Mazur, J. Wilkins, R. Sherman, P. Holtom, Septopal beads and autogenous bone grafting for bone defects in patients with chronic osteomyelitis, in: *Clin. Orthop. Relat. Res.*, 1993: pp. 112–118. <https://doi.org/10.1097/00003086-199310000-00016>.
- [30] J.D. Blaha, C.L. Nelson, L.F. Frevert, S.L. Henry, D. Seligson, J.L. Esterhai, R.B. Heppenstal, J. Calhoun, J. Cobos, J. Mader, The use of septopal (polymethylmethacrylate beads with gentamicin) in the treatment of chronic osteomyelitis, *Instr. Course Lect.* 39 (1990) 509–514.
- [31] J. Gogia, J. Meehan, P. Di Cesare, A. Jamali, Local Antibiotic Therapy in Osteomyelitis, *Semin. Plast. Surg.* 23 (2009) 100–107. <https://doi.org/10.1055/s-0029-1214162>.
- [32] M. Vallet-Regí, L. Ruiz-González, I. Izquierdo-Barba, J.M. González-Calbet, Revisiting silica based ordered mesoporous materials: Medical applications, *J. Mater. Chem.* 16 (2006) 26–31. <https://doi.org/10.1039/b509744d>.
- [33] F. Tang, L. Li, D. Chen, Mesoporous silica nanoparticles: Synthesis, biocompatibility and drug delivery, *Adv. Mater.* 24 (2012) 1504–1534. <https://doi.org/10.1002/adma.201104763>.
- [34] P. Yang, S. Gai, J. Lin, Functionalized mesoporous silica materials for controlled drug delivery, *Chem. Soc. Rev.* 41 (2012) 3679–3698. <https://doi.org/10.1039/c2cs15308d>.
- [35] M. Gisbert-Garzarán, M. Manzano, M. Vallet-Regí, Mesoporous silica nanoparticles for the treatment of complex bone diseases: Bone cancer, bone infection and osteoporosis, *Pharmaceutics*. 12 (2020) 83. <https://doi.org/10.3390/pharmaceutics12010083>.
- [36] V. Nairi, L. Medda, M. Monduzzi, A. Salis, Adsorption and release of ampicillin antibiotic from ordered mesoporous silica, *J. Colloid Interface Sci.* 497 (2017) 217–225. <https://doi.org/10.1016/j.jcis.2017.03.021>.
- [37] M. Vallet-Regi, A. Rámila, R.P. Del Real, J. Pérez-Pariente, A new property of MCM-41: Drug delivery system, *Chem. Mater.* 13 (2001) 308–311. <https://doi.org/10.1021/cm0011559>.
- [38] T. Tamanna, C.B. Landersdorfer, H.J. Ng, J.B. Bulitta, P. Wood, A. Yu, Prolonged and continuous antibacterial and anti-biofilm activities of thin films embedded with gentamicin-loaded mesoporous silica nanoparticles, *Appl. Nanosci.* 8 (2018) 1471–1482. <https://doi.org/10.1007/s13204-018-0807-8>.

- [39] M.Y. Memar, M. Yekani, S. Farajnia, F. Ghadiri Moghaddam, E. Nabizadeh, S. Sharifi, S. Maleki Dizaj, Antibacterial and biofilm-inhibitory effects of vancomycin-loaded mesoporous silica nanoparticles on methicillin-resistant staphylococcus aureus and gram-negative bacteria, *Arch. Microbiol.* 205 (2023) 109. <https://doi.org/10.1007/s00203-023-03447-6>.
- [40] A. Szewczyk, A. Skwira, A. Konopacka, R. Sądej, G. Walker, M. Prokopowicz, Mesoporous silica pellets as bifunctional bone drug delivery system for cefazolin, *Int. J. Pharm.* 588 (2020) 119718. <https://doi.org/10.1016/j.ijpharm.2020.119718>.
- [41] A. Szewczyk, A. Skwira, A. Konopacka, R. Sadej, M. Prokopowicz, Mesoporous silica-bioglass composite pellets as bone drug delivery system with mineralization potential, *Int. J. Mol. Sci.* 22 (2021) 4708. <https://doi.org/10.3390/ijms22094708>.
- [42] F. Balas, M. Manzano, P. Horcajada, M. Vallet-Regi, Confinement and controlled release of bisphosphonates on ordered mesoporous silica-based materials, *J. Am. Chem. Soc.* 128 (2006) 8116–8117. <https://doi.org/10.1021/ja062286z>.
- [43] A. Neumann, A. Christel, C. Kasper, P. Behrens, BMP2-loaded nanoporous silica nanoparticles promote osteogenic differentiation of human mesenchymal stem cells, *RSC Adv.* 3 (2013) 24222–24230. <https://doi.org/10.1039/c3ra44734k>.
- [44] C. Wu, W. Fan, J. Chang, Functional mesoporous bioactive glass nanospheres: Synthesis, high loading efficiency, controllable delivery of doxorubicin and inhibitory effect on bone cancer cells, *J. Mater. Chem. B.* 1 (2013) 2710–2718. <https://doi.org/10.1039/c3tb20275e>.
- [45] M. Prokopowicz, J. Żeglinski, A. Szewczyk, A. Skwira, G. Walker, Surface-activated fibre-like SBA-15 as drug carriers for bone diseases, *AAPS PharmSciTech.* 20 (2019) 17. <https://doi.org/10.1208/s12249-018-1243-5>.
- [46] Y. Li, Y. Duo, S. Bao, L. He, K. Ling, J. Luo, Y. Zhang, H. Huang, H. Zhang, X. Yu, EpCAM aptamer-functionalized polydopamine-coated mesoporous silica nanoparticles loaded with DM1 for targeted therapy in colorectal cancer, *Int. J. Nanomedicine.* 12 (2017) 6239–6257. <https://doi.org/10.2147/IJN.S143293>.
- [47] A. Szewczyk, M. Prokopowicz, W. Sawicki, D. Majda, G. Walker, Aminopropyl-functionalized mesoporous silica SBA-15 as drug carrier for cefazolin: adsorption profiles, release studies, and mineralization potential, *Microporous Mesoporous Mater.* 274 (2019) 113–126. <https://doi.org/10.1016/j.micromeso.2018.07.046>.
- [48] M. Varache, I. Bezverkhy, G. Weber, L. Saviot, R. Chassagnon, F. Baras, F. Bouyer, Loading of Cisplatin into Mesoporous Silica Nanoparticles: Effect of Surface Functionalization, *Langmuir.* 35 (2019) 8984–8995. <https://doi.org/10.1021/acs.langmuir.9b00954>.
- [49] H. Yang, B. Cheng, Z. Li, K. Su, Q. Guo, P. Han, Organically modified MCM-type material preparation and its usage in controlled ibuprofen delivery, *Adv. Mater. Res.* 139–141 (2010) 222–226. <https://doi.org/10.4028/www.scientific.net/AMR.139-141.222>.
- [50] S. Bhattacharyya, H. Wang, P. Ducheyne, Polymer-coated mesoporous silica nanoparticles for the controlled release of macromolecules, *Acta Biomater.* 8 (2012) 3429–3435. <https://doi.org/10.1016/j.actbio.2012.06.003>.

- [51] J.R. Smith, D.A. Lamprou, Polymer coatings for biomedical applications: A review, *Trans. Inst. Met. Finish.* 92 (2014) 9–19. <https://doi.org/10.1179/0020296713Z.000000000157>.
- [52] S. Ghosh, T.J. Webster, Mesoporous Silica Based Nanostructures for Bone Tissue Regeneration, *Front. Mater.* 8 (2021) 692309. <https://doi.org/10.3389/fmats.2021.692309>.
- [53] M. Vallet-Regi, A.J. Salinas, Mesoporous bioactive glasses for regenerative medicine, *Mater. Today Bio.* 11 (2021) 100121. <https://doi.org/10.1016/j.mtbio.2021.100121>.
- [54] M. Vallet-Regí, Ordered mesoporous materials in the context of drug delivery systems and bone tissue engineering, *Chem. - A Eur. J.* 12 (2006) 5934–5943. <https://doi.org/10.1002/chem.200600226>.
- [55] M. Prokopowicz, A. Szewczyk, A. Skwira, R. Sądej, G. Walker, Biphasic composite of calcium phosphate-based mesoporous silica as a novel bone drug delivery system, *Drug Deliv. Transl. Res.* 10 (2020) 455–470. <https://doi.org/10.1007/s13346-019-00686-3>.
- [56] T. Kokubo, H. Takadama, How useful is SBF in predicting in vivo bone bioactivity?, *Biomaterials.* 27 (2006) 2907–2915. <https://doi.org/10.1016/j.biomaterials.2006.01.017>.
- [57] P. Sepulveda, J.R. Jones, L.L. Hench, Characterization of melt-derived 45S5 and sol-gel-derived 58S bioactive glasses, *J. Biomed. Mater. Res.* 58 (2001) 734–740. <https://doi.org/10.1002/jbm.10026>.
- [58] T.H. Dang, T.H. Bui, E. V. Guseva, A.T. Ta, A.T. Nguyen, T.T.H. Hoang, X.V. Bui, Characterization of bioactive glass synthesized by sol-gel process in hot water, *Crystals.* 10 (2020) 529. <https://doi.org/10.3390/cryst10060529>.
- [59] M.R. Filgueiras, G. La Torre, L.L. Hench, Solution effects on the surface reactions of a bioactive glass, *J. Biomed. Mater. Res.* 27 (1993) 721–734. <https://doi.org/10.1002/jbm.820270405>.
- [60] L.L. Hench, Bioceramics: From Concept to Clinic, *J. Am. Ceram. Soc.* 74 (1991) 1487–1510. <https://doi.org/10.1111/j.1151-2916.1991.tb07132.x>.
- [61] L. Souza, J.H. Lopes, D. Encarnação, I.O. Mazali, R.A. Martin, J.A. Camilli, C.A. Bertran, Comprehensive in vitro and in vivo studies of novel melt-derived Nb-substituted 45S5 bioglass reveal its enhanced bioactive properties for bone healing, *Sci. Rep.* 8 (2018) 12808. <https://doi.org/10.1038/s41598-018-31114-0>.
- [62] D. Brézulier, L. Chaigneau, S. Jeanne, R. Lebullenger, The Challenge of 3D Bioprinting of Composite Natural Polymers PLA/Bioglass: Trends and Benefits in Cleft Palate Surgery, *Biomedicines.* 9 (2021) 1553. <https://doi.org/10.3390/biomedicines9111553>.
- [63] J. Crush, A. Hussain, K.T.M. Seah, W.S. Khan, Bioactive Glass: Methods for Assessing Angiogenesis and Osteogenesis, *Front. Cell Dev. Biol.* 9 (2021) 643781. <https://doi.org/10.3389/fcell.2021.643781>.
- [64] R.G. Ribas, V.M. Schatkoski, T.L. do A. Montanheiro, B.R.C. de Menezes, C. Stegemann, D.M.G. Leite, G.P. Thim, Current advances in bone tissue engineering

- concerning ceramic and bioglass scaffolds: A review, *Ceram. Int.* 45 (2019) 21051–21061. <https://doi.org/10.1016/j.ceramint.2019.07.096>.
- [65] W. Götz, E. Tobiasch, S. Witzleben, M. Schulze, Effects of silicon compounds on biomineralization, osteogenesis, and hard tissue formation, *Pharmaceutics*. 11 (2019) 117. <https://doi.org/10.3390/pharmaceutics11030117>.
- [66] S. Lazzeri, C. Montagnani, A. Zanardi, G. Beltrami, L. Galli, Bioactive glass in the treatment of chronic osteomyelitis in children: Description of four consecutive cases and literature review, *Injury*. 53 (2022) 3317–3321. <https://doi.org/10.1016/j.injury.2022.07.014>.
- [67] D. Michał, P. Justyna, C.-K. Katarzyna, Szklą bioaktywne w inżynierii tkankowej, *Inżynieria Biomed. / Biomed. Eng.* 20 (2014) 156–165.
- [68] W. Xia, J. Chang, Well-ordered mesoporous bioactive glasses (MBG): A promising bioactive drug delivery system, *J. Control. Release*. 110 (2006) 522–530. <https://doi.org/10.1016/j.jconrel.2005.11.002>.
- [69] W. Xia, J. Chang, Preparation, in vitro bioactivity and drug release property of well-ordered mesoporous 58S bioactive glass, *J. Non. Cryst. Solids*. 354 (2008) 1338–1341. <https://doi.org/10.1016/j.jnoncrysol.2006.10.084>.
- [70] L. Zhao, X. Yan, X. Zhou, L. Zhou, H. Wang, J. Tang, C. Yu, Mesoporous bioactive glasses for controlled drug release, *Microporous Mesoporous Mater.* 109 (2008) 210–215. <https://doi.org/10.1016/j.micromeso.2007.04.041>.
- [71] G.A. Rico-Llanos, S. Borrego-González, M. Moncayo-Donoso, J. Becerra, R. Visser, Collagen type I biomaterials as scaffolds for bone tissue engineering, *Polymers (Basel)*. 13 (2021) 599. <https://doi.org/10.3390/polym13040599>.
- [72] P.X. Ma, Scaffolds for tissue fabrication, *Mater. Today*. 7 (2004) 30–40. [https://doi.org/10.1016/S1369-7021\(04\)00233-0](https://doi.org/10.1016/S1369-7021(04)00233-0).
- [73] S. Viguet-Carrin, P. Garnero, P.D. Delmas, The role of collagen in bone strength, *Osteoporos. Int.* 17 (2006) 319–336. <https://doi.org/10.1007/s00198-005-2035-9>.
- [74] M. Murshed, Mechanism of Bone Mineralization, *Cold Spring Harb. Perspect. Med.* 8 (2018) 1–12. <https://doi.org/10.1101/cshperspect.a031229>.
- [75] M.J. Olszta, X. Cheng, S.S. Jee, R. Kumar, Y.Y. Kim, M.J. Kaufman, E.P. Douglas, L.B. Gower, Bone structure and formation: A new perspective, *Mater. Sci. Eng. R Reports*. 58 (2007) 77–116. <https://doi.org/10.1016/j.mser.2007.05.001>.
- [76] B.N. Blackstone, S.C. Gallentine, H.M. Powell, Review collagen-based electrospun materials for tissue engineering: A systematic review, *Bioengineering*. 8 (2021) 39. <https://doi.org/10.3390/bioengineering8030039>.
- [77] A. Nagaraj, A.E. Etxeberria, R. Naffa, G. Zidan, A. Seyfoddin, 3D-Printed Hybrid Collagen/GelMA Hydrogels for Tissue Engineering Applications, *Biology (Basel)*. 11 (2022) 1561. <https://doi.org/10.3390/biology11111561>.
- [78] C.M. Murphy, F.J. O'Brien, Understanding the effect of mean pore size on cell activity in collagen-glycosaminoglycan scaffolds, *Cell Adhes. Migr.* 4 (2010) 377–381. <https://doi.org/10.4161/cam.4.3.11747>.

- [79] M.P. Nijsure, V. Kishore, Collagen-based scaffolds for bone tissue engineering applications, in: *Orthop. Biomater. Adv. Appl.*, 2018: pp. 187–224. https://doi.org/10.1007/978-3-319-73664-8_8.
- [80] Z. Tian, C. Li, L. Duan, G. Li, Physicochemical properties of collagen solutions cross-linked by glutaraldehyde, *Connect. Tissue Res.* 55 (2014) 239–247. <https://doi.org/10.3109/03008207.2014.898066>.
- [81] L.-M. Nong, D. Zhou, D. Zheng, Y.-Q. Jiang, N.-W. Xu, G.-Y. Zhao, H. Wei, S.-Y. Zhou, H. Han, L. Han, The effect of different cross-linking conditions of EDC/NHS on type II collagen scaffolds: an in vitro evaluation, *Cell Tissue Bank.* 20 (2019) 557–568. <https://doi.org/10.1007/s10561-019-09790-7>.
- [82] Y.-H. Jiang, Y.-Y. Lou, T.-H. Li, B.-Z. Liu, K. Chen, D. Zhang, T. Li, Cross-linking methods of type I collagen-based scaffolds for cartilage tissue engineering., *Am. J. Transl. Res.* 14 (2022) 1146–1159. <http://www.ncbi.nlm.nih.gov/pubmed/35273719>.
- [83] D. Zhang, X. Wu, J. Chen, K. Lin, The development of collagen based composite scaffolds for bone regeneration, *Bioact. Mater.* 3 (2018) 129–138. <https://doi.org/10.1016/j.bioactmat.2017.08.004>.
- [84] C. Xu, P. Su, X. Chen, Y. Meng, W. Yu, A.P. Xiang, Y. Wang, Biocompatibility and osteogenesis of biomimetic Bioglass-Collagen-Phosphatidylserine composite scaffolds for bone tissue engineering, *Biomaterials.* 32 (2011) 1051–1058. <https://doi.org/10.1016/j.biomaterials.2010.09.068>.
- [85] S. Toosi, H. Naderi-Meshkin, Z. Esmailzadeh, G. Behravan, S. Ramakrishna, J. Behravan, Bioactive glass-collagen/poly (glycolic acid) scaffold nanoparticles exhibit improved biological properties and enhance osteogenic lineage differentiation of mesenchymal stem cells, *Front. Bioeng. Biotechnol.* 10 (2022) 963996. <https://doi.org/10.3389/fbioe.2022.963996>.
- [86] B. Kaczmarek, K. Nadolna, A. Owczarek, O. Mazur, A. Sionkowska, K. Łukowicz, J. Vishnu, G. Manivasagam, A.M. Osyczka, Properties of scaffolds based on chitosan and collagen with bioglass 45S5, in: *IET Nanobiotechnology*, 2020: pp. 830–832. <https://doi.org/10.1049/iet-nbt.2020.0045>.
- [87] C. Xu, Y. Wang, X. Yu, X. Chen, X. Li, X. Yang, S. Li, X. Zhang, A.P. Xiang, Evaluation of human mesenchymal stem cells response to biomimetic bioglass-collagen-hyaluronic acid-phosphatidylserine composite scaffolds for bone tissue engineering, *J. Biomed. Mater. Res. - Part A.* 88 (2009) 264–273. <https://doi.org/10.1002/jbm.a.31931>.
- [88] Y. Song, H. Wu, Y. Gao, J. Li, K. Lin, B. Liu, X. Lei, P. Cheng, S. Zhang, Y. Wang, J. Sun, L. Bi, G. Pei, Zinc Silicate/Nano-Hydroxyapatite/Collagen Scaffolds Promote Angiogenesis and Bone Regeneration via the p38 MAPK Pathway in Activated Monocytes, *ACS Appl. Mater. Interfaces.* 12 (2020) 16058–16075. <https://doi.org/10.1021/acsami.0c00470>.
- [89] T. Arahira, M. Todo, Development of novel collagen scaffolds with different bioceramic particles for bone tissue engineering, *Compos. Commun.* 16 (2019) 30–32. <https://doi.org/10.1016/j.coco.2019.08.012>.
- [90] J. Becerra, M. Rodriguez, D. Leal, K. Noris-Suarez, G. Gonzalez, Chitosan-

- collagen-hydroxyapatite membranes for tissue engineering, *J. Mater. Sci. Mater. Med.* 33 (2022) 18. <https://doi.org/10.1007/s10856-022-06643-w>.
- [91] N. Ribeiro, S.R. Sousa, C.A. Van Blitterswijk, L. Moroni, F.J. Monteiro, A biocomposite of collagen nanofibers and nanohydroxyapatite for bone regeneration, *Biofabrication.* 6 (2014) 035015. <https://doi.org/10.1088/1758-5082/6/3/035015>.
- [92] F. Xing, Z. Chi, R. Yang, D. Xu, J. Cui, Y. Huang, C. Zhou, C. Liu, Chitin-hydroxyapatite-collagen composite scaffolds for bone regeneration, *Int. J. Biol. Macromol.* 184 (2021) 170–180. <https://doi.org/10.1016/j.ijbiomac.2021.05.019>.
- [93] J.H. Kim, T.H. Kim, M.S. Kang, H.W. Kim, Angiogenic Effects of Collagen/Mesoporous Nanoparticle Composite Scaffold Delivering VEGF165, *Biomed Res. Int.* 2016 (2016) 9676934. <https://doi.org/10.1155/2016/9676934>.
- [94] F. Banche-Niclot, G. Montalbano, S. Fiorilli, C. Vitale-Brovarone, PEG-Coated Large Mesoporous Silicas as Smart Platform for Protein Delivery and Their Use in a Collagen-Based Formulation for 3D Printing, *Int. J. Mol. Sci.* 22 (2021) 1718. <https://doi.org/10.3390/ijms22041718>.
- [95] E. Martins, G.S. Diogo, R. Pires, R.L. Reis, T.H. Silva, 3D Biocomposites Comprising Marine Collagen and Silica-Based Materials Inspired on the Composition of Marine Sponge Skeletons Envisaging Bone Tissue Regeneration, *Mar. Drugs.* 20 (2022) 718. <https://doi.org/10.3390/md20110718>.
- [96] C.N. Cornell, J.M. Lane, M. Chapman, R. Merkow, D. Seligson, S. Henry, R. Gustilo, K. Vincent, Multicenter trial of collagraft as bone graft substitute, *J. Orthop. Trauma.* 5 (1991) 1–8. <https://doi.org/10.1097/00005131-199103000-00001>.
- [97] T.A.G. Van Vugt, J.M.B. Walraven, J.A.P. Geurts, J.J.C. Arts, Antibiotic-Loaded Collagen Sponges in Clinical Treatment of Chronic Osteomyelitis: A Systematic Review, *J. Bone Jt. Surg. - Am. Vol.* 100 (2018) 2153–2161. <https://doi.org/10.2106/JBJS.17.01140>.
- [98] G.R.M. Matos, Surface Roughness of Dental Implant and Osseointegration, *J. Maxillofac. Oral Surg.* 20 (2021) 1–4. <https://doi.org/10.1007/s12663-020-01437-5>.
- [99] R. Krishna Alla, K. Ginjupalli, N. Upadhya, M. Shamma, R. Krishna Ravi, R. Sekhar, Surface roughness of implants: A review, *Trends Biomater. Artif. Organs.* 25 (2011) 112–118.
- [100] S. Verma, S. Mohanty, S.K. Nayak, Preparation of hydrophobic epoxy-polydimethylsiloxane-graphene oxide nanocomposite coatings for antifouling application, *Soft Matter.* 16 (2020) 1211–1226. <https://doi.org/10.1039/c9sm01952a>.
- [101] A. Cordoba, E.M. Rivera-Muñoz, R. Velázquez-Castillo, K. Esquivel, PDMS/TiO₂ and PDMS/SiO₂ Nanocomposites: Mechanical Properties' Evaluation for Improved Insulating Coatings, *Nanomaterials.* 13 (2023) 1699. <https://doi.org/10.3390/nano13101699>.
- [102] T. Christoforidou, D. Giasafaki, E.G. Andriotis, N. Bouropoulos, N.F.

- Theodoroula, I.S. Vizirianakis, T. Steriotis, G. Charalambopoulou, D.G. Fatouros, Oral drug delivery systems based on ordered mesoporous silica nanoparticles for modulating the release of aprepitant, *Int. J. Mol. Sci.* 22 (2021) 1896. <https://doi.org/10.3390/ijms22041896>.
- [103] A.A. Abd-Elrahman, M.A. El Nabarawi, D.H. Hassan, A.A. Taha, Ketoprofen mesoporous silica nanoparticles SBA-15 hard gelatin capsules: preparation and in vitro/in vivo characterization, *Drug Deliv.* 23 (2016) 3387–3398. <https://doi.org/10.1080/10717544.2016.1186251>.
- [104] F. Barboza, D.D. Vecchia, M.P. Tagliari, M.A.S. Silva, H.K. Stulzer, Differential scanning calorimetry as a screening technique in compatibility studies of acyclovir extended release formulations, *Pharm. Chem. J.* 43 (2009) 363–368. <https://doi.org/10.1007/s11094-009-0304-1>.
- [105] T.S. Radhakrishnan, Thermal degradation of poly(dimethylsilylene) and poly(tetramethyldisilylene-co-styrene), *J. Appl. Polym. Sci.* 99 (2006) 2679–2686. <https://doi.org/10.1002/app.22813>.
- [106] S. An, Y. Gao, J. Ling, X. Wei, Y. Xiao, Calcium ions promote osteogenic differentiation and mineralization of human dental pulp cells: Implications for pulp capping materials, *J. Mater. Sci. Mater. Med.* 23 (2012) 789–795. <https://doi.org/10.1007/s10856-011-4531-0>.
- [107] B.R. Genge, G.R. Sauer, L.N.Y. Wu, F.M. McLean, R.E. Wuthier, Correlation between loss of alkaline phosphatase activity and accumulation of calcium during matrix vesicle-mediated mineralization, *J. Biol. Chem.* 263 (1988) 18513–18519. [https://doi.org/10.1016/s0021-9258\(19\)81388-1](https://doi.org/10.1016/s0021-9258(19)81388-1).
- [108] M. Moncayo-Donoso, G.A. Rico-Llanos, D.A. Garzón-Alvarado, J. Becerra, R. Visser, M.R. Fontanilla, The effect of pore directionality of collagen scaffolds on cell differentiation and in vivo osteogenesis, *Polymers (Basel)*. 13 (2021). <https://doi.org/10.3390/polym13183187>.
- [109] J. Wei, J. Jia, F. Wu, S. Wei, H. Zhou, H. Zhang, J.W. Shin, C. Liu, Hierarchically microporous/macroporous scaffold of magnesium-calcium phosphate for bone tissue regeneration, *Biomaterials*. 31 (2010) 1260–1269. <https://doi.org/10.1016/j.biomaterials.2009.11.005>.